UNIVERSITY OF OXFORD

The Coupling of Nitrogen-Vacancy Centres in Diamond to tunable Open-Microcavities

by

Sam Johnson

Linacre College

A thesis submitted for the degree of
Doctor of Philosophy

Department of Materials

October 2015

Abstract

The Nitrogen-Vacancy (NV) centre in diamond possesses an optical read out of its spin state and shows great promise for applications in solid state quantum technologies. Its broad phonon assisted emission spectrum, with only 4% of emission from the zero-phonon line, is a major drawback to this. The optical microcavity will be essential in efficiently interfacing these centres with photonic networks. Here we present investigations into the coupling of NV centres in nanodiamond to tunable open-microcavities, both at room temperature and at cryogenic temperatures. These structures will be shown to achieve good photon confinement, with mode volumes down to $5\lambda^3$. Room temperature studies on ensembles of NVs will illustrate the tunable spectral and spatial overlap between the emitter and the cavity mode. It will be shown that small enhancements are possible in this regime. After the preparation and characterisation of single emitters, low temperature coupling to the narrowed zero-phonon line will be the central theme of this thesis. Single photon emission into the cavity mode is verified. We observe the enhancement of the light-matter interaction in this regime, by a 39% increase in the emission rate when cavity-coupled, with the dependence on mode volume also demonstrated. These results are important for the realisation of a spin-photon interface in scalable quantum networks.

Popular Abstract

The development of the silicon transistor heralded the advent of modern computing and the microelectronics industry. There has been an exponential growth in processing speeds since then, with its continual miniaturization. This phenomenal advance is soon to reach a fundamental limit, as transistors will be approaching the atomic scale in the near future. Further progress requires a paradigm shift in how computation is done. Efforts have turned towards the development of quantum computing, exploiting the unique properties of sub-atomic particles. This extends beyond the binary on/off capability of the transistor to exploit the remarkable quantum phenomena of superposition and entanglement, providing a rich and more powerful resource for computation. These devices are expected to enable the simulation of the most complex systems in nature, in turn accelerating new discoveries in areas such as medicine, amongst many others. The task now is to realize such a system in practice.

There are many strategies towards this goal, but Diamond is proving to be one of the most exciting platforms. We know it is coveted for its strength and gemstone quality, however its crystal imperfections are where the interest lies for quantum computing. These defects give many natural diamonds their distinctive colour and it is here that an electron can be isolated in the crystal. This can form a quantum bit or 'qubit', which is the first building block of our quantum system. To be useful for computing we need to read, write and control the qubit precisely. We also need to connect qubits together to start building a processor. Our current processors are controlled by electrical signals. With qubits in diamond this will all be achieved with pulses of *light.*

This thesis studies and develops a light-based (photonic) interface for qubits in Diamond, to allow us to connect them in a network. These consist of a controllable pair of microscopic mirrors in which a nanoscale diamond crystal is contained. In conjunction with laser pulses, we are able to use these micro-mirrors to control the way in which the qubits emit light and even make them *brighter*. If we can make them brighter, then the qubits can perform computations more quickly and with less errors, taking this from being a scientific concept, towards being an achievable technology. The information stored by the qubits is fragile, so to protect it from the environment the diamond must be put in a vacuum and cooled to temperatures around -200C or below. We show how this can be realized and demonstrate how we can control the brightness of the qubit in these conditions. These experiments form the highlight of this thesis.

Acknowledgements

This thesis cannot have happened without the Photonic Nanomaterials Group. Thank you to all group members, past and present, who have provided such a fun, stimulating working environment over the last 3.75 years. Particular thanks goes to Aurelien and Phil for the cavity fabrication and for their support and guidance, they have both been excellent role models and great company down the Royal Oak. That pretty much applies to everyone in the group too. Alex P, Lucas and Dave are acknowledged for their proofreading help. I am very grateful to Simon Fairclough for taking so much time in his final year to train me on arrival. Matthew Wincott is mentioned too, for having written the confocal software which has worked so well. Thanks must also go to people of the Materials department, Richard Turner for help with the TGA, and Colin Johnstone who trained me on the Raman Spectrometer. Ollie Williams of Cardiff University is thanked for providing nanodiamond samples. Alexia Auffeves, Gaston Hornecker and Thomas Grange of Insitut Neel, Grenoble, are gratefully acknowledged for their collaboration on the theoretical work. Thanks also to Prof. Andrew Watt for supervising me in my first year, and allowing me use of his chemistry lab. Outside of the lab there have been so many people who have made my time in Oxford so enjoyable, including 53 Divinity Road housemates past and present and my adopted home of 23 Warneford Road, thanks for having me. I have also loved being part of Linacre College, surely the best in Oxford. Also thanks to Jack, Kieran, Ed, Pete, James and Flic, it was pretty special to have so many of my Bristol friends here with me.

Special thanks must of course go to Prof. Jason Smith. Not everyone is as lucky as we are to have such a fantastic supervisor. Jason always offers excellent scientific guidance and is particularly good at offering encouragement when experiments aren't working out. He is the perfect mentor and this project is wholly indebted to him.

Finally I would like to thank my family, Paul, Tahereh and Zoe. I cannot have been here without your love, inspiration and support throughout my life. Last but not least, much love and thanks go to Isabel Roth, it's been amazing to share my PhD years with you.

Contents

List of Tables

Abbreviations

AFM	**A**tomic **F**orce **M**icroscopy
CQED	**C**avity **Q**uantum **E**lectro**D**ynamics
CVD	**C**hemical **V**apour **D**eposition
CW	**C**ontinuous **W**ave
DBR	**D**istributed **B**ragg **R**eflector
DLS	**D**ynamic **L**ight **S**cattering
ESR	**E**lection **S**pin **R**esonance
FDTD	**F**inite **D**ifference **T**ime **D**omain
FIB	**F**ocused **I**on **B**eam
FWHM	**F**ull **W**idth **H**alf **M**aximum
fND	**f**luorescent **N**ano**d**iamond
HBT	**H**anbury **B**rown **T**wiss
HPHT	**H**igh **P**ressure **H**igh **T**emperature
LT	**L**ow **T**emperature
NA	**N**umerical **A**perture
ND	**N**ano**d**iamond
NV	**N**itrogen **V**acancy
ODMR	**O**ptically **D**etected **M**agnetic **R**esonance
PCC	**P**hotonic **C**rystal **C**avity
PL	**P**hoto**L**uminescence
PLE	**P**hoto**L**uminescence **E**xcitation
PSB	**P**honon **S**ide **B**and
RIE	**R**eactive **I**on **E**tching
RT	**R**oom **T**emperature
SEM	**S**canning **E**lectron **M**icroscopy

SNR	**S**ignal to **N**oise **R**atio
SiV	**Si**licon **V**acancy
SPAD	**S**ingle **P**hoton **A**valanche **D**etector
TGA	**T**hermo**G**ravimetric **A**nalysis
ZPL	**Z**ero **P**honon **L**ine

Physical Constants

Speed of Light	c	=	$2.997\ 924\ 58 \times 10^{8}$ m s^{-1}
Planck's Constant	h	=	6.626×10^{-34} J s^{-1}
Reduced Planck's Constant	$\hbar$	=	1.054×10^{-34} J s^{-1}
Permittivity of Free Space	ε_0	=	8.85×10^{-12} F m^{-1}
Boltzmann constant	k_B	=	1.38×10^{-23} J K^{-1}

Symbols

$\mathcal{F}$	Finesse	
$\mathcal{L}$	Round Trip Loss	
Q	Q-factor	
$\mathcal{B}$	Cavity emission efficiency	
q	Longitudinal mode index	
F_P	Purcell Factor	
β	Radius of curvature	μm
L	Cavity length	μm
V	Mode volume	μm^3
w_0	Mode waist	μm
$\Delta\lambda$	Free spectral range	nm
$\delta\lambda$	Spectral linewidth	nm
$\rho(\omega)$	Optical density of dtates	
R	Reflectance	
T	Transmission	
$\mathcal{E}$	Electric Field	V m^{-1}
n	Refractive Index	
τ	Lifetime	ns
γ	Emission decay rate	Hz
$\gamma*$	Pure-dephasing rate	Hz
g_0	Atom cavity coupling rate	Hz
$\mathcal{R}$	Effective atom cavity coupling rate	Hz
κ	Cavity decay rate	Hz
ξ	Dipole orientation factor	
ζ	Debye-Waller factor	

For Paul, Tahereh, Zoe & Isabel ...

Chapter 1

Introduction

1.1 Quantum Computing

The realisation of quantum information processing (QIP) will represent a new paradigm in computation. Since the development of the traditional silicon transistor and the microelectronics industry there has been an exponential growth in processing power. The miniaturisation of the microprocessor will approach a fundamental limit in the near future, which will precipitate the break down of Moore's law [1]. Ambitions to apply computational resources to the most complex systems in nature will have to be curtailed. Efforts have turned towards the development of a quantum computer, which aims to exploit unique properties of quantum systems, namely superposition and entanglement, to provide a rich resource for computation. Since they were first conceptualised [2], there have been rigorous theoretical demonstrations of how and where quantum computers could outperform their classical counterparts. These scenarios include the factorisation of large numbers [3], integral to cryptography, and the simulation of quantum systems, leading to significant advances in the field of molecular chemistry and biology amongst others [4]. It is now the responsibility of the experimental community to realise these goals in practical terms.

The requirements of a quantum bit (qubit) are laid out by DiVincenzo [5]. The system must be prepared into a well-defined quantum state, and subsequently coherently manipulated in a deterministic fashion. The information represented by the new quantum state must be read out with a high fidelity. All of these require the system to have long coherence times, defined as T_2, such that many operations can be performed without a compromise of information. Finally these qubits must be networked together to form a scalable system. There are multiple proposals for the fundamental building blocks of a large scale quantum architecture, such as trapped ions/neutral atoms, donor spins in IV, VI, III-V group materials and superconducting qubits [1]. However there is a significant challenge in networking these together to form a realisable system. The quantum states of any system are extremely fragile, and information is readily lost through interactions with the environment. Isolating the system from the surrounds is a key requirement. This is at odds with the necessity to locate the qubits close enough to each other such that entanglement can be generated through coherent mutual interactions, thus reducing the prospects for scalability [5, 6].

This led to proposals for new ways in which to network qubits, that promise to overcome some of the aforementioned challenges [7, 8]. If a quantum system has the ability to impart its state onto a photon, then one can utilise these photons as flying qubits, to connect a network of stationary nodes, spatially separated in order to preserve their isolation and maintain long coherence times. Here the optical microcavity could mediate the spin-photon interaction and efficiently interface each node with the large-scale photonic network. The quantum computer no longer needs to consist of a single device with an array of locally interacting qubits [9]. Neutral atoms/trapped ions display amongst the best coherence times and read-out fidelities [10], linked to optically addressable atomic states. These may be the obvious choice for the realisation of distributed quantum computing, however the technical overhead in creating arrays of trapped individual ions/atoms in optical cavities has encouraged the pursuit of a solid-state alternative [11]

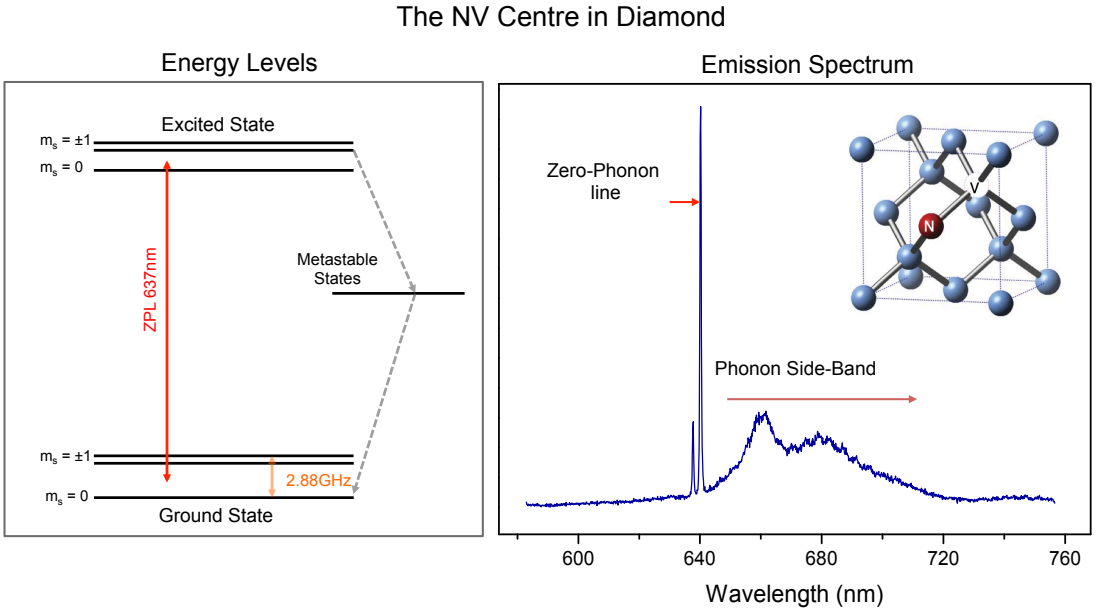

FIGURE 1.1: The NV centre in diamond. Left: the energy level structure. There is a splitting of 2.88GHz between the spin sublevels (m_s) of the ground state. The zero-phonon line (ZPL) occurs at 637nm. Spin-selective shelving into the metastable states are responsible for the spin polarisation and optical spin readout. Right: Emission Spectrum of a single NV centre in nanodiamond at 77K. The ZPL at 637nm and phonon side-band (PSB) from 640nm are indicated. Inset: the crystal structure. A Nitrogen atom sits adjacent to a vacancy site along the [111] axis, reproduced with permission from [13].

1.2 The NV Centre in Diamond

Diamond has several enabling properties that have established it as a platform for QIP. Firstly, it is a mostly spin-free lattice, with only 1.1% ^{13}C (spin = 1/2) natural abundance, which would benefit the coherence of any confined spin system. The robust mechanical properties are also of enormous practical benefit. The wide semiconductor band-gap of 5.5eV has allowed the identification of hundreds of optically emissive impurities [12]. Of these 'colour centres', the negatively charged Nitrogen-Vacancy defect (NV), shown in figure 1.1, is by far the most well studied and has been established as one of the leading candidates for solid state quantum computation.

Formed by a substitutional Nitrogen atom with an adjacent vacancy, the symmetry of the surrounding orbitals form a tightly confined, well isolated quantum system at the vacancy, analogous to a trapped atom. Crucially, the optical transitions are directly related to the spin state of the electron. The intermediate metastable states form a

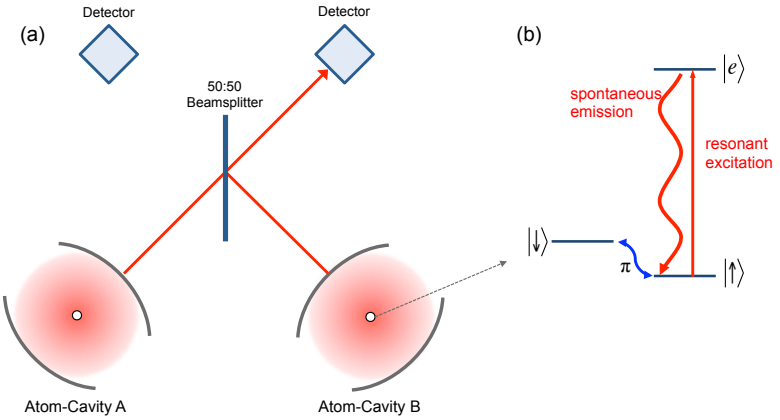

FIGURE 1.2: Scheme for generating remote entanglement by measurement. (a) Two simple atoms are situated in separate cavities. Emission is imparted onto a 50:50 beamsplitter with two-photon interference leading to detection at just one output. (b) The required atomic energy level structure. State $|\uparrow\rangle$ is linked to the optically excited $|e\rangle$. Resonant microwaves can coherently manipulate the electrons between state $|\uparrow\rangle$ and $|\downarrow\rangle$. Figure adapted from [9]

non-radiative spin-selective relaxation pathway as shown in figure 1.1, polarising the electron spin into the $m_s = 0$ level after a few optical cycles. The splitting of the ground state triplet is accessible at microwave energies and manipulation into the degenerate m_s=$\pm$1 levels manifests in reduced optical emission. This is known as optically detected magnetic resonance (ODMR). Long lived coherent control of the electron spins have been demonstrated, thus satisfying the DiVincenzo criteria [5]. The NV centre was recently the first solid-state system to have demonstrated remote entanglement of a distributed quantum system [14], which is a significant milestone in QIP. Figure 1.2 demonstrates schematically how this measurement based entanglement is generated.

The protocol follows that of Barrett & Kok [15]:

1. An electron in the ground state of each atom is prepared in the superposition state $\frac{1}{\sqrt{2}}(|\uparrow\rangle + |\downarrow\rangle)$ using resonant microwaves.

2. Excitation resonant with $|\uparrow\rangle \rightarrow |e\rangle$ is applied.

3. Spontaneous emission locally entangles the spin and photon number such that $\frac{1}{\sqrt{2}}(|\uparrow 1\rangle + |\downarrow 0\rangle)$ where ((0)1 - (no)emission)

4. The photons from both atoms are input to a 50:50 beamsplitter

5. The outcomes are measured by two single photon detectors

If the photons emitted are *indistinguishable* in all aspects, two-photon interference will result in both photons leaving the 50:50 beamsplitter through the same exit port and only registering one count. This 'path erasure' [9] provides no way of determining from which qubit the photon originated from and both A & B are projected into the entangled state $|\psi\rangle = \frac{1}{\sqrt{2}}(|\uparrow_A\downarrow_B\rangle \pm e^{-i\phi}|\downarrow_A\uparrow_B\rangle)$, where ϕ is the phase accumulated over the optical path length.

1.3 Optical Microcavities

The low temperature emission spectrum of the NV centre is shown in figure 1.1. There is a sharp zero-phonon line (ZPL), akin to an atomic transition, corresponding to just 4% of the emission, with the rest emanating from the phonon side band (PSB). For the generation of indistinguishable photons, only the ZPL emission will be of use. It is clear that this will result in very low entanglement generation efficiencies. The recent demonstration of remote entanglement achieved one event/10 mins, requiring a week long experimental run to verify [14], even with the aid of enhanced light collection techniques.

The role of the optical microcavity will be to offer both enhanced light collection *and* the enhancement of the *light-matter interaction* by selectively coupling to the ZPL of the NV centre, and increasing its proportion of the total emission, through the Purcell effect. The optical microcavity will be central to realising this system as a viable technology.

This thesis will present the coupling of the NV centre in diamond to tunable open-microcavities as in figure 1.3. It is proposed that these will help realise an efficient, scalable, spin-photon interface for use in distributed quantum networks. There are many competing strategies for optical microcavitation. This thesis will demonstrate the key, enabling features of the open-cavity - namely the in-situ, facile, tuning of the optical resonances by adjusting the substrate separation, and the direct access of the

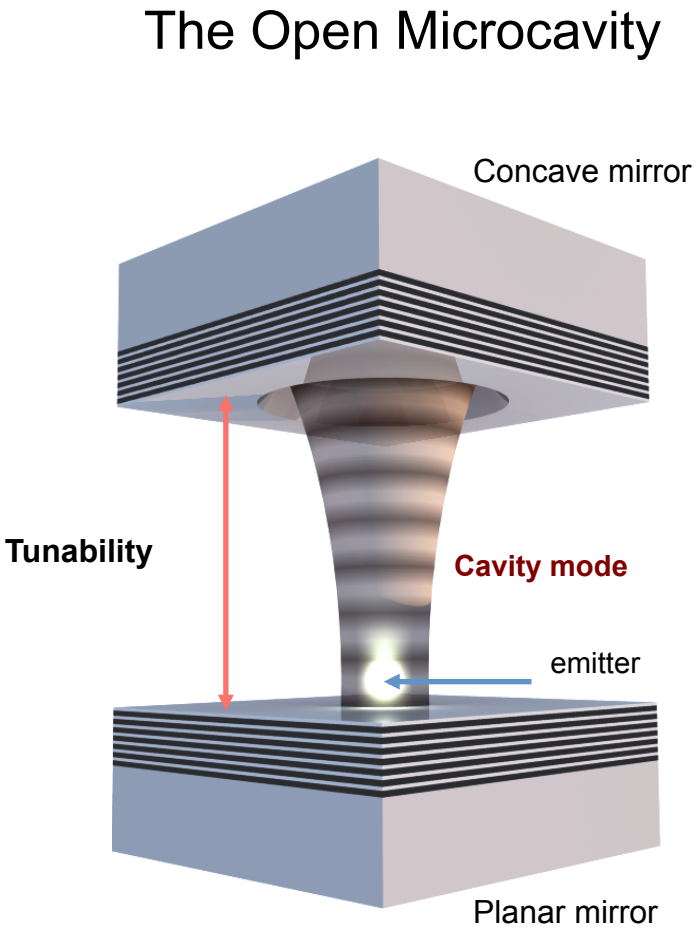

FIGURE 1.3: A schematic of the open-cavity system. Figure courtesy of David Coles.

emitter to the electric field of the cavity. The resonators take the form of highly-reflective Fabry-Perot mirrors with a planar-hemispherical geometry. The compelling advantage of the resonators fabricated within this reach group, are the ultra-small mode volumes that can be achieved through focused ion-beam (FIB) fabrication of the hemispherical features. The fundamental objective of this project is to couple to the ZPL of a single NV centre at cryogenic temperatures. It is in this regime where the enhancement of the light-matter interaction will be maximised. This will be a central constituent for the development of scalable measurement-based entanglement schemes in the future. This would also represent the first time that a tunable open-resonator has been applied to a single-colour centre at low temperature.

1.4 Thesis Outline

In the build-up to the low temperature NV-open cavity coupling experiments which are the focus of this project, the thesis will be structured as follows:

Chapter 2: Literature Review

A discussion of the NV centre will first take place, focusing on the key experimental and theoretical developments that enabled the demonstration of remote NV entanglement by measurement. The diversity of applications of the NV will also be briefly mentioned along with other notable colour centres in diamond. The review will then discuss the alternative strategies for NV-cavity coupling. This will concentrate on systems for which an observable Purcell emission enhancement has been achieved, which will encompass the monolithic all-diamond resonators and the hybrid-approaches. It will be seen that the open cavity possesses an advantage over these strategies with regards to their tunability. The open cavity literature will then be reviewed. It will be seen how the FIB milled cavities are distinguished from the alternative strategy of CO_2 laser ablation, which will require an appreciation of the fabrication process.

Chapter 3: Theoretical Background

The fundamental theoretical elements required to describe the NV-open-cavity coupling process, will be discussed in three parts. Firstly the open-resonator will be presented, with the concept of the Hermite-Gaussian beam being required fully describe the optical modes of the resonator. Secondly a consideration of the basics of cavity quantum electrodynamics are needed to understand how best to maximise the light-matter interaction in the weak coupling limit - the Purcell effect. Finally an overview of the NV centre will be given, the energy level structure, so crucial in defining the spin-readout mechanism, and the vibrational mechanisms responsible for the undesirable PSB emission. The temperature-dependent dephasing mechanisms of the ZPL are also stated, as these are critical when considering experimental design and the theoretical analysis framework. The chapter will

conclude with a consideration of the established NV-cavity coupling models and finally to anticipate the Purcell factors that are achievable within the experimental constraints of this project.

Chapter 4: Experimental Methods

The cavity fabrication process is first outlined (conducted by Philip Dolan & Aurelien Trichet). The materials characterisation methods necessary in preparing suitable nanodiamond samples will then also be discussed here, along with the optical spectroscopy, cavity mounting and low temperature protocols. Finally there are several experimental aspects of NV-cavity coupling that must be understood and overcome for a successful experiment. These will be discussed in depth.

Chapter 5: Room Temperature Cavity Coupling

This chapter describes the first experiments into NV-cavity coupling which were conducted at room temperature (RT). To aid with the development of the set-up, bright fluorescent nanodiamonds (fNDs) containing multiple NV centres were used. It will be seen that the open-cavity system, is the ability to directly compare the emission in and out of the cavity, for the same emitter. This experimental design enables small enhancements to be quantified through the relative emitted spectral intensity. The effective Purcell factor is established to be 3% in the bad emitter regime. The mode volume dependence is demonstrated with a reasonable comparison to theory. Such an observation is enabled by the small mode volumes of the FIB milled open-resonator. Finally the cavity mode structure will be mapped out with the NV emission. It will be shown here how the emitter can be directly placed at the electric field maximum.

Chapter 6: Characterisation of Single NV Centres in Nanodiamond

The NV centres here are hosted in nanodiamond (ND). Aggregation, as a consequence of their synthesis, is common, prohibiting the regular identification of single NV centres. It is necessary to use an air-oxidation process to selectively etch the graphitic material whilst keeping the diamond intact. For this a parameter space investigation was carried out to determine the optimal thermal conditions. Single

NV centres are regularly identified on application of this surface treatment. A survey of the optical and spectral properties will be presented. Prominence will be given to the NVs for which the low temperature cavity coupling will be conducted.

Chapter 7: Low Temperature Cavity Coupling

Here the main results of this thesis are presented: the low temperature (LT) coupling of a single NV to an open cavity. This will fully demonstrate the capability of this system. The controlled tuning of the cavity mode across the ZPL of the NV centre is shown, with single photon emission into the cavity mode verified. The observation of an increased cavity coupled emission rate establishes the enhancement of the light-matter interaction. A theoretical discussion of these results is presented (work in collaboration with Alexia Auffeves, Gaston Hornecker, Thomas Grange of Institut Neel in Grenoble).

Chapter 8: Conclusions

Here the thesis will be summarised and the future outlook discussed

Chapter 2

Literature Review

Colour centres in diamond are firstly discussed, focusing predominantly on the NV centre. A review of the NV literature will be organised as a series of milestones that made the demonstration of remote entanglement possible. However, an appreciation of the diversity of NV research will also be given. It is also necessary to review the synthesis and materials properties of nanodiamond along with methods for purification.

This chapter will then highlight the progress that has been made in coupling NV centres to optical microcavities. Within cavity quantum electrodynamics (CQED) there are a multitude of strategies that aim to enhance the light-matter interaction. The reader is directed to Vahala [16] for a general overview of optical microcavities. The strategy taken here is to review the pre-eminent NV-cavity coupling papers in-depth. Through this an exposure to the diversity of CQED will be gained. The differing efforts are split into the following sections. The monolithic, all-diamond, resonators, that are fabricated in the bulk material, which have shown some of the best NV-cavity emission enhancements. Then there are the hybrid-approaches. Here the resonator is external to the diamond material and the with efforts mostly restricted to room temperature experiments.

The open cavity system will then be introduced. It is important to gain an understanding of the relative merits of these two main approaches and for this reason the construction of the CO_2 ablation and FIB milling process will be briefly discussed. This will be followed

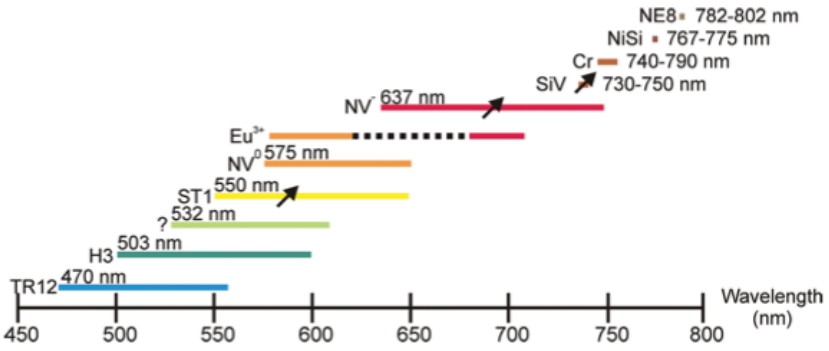

FIGURE 2.1: A summary of the single emitters discovered in diamond to date. The spectral emission bands are shown. Arrows indicate centres for which spin-dependent optical properties have been identified. Reproduced with permission from [18].

by a review of the NV-open-cavity coupling experiments that have been demonstrated to-date, which have been conducted at room temperature.

It must also be stated that this review will only discuss structures that could enhance the light-matter interaction. There are a vast-number of strategies that focus on improving the light-collection. These include solid-immersion lenses, diamond nanowires and waveguides, the reader is directed to Aharonovich [17] for a comprehensive review.

2.1 Colour Centres in Diamond

Permutations of substitutional impurities and vacancies in the diamond lattice combine to form the multitude of optically emissive 'colour centres' observed. Nitrogen is readily incorporated as a substitutional ion and is the most common impurity, giving rise to the two general classifications of diamond materials. Type I, with Nitrogen as the predominant impurity in concentrations >20 ppm (parts per million), and Type II that are generally Nitrogen-pure. Further relevant sub-divisions of these classes are stated as Type Ib: the majority of Nitrogen is in single substituional form, and Type IIa: ultra-pure diamond with <20ppm Nitrogen concentration. Despite the rich variety of centres observed, there are relatively few that have been identified as single photon emitters. These are summarised in figure 2.1

This review will focus on the NV^- centre. However, notable amongst the alternative single photon emitters in diamond is the negatively charged Silicon-Vacancy centre (SiV^-). This has demonstrated some outstanding spectral properties with up to 70% of the emission into its ZPL, with a narrowband room temperature linewidth down to 0.7nm (compared to 4% and 2.7nm for the NV), ideal for applications as single photon sources. More is becoming known about this centre all the time and the electronic structure has only relatively recently been established [19, 20]. Recently it was observed to possess spin dependent optical transitions at low temperature and high magnetic fields [21].

2.1.1 The NV^- Centre

The entanglement of remote NV centres, described in chapter 1, is the culmination of over 50 years of concerted research since the first optical studies. This section will present a chronological overview of the key papers and technological advances that made this feat possible.

1965 *Du Preez*: The first systematic studies into the 1.945eV (637nm) optical emission band in diamond, observed after the electron irradiation and subsequent 900K annealing of type 1b material, representing the first recipe for defect generation [22].

1977 *Loubser & van Wyk*: Low temperature electron spin resonance (ESR) studies of the NV centres ensembles reveal a paramagnetic spin-triplet state with 2.88GHz energy splitting [23]. This is only observed under continuous optical excitation.

1988 *Glasbeek et al*: The first ODMR experiments at low temperature [24]. An attenuation of the fluorescence signal is observed at the 2.88GHz frequency of the triplet state. The triplet is here assigned to be the ground state of the NV centre. The significance of this is that any electron spin coherence will not be limited by the lifetime of an excited state. The authors demonstrate coherent spin manipulation of the defect centres.

1997 *Gruber et al*: Scanning confocal microscopy and magnetic resonance of single NV centres [25]. By systematically lowering the electron irradiation dosage in defect generation, single NV centres are isolated. With continuous wave (CW) laser excitation, the pump rate is sufficient to maintain a spin polarisation in the ground state, allowing for room temperature ODMR. This paper represents one of the first examples of scanning confocal microscopy as a tool in the study and characterisation of point defects in diamond. This is a seminal paper, largely responsible for the subsequent flourishing of NV research.

2000 *Kurtsiefer et al*: The NV centre is revealed as a single photon source by the observation of non classical photon anti-bunching via Hanbury-Brown Twiss (HBT) interferometry measurements [26] (described in section 3.3.4). The remarkable photostability was also demonstrated. The NV is here seen to have great potential for experiments in quantum optics.

2004 *Jelezko et al*: Observation of coherent oscillations of a single electron spin [27]. One of the first such demonstrations in a solid state system. Coherent control is demonstrated for up to 2μs at room temperature. The NV centre is here established as a leading solid-state spin qubit candidate with the additional benefit of an optical readout mechanism. This raises the prospect of photonic network integration.

2006 *Tamarat et al*: Demonstration of electrostatic control over the optically excited state [28]. The importance of this work is twofold: Firstly this is the first observation of transform-limited emission lines of just 13MHz spectral linewidth, made possible by studying NV defects in type IIa materials, which do not suffer from excessive inhomogeneous broadening. Secondly, the controlled energy level tuning is essential in achieving two photon quantum interference from distinct centres (as discussed in section 1.2).

2009 *Balasubramanian et al*: Isotopic engineering of Diamond. The ^{13}C isotope has 1.1% natural abundance, with a nuclear spin-1/2, which creates a spin bath in the

diamond lattice, one of the primary sources electron spin dephasing. Isotopically pure CVD grown diamond with 0.3% ^{13}C abundance. The extended coherent control is demonstrated over $T_2 = 1.8$ms.

2009 *Batalov et al*: Determination of the excited state structure and properties at low temperature [29]. Detailed investigations into the excited state establishes a complete picture of the energy level structure, allowing the optical transitions linking the spin sub-levels to be discriminated. This enables spin-photon entanglement.

2010 *Togan et al*: Spin-photon entanglement [30]. Here the electron spin state is imparted onto the polarisation state of a photon. This is a fundamental constituent of distributed quantum networks.

2010 *Hadden et al*: Improvement of NV photon collection [31]. Integrated solid immersion lenses are FIB milled into the diamond crystal. These negate the refraction losses at the planar diamond-air interface, improving photon collection by a factor of 10. There is no requirement for the NV defects to be close to a surface, thus preserving the coherence properties.

2012 *Sipahigil et al, Bernien et al*: Demonstration of two-photon interference, (described in section 1.2), from distinct NV centres, the central constituent of protocols to entangle spatially remote quantum systems. The distinction between these papers is related to the proximity of the separated NVs [32] [33].

This list is by no means exhaustive, representing just a fraction NV related research. It is important to mention that the coherence times demonstrated for the electron spin are sufficient to observe coupling to nearby ^{13}C nuclear spins [27] owing to the fact that 11% of the electron wave function is distributed over the nearest neighbour carbon atoms. Their mutual hyperfine interaction allows for a transfer of a quantum state between the two [34]. Nuclear spins are well isolated from their environment offering a long term storage mechanism in quantum information protocols. The local entanglement between these nuclear spins has also been demonstrated at room temperature [35].

Aside from quantum information the NV centre has established itself as a pre-eminent magnetic field sensor. NV centres in nanodiamond have been incorporated onto AFM probes creating scanning magnetometers [36], sensitive to both stationary and alternating fields [37]. Coherent spin control mechanisms are again allowing the sensitivity of these devices to reach unprecedented levels allowing for the detection of a single electron spin [38], and even proton nuclear magnetic resonance [39, 40]. For a review of NV magnetometry see Rondin et al [41]. Within sensing, NVs have alternatively been applied as electric field sensors [42] and even in thermometry [43]. The operation of these sensing mechanisms under ambient conditions has lead to applications in biological specimens [44, 45]. This brief overview gives an appreciation for the diversity of applications in which the NV is now found.

Despite natural occurrence, it becomes desirable to generate these defects artificially. Two approaches are commonly taken, either a Nitrogen ion implantation in type IIa material, or a vacancy generation in type Ib. An annealing process then takes place in a vacuum environment. Above temperatures of 600C, vacancies will become mobile in the lattice and become trapped by substitutional Nitrogen.[46]. Nitrogen ion implantation has recently shown transform limited NV-ZPL emission [47].

2.1.2 Nanodiamond

NV centres hosted in nanodiamond are the material of choice in this project. These are fabricated by high-pressure high-temperature (HPHT) methods. Their synthesis and preparation are reviewed here. Nanodiamonds were initially discovered as a product of the detonation of TNT (trinitrotoluene) in chambers with a CO_2 atmosphere [48]. The shockwaves within the detonation blast provide the HPHT conditions necessary for the formation of the diamond phase of Carbon (sp^3 orbital hybridisation). However, many unwanted forms of graphitic (sp^2 hybridised) Carbon occur as a by-product [49]. HPHT synthesis is also available via mechanical presses. Using graphite as a precursor, local explosions occur in the presence of a catalyst [48]. Materials from HPHT synthesis need

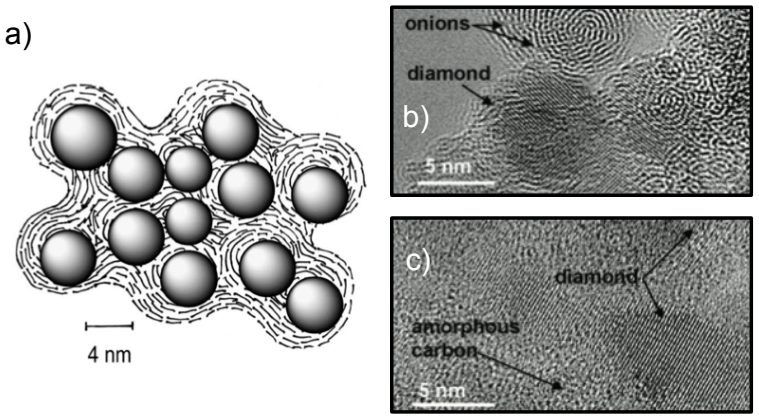

FIGURE 2.2: (a) A simple model of aggregated nanodiamond crystals after detonation synthesis. The particles are bound in graphitic shells and soot which need to be separated. The primary particle sizes are found to be in the region of 5nm. Reproduced with permission from [51]. (b) & (c) Transmission electron micrographs of the post detonation aggregates. Amorphous carbon and graphitic shells, termed onions, are found to bind them tightly together. Reproduced with permission from [52]

subsequent purification. CVD (chemical vapour deposition) has been shown to grow nanodiamond of good crystalline quality but with low yield [50].

The resultant nanodiamond particulates are often bound together in graphitic shells, as shown in figure 2.2. These matrices are covalently bonded preventing de-aggregation using high power sonication [49]. Aggressive surface treatments are required, all of which work on the principle that graphitic Carbon is more easily broken down than the diamond form. Wet chemistry techniques using combinations of oxidising acids have been shown to be successful to this end, involving tri-acid refluxing (Sulphuric, Nitric & Percholric) for up to three days [53, 54]. Osswald [52] presented a thermal oxidation technique. Through thermogravimetric analysis (TGA) and Raman spectroscopy (see chapter 4), they demonstrated selective etching of the sp^2 whilst maintaining the sp^3 phase. Gaebel et al [55] took this one step further and demonstrated controlled etching of the sp^3 phase as a method for reducing primary nanodiamond size. Hees and Williams [56] demonstrated that annealing in a Hydrogen atmosphere was efficient in obtaining a mean particle size of 3nm measured by dynamic light scattering (DLS). The materials characterisation and purification process is the subject of section 6.1.

2.2 Optical Microcavities

2.2.1 Monolithic Diamond Resonators

Photonic crystal cavities (PCCs) rely on a periodicity in the dielectric environment to confine the photon to a particular dimension as seen in figure 2.3. This periodicity is usually realised by the patterning of well defined holes into the material. Confinement in the remaining dimensions is achieved through total internal reflection at the interface. These structures are capable of achieving extremely small mode volumes with good Q-factors. Both 1D & 2D PCCs have been fabricated in bulk diamond with the first successful demonstration of high Q PCCs by Riedrich-Moller et al [57], achieving mode volumes $V = 1.5\ (\frac{\lambda}{n})^3$ (2D PCC) and $V = 0.7(\frac{\lambda}{n})^3$ (1D PCC). Tuning of the cavity resonances presents a technical challenge for all monolithic structures. The structure needs to be precisely modified to bring the mode into resonance with the emitter. Coupling to SiV centres was demonstrated here, with tuning enabled by repeated thermal etching steps. Faraon et al [58], have observed some of the most significant enhancements of the NV emission rate into PCCs. A 200nm diamond membrane was initially produced using reactive ion etching (RIE) in an Oxygen plasma. The authors fabricated PCCs using standard semiconductor masking and patterning techniques, combined with additional RIE. A Finite Difference Time Domain (FDTD) simulation of the structure is shown in 2.3.

The PCC shown in figure 2.3 offers V=$0.88(\frac{\lambda}{n})^3$. Here the tuning is achieved through the condensation of Xenon gas on the surface of the structure at cryogenic temperatures. Lifetime measurements showed a factor of 3 change in the decay rate. Due to branching of the emission into the ZPL, dictated by their measured value of the Debye-Waller factor (ζ=0.03%), this corresponds to a Purcell factor of $F_{\mathrm{P}} = 70$ (see section 3.2.2). Single photon emission from the cavity coupled ZPL was verified with an HBT measurement with $g^{(2)}(0) = 0.38$ (see section 4.5 for details of the measurement).

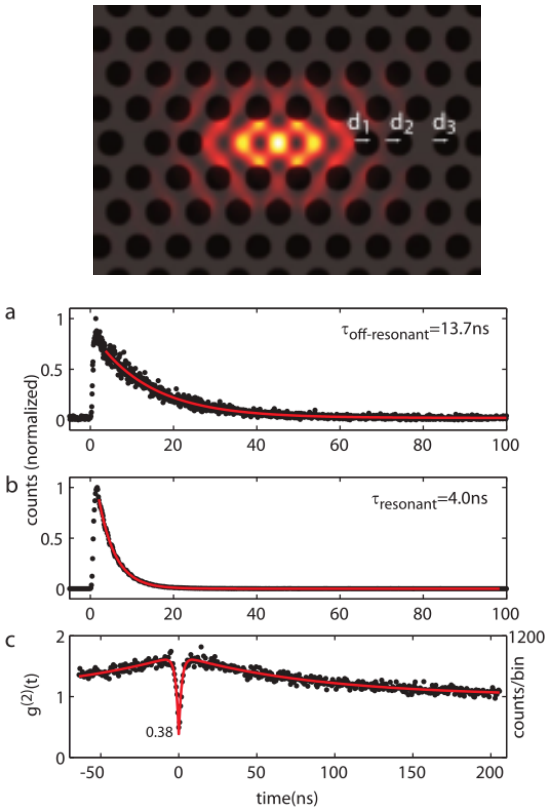

FIGURE 2.3: Top: FDTD simulation of the electric field intensity in the integrated 2D PCC. Periodic hold spacing d is shown. (a) Lifetime of the ZPL with the cavity mode off resonance. (b) Lifetime of the ZPL with the cavity mode on resonance. (c) HBT on the ZPL. Reproduced with permission from [58].

Equally impressive results have been demonstrated for NVs in 1D PCCs. Through their strip-like design, these cavities couple well to propagating waveguide modes, which makes them attractive for incorporation into quantum networks. Li et al [59] fabricated the structures shown in figure 2.4. The figures of merit for this structure were observed to be Q=9900 with V=1.05$(\frac{\lambda}{n})^3$. The starting materials underwent nitrogen ion implantation, giving a statistical density of NV defects in the crystal. By patterning many nanobeams into the diamond, the authors were able to obtain cavity-coupled NVs through a statistical process.

The whole PL spectrum when tuning the cavity into resonance can be observed. Being able to monitor the total intensity on and off resonance, showed a fraction $\mathcal{B} \approx 50\%$ of the emission being channelled into the cavity mode (see section 3.2.2). Fluorescence lifetime measurements gave $F_{\mathrm{P}} = 62$ where ζ =0.019. Unlike the majority of NV-cavity coupling experiments presented here, this paper proceeds to demonstrate that the coherent spin

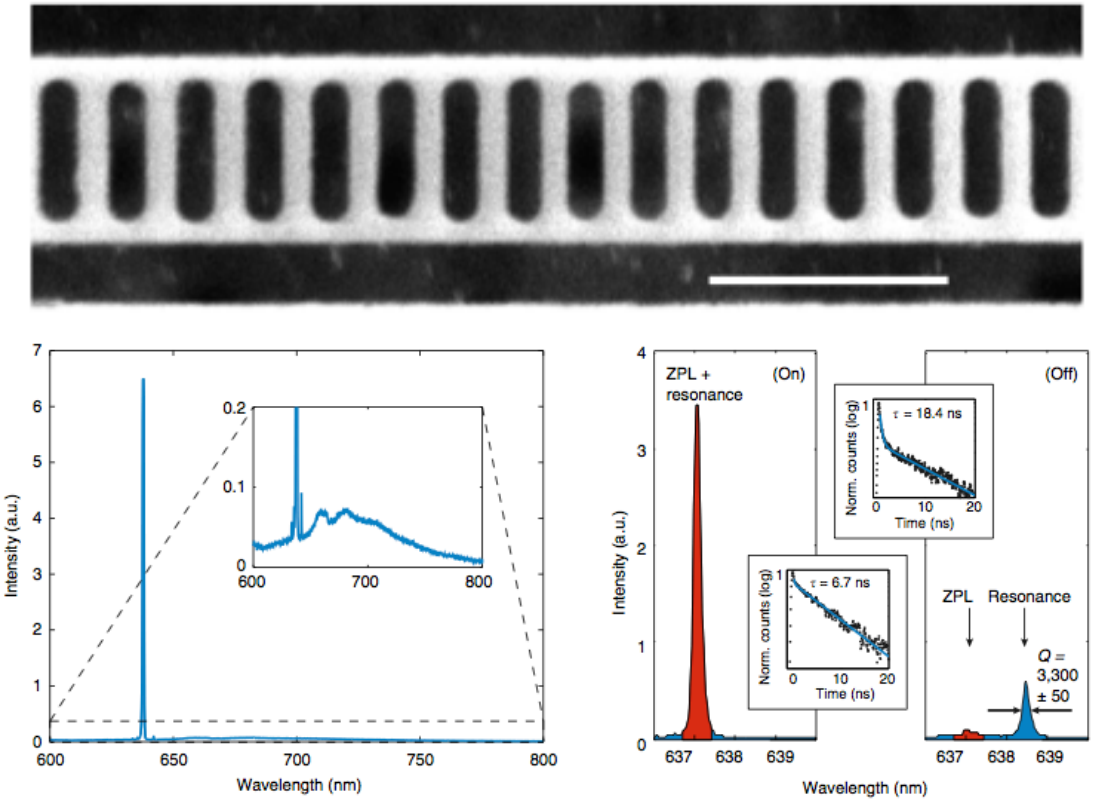

FIGURE 2.4: a) Above: Nanobeam cavity in diamond. The scale bar represents $1\mu m$. Left; Spectrum of the single NV centre with the cavity mode in resonance with the ZPL. Right: Tuning the nanobeam cavity into resonance with the ZPL, the lifetimes corresponding to the on and off resonant cases are shown inset. Reproduced with permission from [59].

control of the electron is unaffected upon fabrication of the resonator. This is often a concern when defining surfaces close to the defect as free electrons spins contribute a fluctuating, inhomogeneous magnetic field.

Hausmann et al [60] have also explored the creation of 1D PCCs. here the authors demonstrate both red and blue turning of the cavity resonances. In this work they found red tuning via Xe gas deposition to be much more controllable, and a 7nm fine tuning was demonstrated. The structures here are therefore initially fabricated to define the cavity mode at the blue spectral end of the ZPL position. The Xe condensation process is reversible to the extent that the condensation evaporates upon taking the system to room temperature. Coupling of the cavity modes was demonstrated to give $F_{\mathrm{P}} = 7$ on the ZPL, determined by inspection of the on and off resonant intensity. The metrics here were V=$3.7(\frac{\lambda}{n})^3$ and $Q = 1634$.

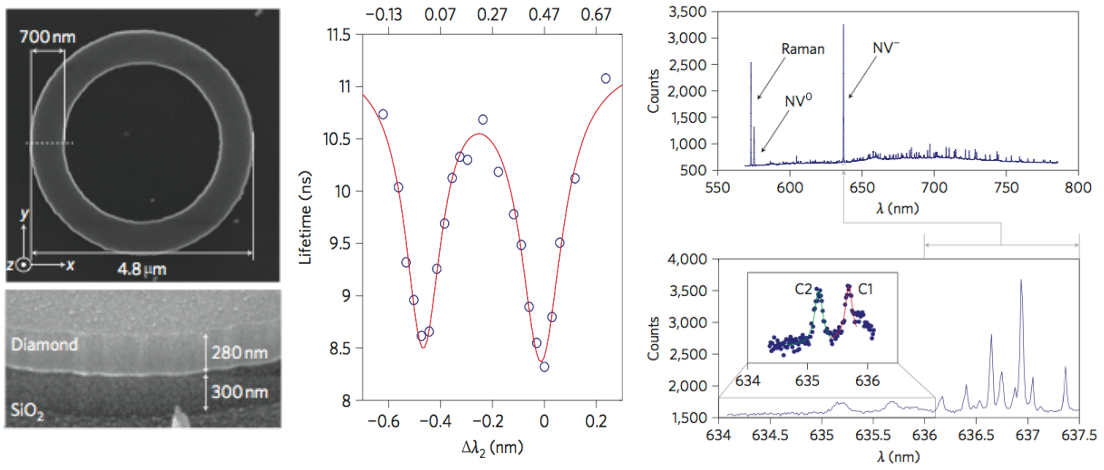

FIGURE 2.5: Left: SEM micrographs of the diamond microring resonator on a Silicon substrate. Centre: The lifetime of a NV ZPL as a function of cavity detuning. Two cavity modes of the resonator are tuned across the ZPL. Right: The PL spectra of the NVs. One can see many modes of the resonator coupling to the PSB. There are many NV centres present in the collection region. The cavity modes C1 and C2 are shown inset, detuned from the ZPL. Reprinted with permission from [61].

An alternative all-diamond approach is to fabricate microring resonators. Rather than relying on a periodicity in the refractive index to confine the light, these rely on total internal reflection at the interface before eventually coupling out of the structure. Faraon et al [61] developed mirroring resonators consisting of 280nm diamond membranes with a 4.3μm outer diameter, as in figure 2.5. The structures had mode volumes in the range V=17-32$(\frac{\lambda}{n})^3$, with $Q = 4000$. Originally the diamond had a significant NV defect density, such that many centres were being interrogated simultaneously in one confocal spot. One observation is that the fabrication of the resonator incorporates strain into the membrane, leading to an initial 20GHz ensemble linewidth being spread out over 1THz allowing them to be individually resolved. Another feature of these devices is the plethora of cavity modes that are supported, as observed in the coupling to the PSB in figure 2.5. With multiple ZPLs the cavity modes are only distinguished by observing their tuning. The modes C1 and C2 were postulated to be two counter propagating modes of the ring resonator. As a clear demonstration of cavity-coupling, the fluorescence lifetime was measured as a function of cavity detuning, shown as both cavity modes tune through the ZPL. A Purcell factor of $F_{\mathrm{P}} = 12$ was achieved corresponding to a fraction $\mathcal{B} = 25\%$ of the total emission rate.

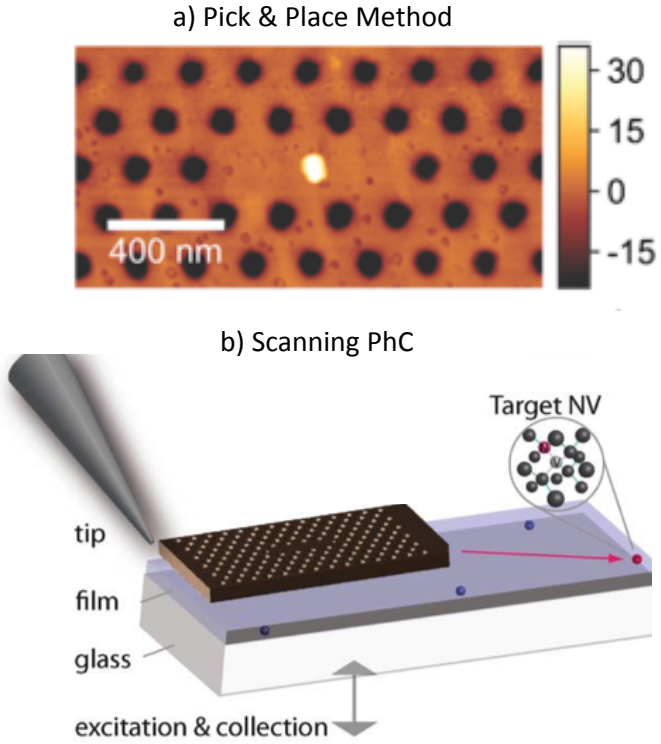

FIGURE 2.6: (a) Above: AFM image of diamond nanocrystal upon successful manipulation and positioning on top of the PCC. Reprinted with permission from [62]. (b) The opposite approach. A tungsten tip manipulates a PCC substrate allowing deterministic placement over a desired nanodiamond. Reprinted with permission from [63].

2.2.2 Hybrid Approaches

Hybrid approaches to NV-cavity coupling usually comprise of the resonator fabricated from a non-diamond material commonly Gallium Phosphide (GaP) - with the emitter located externally. Several novel approaches have been demonstrated to this effect. Using a PCC fabricated from GaP, V=0.75 $(\frac{\lambda}{n})^3$, Wolters et al [62] used a pick and place method to position a pre-identified NV centre, hosted in nanodiamond, at the centre of the PCC. The tuning method in this case was through heating of the PCC with a high energy laser - it was postulated that the GaP oxidised, changing the refractive index and bringing the mode into resonance. However this resulted in compromised Q-factors from Q=1000 to Q=600. Inspection of the peak in ZPL on and off resonance yielded $F_{\mathrm{P}} = 12$.

The opposite approach was taken by Englund et al [63]. Nanodiamonds were situated in a PMMA film. Using a tungsten tip, a GaP PCC was manipulated on the surface of

the film, deterministically bringing the cavity towards to the emitter. The group used a 2D PCC similar to those above. Lifetime measurements were taken showing a change from $\tau = 16.4$ns to $\tau = 12.7$ns. However this is primarily attributed to the substantial change in the refractive index environment upon placing the GaP (n=3.4) PCC over the selected nanodiamond. Channelling of the NV emission into the cavity mode was observed. Both of these Hybrid approaches are summarised in figure 2.6.

2.2.3 Open Cavities

Coupling of NV centres to open-cavities is the central theme of this thesis. These consist of two opposing mirrors with separation L, as in a Fabry-Perot resonator. A spherical mirror, with radius of curvature β, provides transverse confinement, whilst also ensuring it is robust to misalignment. A key figure of merit for the resonator quality is the finesse $\mathcal{F}$, depending on the reflectivity of the mirror coatings and the optical quality of the surfaces. The principles of Fabry-Perot resonators are well understood (outlined in chapter 3), with such structures used extensively in laser technology for many years [64]. However key advances in design and fabrication have enabled the minimisation of β, allowing for small V. These have rendered them useful for emitter-cavity coupling experiments, with the compelling advantages of the direct access of the emitter to the electric field maximum and their inherent tunability. This overcomes the technical challenges presented by monolithic and hybrid resonators discussed so far.

2.2.3.1 Fabrication

Whilst this project focuses on open-cavity NV coupling experiments, it is the FIB milling process that differentiates the resonators used here with alternative strategies. There have been several approaches to constructing these types of concave features, all them with the goal of combining small mode volumes and high finesse. These include wet etching techniques [65], deposition and lifting off mirrors from concave surfaces [66] [67] and bubble trapping in glass to create highly smooth spherical surfaces [68]. These have

achieved a minimum of $\beta = 10\mu$m and finesses of up to $\mathcal{F} = 10^3$. However these have been surpassed by the techniques of CO_2 laser ablation and FIB.

CO_2 lasers are commonly used in the surface treatment of silica substrates. With a wavelength of $\lambda = 10.6\mu$m, it is strongly absorbed by vibrational modes in silica. This local heating effect causes melting and evaporation. Working in a regime where surface evaporation dominates, with melting being restricted to just a thin layer of the surface, this results in a concave imprint into the silica. The molten layer of silica results in an extremely low surface roughness as the surface tension smoothes out the concave feature. This has been used to great effect in producing high finesse optical microcavities, and CO_2 ablation is currently being pursued by a growing number of groups round the world [69–73]. The current state of the art is summarised in table 2.1.

TABLE 2.1: CO_2 Laser Ablation: State of the Art

Author	$\beta(\mu$m)	σ_{rms} (nm)	$\mathcal{F}$	V$(\frac{\lambda}{n})^3$
Hunger 2012 [71]	20	0.2	-	-
Hunger 2010 [72]	45	0.2	1.3×10^5	42
Muller 2010 [69]	60	0.4	1.3×10^5	154
Greuter 2014 [73]	13	0.2	1.5×10^4	2.3

Recently Greuter et al [73] pushed the geometrical limits of this technique to β= 13μm with V =2.3$(\frac{\lambda}{n})^3$. The relationship between feature depth and radius of curvature is shown in figure 2.7. This figure shows that in order to achieve smaller radii of curvature, a greater imprint depth is required. Through an improved alignment of the substrate and the ablation beam, they are able to ablate further into the material, corresponding to an imprint depth of 1μm. eventually one enters a regime where the depth $> \beta$ where no stable cavity modes are able to form. Post processing will become necessary to develop this technique further.

The FIB is an established machining tool within materials science and the semiconductor industry. Consisting of an accelerated ion beam, that is shaped by magnetic lenses, very narrow focal spots are achieved from 1μm down to 5nm depending on the beam current. This allows for great control over the size and shape of the concave mirrors. Crucially it

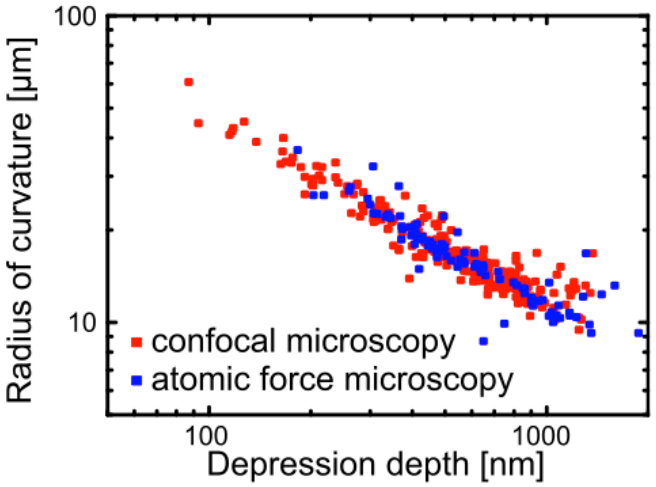

FIGURE 2.7: Relationship between feature depth and radius of curvature for CO_2 ablated cavities. The data points show measurements from the cavity mode spectra (red) supported by Atomic Force Microscopy (AFM) measurements of the surface profile. Reprinted with permission from [73].

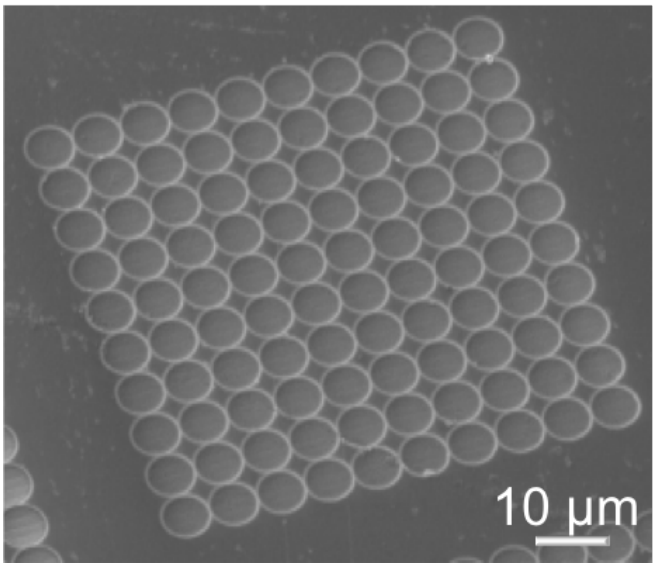

FIGURE 2.8: Scanning electron microscopy (SEM) image: Arrays of $\beta = 25\mu$m cavities FIB milled onto a Silicon substrate. Reprinted with permission from [74].

allows for very small radii of curvature to be produced, combined with a shallow feature depth, thus allowing the cavity systems to form stable modes such that $L < \beta$.

The structures in figure 2.8 were first demonstrated in 2010 by Dolan et al [74]. Arrays of concave features with $\beta = 25$, 12 & 5μm are milled onto silica substrates. The larger cavities displaying a finesse which was only 12% less than theoretically expected from the coating reflectivities. After improvements in the mirror separation, mode volumes of

$V = 1.9(\frac{\lambda}{n})^3$ were reached in later work, amongst the smallest mode volumes achieved in an open-cavity system [75]. There are now multiple research groups pursuing the FIB milling of cavities. Albrecht et al have incorporated FIB milling on fiber facets, with low surface roughness of $\sigma_{\text{rms}} = 0.3$nm [76]. Mai et al [77] have reported FIB milled open cavities down to $0.4\mu\text{m}^3$ in volume however this was a simulated value.

2.2.3.2 Coupling Experiments

To date there have only been room temperature studies of NV coupling to open-cavities. With the requirement that $L < \beta$, there are just a few microns separating the substrates, meaning that NV centres hosted in nanodiamonds are most easily incorporated into this structure. Albrecht et al [78] were the first to demonstrate single NV centre coupling to a fiber integrated cavity. The broad PSB emission allows for single photon emission into the cavity mode to be displayed over a wide spectral range. With the cavity parameters in their system, no lifetime change was expected as the Purcell factor was only anticipated to be $F_{\text{P}} = 10^{-2}$. By performing saturation measurements on the cavity mode coupled at the ZPL and PSB maximum respectively, the saturations counts were observed to be $I_{\text{sat}} = 770(3700)$photons/s, beyond the 2photons/s value expected from spectral filtering effects. Outside the Purcell regime, the cavity coupling was well described by a dephasing assisted regime, allowing for predictions of the emission rate into the cavity mode (details of this model are described further in section 3.4.1).

As a development of this work the same group constructed an all fiber cavity consisting of a concave-concave design. One facet was CO_2 ablated, whilst the other was FIB milled. Using an AFM pick-and-place technique similar to those outlines by Wolter et al [62], they deterministically placed a pre-selected single NV nanodiamond into one of the milled facets. The all-fiber approach offers a ready integration with photonic networks [76].

Kaupp et al [79] explored NV cavity coupling with bright fNDs with up to 300NV centres per crystal. This was to overcome the background fluorescence and explore the scaling

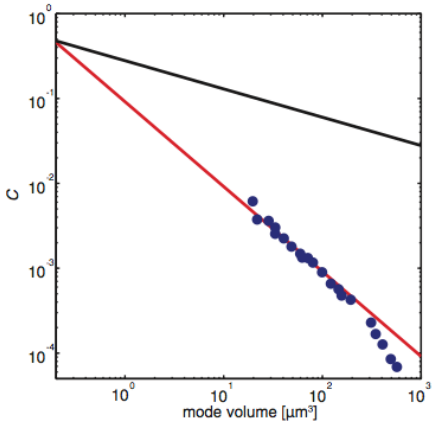

FIGURE 2.9: The scaling of the effective Purcell factor (C) with mode volume in the bad emitter regime, for NV centres coupled to a fiber cavity of $\beta = 100\mu$m. Data points (blue) are compared to theory (red). The grey line is not discussed here [79].

of the cavity coupling parameters with the mode volume over three orders of magnitude down to $73(\frac{\lambda}{n})^3$. At room temperature the NV-cavity coupling proceeds well within bad emitter regime of CQED, whereby only a fraction of the emission was coupled to the cavity mode. (This is discussed in section 3.2). With the broadband emission, the mode volume was far from the regime necessary to readily observe fluorescence lifetime changes. A Purcell factor was alternatively quantified by comparing the integrated intensity into the cavity mode with the entire emission into free space. With a careful consideration of the differing experimental photon collection efficiencies in each case. The scaling of the effective Purcell factor was mapped out in the range 10^{-5} to 10^{-3}, shown in figure 2.9. This analysis framework forms the basis of the room temperature cavity coupling experiments in chapter 5.

2.3 Conclusion

This chapter initially discussed the NV-cavity coupling experiments conducted with the monolithic and hybrid resonator structures. Table 2.2 summarises these key experiments presenting the Q-factors, mode volumes along with the Q/V ratios allowing comparisons to be made. It must be noted that where possible, the Q-factor of the actual resonator used for coupling is listed. It is common for a range of Q-factors to be quoted in each paper, to account for the fact that many structures are fabricated within each investigation.

These structures typically have the benefit of being able to observe the off-resonant emission spectrum, allowing for a simple comparison of the emission intensity when optimally coupled. This is in contrast to the open resonator geometry. The Purcell factors are often determined in this manner with a consideration of altered collection efficiency where necessary. Prominence has been given to the experiments where there has been a clear lifetime measurement on the cavity coupled ZPL. To date, the PCC cavities represent the state of the art within NV-CQED [58, 59].

TABLE 2.2: NV Centre-Cavity Coupling (**Lifetime Measurement*)

Cavity	$V(\frac{\lambda}{n})^3$	Q	Q/V	F_P (measured)	Group
			Monolithic Diamond Resonators		
2D PCC	0.88	3000	3400	70*	Faraon 2012 [58]
1D PCC	1.05	3300	3150	62*	Li 2015 [59]
1D PCC	3.7	1634	440	7	Hausmann 2013 [60]
Microring	17	4300	252	12*	Faraon 2011 [61]
			Hybrid Resonators		
2D PCC-ND	0.74	610	820	7	Englund 2010 [63]
2D PCC-ND	0.75	1000	1330	12	Wolters 2010 [62]

Important to consider in practical terms is whether the emitters can be deterministically situated. The monolithic diamond resonators are able to incorporate the emitter within the resonator structure, enabling a better positioning of the emitter in the electric field. The structures can be constructed around an pre-determined emitter location to an extent. This is demonstrated by Riedrich-Moller [80], as a 2D PCC was fabricated

around a pre-selected SiV centre, with the aid of registration features on the diamond surface. The optimisation of the coupling is subsequently fixed. Some of these methods certainly rely on a semi-stochastic process, by fabricating large quantities of resonators in diamonds of appropriate defect density, as observed in the work of Li [59]. Conversely the hybrid approaches discussed offer deterministic pick and place methods [63] [62]. This positioning can be optimised iteratively, however the situation of these emitters outside the cavity requires evanescent coupling.

The open-cavities discussed are summarised in table 2.3. To attain comparison with the previous resonators, the Q factors have been calculated from the stated finesse and the minimum length achieved in the experiment (see chapter 3). This is a nascent field such that there have been relatively few emitter-cavity experiments. Because of this some of the maximum 'bare-cavity' parameters have been displayed alongside emitter-cavity coupled structures.

TABLE 2.3: Open-Cavity Potential

Cavity	$V(\frac{\lambda}{n})^3$	Q	Q/V	Author
		Bare Cavity		
CO_2	42	9.5×10^5	22,600	Hunger 2010 [72]
CO_2	154	4×10^6	26,600	Muller 2010 [69]
CO_2	2	6×10^4	30,000	Greuter 2014 [73]
FIB	9	2×10^3	220	Dolan 2010 [74]
		Semiconductor Nanocrystal Film-Cavity Coupled		
FIB	3	6.4×10^3	2100	Di 2012 [75]
		2D Film-Cavity Coupled		
FIB	6	7.4×10^3	1200	Schwarz 2014 [81]
		ND-Cavity Coupled		
CO_2	32	8.4×10^3	264	Albrecht 2013 [78]
CO_2	53	3×10^5	5700	Kaupp 2013 [79]
FIB	22	6×10^4	2700	Albrecht 2013 [76]

It is clear from that table that some of the CO_2 fiber cavities are able to attain very impressive $\mathcal{F}$ values, through the ultra-smooth surfaces that the ablation method is able to produce. The 'bare cavity' is of course is an idealised scenario where transmission or reflectivity measurements are conducted to measure $\mathcal{F}$. Introduction of an emitter into the intra-cavity medium leads to additional loss mechanisms. The semiconductor

nanocrystal and 2D thin-film coupling experiments are shown here as they represent the most up-to-date capabilities of the FIB cavities produced within this research group [75, 81]. It has been shown that the FIB method is able to produce amongst the smallest mode volumes, although the recent work of Greuter et al [73], demonstrate that CO_2 cavities have made great advances. However the FIB is certainly leading the way in terms of minimising β. Finally the NV-open cavity coupling experiments are shown. Reference [79], was able to retain very a substantial finesse, which showed only a 20% reduction when coupling to the ND. In reality this is strongly dependent on the nanodiamond size. Reference [78] saw the finesse drop by a factor > 3 upon introduction of the ND.

There is clear potential for the open-cavity system to contribute significantly in the efficient coupling of NV centres to optical networks. The Q/V figure of merit for the open resonators are shown to be very competitive with the PCC and hybrid resonators. What is more, the direct and deterministic access of the emitter to the electric field maximum is going to be of substantial benefit. The tunability of the system is the unique selling point, lending itself for incorporation into scalable future technology. For example, they could provide an individual and adjustable optical interface for each qubit in a distributed quantum network, comprised of multiple nodes. The requirement now is for those within the community to experimentally demonstrate open-cavity Purcell factors that are competitive with those seen in monolithic resonators. This is the central theme of this project.

Chapter 3

Theoretical Background

The following chapter will outline, step-by-step, the theoretical background that is necessary to describe the coupling of the NV^- centre to the plano-concave open-cavity resonator. The basic principles of the planar Fabry-Perot resonator will firstly be introduced, with the conditions for resonance, the effect of mirror losses on the photon lifetime and the consequences for the cavity metrics such as the finesse and quality factor. To describe the modes of the spherical mirror resonators used in this project, the concept of Gaussian beam optics will need to be considered. The relationship between the full Hermite-Gauss mode structure of the confined electric field and the geometrical parameters of the cavity are an essential tool in determining the mode volume and tailoring the light-matter interaction in-situ.

The theory of CQED will then be introduced with an initial discussion of the free space optical density of states. The optical microcavity increases the optical density of states at resonance, allowing for the enhancement of the light matter interaction in the limit of weak-couping, otherwise known as the Purcell effect. It will be demonstrated how the open-cavity system can ensure that this effect is maximised. The CQED parameters g, κ, γ, familiar to those in the atom-optics community, will be introduced in this context, solid state emitters however, most-often experience dephasing mechanisms that impede cavity coupling. It will be seen that the optical transitions within the NV experience

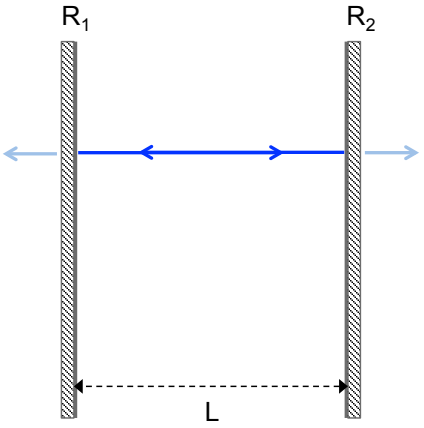

FIGURE 3.1: The basic Fabry-Perot optical resonator, formed by two opposing mirrors of reflectivity R, separated by a distance L. Imperfect reflectance leads to transmission through the mirror and loss from the cavity

a temperature dependent dephasing, meaning that it is necessary to consider both the good and bad emitter regimes of CQED.

There will be a full outline of the NV^- centre in diamond. It's location within the unit cell of the diamond lattice defines the symmetry of the defect, which is imparted on the electronic structure of the emitter. It is the energy level structure, with the ability to impart the spin state of an electron onto the photon number that is the fundamental reason why the NV^- is of interest in this project. However the quantity of 'useful' light emitted is shown to be just a fraction of the total emission, through the interaction with the vibrational modes of the lattice. For this reason cavity enhancement is expected to play an important role as the spin-photon interface.

This chapter will finally conclude with a discussion of the consequences of the PSB emission on the observable enhancements. Purcell factors that are within reach of this thesis are anticipated, given the optical resonators, mirror materials and operating temperatures that will be used, which will serve as a benchmark for the rest of the thesis.

3.1 Optical Resonators

This section will describe the principles of a Fabry-Perot resonator, following those outlined in references [82] and [83]. The resonant frequencies, ν_F must satisfy the boundary

conditions imposed by two opposing mirrors of separation L, as in figure 3.1, maintaining a constant phase over one round trip:

$$\nu_F = q\frac{c}{2L} \tag{3.1}$$

Where the mode index q denotes the number of antinodes between the mirrors. Each discrete resonant frequency thus has a constant separation $\Delta\nu = \frac{c}{2L}$, known as the free spectral range (FSR). The finesse $\mathcal{F}$ is a key metric, related to the number of round trips the photon will make, which would be infinite for the case of the perfect cavity with reflectivity $R = 1$. In practice, where $R < 1$, the finesse is expressed as:

$$\mathcal{F} = \frac{\pi(R_1R_2)^{1/4}}{1 - \sqrt{R_1R_2}} \tag{3.2}$$

Noticeably this is independent of the mirror separation. In the case of additional intra-cavity scattering, the losses are described by the total round-trip loss factor, $\mathcal{L}$

$$\mathcal{L} = 2\alpha_s L + \ln\frac{1}{\mathrm{R}_1} + \ln\frac{1}{\mathrm{R}_2} \tag{3.3}$$

Where α_s is the scattering coefficient. In the limit of high-reflectivities ($R \approx 1$), the finesse is simply related to the total loss factor by:

$$\mathcal{F} = \frac{2\pi}{\mathcal{L}} \tag{3.4}$$

This results in an attenuation of the electric field, decaying a rate $\kappa = 1/\tau_c$, where τ_c is the cavity photon lifetime. This breakdown of the strict resonance condition (shown in 3.2), results in the characteristic spectral linewidth $\delta\nu$

$$2\pi\delta\nu_c = \kappa \tag{3.5}$$

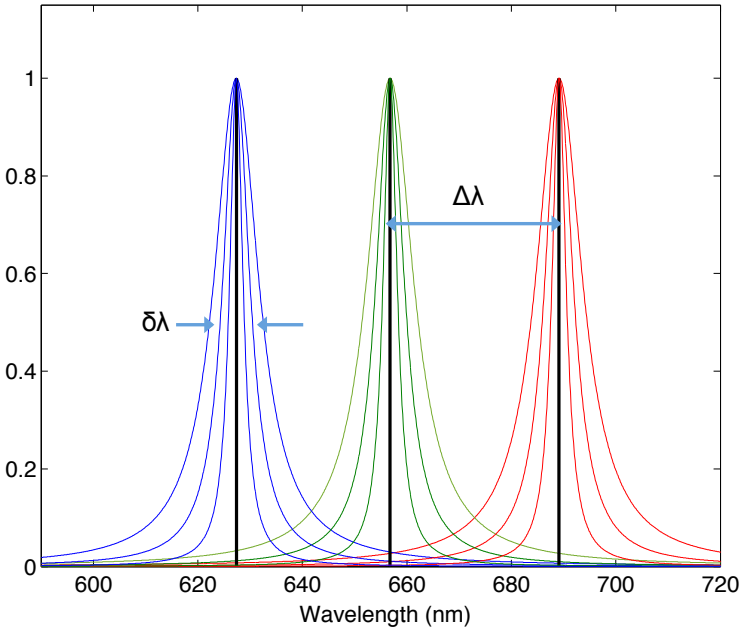

FIGURE 3.2: The resonant frequencies, in terms of λ, for the Fabry-Perot resonator. As the finesse of the cavity is increased the width of the Lorentzian line shape is reduced. Resonances of infinite $\mathcal{F}$ finesse are shown in black. The free spectral range is also indicated.

The cavity decay rate κ, is a key parameter in the discussion of CQED in section 3.2. Finally the finesse is related to the properties of the cavity spectrum in figure 3.2 as:

$$\mathcal{F} = \frac{\Delta\nu}{\delta\nu} \tag{3.6}$$

The Q-factor of the cavity is another key parameter that describes the capacity of the cavity to store energy, and is a figure of merit for any resonator structure. This allows for a direct comparison to alternative cavity geometries and defined:

$$Q = \frac{2\pi \times \text{Maximum Energy Stored}}{\text{Energy Loss per Cycle}} = \frac{\omega}{\Delta\omega} = q\mathcal{F} \tag{3.7}$$

The open-cavity thus has the ability to sample a wide large range of Q-factors as the mode index is increased. The planar cavity geometry has been discussed here for the purposes of this introduction. However, spherical mirror resonators are a necessary condition to achieve a good photon confinement and a small mode volume.

3.1.1 The Gaussian Beam

The concept of Gaussian beam optics will need to be introduced. A paraboloidal wavefront curvature is well matched to spherical mirrors and thus the Gaussian beam fully describes the modes of these optical resonators. The wave-like solutions to Maxwell's equations will first be considered.

When Maxwell's equations are considered for the case of no free currents ($\mathbf{j} = 0$) or static charges present ($\rho = 0$), a wave equation can be obtained, propagating with velocity: $c = \frac{1}{\sqrt{\mu_0 \epsilon_0}}$

$$\nabla^2 \mathcal{E} - \frac{1}{c^2} \frac{\partial^2 \mathcal{E}}{\partial t^2} = 0 \tag{3.8}$$

Solutions of this equation describe the nature of the electromagnetic radiation and can take the following form, describing a monochromatic plane wave

$$\mathcal{E}(\mathbf{r}, t) = A e^{-ikz} e^{i\omega t} \tag{3.9}$$

Equation 3.9 consists of a time-independent complex amplitude $\mathcal{E}(\mathbf{r}) = A e^{-ikz}$ with an associated phase $e^{i\omega t}$. Upon substitution into the wave equation, a time independent form, known as the Helmholtz equation is obtained [82].

$$(\nabla^2 + k^2)\mathcal{E}(\mathbf{r}) = 0 \tag{3.10}$$

The monochromatic plane wave describes a constant envelope A propagating along z. The wavefront normals can be appropriately described by ray optics. The Gaussian beam approximation represents a small deviation from the simple picture, by considering the propagation of paraxial waves. The wavefront normals this time make a small angle θ to the optical axis such that the paraxial approximation, $\sin(\theta) \approx \theta$, can be applied. A

paraxial wave is obtained through a perturbation of the complex envelope A, which is now a slowly varying function along the propagation direction where:

$$\mathcal{E}(\mathbf{r}) = A(\mathbf{r})e^{-ikz} \tag{3.11}$$

The condition that $\frac{\partial A}{\partial z} \ll kA$ and $\frac{\partial^2 A}{\partial z^2} \ll k^2 A$, ensures the envelope variation is low per unit λ and the paraxial approximation is valid. The substitution of 3.11 into 3.10, results in the paraxial Helmholtz equation.

$$\nabla_T^2 A - 2ik\frac{\partial A}{\partial z} = 0 \tag{3.12}$$

Where ∇_T^2 is the transverse laplacian operator. The full description of the Gaussian beam now comes from a solution to the paraxial Helmholtz equation and is shown in equation 3.13, along with a description for the physical meaning of each component [83].

$$\begin{aligned}
\mathcal{E}(\mathbf{r}) = A_0\frac{w_0}{w(z)} \quad & \textit{amplitude reduction with } z \\
\times e^{-\frac{r^2}{w(z)^2}} \quad & \textit{Gaussian profile of wavefronts with waist } w(z) \\
\times e^{-ikz} \quad & \textit{propagation along } z \\
\times e^{-ik\frac{r^2}{2\beta(z)}} \quad & \textit{wavefront radius of curvature } \beta(z) \\
\times e^{i\varsigma(z)} \quad & \textit{Gouy phase shift } \varsigma(z)
\end{aligned} \tag{3.13}$$

Where w_0 and A_0 are the beam waist and amplitude at the focus, whilst r is the radial distance from the optical axis. Equation 3.13, fully describes the behaviour of the beam in terms of the beam waist $w(z)$, radius of curvature $\beta(z)$ and the Gouy phase $\varsigma(z)$ as it propagates along z away from the focal point. These are the parameters of the Gaussian beam and can be expressed as:

$$w(z) = w_0 \left(1 + \left(\frac{z}{z_R}\right)^2\right)^{1/2} \tag{3.14}$$

$$\beta(z) = z \left(1 + \left(\frac{z_R}{z}\right)^2\right) \tag{3.15}$$

$$\varsigma(z) = \arctan\left(\frac{z}{z_R}\right) \tag{3.16}$$

$$w_0 = \left(\frac{\lambda z_R}{\pi}\right)^{1/2} \tag{3.17}$$

Where z_R is the Rayleigh length, describing the distance over which the beam waist w_0 has spread by a factor of $\sqrt{2}$ as can be seen in figure 3.3. It is closely related to the depth of focus of the beam or confocal parameter $b = 2z_R$. The divergence θ of the Gaussian beam, which defines the numerical aperture (NA) in turn. This is useful when considering the coupling of the beam to external optical elements, related to the beam waist by:

$$\mathrm{NA} = \sin\theta = \sin\left(\frac{\lambda}{\pi \mathrm{w}_0}\right) \tag{3.18}$$

Figure 3.3 shows the schematic of the Gaussian beam within a half-symmetric optical resonator, which is just one of many possible open cavity geometries. The cavity resonances are subject to a strict condition on the cavity length L and the radius of curvature β, of each mirror if they are to form stable optical modes. This may be defined as

$$0 \leq g_1 g_2 \leq 1 \tag{3.19}$$

Where $g_i = 1 - L_i/\beta_i$. In the case of mirror 1 in figure 3.3, $g_1 = 1$ as $\beta_1 \to \infty$. The mode waist $\omega(z)$ in equation can be defined in terms of the g parameters.

Table 3.1, displays the expressions for the minimum mode waist, and the waist at each mirror for both the general case pertaining to all open resonator geometries, and the specific case of the half-symmetric cavity in this project. In this case $w_0 = w_1$, and is

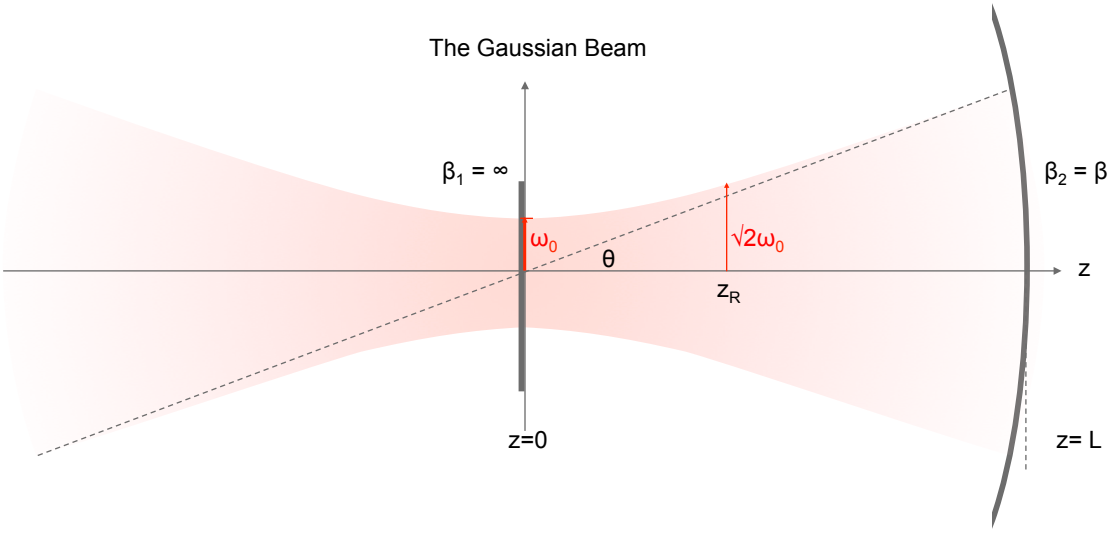

FIGURE 3.3: The Gaussian Beam. The beam waist $\omega(z)$ is a minimum at z=0. The Rayleigh range, z_R is defined as shown. Away from the waist the beam is divergent at an an angle θ. A plano-concave, or half-symmetric cavity is shown in the figure. ω_0 will be located on the planar mirror with $\beta_1 = \infty$, and the concave mirror is placed at a cavity length $z = L$, with $\beta_2 = \beta$.

TABLE 3.1: Mode Waist

General Case	Half-Symmetric Cavity
$\omega_0^2 = \frac{L\lambda}{\pi}\sqrt{\frac{g_1 g_2(1-g_1 g_2)}{(g_1+g_2-2g_1 g_2)^2}}$	$= \frac{\lambda}{\pi}\sqrt{\beta L - L^2}$
$\omega_1^2 = \frac{L\lambda}{\pi}\sqrt{\frac{g_2}{g_1(1-g_1 g_2)}}$	$= \omega_0^2$
$\omega_2^2 = \frac{L\lambda}{\pi}\sqrt{\frac{g_1}{g_2(1-g_1 g_2)}}$	$= \frac{\lambda}{\pi}\sqrt{\frac{L\beta^2}{\beta-L}}$

located on the planar mirror. It is at this position of the electric field maximum, that the emitters are placed. The mode waist ω_2 on the concave mirror with radius of curvature β_2, is an important parameter when considering the spherical mirror fabrication. ω_2 must be well within the bounds of the featured mirror diameter, for the desired cavity length range in the experiment, in order to avoid diffraction losses, as the mode clips the edge of the concave profile [72, 84].

3.1.2 The Hermite-Gaussian Beam

There exist other solutions to the paraxial Helmholtz equation, namely the Hermite-Gaussian beam, whose higher-order solutions have transverse and distinct intensity distributions. The Hermite Gaussian beam fully describes the modes that form within spherical mirror resonators. This is shown in equitation 3.20, where l, m are the eigenvalues of the Hermite polynomials, G, that describe the transverse field profile. The eigenvalues $l+m=0$ represents the lowest order, which recovers the form of the original Gaussian beam 3.13.

$$\begin{aligned}\mathcal{E}_{l,m}(x,y,z) = A_{l,m}\frac{w_0}{w(z)} \qquad & \textit{amplitude reduction with } z \\ \times G_l\left[\frac{\sqrt{2}x}{w(z)}\right] G_m\left[\frac{\sqrt{2}y}{w(z)}\right] \qquad & \textit{Hermite-Gauss transverse intensity profile} \\ \times e^{-ikz} \qquad & \textit{propagation along } z \\ \times e^{-ik\frac{r^2}{2\beta(z)}} \qquad & \textit{wavefront radius of curvature } \beta(z) \\ \times e^{i(l+m+1)\varsigma(z)} \qquad & \textit{increased phase shift}\end{aligned} \tag{3.20}$$

Where $A_{l,m}$ is a constant. The phase terms are collectively expression in equation 3.21.

$$\varphi(r,z) = kz - (l+m+1)\varsigma(z) + \frac{kr}{2\beta(z)} \tag{3.21}$$

Where $r=0$ on the optical axis. Supporting an optical mode requires that $\Delta\varphi = 2\pi q$, over the round trip length $2L$. Thus the longitudinal ($\mathrm{TEM}_{m+n=0}$) and transverse modes ($\mathrm{TEM}_{m+n\geq 1}$) are fully described by equation

$$\nu_{l,m,q} = \frac{c}{2L}\left[q + (l+m+1)\frac{\cos^{-1}\sqrt{g_1 g_2}}{\pi}\right] \tag{3.22}$$

Where the $\frac{c}{2L}$ is longitudinal mode spacing, independent of β, as for a planar-planar resonator in equation 3.1. The final term results in a perturbation of all resonances due to β, also defining the transverse mode spacing. The spectral profile of the longitudinal and transverse modes for a given mode number are illustrated in figure 3.4. The higher-order transverse modes of index $m+n=x$ are made up of energetically degenerate but spatially distinct electric field profiles in the cavity, defined in cartesian co-ordinates. Any symmetry breaking within the cavity structure will lift this degeneracy. One of the key points to note is that the mode waist of the electric field intensity profile, defined as the point at which the electric field intensity falls to $1/e^2$ of it's maximum value, decreases with higher mode index. Coupling into external optics thus becomes harder to achieve.

The mode volume, V, of the electric field within the cavity, is another parameter, critical for the success of the emitter-cavity coupling experiments in this work. Integrating equation 3.20 over the dimensions of the cavity results in:

$$V = \frac{1}{\mathcal{E}_0}\int_0^L \int_\infty^\infty \int_\infty^\infty \mathcal{E}^*(x,y,z)\mathcal{E}(x,y,z)dxdydz = \frac{\pi\omega_0^2 L}{4} = \frac{\lambda L^2}{4}\sqrt{\frac{\beta}{L}-1} \tag{3.23}$$

The solution for the TEM_{00} mode of a half-symmetric resonator is shown in equation 3.23, yielding a simple analytic expression for the electric field within the cavity as a function of ω_0 and the cavity length L. It will be seen later in this thesis that a range of features with different β, are able to be produced via the FIB milling process. The anticipated mode volumes for a selection of these cavities are plotted in figure 3.5 as a function of mode number q coupled at 637nm. Mode volumes down to $0.1\mu m^3$ are entirely possible. Achieving such short cavity lengths is a technical challenge however. It must be noted that these calculated volumes take into account the volume of the mode penetrating into the DBR stack, which is discussed below in section 3.1.3

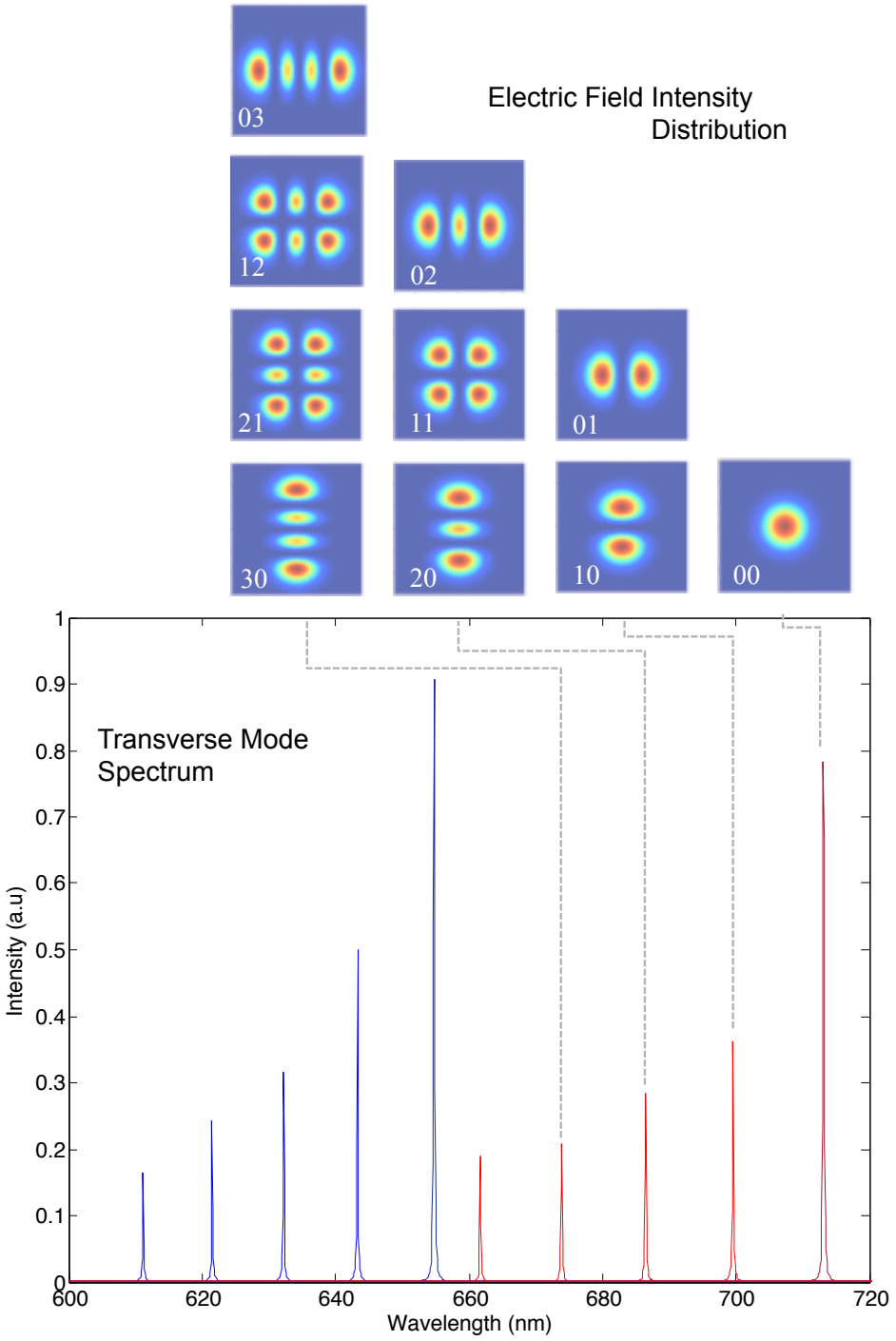

FIGURE 3.4: Schematic of the transverse mode spectral profile for a given longitudinal mode index q. The higher order transverse modes are energetically degenerate, and are composed of spatially separate Hermite-Gaussian modes as indicated. The intensity profiles represent a 6x6μm area at the mode waist $\omega(z = 0)$

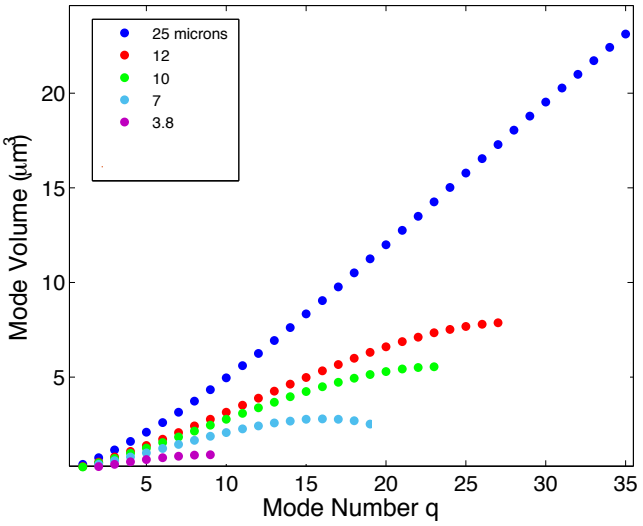

FIGURE 3.5: Mode Volumes for different radii of curvature, plotted as a function of mode number q, where λ=637nm.

3.1.3 Distributed Bragg Reflectors

The resonators discussed thus far have been near perfect, idealised systems. In practical terms, the mirror materials must also be considered. The most familiar case will be the half silvered or metallic mirror. However these systems would not be capable of achieving a high finesse, with reflectivities in the range of $\approx 95\%$. The broadband reflectivity is also a feature, which prevents efficient coupling of non-resonant excitation in the desired epifluorescence geometry. To achieve both these conditions simultaneously distributed Bragg reflectors (DBRs), are employed. The principles of operation are as follows: DBRs are constructed of alternating layers of high and low refractive index thin films, with a $\frac{\lambda}{4n}$ layer thickness, where n is the refractive index of each medium, and λ is the design wavelength for high reflectivity. Light will be partially reflected and transmitted at each interface. Propagation across a boundary from a low to high index medium, results in a π phase shift of the reflected light, which is not true in the opposite case. The $\frac{\lambda}{4n}$ thickness ensures that the reflected component from each layer is in phase. Stacking large numbers of these pairs can result in reflectivities of 99.9999%.

The choice of mirror materials is also important. The reflection and transmission of light at an interface is governed by the Fresnel equations [85]. With a greater number

of interfaces, the situation becomes increasingly complex, as multiple reflections occur between the mirror stacks. Fortunately the transfer matrix method simplifies such calculations. By recognising that the boundary conditions on Maxwell's equations, require the tangential component of the electric field $\mathcal{E}$ and magnetic field strength $\mathcal{H}$, to be continuous across the interface, a characteristic matrix can be derived to relate the field across the boundaries of the interface. The transfer matrix allows for the generalisation of the Fresnel equations to multiple interfaces. The resulting reflected intensity from an N-pair DBR stack, at normal incidence is as follows

$$R = \left[\frac{n_{\mathrm{or}} n_{\mathrm{H}}^{2N} - n_{\mathrm{sub}} n_{\mathrm{L}}^{2N}}{n_{\mathrm{or}} n_{\mathrm{H}}^{2N} - n_{\mathrm{sub}} n_{\mathrm{L}}^{2N}}\right]^2 \tag{3.24}$$

Where n_{H} and n_{L} are the high and low indices respectively, whilst n_{or} and n_{sub}, are the originating and substrate medium respectively. The reader is referred to Hecht [85] for a more complete mathematical description. It is also noted that dielectric materials are assumed to be non-magnetic. Broadly speaking, the reflectivities are governed not only by the number of pairs but the refractive index contrast, or impedance mismatch, between the layers. The contrast also dictates reflection bandwidth as illustrated in figure 3.6.

A key feature of the DBR mirrors is the penetration of the electric field into the coating layers. This is demonstrated by FDTD simulations in figure 3.7 (method described in section 4.9.1). The resulting properties are dependent on the terminating layer. With high termination, there is node at the air-substrate interface, with one antinode penetrating into the substrate. On the low terminated planar mirror, the antinode is at the interface. This is a conscious design feature that places the electric field maximum at the emitter position. There are correspondingly two antinodes penetrating into the planar mirror stack.

This penetration into the mirror stack is a consistent feature, largely independent of cavity length. It now becomes more useful to define the geometrical length of the cavity

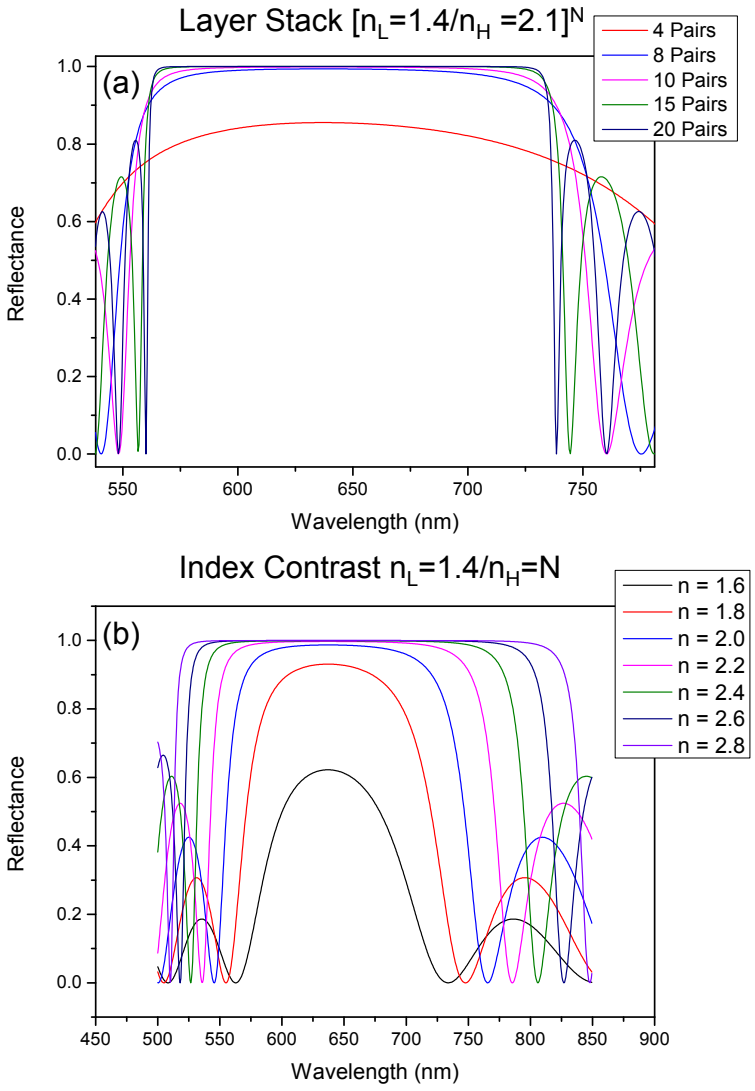

FIGURE 3.6: (a) Reflectivity as a function of pair number. Most pairs lead to a greater reflectivity. (b) Reflectivity as a function of index contrast for an 8 pair stack. Both the stop band and and the reflectivities are increasing with the pair contrast.

L_{geo}. Converting equation 3.1 in terms of λ, the FSR defines only the optical length of the cavity mode, L_{opt}

$$\Delta\lambda = \frac{\lambda^2}{2L_{\text{opt}}} \tag{3.25}$$

Where

$$L_{\text{opt}} = L_{\text{geo}} + L_{\text{DBR}} \tag{3.26}$$

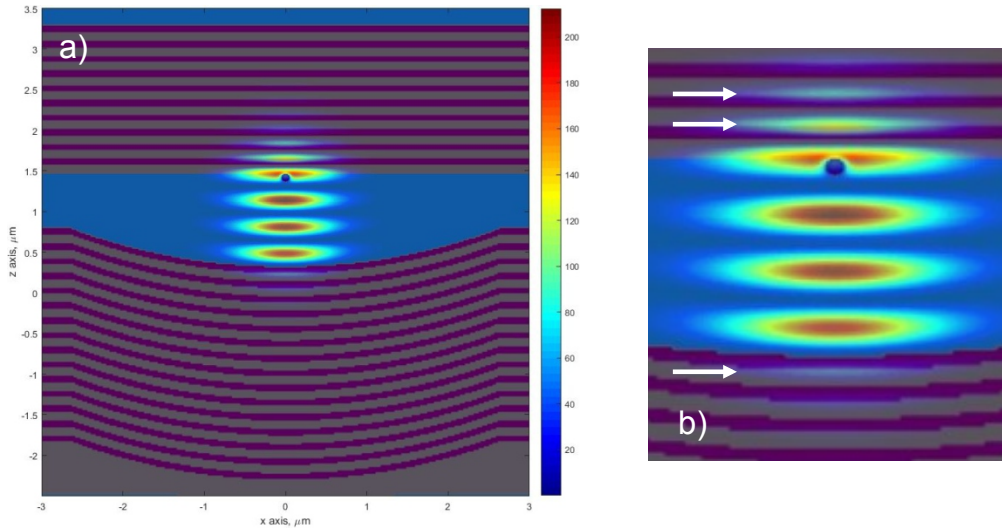

FIGURE 3.7: (a) FDTD simulation of the intensity distribution for a planar-concave cavity structure, with β=7μm and q=4 between the mirrors. The planar substrate has 10 pairs of high (purple) and low (grey) index materials of thickness $\frac{\lambda}{4n}$, whilst the featured mirror has 15. The cavity medium has n=1. (b) Close-up profile of the cavity mode. The white arrows indicate an antinode penetrating into the mirror stack.

Recalling equation 3.27, the resonance modes of the the half-symmetric cavity geometry, with a DBR mirror coating, are now related to the length by

$$L_{\text{opt}} = \frac{\lambda}{2}\left[q + (l+m+1)\frac{\cos^{-1}\sqrt{g_2}}{\pi}\right] \tag{3.27}$$

Where where the parameter $g_2 = 1 - \frac{L_{\text{geo}}}{\beta_2}$ and the stability criterion now depend on geometrical length, rather than the optical length. It must be noted that for the mode volume calculation, L_{opt} is still required and the field in the mirrors still contributes to the total mode volume. The DBR mirrors are clearly a requirement for high finesse, however the penetration of the field into the mirrors presents a limit of how small the mode volumes could go. The convention throughout this thesis will be to express q, as the number of antinodes between the mirrors themselves, excluding the three antinodes in the mirror stack. This is to be clear about how far the cavity is from the fundamental limit of q=1 between the substrate.

3.2 Cavity Quantum Electrodynamics

The interaction between light and matter is the central theme of this thesis. Cavity quantum electrodynamics provides the theoretical basis for this interaction and has lead to concerted research efforts aiming to exert a high degree of control over such systems. Experimental demonstrations of the fundamental postulates of CQED were initially conducted with atomic transitions in both the microwave and the optical regimes [86]. The theoretical outline presented will be discussed initially in the context of a two level system interacting with the electromagnetic field. Solid state CQED systems are a more recent development starting with work on self-assembled quantum dots [87]. The theoretical description of solid-state CQED is of course most relevant for the work at hand and will be developed through this discussion. It will be seen that these emitters present a great challenge for cavity-coupling.

The electromagnetic vacuum field permeates all space, $\mathcal{E}_{\text{vac}}$ and has a finite zero-point energy as a consequence of the quantisation of the radiation field. This is the starting point for discussions of the light-matter interaction. Spontaneous emission in free space is itself a direct result of the interaction between and excited state atom and these vacuum fluctuations (see section 3.2.1.2). The optical microcavity, has the capacity to concentrate these vacuum field fluctuations to a small modal volume V_0, which is the fundamental reason for the enhanced light matter interaction. The principal parameter that describes the coupling of a quantum system to an optical cavity is the coherent atom-cavity coupling rate g_0 [88].

$$\hbar g_0 = \mu_{12}\mathcal{E}_{\text{vac}} \tag{3.28}$$

$$g_0 = \left(\frac{\mu_{12}^2\omega}{2\varepsilon_0\hbar V_0}\right)^{1/2} \tag{3.29}$$

Where V_0 is the mode volume of the cavity, and μ_{12} is the matrix element of the electric dipole transition. Evidently the more that can be done to reduce the modal volume,

the greater the interaction rate becomes. In practical terms, there are two forms of decoherence may inhibit the cavity coupling process, namely the cavity-photon decay rate, κ and the emitter decay rate γ. The latter term encompasses the emission into free space modes, acknowledging the fact that the emission occurs in all directions.

The relative magnitude of these three parameters define the boundaries the CQED regimes. When $\kappa, \gamma \gg g_0$, the light-matter interaction proceeds within the weak coupling regime. Here the decohrence processes are still dominant over the cavity coupling rate, however an enhancement of the light-matter interaction is still attainable through the significant reduction of mode volume and tailoring of the cavity decay rates. This is the Purcell effect [89], which changes the spontaneous emission rate in the presence of a modified optical density of states. A further distinction is made between the case where: $\kappa > \gamma \gg g_0$, the 'good emitter/bad cavity' regime for a spectrally narrow emitter in a broad cavity mode, and vice versa for the 'bad emitter' regime where $\gamma > \kappa \gg g_0$. Both of these regimes are applicable to the coupling of NV centres to optical microcavities and will thus be presented in the following discussion. The final scenario $g_0 \gg \kappa, \gamma$, is known as the strong coupling regime. Here the coupling rate dominates over the decoherence mechanisms, and there is a coherent and reversible exchange of energy between the emitter and the cavity. The strong coupling regime is beyond the scope of this project and will not be discussed further.

3.2.1 Free Space Emission

3.2.1.1 Optical Density of States

This treatment follows one outlined in by Fox [90], for the case of an electromagnetic field in a volume V. For simplicity this volume is a cube with side d, such that $V = d^3$. The solution for the electromagnetic field in this volume takes the form in equation 3.30

$$\mathcal{E}(\mathbf{r}, t) = \sum_k \mathcal{E}_{\mathbf{k}} e^{i(\mathbf{k}\cdot\mathbf{r} - \omega t)} \tag{3.30}$$

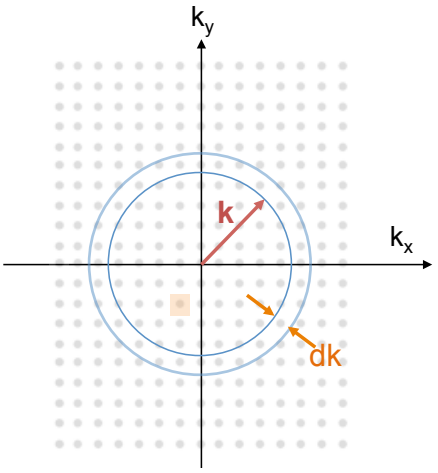

FIGURE 3.8: A 2D schematic of the optical density of states in **k**-space. Each points represents a permitted k-state and taking up area $(2\pi/d)^2$ shown by the orange square. dk represents an infinitestimal shell of **k**-space used as a computational tool for the optical density of states calculation. Adapted from [90]

This gives an expression for the field inside the volume V, which can be decomposed into the components of the individual **k**-state as $k = \frac{2\pi}{d}n$ where n is an integer.

$$\mathbf{k} = (k_x, k_y, k_z) = \frac{2\pi}{d}(n_x, n_y, n_z) \tag{3.31}$$

The permitted **k**-states are represented in two-dimensional in **k**-space in figure 3.8, with each state separated by $\frac{2\pi}{d}$, and thus occupying a volume $V = (\frac{2\pi}{d})^3$.

The aim is to obtain the density of these optical states in any given volume. Each **k**-state is represented by a vector with magnitude k. To find how many states there are in an arbitrary volume, one can consider the number of states with magnitudes between k & $k + dk$. Finding the volume of an infinitesimal shell of radius k, then dividing by the volume per **k**-state leads to the 3D optical density of states in equation 3.32

$$\rho(k)dk = \frac{4\pi k^2 dk}{(2\pi/d)^3} = V\frac{k^2}{2\pi^2}dk \tag{3.32}$$

It is now possible to map this density in **k**-space to the density of photon states at their corresponding angular frequencies $\rho(\omega)$. We normalise by V and also remember that there are two possible polarizations for each **k**-state.

$$\rho(\omega)d\omega = 2\rho(k)dk \tag{3.33}$$

Using $\omega = ck$ results in the photon density of states in free space:

$$\rho(\omega) = \frac{\omega^2}{\pi^2 c^3} \tag{3.34}$$

3.2.1.2 Spontaneous Emission Rate

The discussion of spontaneous emission transition rates, must always start with Fermi's golden rule. This itself is derived from time dependent perturbation theory. Starting with a two level system in the excited state $|2\rangle$, described fully by the time-independent Hamiltonian, $\hat{H}_0(r)$, a time-dependent perturbation is then applied to the system, $\hat{H}'(r,t)$. The transition to the ground state $|1\rangle$ proceeds via the electric dipole interaction. This rate will also depend on both the final state distribution of the atomic transition $\varrho(\omega)$ and the density of optical states at the emission frequency $\rho(\omega)$. Fermi's golden rule is presented in this generalised from in equation 3.35

$$\gamma_{2\to1} = \frac{2\pi}{\hbar} |\langle 1| \hat{H}' |2\rangle|^2 \int_0^\infty \varrho(\omega)\rho(\omega)d\omega \tag{3.35}$$

The final state distribution of the atomic transition $\varrho(\omega)$ arises due to the finite lifetime of the state and consequently is takes the form of a homogeneously broadened normalised Lorentzian function with spectral linewidth $\delta\omega_{em}$. In the limit that this transition linewidth becomes infinitesimally narrow, this lineshape acquires the properties of a delta-function and the integral in equation 3.35 becomes:

$$\int_0^\infty \varrho(\omega - \omega_0)\rho(\omega)d\omega \longrightarrow \rho(\omega_0) \tag{3.36}$$

Fermi's golden rule is now expressed in equation 3.37. This is the appropriate form for the discussion of narrow emission lines, emitting into a relatively broad distribution of final photon states, and is usually seen in the context of atom optics. Homogenous broadening more readily occurs in solid state systems and the discussion will return to the generalised form in equation 3.35, later in this chapter.

$$\gamma_{2\to1} = \frac{2\pi}{\hbar}|M_{12}|^2\rho(\omega) \tag{3.37}$$

M_{12} is the matrix element for the transition. This electric dipole interaction will depend on the electric transition dipole μ_{12}, and electromagnetic field environment. In free space this is the the zero point fluctuations of the vacuum field.

$$|M_{12}|^2 = \frac{1}{3}\mu_{12}^2\mathcal{E}_{\text{vac}}^2 = \frac{\mu_{12}^2\hbar\omega}{6\varepsilon_0 V_0} \tag{3.38}$$

The factor of $\frac{1}{3}$ in equation 3.38 represents the average dipole orientation factor. This is applicable to the spontaneous emission of an isolated atom in free space, which has no fixed quantisation axis, or to an ensemble of fixed but randomly oriented solid-state emitters (see section 5.2.0.3). Thus using $\rho(\omega) = \frac{\omega^2}{\pi^2c^3}V_0$, we obtain the transition rate of spontaneous emission in free space.

$$\gamma_{\text{fs}} = \frac{\mu_{12}^2\omega^3}{3\pi\varepsilon_0\hbar c^3} \tag{3.39}$$

3.2.2 Cavity Emission: Weak Coupling

3.2.2.1 Good Emitter Regime

The spectral intensity distribution of a resonant cavity mode is directly related to the optical density of states between the mirrors. $\rho(\omega)_{\text{cav}}$ is taken to be a normalised Lorentzian

in equation 3.40, centred at ω_c, with a decay rate $\kappa = \delta\omega_c$. A transform limited emitter is at ω_0.

$$\rho(\omega_0)_{\text{cav}} = \frac{2}{\pi\delta\omega_c}\frac{\delta\omega_c^2}{4(\omega_0-\omega_c)^2+\delta\omega_c^2} \tag{3.40}$$

$$\rho(\omega_0=\omega_c)_{\text{cav}} = \frac{2Q}{\omega_c} \tag{3.41}$$

With this cavity-modified density of final optical states, Fermi's Golden Rule is again applied to calculate the transition rate.

$$\gamma_{cav} = \frac{2Q\mu_{12}^2}{V_0\epsilon_0\hbar}\xi^2\frac{\delta\omega_c^2}{4(\omega_0-\omega_c)^2+\delta\omega_c^2} \tag{3.42}$$

Where ξ is the orientation factor between the emitter dipole $\mathbf{p}$ and cavity field $\mathbf{E}$:

$$\xi = \frac{|\mathbf{p}\cdot\mathcal{E}|}{|\mathbf{p}||\mathcal{E}|} \tag{3.43}$$

The Purcell factor defines the enhancement of the light matter interaction as the ratio of spontaneous emission in the cavity to that of free space. Equation 3.44 presents the Purcell factor in it's complete form.

$$F_{\text{P}} = \frac{3\lambda^3}{4\pi^2}\frac{Q}{V_0}\xi^2\frac{\delta\omega_c^2}{4(\omega_0-\omega_c)^2+\delta\omega_c^2} \tag{3.44}$$

The increased emission efficiency into the cavity mode is often a useful metric in the discussion of cavity coupling, quantified as:

$$\mathcal{B} = \frac{\gamma_{\text{cav}}}{\gamma_{\text{cav}}+\gamma_{\text{fs}}} = \frac{F_{\text{P}}}{1+F_{\text{P}}} \tag{3.45}$$

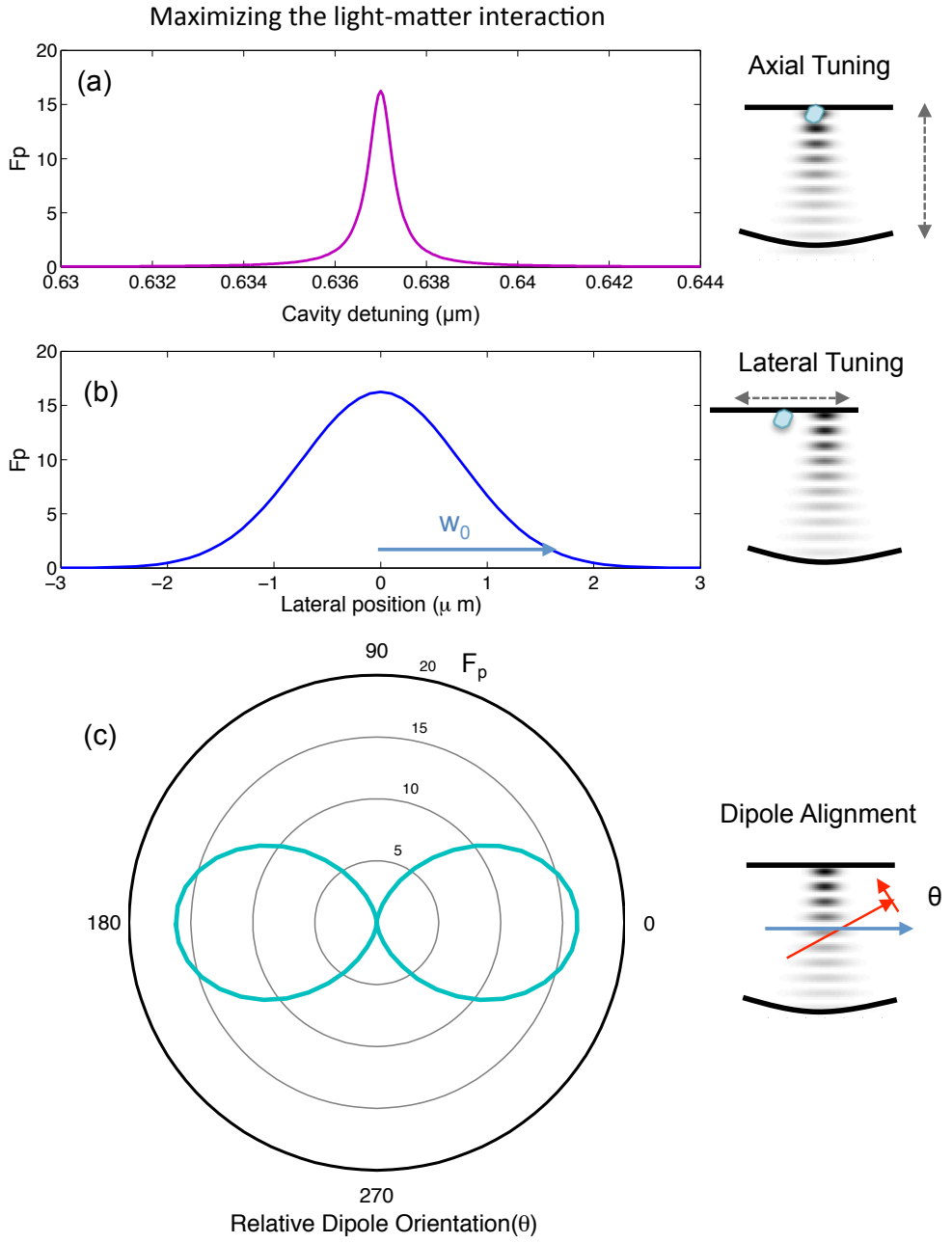

FIGURE 3.9: Maximising the light matter interaction. Each plot represents the maximisation of F_{P} in equation 3.44, with an adjacent schematic of how this is achieved in the open-resonator geometry. (a) Cavity-Emitter detuning with emitter $\lambda_0 = 637$nm. (b) Lateral tuning of the emitter in the cavity mode on the planar mirror such that $\mathcal{E} = \mathcal{E}_{\max}$ in the centre of the mode waist w_0. (c) Relative diploie orientation between the emitter and the cavity field such that $\xi = 1$ when the dipoles are aligned

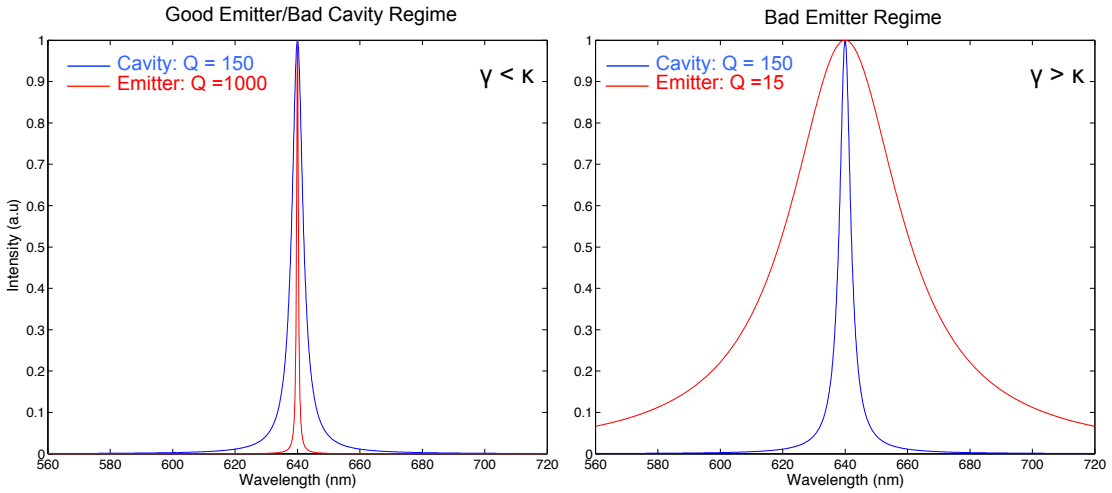

FIGURE 3.10: Left: the good emitter/bad cavity regime. Right: the Bad emitter regime.

The dependence of F_{P} on each of the detuning mechanisms is outlined in figure 3.9. On condition of perfect spatial alignment of the emitter-cavity dipole (ξ=1) and optimal resonance ($\omega_0 = \omega_c$) the Purcell factor is finally expressed as:

$$F_{\mathrm{P}}^{\max} = \frac{3\lambda^3}{4\pi^2}\frac{Q}{V_0} \tag{3.46}$$

This can be expressed in terms of the cavity decay rate κ and the free space emitter decay rate γ by noticing that the matrix element $|M_{12}|^2 = \hbar^2 g_0^2$ such that:

$$F_{\mathrm{P}}^{\max} = \frac{4g_0^2}{\kappa\gamma} \tag{3.47}$$

3.2.2.2 Bad Emitter Regime

As previously stated, the aforementioned treatment of the weak coupling regime considered only a transform limited emitter linewidth coupling to a large cavity bandwidth in the bad cavity regime. In the work at hand however, the emitter linewidth spans the regime whereby $\gamma < \kappa$ through to $\gamma \gg \kappa$, as shown schematically in figure 3.10.

Thus at no point can the emitter linewidth be approximated to be narrow with respect to the cavity and a more general treatment is required. One must invoke the general form

of Fermi's golden rule, as in equation 3.35, for a homogeneously broadened emitter. For these two independently broadened processes, the resultant interaction between them is governed by the convolution of their line Lorentzian line profiles as in equation 3.48. This results in an effective Q-factor for the interaction Q_{eff}.

$$\int_0^\infty \varrho(\omega)\rho(\omega)d\omega = \varrho(\omega) \otimes \rho(\omega) \tag{3.48}$$

Recalling the convolution theorem, the convolved functions in the frequency domain can be related to the product of their Fourier transforms. This yields another exponentially decaying function where the cavity decay constant is the sum of $\tau_c + \tau_{\text{em}}$ as in 3.49

$$\tilde{\varrho}(t)\tilde{\rho}(t) \propto e^{t/2(\tau_c+\tau_{\text{em}})} \tag{3.49}$$

Transforming this function back into the frequency domain therefore obtains another Lorentzian function of width $\delta\omega_{\text{em}} + \delta\omega_c$. The Purcell factor in equation 3.46 now depends on the *effective* Q-factor: $Q_{\text{eff}} = \omega/(\delta\omega_{\text{em}} + \delta\omega_c)$, in the generalised case. In the language of CQED, the cavity decay rate κ in equation 3.47 is substituted for the sum of $(\kappa + \gamma + \gamma*)$, as outlined by Auffeves et al [91] . The quantity $(\gamma + \gamma*)$ describes the decay rate of the transition and additional pure-dephasing processes $(\gamma*)$, which are widely experienced in solid state systems.

The generalised form of the Purcell factor (at the condition of perfect resonance) is therefore expressed as

$$F_{\text{P}}^{\text{max}} = \frac{4g_0^2}{\gamma(\kappa + \gamma + \gamma*)} = \frac{\mathcal{R}}{\gamma} \tag{3.50}$$

Where $\mathcal{R}$ is an effective coupling rate between the emitter and the cavity [91, 92].

3.3 The NV centre in diamond

3.3.1 The Energy Level Structure

A substitutional Nitrogen atom exists together with a neighbouring vacancy with an orientation along the [111] crystal axis in diamond. The five unsatisfied active bonding electrons, two from the Nitrogen atom and one from each of the three Carbon atoms surrounding the vacancy form the neutral NV^0 defect [93]. The neutral NV^0 defect is also a single photon source with a ZPL at 575nm [94]. However, the complex can act as a trap site and forms the negatively charged Nitrogen-Vacancy NV^- upon acquisition of a sixth electron.

The language of group theory is used to describe the symmetry of the defect and to construct the molecular orbitals giving rise to the electronic structure. The orbitals are formed from linear combinations of the surrounding sp^3 hybridised orbitals from the neighbouring atoms. The combinations permitted are only those which transform according to the C_{3v} symmetry representation. Correspondingly there are two a_1 orbitals and a doubly degenerate e orbital [95] [96]. These are filled with the 6 electrons of the defect according to Hund's rules as in figure 3.11. Theoretical studies show that the a_1' orbital is located below within the valence band. Thus the observed properties are governed by the molecular orbitals within the band-gap.

A series of interactions result in a perturbation of the NV^- centre energy levels giving them a fine structure as in figure 3.12. Spin-Spin interactions split the spin projections of the $^3A_2$ ground state triplet into an $m_s = 0$ and a degenerate $m_s = \pm 1$ separated by 2.88GHz in energy. A combination of the Spin-Spin and Spin-Orbit interaction splits the excited state ^3E into multiple levels labeled according to their symmetry in the C_{3v} representation A_1, A_2 and two doubly degenerate levels E & E' [29]. Due to the symmetry of the excited state, it is highly sensitive to electric fields and correspondingly, strain fields within the diamond lattice. Axial strain leads to a linear shift of all levels, however lateral strain splits the levels into the two orbital doublets E_x and E_y of the

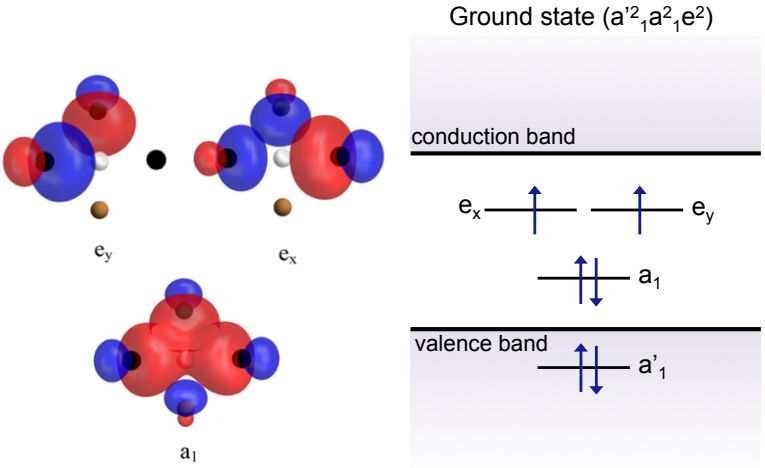

FIGURE 3.11: Left: The molecular orbitals for the states e_x, e_y and a_1 that lie within the band-gap. Contributions from the Nitrogen atom (brown) and Carbon atoms (black), result in highly localised molecular orbitals at the vacancy (white). Positive and negative contributions to the molecular orbitals are shown in red and blue respectively. Right: Positions of the molecular orbitals relative to the band structure of Diamond. The electron spins (blue) fill the molecular orbitals according to Hund's rules. The occupancy shown corresponds to that of the ground state. Reproduced with permission from [95].

excited state [97], each corresponding to a spin-triplet. The ability to electrostatically tune the excited state energy levels was demonstrated by Tamaret et al [28].

The intermediate singlet levels at $^1A_1$ and ^1E separated by 1.19eV. The predominant transitions are from the $m_s = \pm 1$ spin projections of the excited state, which then preferentially transfers the spins in to the $m_s = 0$ level of the ground state. The non-radiative transitions to and from these shelving levels are therefore responsible for the spin-polarisation mechanism, and are of central importance optical-read out of the electron spin state.

3.3.2 Vibrational Structure

The Huang-Rhys model provides the theoretical description of the NV centre vibronic structure. The electronic transitions within the NV centre simultaneously create vibrational quanta of the host lattice [100]. The coupled electronic-vibrational degrees of freedom give rise to the observed vibrational spectra in the PSB. This is a common feature of optical transitions in crystalline and molecular materials, in contrast to the

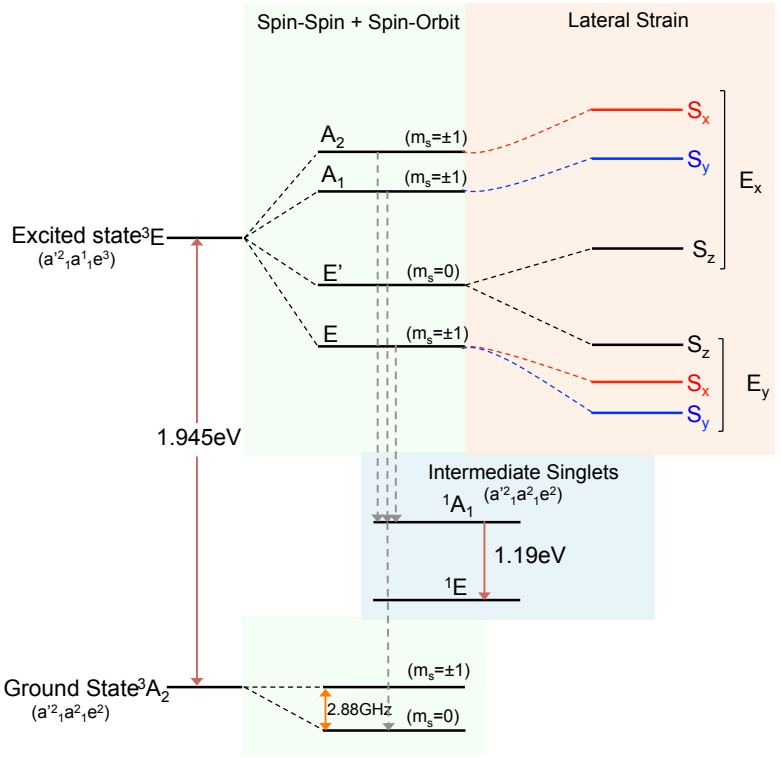

FIGURE 3.12: The electronic structure of the NV^- centre in diamond with perturbations from the spin-spin, spin-orbit and lateral strain interactions included. The ground, excited and intermediate states have their molecular occupancy indicated in brackets. Lateral strain fields splits the orbital doublet of the excited states into it's E_x and E_y components. The ground and excited states are separated by 1.945eV corresponding to the ZPL energy. The key transitions are highlighted as the optical (red), microwave (orange) and non-radiative (grey-dashed). Figure adapted from [98, 99]

behaviour of isolated systems such as atoms. Upon excitation to a new electronic state, the nuclei undergo undergo a displacement from their original equilibrium position, due to the redistribution of electric charge, to new equilibrium displacement configuration [93]. Such behaviour follows from the Born-Oppenheimer approximation, that electron displacement occurs much more rapidly than in nuclei owing to their relative masses.

This behaviour is represented in the configuration diagram of figure 3.13, which plots electronic energy as a function of the generalised nuclear co-ordinates Q_n. The electronic states have a harmonic dependence on the displacement co-ordinates, as the displacement eventually reaches it's equilibrium position after excitation. Upon optical excitation from the ground equilibrium state to a higher order vibrational mode in the excited state, the energy is lost through rapid relaxation through the quantised vibronic levels until equilibrium is reached.

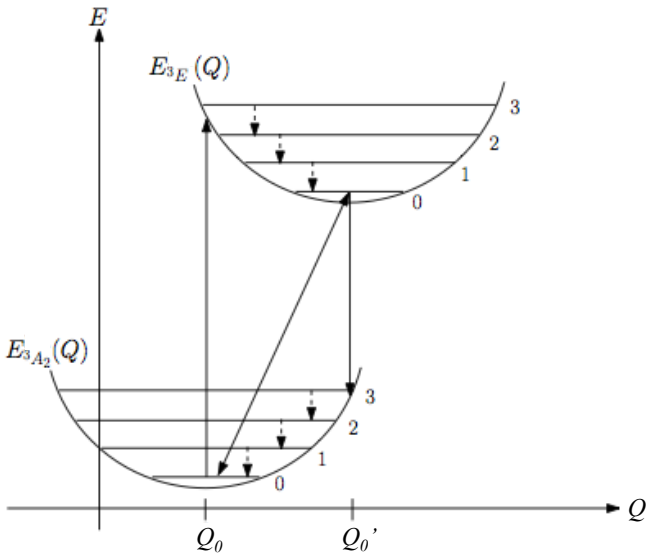

FIGURE 3.13: Configuration diagram reprinting the vibronic structure of the NV^- centre. $E_{^3A_2}(Q)$ and $E_{^3E}(Q)$ are the ground and optically excited electronic states respectively, which have a harmonic dependence of the nuclear displacement co-ordinate Q. The vibrational manifolds for each state are represented by the horizontal lines. Optical transitions are indicated by the arrows, only a selection have been depicted for clarity. The diagonal line represents the zero vibration transition (ZPL), whilst the dashed lines represent non-radiative vibronic transitions. Reproduced with permission from [93].

The difference between the ground and excited nuclear equilibrium states of the NV centre means that the overlap integrals of the vibration wave functions are non zero, as a consequence, optical transitions are allowed between all vibronic levels of the the ground and excited state, with transition rates proportional to their Franck-Condon factors giving rise to the broad PSB. The minimal overlap between the lowest vibrational levels in the ground and excited states leads to a debye-waller factor $\eta \approx 0.04$, of emission into the ZPL represented by the diagonal transition in 3.13.

3.3.3 Broadening of the ZPL

3.3.3.1 Homogeneous Mechanisms

The lifetime limited linewidth of the ZPL transition is 13MHz as regularly observed in high quality, low nitrogen content type IIa bulk diamond at 4K [28] [101]. Similar results have only once been reported in diamond nanocrystals by Shen [102]. With increasing temperature, the electrons in the ^3E excited state scatter with phonon modes of the

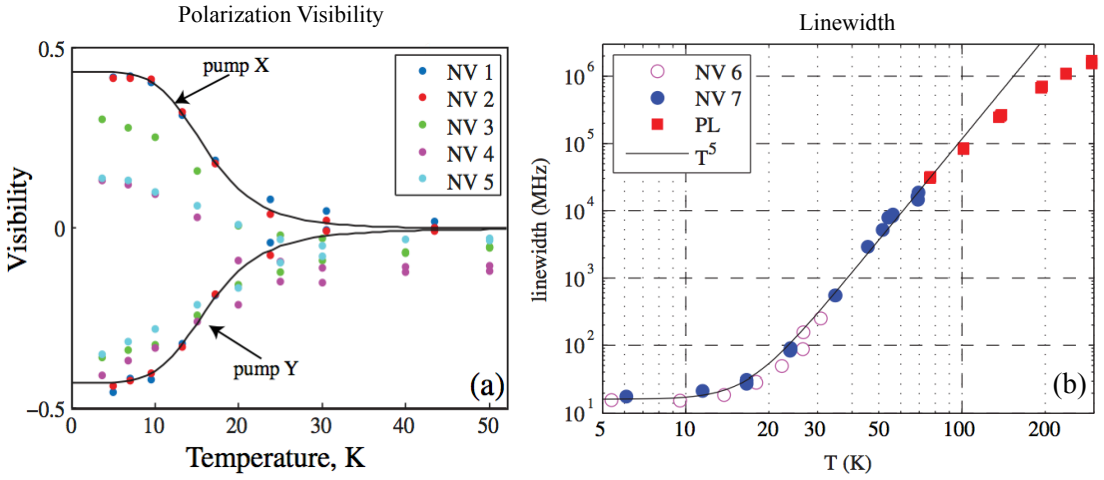

FIGURE 3.14: (a) The polarisation visibility of the strain split orbital doublet as a function of temperature. The pump polarisation of each branch is indicated in the figure. The black curve is a fit to the data. More details to be found in [101]. b) The Temperature dependent linewidths of two NV centres. The circles indicate measurement by PLE, whilst PL only measurements are shown by the red squares. The black line is a T^5 fit to the data as discussed in the main body. Both figures reproduced with permission from [101].

diamond lattice, serving to homogeneously broaden the ZPL. Fu et al observed the ZPL linewidth to have a T^5 dependence at low temperatures as in equation 3.51 [101].

$$\gamma(T) = \gamma_0 + c_2 r T^5 \tag{3.51}$$

Where $\gamma_0 = 2\pi\times$ 16.2MHz, c_2= $9.2\times10^{-7}K^{-5}$ and r= $(12.5\text{ns})^{-1}$. Such a relationship strongly indicated that the dynamic Jahn-Teller effect is the dominant broadening mechanism in this temperature range. At higher temperatures, this mechanism alone is not sufficient to fully describe the observed temperature dependence and the interaction with symmetric phonon modes becomes important to consider. Plakhotnik & co-workers recently presented a more complete description (see [103]).

The behaviour of the strain split orbital doublet with temperature is also important to note. Fu and coworkers studied to the polarisation visibility $V = (I_X - I_Y)/(I_X + I_Y)$ of the doublet with temperatures between 4-50K as seen in figure 3.14a [101]. Each doublet (denoted X,Y) was pumped with optimally aligned excitation. The polarised emission from each doublet was monitored. At 4K the thermalisation rate between

the orbital doublets is less than the radiative recombination rate. Hence by optimally pumping the X doublet, only X polarised emission is seen. The polarisation visibility was almost completely washed out at 30K. This is extremely important to consider in the presence of strain splitting. With the equipment available in this project, there is only a capacity for studies under isothermal conditions. Thus the cavity coupling is limited to the temperature of the cryogens available. The ZPL linewidths in the presence of pure dephasing mechanisms in bulk diamond are summarised for Liquid Helium, Nitrogen and Room Temperatures in table 3.2

TABLE 3.2: Temperature dependence of the ZPL

Temperature	$\gamma + \gamma*$	$\delta\lambda$ (nm)
4K	80MHz	1.8×10^{-5}
77K	310GHz	0.067
300K	12.5THz	2.7

3.3.3.2 Inhomogeneous Mechanisms

In most cases, the ZPL linewidth is also imhomogenously broadened due to the effect of fluctuating local electric fields in the presence of the NV centre, through the Stark effect [28]. In the presence of free charges in the conduction band the ZPL experiences transient energy shifts. The effect of spectral wandering can be illuminated by taking repeated PLE (photoluminescence excitation) scans of the ZPL as in figure 3.15. These free charges are mainly due to Nitrogen impurities, since this is an electron donor to the diamond lattice, with an ionisation energy of 1.7eV below the conduction band. Any Nitrogen impurities in the focal volume of the excitation beam are therefore easily ionised by an excitation wavelength of 532nm (2.34eV), resulting in fluctuating charges [28]. It can be calculated that the Stark shift of the ^3E state due to a single elementary charge within 10nm of the NV can be up to 100's of GHz [104]. Fluctuating electric field environments can also be caused by trapped charges, due to defects such as nearby vacancies and dangling bonds at the surface. These problems are particularly acute for nanodiamonds (especially those formed by HPHT) and any NV centres that are in close proximity to a surface.

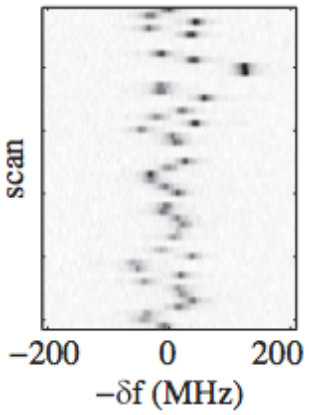

FIGURE 3.15: Spectral wandering of the NV ZPL in a bulk diamond crystal. Repeated PLE scans are able to reveal the dynamics if the spectral jumps. This is an inhomogeneous process, reproduced with permission from [101]

3.3.4 Single Photon Emission

The NV centre displays single photon emission, however the energy level structure shown represents a deviation from the a simple two level system. It is therefore important to discuss the effect this will have on the observed photon-statistics. The HBT photon correlation measurement is the key mechanism for detecting the presence of a single photon emitter. This is based on the simple principle that two detectors at the output of 50:50 beam-splitter, cannot be triggered simultaneously by a single photon (the experimental method is described in section 4.5). In short - the measurement builds up a histogram of the detection events as a function of the delay time τ between them. This is the second order correlation function of the intensities at $I(t)$ & $I(t+\tau)$:

$$g^{(2)}(\tau) = \frac{\langle I(t)I(t+\tau)\rangle}{\langle I(t)\rangle\langle I(t+\tau)\rangle} \tag{3.52}$$

Here the brackets $\langle ...\rangle$ denote the time average. At long time delays, the correlation function tends towards unity for all types of light, signifying that there is no correlation between the two detection events. As a single photon source, the NV centre will show perfect photon anti-bunching at $\tau = 0$. The correlation function is shown schematically in figure 3.16(a). However the convergence to unity at long time delays will depend on the internal dynamics of the system. The two level system, represents the simplest

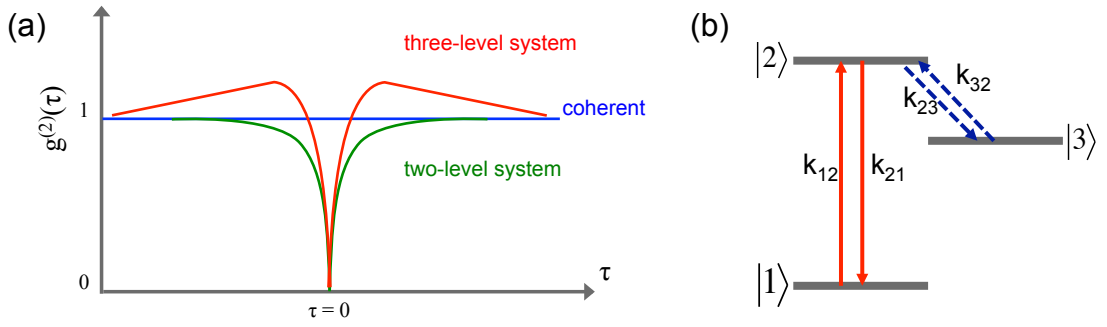

FIGURE 3.16: (a) Theoretical HBT histograms for coherent light (blue), a two level quantum system (green) and a corresponding three level system (red). (b) The effective three-level system of the NV centre with the relevant transition rates k shown

case with only the transition pumping rate and spontaneous emission lifetime of the transition contributing to the behaviour of the correlation function:

The internal dynamics of the NV are influenced by the metastable state leading to an effective three level system in figure 3.16(b). The measured correlation functions can be fit to the equation 3.53 [26]. Pumping into the metastable state for increasing excitation powers, results in photon-bunching at intermediate time delays such that $g^{(2)} > 1$.

$$g^{(2)}(\tau) = 1 + c_2 e^{-\frac{\tau}{\tau_2}} + c_3 e^{-\frac{\tau}{\tau_3}} \tag{3.53}$$

Where τ_2, τ_3 are the decay constants. All coefficients including $c_{1,2}$ are dependent on the pumping rate of the optical excitation. In the low power limit, τ_2 tends towards the spontaneous emission lifetime of the excited state. The parameters $\tau_{2,3}$ and $c_{1,2}$ have the following interdependencies on the intersystem decay rates, arising from the solution of the coupled intersystem rate equations with the NV initially in state $|1\rangle$.

$$\tau_{2,3} = \frac{2}{A \pm \sqrt{A^2 - 4B}}$$

$$c_2 = \frac{1 - \tau_2 k_{32}}{k_{32}(\tau_2 - \tau_3)} = -(c_3 + 1)$$

$$A = k_{12} + k_{21} + k_{32} + k_{23}$$

$$B = k_{12}k_{23} + k_{12}k_{32} + k_{21}k_{32}$$

3.3.5 Optical properties of NV centres in nanodiamond

The surrounding environment has been shown to be very important in determining the properties of the NV centre. The NV centre has always been touted at as a reliable photostable emitter, as the electron wave function is highly localised at the centre, well isolated from it's surroundings. It was therefore initially surprising to observe on-off 'blinking' of the fluorescence in monodisperse single digit diamonds of average size 5nm [54]. This phenomenon is commonly observed in semiconductor nanocrystals, where the excited electron can be trapped at a surface state, quenching the PL. However this was unsurprising, as the electron wave function is de-localised over the whole crystal. The case for why this happens with the NV centre is less obvious. Surface passivation of the emitters by encapsulating them in a polyvinyl alcohol (PVA) matrix (0.25% dispersed in deionised water), completely suppressed blinking, suggesting the surface states do play a role in such a small host, with the possibility that the defects were located near the surface in these cases.

It has been demonstrated that the NV centres in nanodiamond display longer lifetimes with respect to their bulk counter parts (where τ = 12.5ns) [53, 105, 106]. There is a significant change in the refractive index of the surrounding medium when incorporated in ND, which consequently reduces the optical density of states. Tisler et al [53] demonstrated a large distribution of NV lifetimes in 7nm nanodiamonds, centred at 17ns, with a spread of 15ns in the lifetime survey. This large distribution of times is attributed to the relative dipole-substrate orientation, as the substrate (n=1.5) plays a

role in the emission rate. The differing electromagnetic environment also means that the NVs can be considered as point-like emitters, which do not experience the problems of total internal reflection experienced in bulk (n=2.4) [106].

There have been relatively few detailed spectroscopic studies on the ZPL structure of NV centres in NDs at low temperature, owing to blinking and spectral instability. Zhao [107] et al have reported PL line widths of 1.2GHz at 4K, showing temperature dependence up to 20K, measured using a fabry-perot interferometer. Shen et al have been the only ones to report nearly lifetime limited line widths of 16MHz, measured using PLE [102]. Both investigations stated that the overwhelming majority of NDs studied displayed large amounts of spectral diffusion, and an amount of preselection and determination was needed to find well behaved defects. No one has since reported lifetime limited line widths in NDs, highlighting the one-off nature of this observation.

3.4 NV-Open Cavity Coupling

This section will first outline the consequences of the vibrational structure on the cavity coupling of the NV centre. For the case of ZPL coupling in the Purcell regime at LT, the emission rate into the PSB remains largely unchanged to a first approximation. A more comprehensive model of the NV cavity coupling developed by Albrecht et al [78] will then be discussed. This treatment is generalised to include the dephasing mediated coupling from all NV sub-level transitions, allowing for coupling across the NV emission range to be well described.

The final section will explore the potential for the ZPL coupling at LT, within the boundaries of the cavity parameters $(\mathcal{F}, \beta, V)$ that are currently available in this project. The predictions made will be largely for the F_{P} acting on the homogeneously broadened ZPL only, based on the linewidths observed in bulk diamond [101].

3.4.1 Consequences of the PSB for Cavity-Coupling

The presence of alternative emission pathways will affect the cavity-coupling of the NV centre and the observable Purcell factor. The optical transitions from the excited to the ground state are summarised in figure 3.17(a) [108]. There are multiple transition rates that contribute to the total emission, with only $\zeta = 0.04$ of the emission in the ZPL. This reduces the atom-cavity coupling rate g_0 by the factor $\sqrt{\zeta}$ when coupling to the ZPL only (with respect to atomic transitions, for example). In the simplest case, the consequence of the Debye-Waller factor (ζ) is that the total emission into free space can now be written as the sum of the rates into the ZPL and the total PSB as

$$\gamma_{\mathrm{fs}} = \gamma_{\mathrm{ZPL}} + \gamma_{\mathrm{PSB}} \tag{3.54}$$

Where $\gamma_{\mathrm{ZPL}} = \zeta\gamma_{\mathrm{fs}}$ and $\gamma_{\mathrm{PSB}} = (1-\zeta)\gamma_{\mathrm{fs}}$. The emission rate of the cavity coupled ZPL can then be expressed as:

$$\gamma_{\mathrm{cav}} = (1 + F_{\mathrm{P}})\gamma_{\mathrm{ZPL}} + \gamma_{\mathrm{PSB}} \tag{3.55}$$

With the approximation that the emission into the PSB is unperturbed by the cavity. The total enhanced emission into the cavity F_{tot} is expressed as the ratio of the cavity to the free space emission rate:

$$F_{\mathrm{tot}} = \frac{\gamma_{\mathrm{cav}}}{\gamma_{\mathrm{fs}}} \approx 1 + \zeta F_{\mathrm{P}} \tag{3.56}$$

Albrecht et al [78] presented a sophisticated model of the NV-cavity coupling process. At room temperature the cavity-coupling is predominantly mediated by the homogeneous dephasing of all optical transitions within the NV. Figure 3.17(b) shows the consequence of the vibrational sub-levels on the emission spectrum of the NV at room temperature.

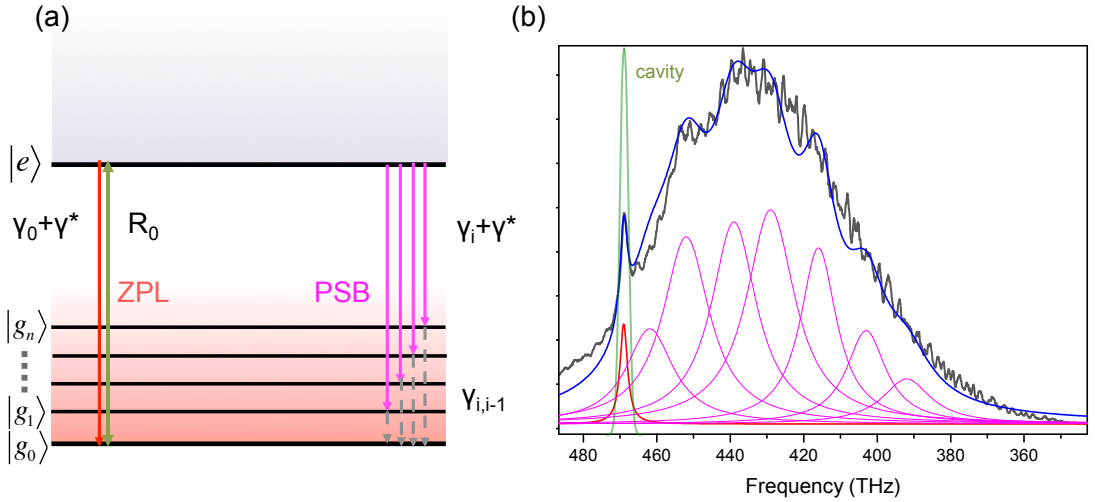

FIGURE 3.17: (a) NV optical transition from the excited state $|e\rangle$ to $|g_0\rangle$ (red) and $|g_1...n\rangle$ (pink). The associated natural and pure-dephasing rates $\gamma + \gamma*$ are shown with the additional rate $\gamma_{i,i-1}$ of the non-radiative sub level transitions (grey dashed). Adapted from [108, 109]. The effective cavity coupling rate R_0 is shown (b) Experimental spectrum of NV in bulk diamond at RT. The spectrum (black) is well reproduced (blue) by the ZPL (red) and individual PSB transitions (pink). A cavity resonance (green) is shown at the ZPL position. Adapted from [78]

Transitions between the excited state $|e\rangle$ and the ground state sub levels $g_{0...n}$ in figure 3.17(a), undergo a natural broadening γ_0 (ZPL), γ_i (PSB). All transitions from the excited state are primarily affected by the dynamic Jahn-Teller effect, discussed in section 3.3.3.1, providing an additional pure-dephasing $\gamma* = 15$THz. Finally the PSB transition will undergo an additional broadening $\gamma_{i,i-1} = 65$-85THz [109], through rapid non-radiative transitions between the vibronic levels to the ground state. This difference in transition width can be observed in the figure.

A cavity resonance (green) at the ZPL transition energy is shown schematically in figure 3.17(a),(b). Despite the detuning from the PSB sub-levels, the dephasing of the transitions leads to feeding of the emission into the cavity mode. Figure 3.18 presents a schematic of the coupling mechanism.

$\mathcal{R}_0$ represents the effective coupling rate (see section 3.2.2.2) between the cavity and ZPL transition. This is a reversible process as shown in the figure. The feeding from the PSB transitions with rates R_i are uni-directional. The effective coupling rates for the ZPL and PSB transitions are now described as:

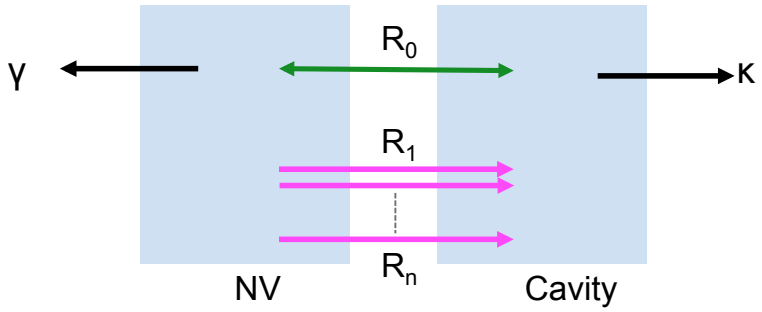

FIGURE 3.18: Schematic of the NV-cavity coupling. The Cavity is coupled to the ZPL transition with effective coupling rate $\mathcal{R}_0$ (green) between the emitter and cavity. The effective coupling rate from the PSB are shown feeding into the cavity $\mathcal{R}_{1...n}$ (pink). The NV γ and cavity κ decay rates are shown to be the loss mechanisms for the system. Adapted from [91, 109]

$$\mathcal{R}_0 = \frac{4g_0^2}{\kappa + \gamma + \gamma*} \frac{1}{1 + (\frac{2\delta_0}{\kappa+\gamma+\gamma*})^2} \tag{3.57}$$

$$\mathcal{R}_i = \frac{4g_i^2}{\kappa + \gamma + \gamma_{i,i-1} + \gamma*} \frac{1}{1 + (\frac{2\delta_0}{\kappa+\gamma+\gamma_{i,i-1}+\gamma*})^2} \tag{3.58}$$

Where $\gamma = \gamma_0 + \gamma_1 + ...\gamma_n$. The final terms on the right hand side describe the detuning of each transition from the cavity resonance where $\delta_0 = \omega_0 - \omega_c$.

The efficiency $\mathcal{B}_{\text{tot}}(\lambda)$ of NV emission into the cavity mode can be quantified as the ratio of all rates into the cavity, to the total loss rates from the NV (see figure 3.18), such that:

$$\mathcal{B}_{\text{tot}}(\lambda) = \frac{\Sigma_i \mathcal{R}_i(\lambda)}{\gamma + \Sigma_i \mathcal{R}_i(\lambda)} \tag{3.59}$$

Where $i = 0, ..., n$. This is valid at all detunings across the NV emission spectrum, and was well matched by experimental investigations into single NV open-cavity coupling at room temperature [78]. The incorporation of the pure dephasing rate $\gamma*$ means that the efficiency at low temperature can readily be determined, where the Purcell regime will dominate cavity coupling of the ZPL. This represents the most complete model of the NV-cavity coupling mechanisms to date.

3.4.2 ZPL-Open Cavity Coupling

The cavity coupling to the ZPL at LT is now considered, with an anticipation of the Purcell factors that may be possible within this project. The ZPL widths are taken to be of those observed in the bulk [101]. The discussion starts with a consideration of the mirror finesses available, summarised in table 3.3.

TABLE 3.3: Ideal Mirror Finesse in this project

Coating	Featured Mirror	Planar Mirror	Finesse at 637nm
A	$(TiO_2\ SiO_2)^{10}$	$(SiO_2)(TiO_2\ SiO_2)^{10}$	1754
B	$(TaO_5\ SiO_2)^{20}$	$(SiO_2)(TiO_2\ SiO_2)^{10}$	2664

The reflectivities are calculated via the transfer matrix method and therefore the finesse shown represents the theoretical *maximum* that these coatings can achieve. The realistic scenario will see a reduction in this, both from the finite roughness of the mirror coatings and the scattering from the emitter itself. It was seen in section 3.1, that this parameter is independent of length and thus constant in the ideal case. The cavity Q-factor scales linearly however as $Q = q\mathcal{F}$. By accounting for the presence of a DBR mirror, the Q-factor is now defined as $Q = (q + 3)\mathcal{F}$, where q=1 represents the smallest cavity length that can be achieved, with 3 antinodes penetrating into the mirror stack. Figure 3.19a shows the evolution of Q with increasing mode index. This Q/V figure of merit is shown for the $\mathcal{F} = 1754$ in figure 3.19b and is given in μm^{-3} units. The Q/V ratio is maximised for shortest cavity lengths. The ratios for a selection of feature radii are shown, including all the cavity types used in this thesis (β = 7, 10, 12μm) with some additional structures that have been achieved within the group. Below q=5, the improvement in Q/V is noticeable for all cavities.

Through the temperature dependence of the electron-phonon scattering, it will be necessary to describe the ZPL using the effective Q-factor of the system. Figure 3.20 now shows Q_{eff} of the mode number of the cavity. The cavity finesse is set to be a very modest $\mathcal{F}$=200 in this figure. At 4K the ZPL is well within the cavity linewidth for all mode indices thus $Q_{\text{eff}} = Q_{\text{cav}}$. There is a clear deviation from this behaviour at 77K as the ZPL has increased by a factor of over 10^3. The behaviour of Q_{eff} is seen as the ZPL

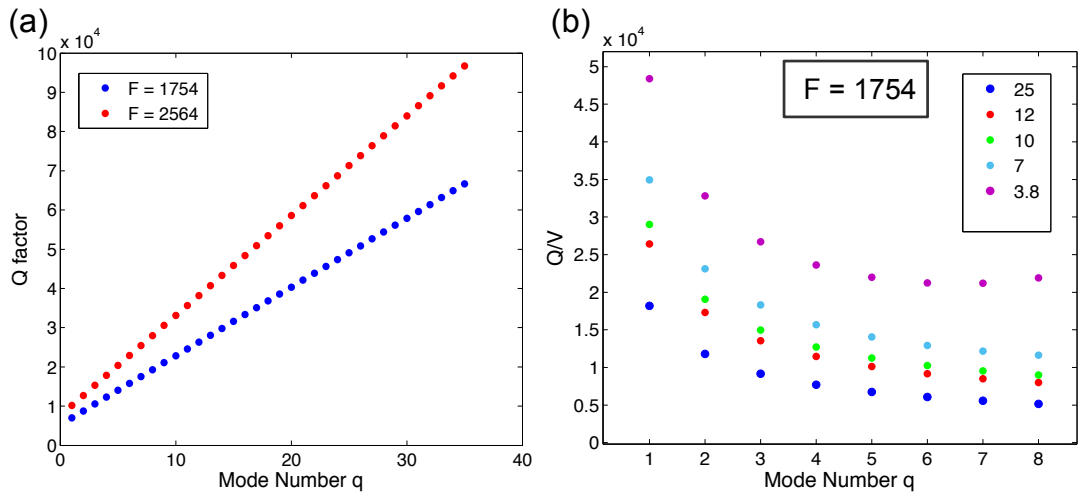

FIGURE 3.19: (a) Q-factor as a function of mode number for two different finesse values pertaining to the mirror coatings used in this thesis.(b) The Q/V parameter (units μm^{-3}) for $\mathcal{F}$=1754, plotted as a function of mode number for a selection of β available in this project

is incremented towards its room temperature value. Finally at room temperature, Q_{eff} is constant with mode index as it recovers Q_{em} in the bad emitter regime. A complementary way of considering the good-bad emitter transition is displayed in figure 3.20b. The mode index is set at $q = 4$, and the effective Q-factor is shown as the emitter linewidth is decreased. The vertical lines indicate the values taken at 4K, 77K and 300K, for an increasing finesse. All low temperature cavity coupling experiments in chapter 7 are conducted at 77K.

The Purcell factors that may be attained for the NV-open cavity system in this project are anticipated in figure 3.21. ZPL width is taken to be 0.067nm at 77K (from the bulk value [101]) and the scaling of the Purcell factor with mode index is shown for a β=7μm cavity, with coating B (cf. table 3.3) in figure 3.21(a), whilst a β=12μm cavity with coating A is shown in 3.21(b). These represent the absolute ideal case with perfect emitter-cavity spatial, spectral and dipole alignment. With the system at hand it is reasonable to expect that the emitter may be placed within the centre of the cavity mode on the planar mirror, whilst spectral alignment is a consequence of the mirror separation. The dipole alignment is non-deterministic as the emitters may be oriented randomly. Additionally, the Purcell factors shown pertain to an emitter with a single

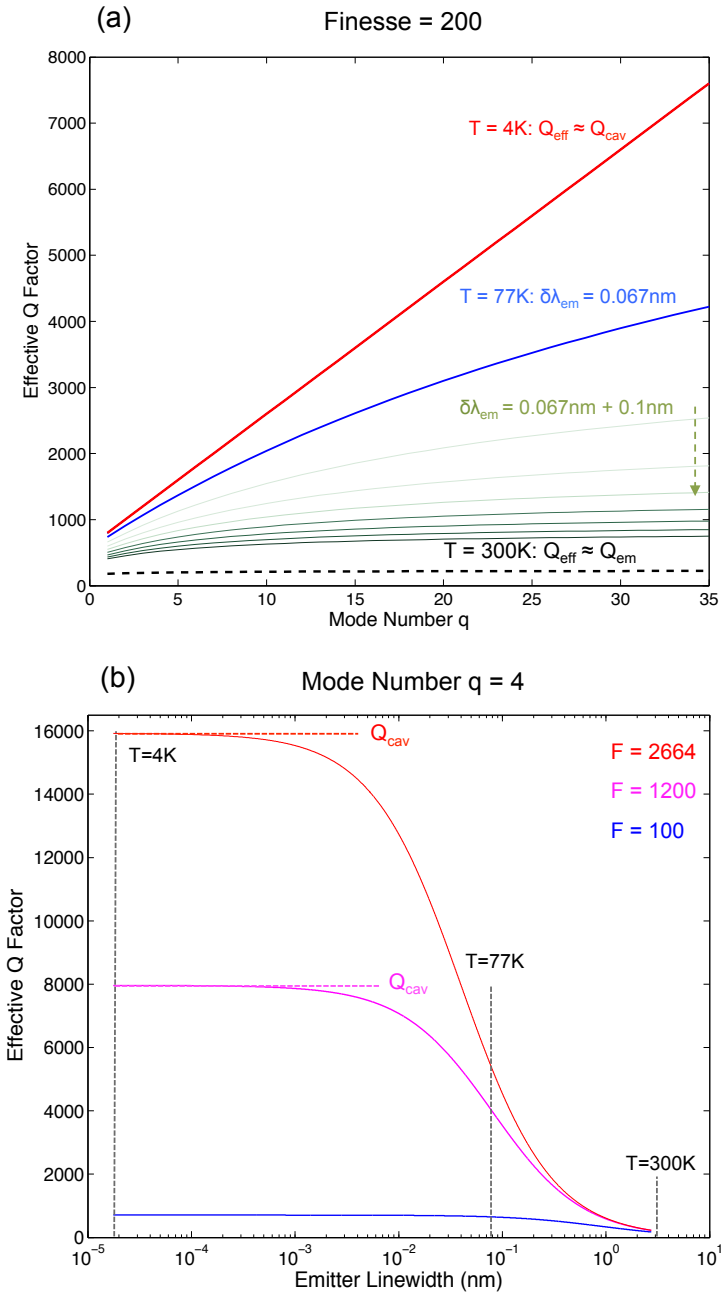

FIGURE 3.20: The transition between the good and bad emitter regime. (a) Effective Q-factor as a function of mode index for the emitter linewidth's indicated on the figure, for a modest cavity finesse. (b) The effective Q-factor as a function of emitter linewidth plotted for a range of cavity finesse. The vertical dashed lines represent the ZPL at 4K, 77K and 300K according to reference [101]. The horizontal lines indicate the cavity Q-factor. The good emitter regime is achieved for all finesses at 4K.

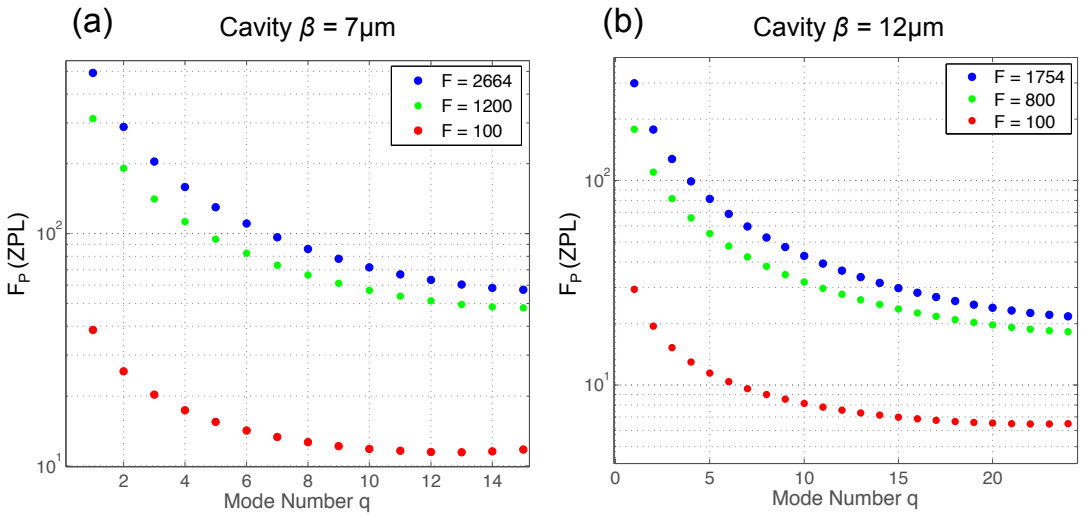

FIGURE 3.21: Anticipated Purcell Factors for NV-open cavity system at 77K for (a) β=7μm cavity, with coating B and (b) β=12μm cavity with coating A

optical transition, which has undergone pure dephasing. The perfect case as shown here serves as a benchmark for the system at hand. $\mathcal{F}$=100 represents an approximate lower bound on the experimental values observed with the nanodiamond in-place, likely due to scattering from the crystal (see chapters 5 and 7). A cautious prediction for the β=7μm mirror of F_{P}=40 may be expected in the small cavity limit. This compares with F_{P} =500 expected from the coating finesse. On accounting for the branching into the PSB, the total enhanced emission into the cavity would be F_{tot}=2.6, representing the observable enhancement in a lifetime measurement.

3.5 Conclusion

The theoretical framework within which the NV open-cavity coupling occurs has been established. The NV has been shown to span the good and bad emitter regimes of CQED. Simple predictions of the ZPL enhancement at 77K have been made on the basis of ideal spectral, spatial and dipole alignment and serve as an upper limit on the potential cavities at hand. The predicted values of F_{P} are solely for the ZPL, whilst F_{tot} accounts for the total emission. The anticipated values were also made purely on the basis that $\delta\lambda_{\mathrm{ZPL}} = 0.067\mathrm{nm}$, following the work outlined in reference [101], for centres in bulk diamond. When considering the cavity coupling results of this thesis, the appropriate geometrical and CQED parameters will be introduced in-context, for adequate comparisons to theory. The room temperature coupling results of chapter 5 will be purely within the bad-emitter regime. The entirety of the NV emission spectrum into the PSB will be approximated as a single entity with $Q_{\mathrm{eff}} = Q_{\mathrm{em}} \approx 10$. The low temperature results of chapter 7, are very much described with the cavity and emitter linewidths of the same magnitude, representing the general case Q_{eff}. Developments of this model are required as it is seen in practice that both the emitter and the cavity are inhomogeneously broadened. The theoretical description of this will be introduced in the discussion of these results.

Chapter 4

Experimental Methods

The experimental methods involved in a successful emitter-cavity coupling experiment are discussed here. Firstly, the materials characterisation tools that were required for the investigation and development of a robust sample preparation protocol are discussed. These were essential in being able to isolate singe NV centres in nanodiamond.

The cavity fabrication process will then be presented in two stages. Firstly, FIB milling into silica, followed by subsequent DBR coating. It is the FIB that provides these open-cavities with their competitive advantage in CQED in being able to construct concave profiles, both with a small radius of curvature and a shallow feature depth, allowing for small mode volumes, essential for the enhancement of the light-matter interaction.

Construction of the cavity assembly, the system by which the resonator mirrors are independently actuated will then be illustrated. This includes the deposition of the nanodiamond solutions and the critical process of mirror alignment. The optical set-up and characterisation methods will also be detailed, including an overview of scanning confocal microscopy and HBT measurements for single emitter identification. It will be demonstrated how the equipment can be reconfigured for low temperature operation. A comparison between the optical performance at RT and LT will be made. Two key experimental considerations in the optical spectroscopy of NV centres in cavities are also presented. Firstly, the optical properties of the mirror coatings, including the spectral

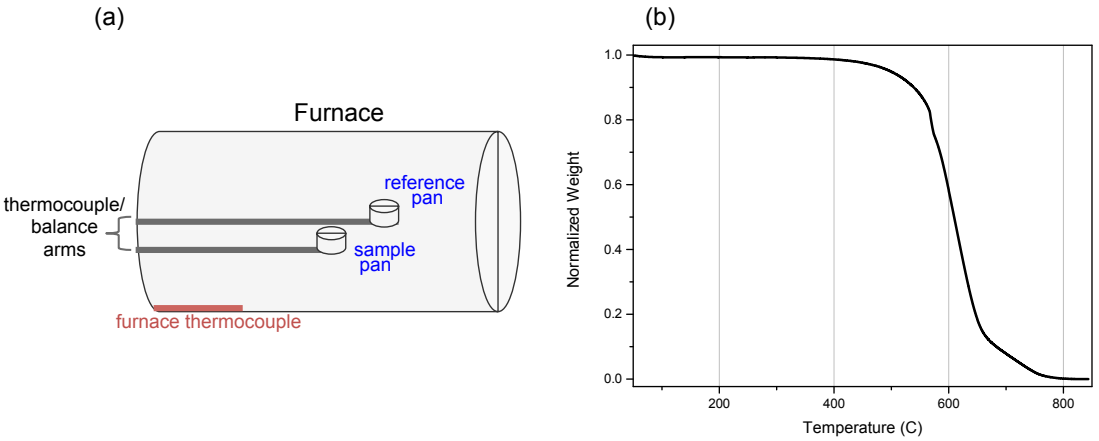

FIGURE 4.1: Thermogravimetric Analysis (a) Schematic of the TGA furnace (b) Typical TGA curve showing the sample weight as a function of furnace temperature

profile of the background fluorescence, and then the transmission of the mirror coatings for intra-cavity emitter identification. It is crucial that both of these are understood, as a pre-requisite for successful emitter-cavity coupling

Finally the FDTD method will be outlined, which was necessary in the analysis of the low temperature NV-cavity coupling results in section 7.3.2.

4.1 Materials Characterisation

4.1.1 Thermogravimetric Analysis

Thermogravimetric Analysis (TGA) is a method by which the changes in the physical and chemical properties of materials can be measured as a function of the thermal conditions. It is widely used in the analysis of carbon nanomaterials. Its purpose in this investigation is to determine the optimal conditions under which to anneal the nanodiamond samples, in order to selectively remove surface graphitisation and sp^2 content, thus breaking apart the graphitic matrices that bind the nanodiamond agglomerates together, whilst maintaining sp^3 content. Carbon materials readily oxidise at high temperatures in air, however the onset of oxidation will differ for each phase.

The instrument [Perkin Elmer Pyris Diamond TG/DTA] consists of a crucible into which the powdered material is placed, supported by a precision balance to measure changes in weight. This apparatus is situated inside a furnace with the options for different ambient conditions, such as air or an inert gas environment, shown schematically in figure 4.1(a). A typical TGA trace is displayed in figure 4.1(b). As the temperature is increased with a specific ramp rate, the sample weight is monitored, thus one can observe the onset of mass-changing phase transitions such as oxidation, sublimation or vaporisation. Graphs of mass as a fraction of total weight are plotted against sample temperature, monitored by a thermocouple at the base of the crucible. Measuring the temperature at the sample with respect to an adjacent reference crucible can allow the observation of endo/exothermic transitions [110]. Setting the system to isothermal conditions is also possible. This will be informative of the mass loss rate (dM/dt) that can be expected during the annealing process. The melting points of Indium and Tin samples are used to calibrate the thermal readings.

4.1.2 Raman Spectroscopy

Raman spectroscopy is widely used in the study of molecular and crystal structure. In this context, the principles of Raman spectroscopy and the spectral features of Carbon materials are briefly discussed. Raman scattering constitutes the inelastic scattering of incident light by the crystal structure. In basic terms, some of the incident energy is transferred to interatomic oscillations, and the scattered energy will be lower depending on the vibrational frequency of the specific degree of freedom that has been excited. The vibrational frequency will be sensitive to the atomic masses involved, the type and the orientation of the bonding between them. Hence there are distinct Raman signals for Diamond, Silicon and Germanium despite having identical diamond cubic crystal structure [112]. It is also well placed to distinguish between the allotropes of Carbon, due to the multitude of possible crystal structures, bond hybridisations and orientations. Due to its overall uniformity and periodicity, bulk diamond has a particularly high Raman cross-section, with a Raman shift of 1332cm^{-1} corresponding to the vibrations

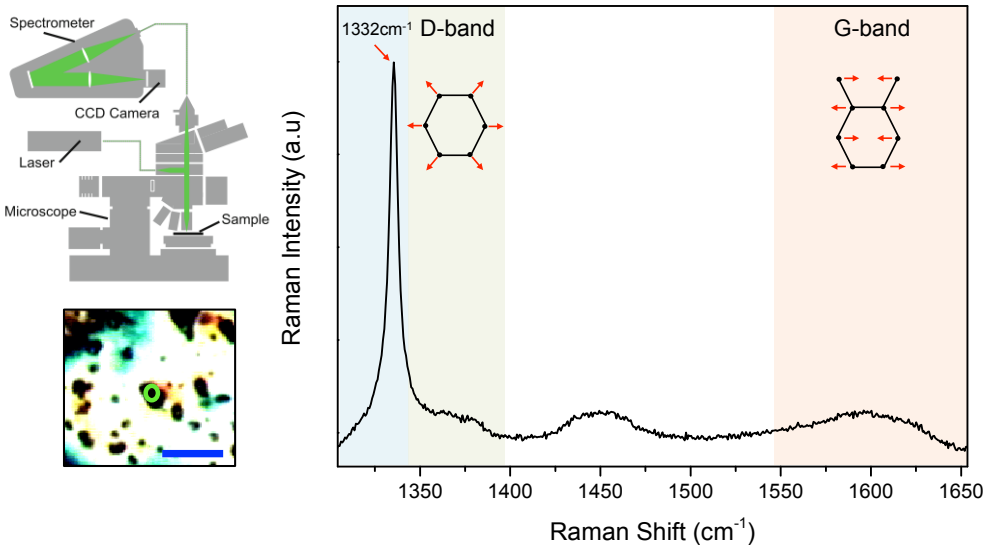

FIGURE 4.2: Top left: Schematic layout of the Raman Spectrometer [Horiba Jobin Yvon: LabRam Aramis]. Reproduced from [111]. Multiple objective lenses are available on the turret [Olympus MPlan x10 0.25NA, Nikkon SLWD x50 0.45NA, Olympus MPlan x100 0.9NA]. Scattered light is sent to a spectrometer with a 1800lines/mm grating and a peltier cooled CCD. Bottom left: White light reflection image of nanodiamonds spin coated on a Silicon wafer. The blue scale bar indicates $10\mu m$. The green circle indicates the target of the laser during acquisition. Right: Raman spectrum of a nanodiamond sample in this thesis, chosen to highlight the typical key features of Diamond (1332cm^{-1}, D and G band scattering

of the two interpenetrating cubic sub-lattices [113]. Crystalline graphite on the other hand, has a Raman shift of 1582cm^{-1}. It gives name to the sp^2 related G-band of Raman features, which can appear as a broad peak around this energy in graphitic samples. In the molecular picture, this peak corresponds to the bond stretching of sp^2 pairs, both in rings and in chains. When the system becomes more disordered, 'breathing' vibrational modes of the sp^2 rings become available, which gives rise to the D-band at 1360cm^{-1} [114]. This mode is forbidden in perfect crystalline graphite [111] These signatures are summarised in figure 4.2.

The interpretation of Raman spectra can therefore yield semi-quantitative information about the relative sp^2/sp^3 ratios, through the comparison between the relative intensities of the diamond peak and the G-band. In addition it can give an indication of the disorder in the system as broadening of these peaks suggests more Raman vibrational modes becoming active as the Raman selection rules break down [115]. Reducing the size of the crystal is one way of increasing the relative disorder and thus the 1332cm^{-1} peak

is observed to be broadened in nanodiamond. The Raman cross section varies between the sp^2 π-bonded material and the sp^3 σ-bonds, depending on the excitation energy. The cross section for the π bonds are greater in visible excitation (a factor of 50-200 $> \sigma$ bonds at 514nm), meaning that non-diamond or amorphous sp^3 is challenging to detect. Conversely with UV excitation, σ come to dominate over π. There are many subtleties when interpreting the Raman spectra of carbon material (the reader is directed to Ferrari [116], and Prawer [113] for more detailed insights), however for these purposes it will be sufficient to have a qualitative picture of the main spectroscopic signatures. The key features in the Raman spectrum of diamond are shown in 4.2. A Raman spectrometer [Horiba Jobin Yvon: LabRam Aramis] is used to take these measurements. These essentially consist of an optical microscope adapted for laser excitation in an epi-configuration, with the scattered light and fluorescence being sent to the spectrometer for analysis. The grating has a resolution of 1800lines/mm and is collected on a Peltier-cooled CCD. 532nm excitation is used for this project. The microscope takes white light reflection images to assist the navigation around the sample and the instrument is operated using the Labspec 6 software package. The samples are prepared on Silicon wafers, chosen as it has a well defined Raman peak at 520cm^{-1}, which is well away from the region of interest in this study (1000-1700cm^{-1}). It is also necessary to use the Raman peak of Silicon in the automatic calibration process prior to starting every set-up process.

4.1.3 Dynamic Light Scattering

Dynamic light scattering (DLS) is a technique through which the size distribution of nano particles in solution can readily be measured. The basic principle of DLS is illustrated in figure 4.3. The nanodiamond in solution is placed in a 10ml disposable sizing cuvette. Laser light (633nm) incident on the solution, is scattered by the particles dispersed within. The single photon avalanche detector (SPAD) is set-up in a 173° backscatter configuration, this is to reduce undesired signal from large contaminants which tend to scatter in the forward direction (Mie Scattering). The short optical path length also

ensures that multiple photon scattering events are reduced, which interfere with the outcome. The system monitors the fluctuating intensity of the scattered light as the particle diffuse in the solution through brownian motion. The scattered intensity is then analysed with a digital correlator. An attenuator prevents saturation of the detector to ensure maximum sensitivity. At short delay times, τ, after the start of the measurement ($\approx$ ns), the correlation between the measured intensities will be high as the particles will not have dispersed much in this time interval. With time, any correlation with the first measurement is lost ($\tau \approx$ ms) through the random motion of these particles. The key principle is that larger particles will diffuse slower than smaller ones, thus taking longer for the correlation to decay away. This allows for the distinction between particle size. Through fitting the correlation function to an exponential, the diffusivity ($\propto$ the decay constant) can be calculated. The particle size is related to the diffusivity, D by the Stokes-Einstein equation

$$D = \frac{k_B T}{3\pi\eta d} \tag{4.1}$$

Where T is the temperature, η is the viscosity of the solution and d is the particle diameter. It must be noted that this simple relation regards the particles to be spheres. This is usually not exactly the case, especially for nanodiamonds. The instrument measures the hydrodynamic diameter - which is described as the diameter of a hard sphere that diffuses as the same time as the particle being measured. Further details on the operating principles of DLS specific to the instrument used in this investigation [Malvern Zetasizer Nano ZS] can be found in the manual [117].

4.2 Cavity Construction

The hemispherical features are fabricated by FIB milling, which distinguishes these open cavities from alternative techniques. Cavity development and fabrication are carried out by Aurelien Trichet & Philip Dolan within the Photonic Nanomaterials Group.

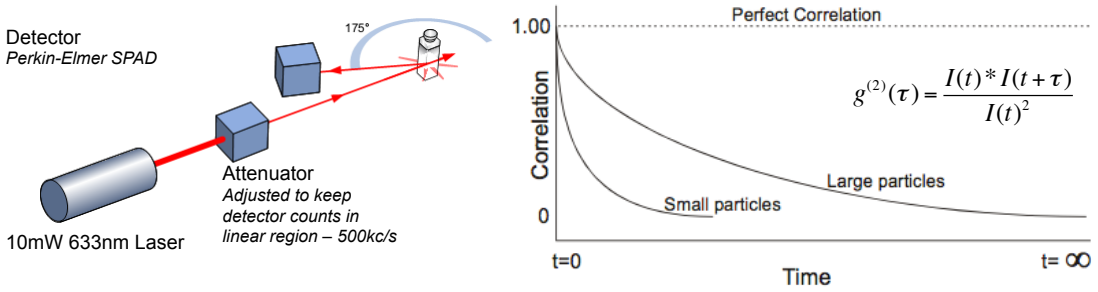

FIGURE 4.3: Left: Schematic layout of the DLS instrument [Malvern Zetasizer Nano ZS]. Reproduced from [117]. Backscattered laser light is detected by a SPAD. Right: The instrument measures the correlation function of the scattered intensities

The basic fabrication steps are outlined in figure 4.4. The initial structures are milled onto fused silica substrates [UQG Optics PFS-5005] with an initial surface roughness of σ_{rms}=1.5nm. These must be sputtered with a $\approx$ 50nm conductive layer of gold prior to fabrication, to avoid charging of the substrate. This can result in deflection of the Gallium ion beam, compromising the structural quality of the features. By varying the dwell time as the beam scans across the surface, a concave profile can be produced. The Ion beam allows for beam diameters of 5nm-1μm depending on the current. With this a full control over the size and shape can be achieved. A low surface roughness of these features is crucial as this directly impacts the finesse and Quality factors of the final structures. The FIB milling process has an intrinsic polishing effect, as the sputtering rate depends on the incident angle. It is seen that an improved surface roughness of σ_{rms}=0.7nm is achieved after the milling process, making these structures suitable for high-reflectivity mirror coating.

After milling, and subsequent cleaning, the substrates are sent for DBR mirror coating. Alternating layers of high/low reflective index materials are deposited through physical vapour deposition (PVD) [Thin Film Facility, Department of Physics, University of Oxford]. The samples are mounted at the top of a vacuum chamber. The deposition materials are heated and evaporated and the vapour then condenses on the substrate. The technique has the capacity to exert great control over the layer thicknesses, d. The mirror are chosen such that $d = \frac{\lambda}{4n}$ (see section 3.1.3), where λ = 637nm, providing the highest finesses at the ZPL wavelength. At the in-house facility, 10 pairs of SiO_2 (n=1.4) and TiO_2 (n=2.1) are deposited. Mirror coatings from commercial sources

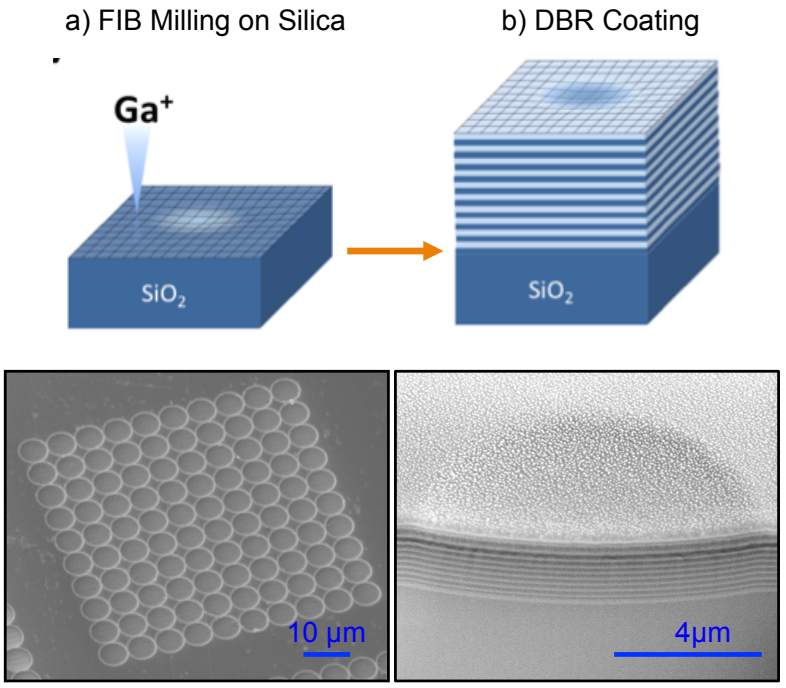

FIGURE 4.4: (a) Above: the hemispherical features are milled into a silica substrate. Below: SEM image of a hemispherical array milled into Silicon to achieve best contrast in the SEM. (b) The DBR mirrors are subsequently coated onto the milled substrate. The coating layers take the profile of the underlying feature. Below: cross sectional SEM after DBR coating. The alternating layers of SiO_2 and TiO_2 are clearly observed. A conductive layer of gold is deposited on top for the imaging process leading to the patchy deposits on the final layer. Schematic diagrams and SEM images are courtesy of Aurelien Trichet.

are occasionally used in this thesis. 20-pair, ultra-high reflectivity coatings are sourced from LaserOptik in chapter 7, whilst the optical properties of DBR coatings from Helia Photonics and SLS Optics are also explored in section 4.7.

The coating growth mechanism must be carefully considered in the fabrication process in order to maintain high finesses. With such small radii of curvature, the concave features can have sharp edges, which translates to the mirrors upon coating resulting in cracks. These are detrimental to the optical properties and can be observed as a reduction in finesse with increasing cavity length. As the mode waist on the concave mirror spreads with increasing cavity length, diffraction losses occur at these edges and the Finesse is compromised. This is demonstrated prior to optimisation in figure 4.5b, for a cavity with $\beta = 19\mu$m. By considering the growth mechanisms of the mirror, this can be fed back into the fabrication process, altering the profile of the milled feature to achieve subsequent mirror coatings with the desired radius of curvature and smooth

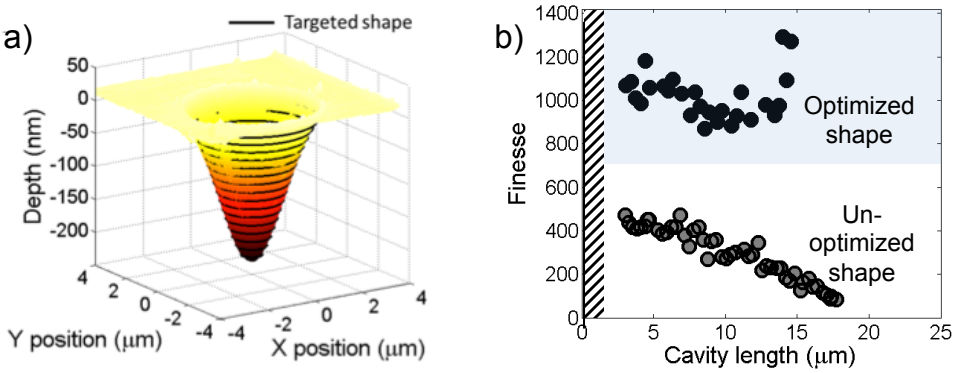

FIGURE 4.5: (a) AFM topography of a concave feature prior to mirror coating. The black lines represent the contours for the desired shape fed into the fabrication process, demonstrating an excellent match to the final structure. The shallow feature depth relative to the lateral profile can be observed here. (b) Finesse measurements in transmission for β=19μm cavity, as a function of cavity length. Optimisation of the milled shape to account for the mirror growth mechanisms ensures the Finesse is largely constant with length as expected. Measurements and figures courtesy of Aurelien Trichet.

.

edges. The optimisation is seen to achieve a consistent Finesse with increasing the length, as expected. With progressively smaller radii of curvature, this optimisation becomes more challenging, and is the subject on ongoing work within the group. This process however, demonstrates the power and flexibility of the FIB, in being able to tailor the cavity structures and achieving full topographical control.

The final structure is shown in figure 4.6b. Starting with a 1mm fused silica substrate, a plinth is constructed using a dicing saw, prior to milling. This extends 250μm above the rest of the substrate and is 380x320μm in area. This avoids the substrates coming into contact, away from the region of interest, which assists the reduction in cavity length. An array of concave features are milled with differing β, allowing the cavity-coupling parameter space to be explored in one experimental run. These parameters are shown in figure 4.6a. Registration grids are FIB milled onto the planar mirror as in figure 4.6c [FIB milling courtesy of Philip Dolan]. This is an essential design feature to allow the location and re-location of NV centres at room and low temperature. It is also enables features to be imaged on the underside of the mirror as in section 4.8. Guiding marks and orientation features enable to location of the region of interest.

(a) Feature Properties

R	19	16	12	10	5.6	7.5	3.8	1.7	2.5
dia	10.5	10.5	8	6	4	5	3.7	1.8	2
depth	0.65	0.75	0.55	0.45	0.35	0.40	0.25	0.22	0.22

(b) Plinth Profile (c) Plinth Profile (d) Planar Mirror

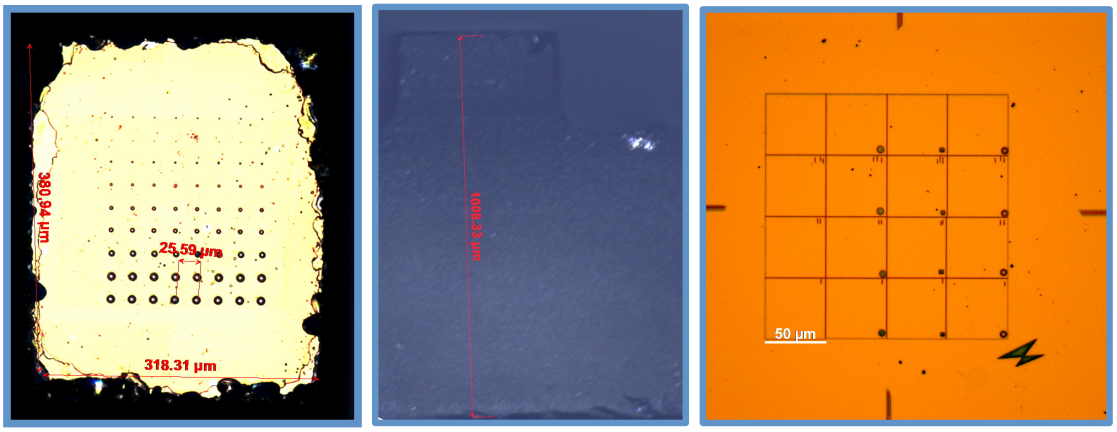

FIGURE 4.6: (a) Concave feature properties, dimensions are in microns. (b) Optical microscope images of the finished plinth after coating. (c) Optical microscope image of the plinth, side-on. The plinth extends 250μm above the rest of the substrate (c) A 4x4 grid, each of side 50μm, is FIB milled onto the planar mirror after coating. An orientation mark and guides are also milled, to locate this region of interest

.

4.3 Cavity Mounting

The mirror substrates are cleaned by sonicating in acetone, before wiping with an isopropanol soaked lens tissue. As a final step, the substrates are subject to an oxygen plasma clean, which cleans organic residue from the surface, and also has the added effect of making the substrates hydrophilic. This allows for a uniform converge on deposition of nanodiamond solutions prior to spin coating. Nanodiamond solutions dispersed in de-ionised water are passed through a 200nm syringe mesh filter [PTFE], ensuring no large contaminants. A single droplet of solution is spin coated [SPS Spin150], in a two stage program. First at 500RPM for 5 minutes to allow the droplet to spread uniformly, and for the nanodiamonds to adhere to the surface. Finally at 3000RPM for 30s, to spin off the excess solution.

The mirror substrates are mounted onto the cavity apparatus as shown in figure 4.7, with the orientation dependent on the experiment at hand. This system is specifically

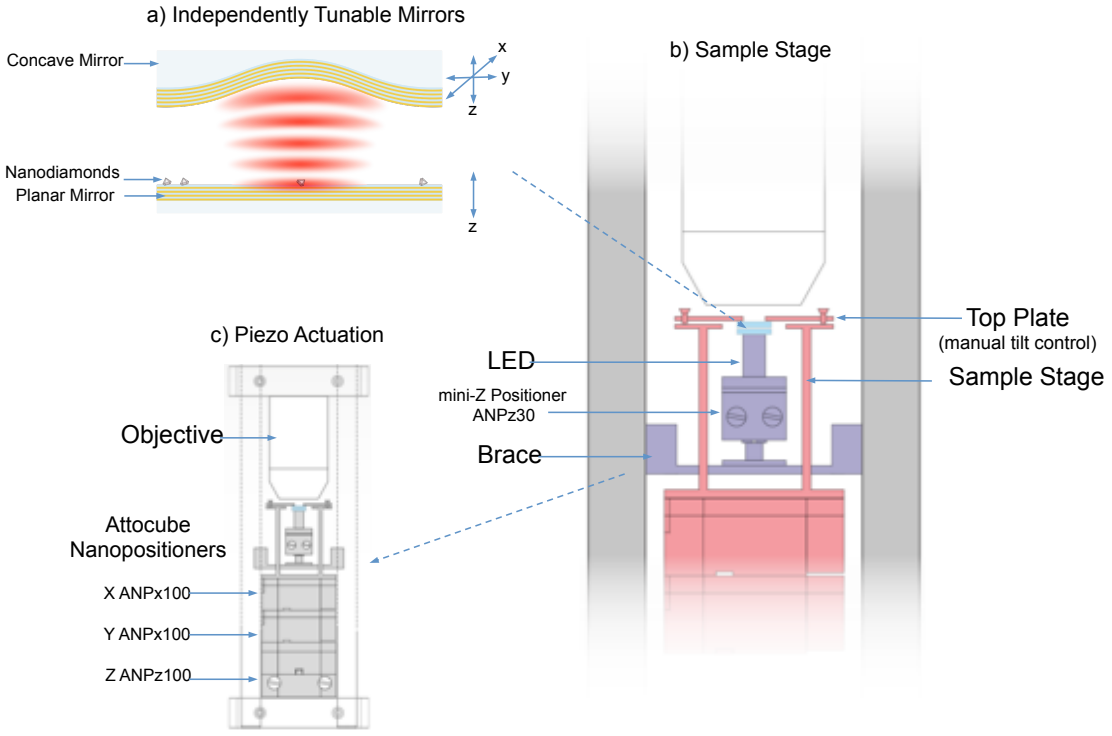

FIGURE 4.7: Schematic diagram of the cavity apparatus. (a) The mirrors are mounted to be independently tunable. The degrees of freedom of the top and bottom mirrors are indicated by the blue arrows. The emitters are always spin coated onto the planar mirror. (b) The sample stage used to mount the mirrors to the actuators. The bottom mirror assembly [Purple] consists of an LED on a mini-z piezo, which is then braced to the outer cage rods. The top mirror assembly [Red] is independent of this, consisting of an aluminium table that extends to the larger XYZ piezo stack. Optical access is achieved from above the structure (c). The complete apparatus which can interface with the confocal microscope. Figures (b), (c) courtesy of Philip Dolan [118]

.

designed for low temperature operation, and it will be seen in section 4.6, how the apparatus can be re-configured. The top mirror has the three translational degrees of freedom allowed by the Attocube piezo nanopositioner stack [ANPz100, ANPx100, ANPx100]. The piezo control modules [ANC300 Controller, 3xANM150 Modules] do not have piezo scanning capabilities. Instead the movement is achieved by a stepping motion with the precision dictated by the minimum threshold voltage for actuation, which is increased at LT. For the majority of of the emitter-coupling experiments, the piezos were operated with this limitation in place. This obstacle was overcome in the final LT-coupling experiments (section 7.2) by implementing an external voltage source [Keithly SourceMeter 2400], to bypass the control module. This provides a voltage to fine tune the piezo crystal. The cavity mode was then able to be precisely and deterministically

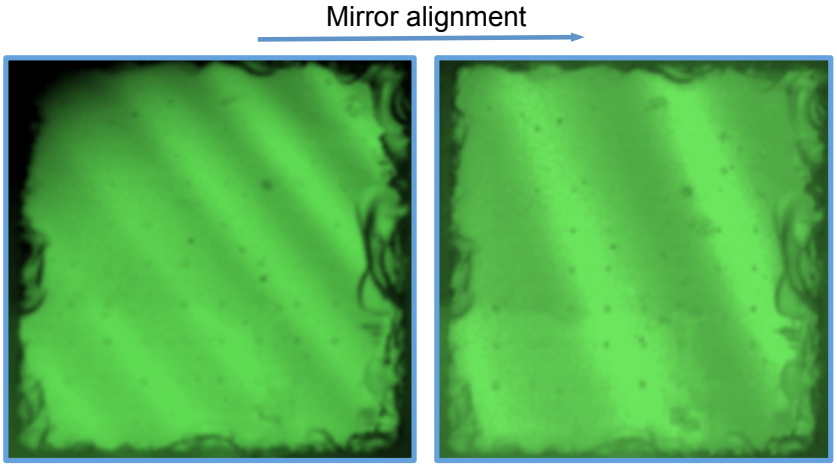

FIGURE 4.8: The mirror alignment process. While light transmission images through both mirror substrates, when in contact. A 532nm bandpass filter is placed in the optical path to allow the fringes to be observed. The substrates are brought into alignment through the manual tilt control of the top mirror, to reduce the number or fringes observed.

positioned, which gave the subsequent experiments a significant advantage.

The sample stage is constructed from aluminium. The mirror is attached to the top plate using a transparent adhesive. The top plate has adjustable grub screws, which allow for rudimentary tilt control essential for the alignment of the mirror substrates. The bottom mirror is independently adjustable with only the z-degree of freedom facilitated by the mini-z positioner [ANPz30].

The LED allows the mirrors to be observed in white light transmission, which is purely for alignment purposes as seen in figure 4.8. A band 532nm band-pass filter is used to observe planar Fabry-Perot modes as fringes in transmission, owing to the residual reflectivities of the mirrors at 532nm ($R = 0.55$). Bringing the mirrors into parallel reduces the number of fringes observed. This process is applied iteratively until completion.

4.4 Optical Spectroscopy

The entirety of the optical characterisation in this project is carried out using a home-built beam-scanning confocal microscope. The principle feature of confocal microscopy is the depth resolution that can be achieved. Point source illumination is first focused

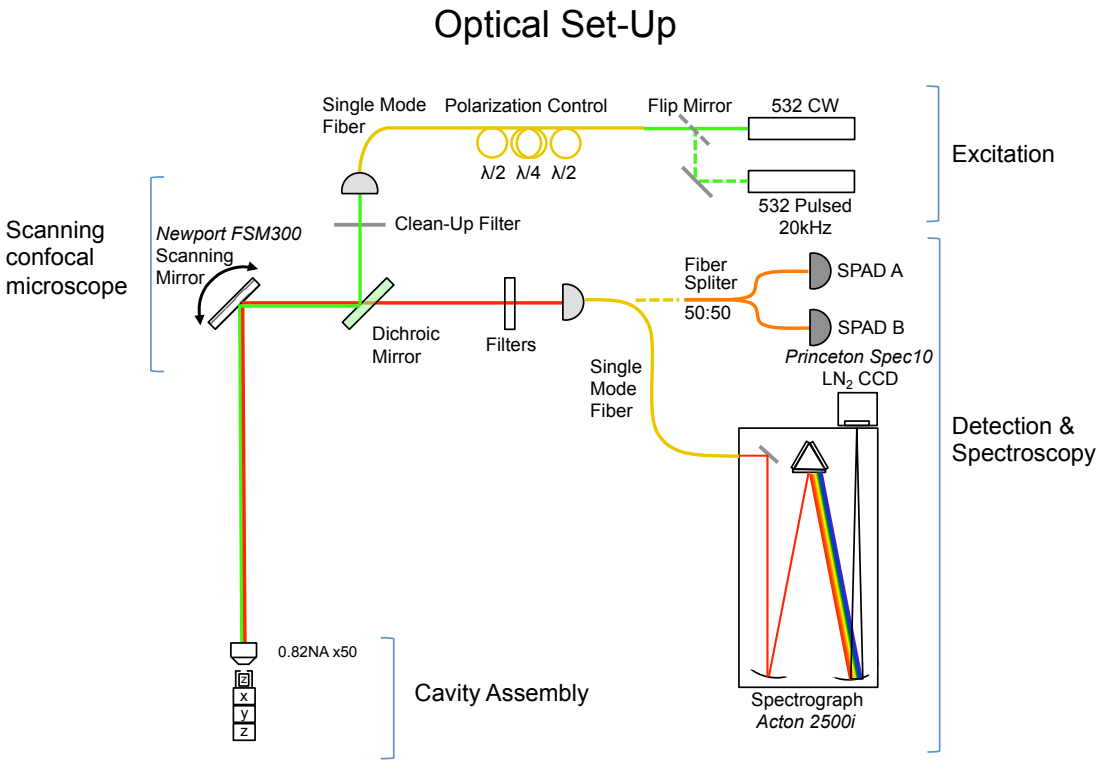

FIGURE 4.9: A schematic layout of the Optics Lab for Room Temperature operation. All optical components are mounted onto an optical table. A periscope construction allows the sample to be mounted vertically

onto the sample, with the image then focused through a pin-hole before reaching the detector. If this aperture is placed in the image plane of the microscope, then it becomes confocal with the focal plane. This serves to suppress scattered light and fluorescence outside of the focal plane and thus depth resolution through the sample is achieved. The confocal microscope is necessary for applications where such resolution is required and is widespread in the biological sciences. It is also central to the study of colour centres in diamond, and other single quantum emitters, where depth sectioning and rejection of background fluorescence are crucial in achieving high single photon fidelity.

The full optical setup can be seen in figure 4.9. Laser excitation at 532nm is used to excite the NVs in CW [CNI MGL-III-532, 200mW] or pulsed mode [Teem Photonics-SNG-20F-1SO, 20KHz]. The excitation is coupled through a single mode fiber (Thorlabs SM460HP), which is coupled to the excitation arm of the scanning head (figure 4.10). The output aperture of the fibre provides the point source illumination in this case. Fiber polarisation control (Thorlabs FPC030) is achieved with three independent spools that

exploit stress-induced birefringence to create independent wave plates ($\lambda/4, \lambda/2, \lambda/4$). In theory these allow full polarisation control and in practical terms are positioned such that the excitation of the NV centre is optimised. The excitation and fluorescence are collimated as they propagate within the scanning head. A fast-steering mirror (Newport FSM300) rapidly scans the excitation spot over the sample. The objective is situated in a 4f configuration from the steering mirror, mediated by opposing telecentric lenses (f = 250mm), ensuring the beam enters through the centre of the objective. The resulting large field of view is advantageous for identifying suitable emitters quickly. Fluorescence is coupled through the collection arm into single photon avalanche detectors for imaging (Perkin-Elmer SPCM-AQRH), via a single mode fiber (Thorlabs SM600), which provides the confocal aperture of the microscope. A wire-grid polariser is placed on a rotation mount [Thorlabs CRM1] for polarisation analysis. An Edinburgh Instruments [TCC900] card provides the correlation electronics for the HBT and lifetime measurements. The output fiber can also be coupled to a spectrograph (Acton 2500i), equipped with a liquid nitrogen cooled CCD (Princeton Spec10). Two diffraction gratings are available (300 & 1200 lines/mm) providing 0.13nm and 0.03nm spectral resolution respectively. The decision to use fiber coupled excitation and fluorescence has enormous practical advantages for usability and becomes crucial when mounting the scanning head vertically on the bath-cryostat for low temperature operation, as discussed in section 4.6.

4.5 HBT & Lifetime Measurements

Photon correlation experiments are able to confirm the presence of single emitters. The fluorescence is output to a 1x2 50:50 fiber splitter (Thorlabs FCMM50-50A) with a second SPAD for the HBT measurements as in figure 4.9. A photon detection event on the first SPAD starts the measurement at time $t = 0$. A second photon on the other detector ends the measurement at time $t = \tau$. A histogram of the intensity correlations between the two detectors is built up as a function of the delay time τ, between the start

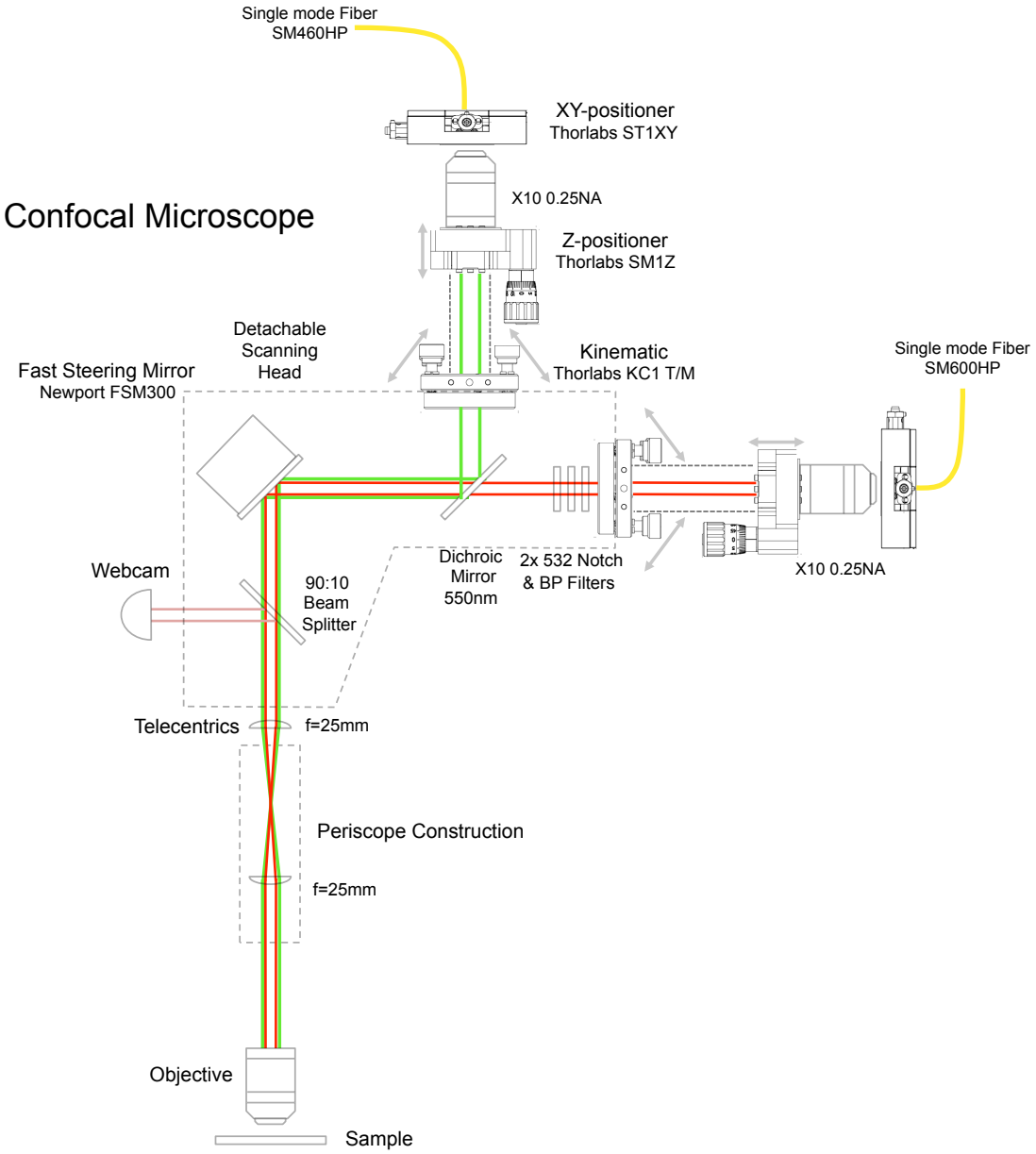

FIGURE 4.10: A detailed schematic of the Confocal microscope, including all actuators necessary in the alignment of the scanning head. The excitation fiber output is mounted to the excitation arm on an xy positioner, with the output beam collimated using a x10 0.25NA objective. A kinematic mount allows the launch angle of the excitation arm to be adjusted. An identical set-up is used on the fluorescence collection arm. A dichroic mirror splits the excitation and fluorescence. Notch filters suppress scattered excitation light from reaching the detector, whilst spectral and polarisation filters are placed in the collection arm as appropriate.

and stop events. The histogram is described by the second-order correlation function of the intensity on each detector $I(t), I(t+\tau)$ in 4.2.

$$g^{(2)}(\tau) = \frac{\langle I(t)I(t+\tau)\rangle}{\langle I(t)\rangle\langle I(t+\tau)\rangle} \tag{4.2}$$

In practice, the resulting histogram must be normalised to obtain the correlation function. This is achieved through dividing by $I_1 \times I_2 \times t_{\text{bin}} \times T_{\text{tot}}$, where $I_{1,2}$ is the mean intensity on each detector through the measurement, t_{bin} is the histogram bin width and T_{tot} is the total integration time [26]. As previously stated, single photon emission cannot result in simultaneous detection events, leading to $g^{(2)}(0) = 0$. Due to the power dependent internal dynamics, a low excitation power is generally used in order to achieve a good resolution on the anti-bunching dip.

As will be seen in section 4.7, the cavity mirror substrates contribute a broadband non-negligible fluorescence background. It becomes necessary to briefly discuss the role of this background in the HBT measurement. For the case where a single NV_A and a fluorescent background contribute to the histogram, the probability for each detection event, P_A, P_bkg is determined by the signal to noise ratio in the measurement. At long time delays, the following detection events add to unity.

$$P_\text{A}^2 + 2P_\text{A}P_\text{bkg} + P_\text{bkg}^2 = 1 \tag{4.3}$$

Since NV_A is a single emitter, $g^2(0)$ is expected to be:

$$g^{(2)}(0)_1 = 1 - P_\text{A}^2 = 2P_\text{A}P_\text{bkg} + P_\text{bkg}^2 \tag{4.4}$$

In other words the uncorrelated detection events, due to the background photons, present a baseline in the measurement. The signal to noise ratio (SNR) must be considered in every measurement when trying to verify single photon emission.

When studying NV centres in nanodiamond, it is non un-common to find multiple NV centres in one crystal, even with adequate sample preparation. In practice it can be found that the emitters appear of un-equal intensity due to selective excitation polarisation and the possibility of favourable dipole orientation with the mirror plane. With the presence of a second single emitter NV_B in the same measurement, $g^{(2)}(0)$ is now expected to be:

$$g^{(2)}(0)_2 = 1 - P_A^2 - P_B^2 \tag{4.5}$$

If $NV_{rmA,B}$ are of unidentical intensity, their contribution to the total signal (probability P_{sig}), can be quantified as:

$$P_A = (1-\alpha)P_{sig}, \qquad P_B = \alpha P_{sig} \tag{4.6}$$

Where α is the fraction of total emission. The $g^{(2)}(\tau = 0)$ can now be expressed as:

$$\begin{aligned} g^{(2)}(0) &= 1 - P_{sig}^2(1-\alpha)^2 - P_{sig}^2\alpha^2 \\ &= 1 - P_{sig}^2(1 - 2\alpha + 2\alpha^2) \end{aligned}$$

For the special case where emitters A & B are of equal intensity, with no background signal present, $\alpha = 0.5$ and $P_{sig} = 1$. The correlation function will then be $g^{(2)}(0)$=0.5. This explains the oft quoted threshold for single emitter detection. However, this applies strictly to identical emitters of equal intensity.

The set-up in figure 4.9, is also capable of taking PL lifetime measurements. Emission is switched from CW to pulsed, via a flip mirror, requiring no re-alignment. With a repetition rate of 20KHz, the bin width, t_{bin} is generally set between 1.9-3.9ns to allow for a more rapid acquisition time. The data is fit by a single exponential of the following form:

$$I(t) = I_0 + Ae^{-\frac{t-t_0}{\tau}} \tag{4.7}$$

Where I_0 is the baseline, A is the amplitude of the fit and t_0 the start of the decay.

4.6 Low Temperature Experimental Methods

This system is capable of low temperature operation. For this purpose, the scanning head of the microscope in figure 4.10 can be detached from the optical bench and mounted onto a bath cryostat [100L Wessington Cryogenics]. The low temperature system can be seen schematically in figure 4.11a, with the scanning head during operation shown in 4.11b.

The cavity apparatus is detached from the RT periscope construction and mounted onto a vertical cage system, with telecentric lenses incorporated. The cage system is then placed inside a vacuum tube, which has optical access and an electrical interface for piezo control. This system is pumped down overnight [BOC Edwards TIC Pumping Station: Rotary & Turbo], removing moisture that could lead to piezo failure at LT. At 10^{-5}mbar the pumpdown is completed. 50mbar of Helium gas is then flushed into the vacuum tube in order to act as an efficient heat exchanger. The Dewar is filled with liquid Nitrogen, and the system is slowly inserted into the dewar over the course of an hour, avoiding a thermal shock to the apparatus. All LT investigations in this thesis were conducted at 77K.

For low temperature operation the cavities are mounted such that the objective [Attocube LT-ASWDO x50 0.82NA] images through the planar mirror (xyz degrees of freedom) with the featured plinth underneath (z degree of freedom). The NDs are situated on the mirror coating on the underside of the planar substrate. As the plinth has no lateral degrees of freedom, it must be positioned in the field of view when mounting. Crucial to the LT cavity experiments is the mounting of the objective lens. If this is done properly then the relative alignment of the objective and the plinth will be maintained

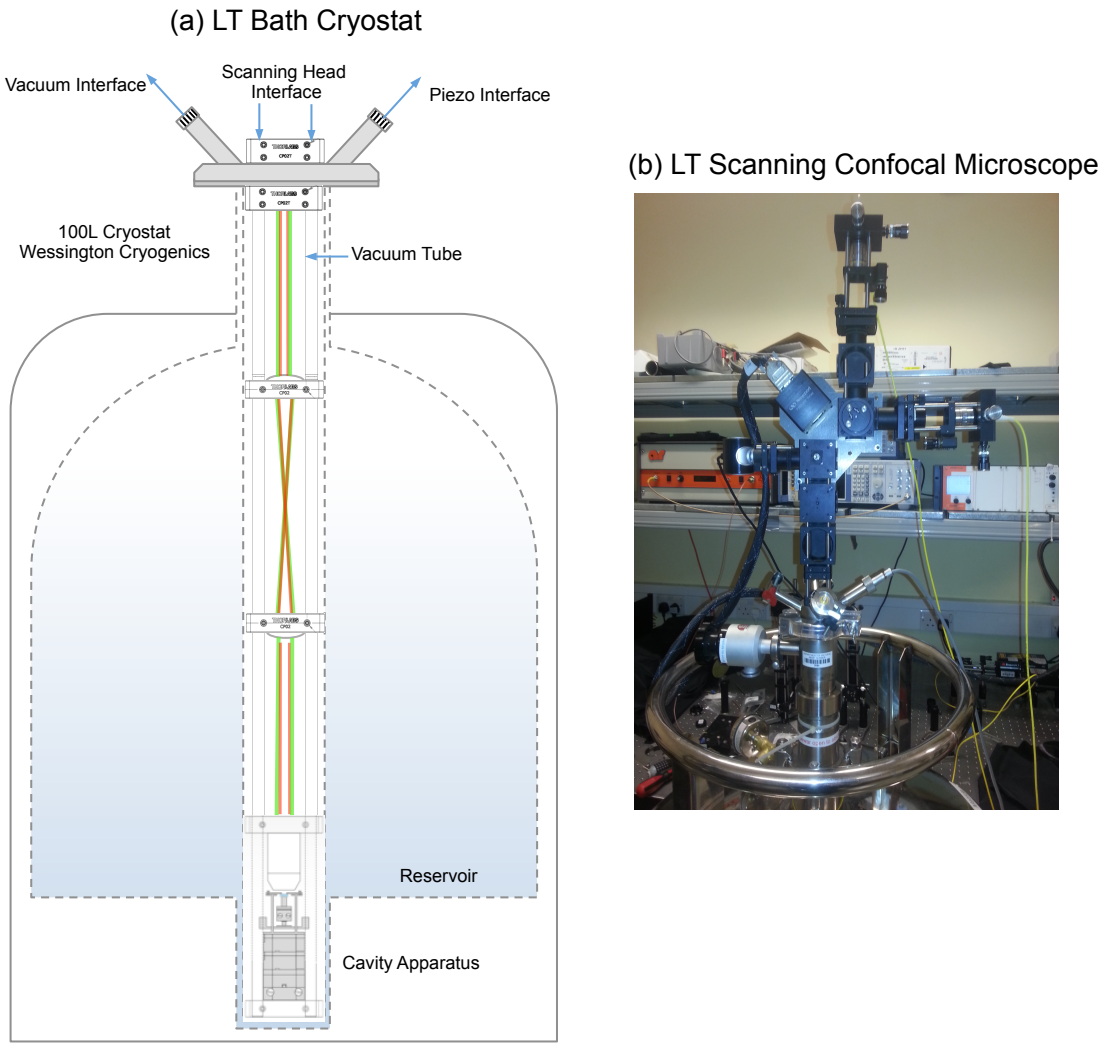

FIGURE 4.11: The Low Temperature System (a) Schematic diagram of the LT dewar. The cavity apparatus in mounted to a cage system inside a He exchange gas environment. (b) The scanning head of the confocal microscope can interface with the dewar for LT operation.

at low temperature. A schematic is shown in figure 4.12. The implementation of this development represented a turning point in the success of these experiments. It must also be noted that there is no piezo tilt control at low temperature. It is generally found that after thermal contraction, the relative alignment of the mirrors has changed slightly, but often it is still sufficient to achieve short cavity lengths. Another drawback of the LT system is that the dewar is situated on a concrete floor, so the vibration isolation insufficient.

The system performance at low temperature must be characterised and understood. Figure 4.13 compares a power saturation measurement curve of a single NV centre (out

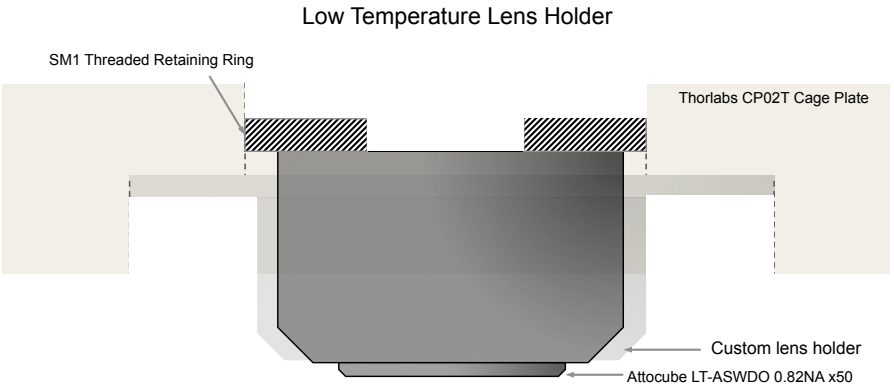

FIGURE 4.12: The LT lens holder. The LT lens rests in a custom built aluminium casing, with a bevel to match that of the lens, preventing lateral movement. The casing is fastened to a modified cage plate [Thorlabs CP02T], and the lens is secured with a custom built SM1 threaded retaining ring.

of cavity) at RT (mounted to the optical table) and LT (in the bath cryostat). The background contribution to the fluorescence signal is subtracted in both cases and the power dependence (P) of the intensity (I) is fitted using equation 4.8.

$$I = \frac{I_{\text{sat}} P}{P + P_{\text{sat}}} \tag{4.8}$$

Where P_{sat} is the power at which half the saturation intensity I_{sat} is achieved. This curve quantifies the performance of the optical system. The first thing to note is that the saturation power is reduced at LT by almost a factor of 2. The RT periscope construction has three silvered mirrors that that allow for vertical cavity mounting. It likely that these cause aberrations of the excitation spot, increasing P_{sat}. The photon collection efficiency falls by a factor of 0.75 indicating that the transmission of the optical components in the cryostat are compromised.

Finally, in order be able to carry out the full range of measurements necessary to determine Purcell factors and to verify single photon emission into the cavity mode at low temperature, an appropriate narrow band-pass filter [Semrock FF01-640/14-25] was acquired to be able to isolate the ZPL emission from mirror background and any other modes within the PSB. This was only implemented for the results in section 7.2.

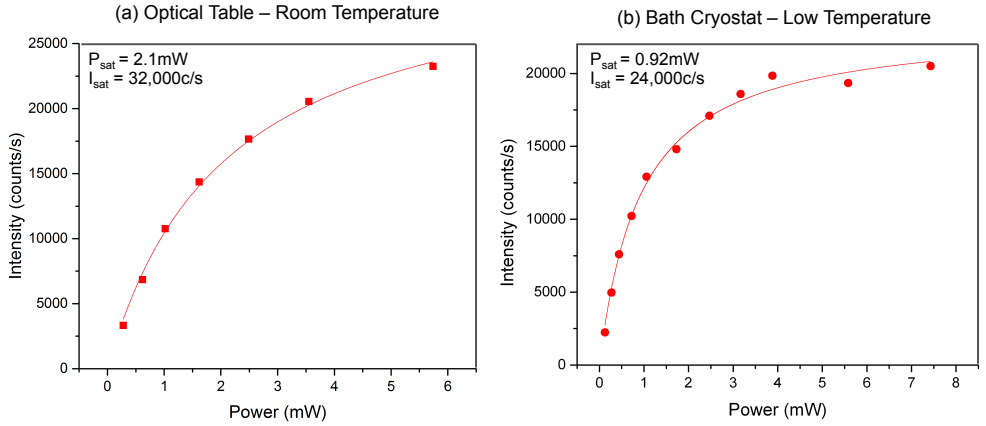

FIGURE 4.13: Comparison of the power saturation measurements the same single NV centre at (a) RT and (b) LT. The saturation power and intensity allow for a relative comparison between the set-ups.

4.7 Optical Properties of Mirror Coatings

The mirror coatings are found to provide a background fluorescence under optical excitation. This is several times greater than that of the fused silica substrates they are deposited on, which suggests that this property is intrinsic to the coatings themselves. For emitter-cavity coupling experiments, especially when initially identifying single emitters, it is important that the optical properties of these coatings are well characterised. Figure 4.14 shows a PL (photoluminescence) image of a planar mirror substrate, deposited with fluorescent NDs, under 532nm excitation. It is observed that the background fluorescence can be photobleached, to an extent, as represented by the dark squares in the centre of the figure. These indicate the location of previous imaging scans. A time trace of the PL signal shows the photobleaching process in figure 4.14. The rate will depend on the excitation power density used, however a baseline is typically reached on timescale of minutes.

The optical properties of the mirror coatings are found to be material dependent. Figure 4.15, shows an investigation into the fluorescence properties of planar mirror substrates from four different sources and three different material combinations. The power dependence shows that the 10 layer SiO_2/TiO_2 mirrors, from Oxford Physics, and alternatively from Helia Photonics, are the most fluorescent. The 9 Pair SiO_2/ZrO_2 from SLS optics prove to be the least fluorescent. The SiO_2/TaO_5 from Laseroptik displays only

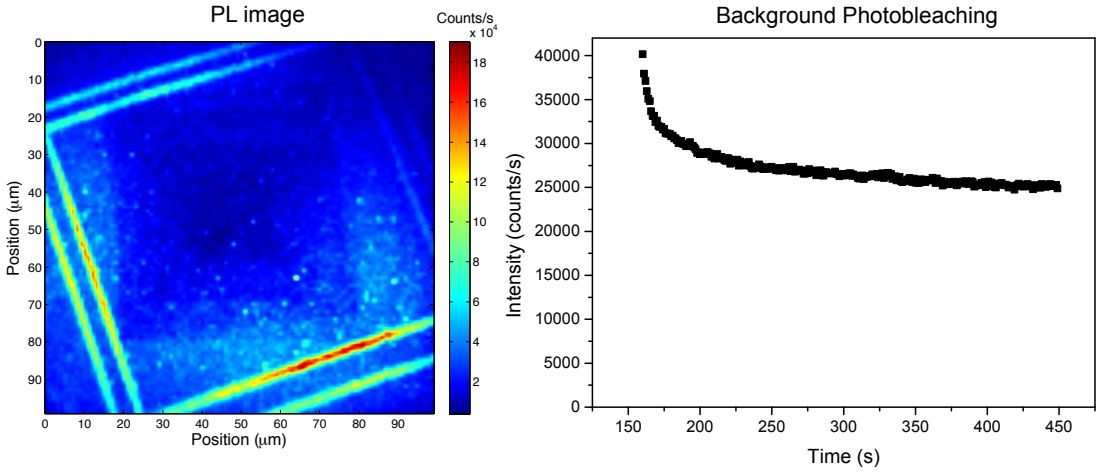

FIGURE 4.14: Left: A PL image of a planar mirror substrate with nanodiamonds dispersed on the surface. The darker squares in the centre indicate previous image scans that have photobleached the background fluorescence. Right: Typical time trace of the photobleaching process. The rate will be dependent on the excitation power

marginally greater fluorescence. It must be noted that this a 20 pair mirror coating. Representative background spectra are shown on the right of figure 4.15. The coatings display a background bearing a resemblance to the transmission spectrum of the mirror stack, evidenced by emission <560nm and >750nm. This indicates the mirror stack serves to suppress the fluorescence from within the coating. It is clear that with appropriate spectral filtering this problem cam be reduced. The Helia and Physics coatings do display some fluorescence in the stop-band region, whilst the Laseroptik coatings have the cleanest profile of all. This thesis uses coatings from the Oxford Physics thin film facility and Laseroptik. The survey presented here, illustrates the variability between coating materials, which can potentially be engineered.

4.8 Imaging Through the Mirror

Any emitter-cavity coupling experiment in the current configuration, will require that emitters be imaged between the mirrors. This is to establish their location prior to cavity coupling. Of course, this presents a challenge, since the stop-band was designed to reflect the emission in the first place. Figure 4.16a shows a typical room temperature NV spectrum, overlaid with the transmission of a 10-pair mirror, as obtained by the a

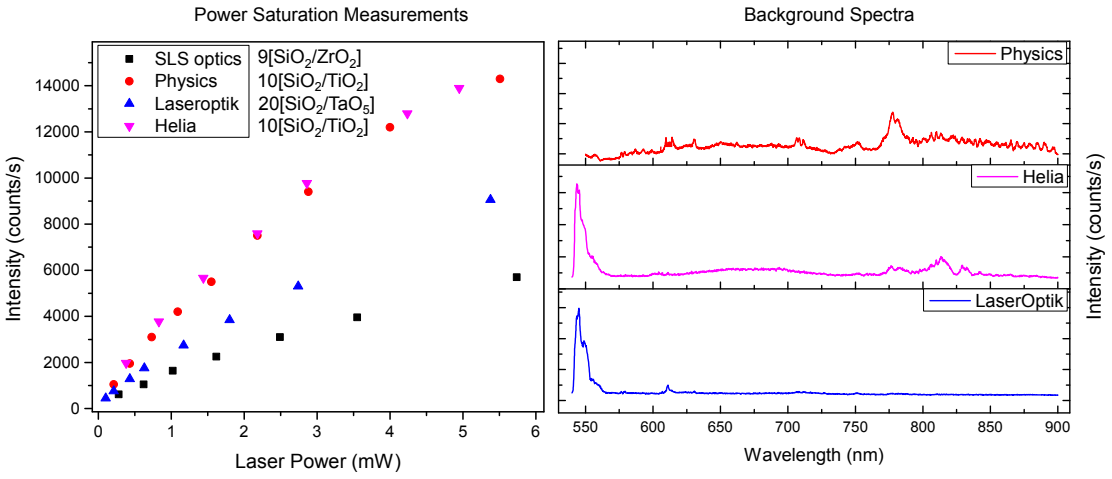

FIGURE 4.15: Left: Mirror background power saturation measurements taken with a x50 0.82NA objective and 532nm excitation, with no spectral filtering. Coatings from four different sources are investigated. The number of mirror pairs and material combinations are listed in the figure. Right: Typical background spectra for the Physics, Helia and LaserOptik coatings.

transfer-matrix model of the mirror coatings. The product between the two spectra is shown, which represents the transmitted intensity of the NV through the mirror coating (with the approximation of normal incidence). Figures 4.16b/c compare the PL image obtained for with the emitters on top of the mirror, to the situation where they are on the underside. Most of the PL is now being reflected by the stop-band and the experiment relies on the small fraction of emission transmitted at the longer wavelengths. The contrast between the signal and backgrounds is now extremely poor. This situation demands long-integration confocal scans.

Figures 4.16(d),(e) show the respective power saturation curves. It is seen that just 4% of the original intensity is now collected through the mirror corresponding to the green shaded area in (a). The saturation power is has also correspondingly increased due to the residual reflectivity of the mirror coatings at 532nm.

Once the cavity has formed, the relative reflectivity of the mirror coating must carefully be considered. An imbalance between the coating reflectance will result in the preferential out coupling of the transmitted light. In the absence of any intra-cavity losses, the fraction of light transmitted through the planar mirror as:

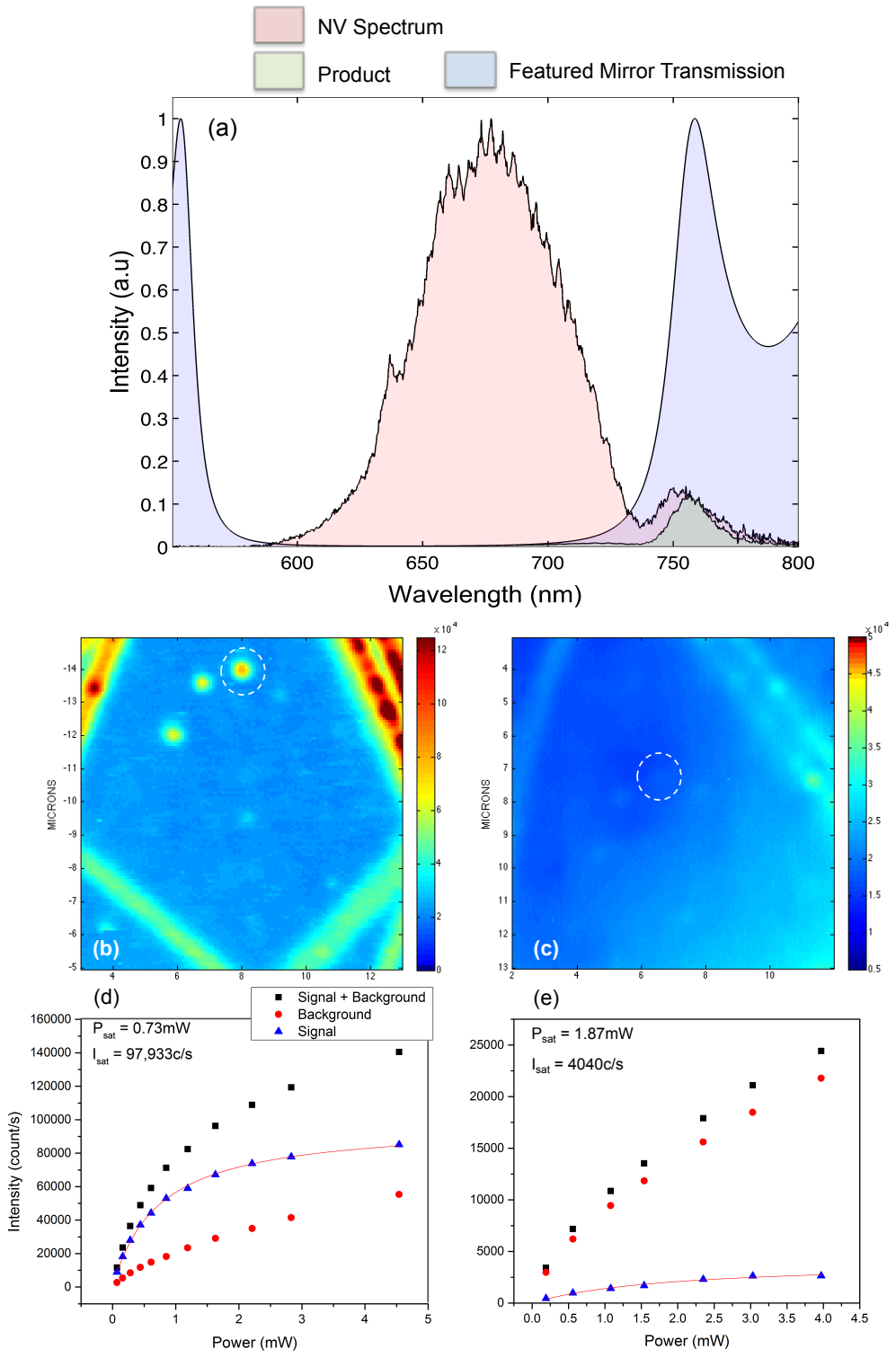

FIGURE 4.16: (a) A comparison of the room temperature emission spectrum of the NV centre (pink) and the calculated transmission of the featured mirror (blue). the peaks are normalised for comparison. The product of the two (green) represents the transmitted intensity through the featured mirror, prior to cavity coupling. (b) PL scan of a single emitter on the mirror and (c) on the underside of the mirror, represented by the white circle. The contrast is reduced due to the mirror stop-band. The respective power saturation curves are shown in (d) & (e) both taken in the 670-810nm spectral window

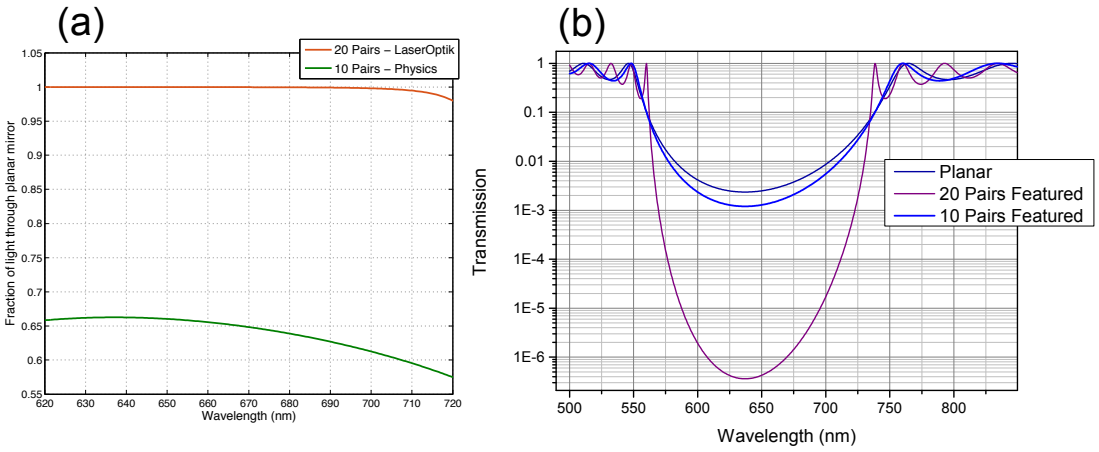

FIGURE 4.17: (a) Fraction of light through the planar mirror. Comparison between 20 pair laseroptik plinth and 10 pair physics plinth. Almost all of the cavity mode on axis is transmitted through the planar mirror for the 20 pair substrate, a 35% improvement on the previous mirror. (b) Transfer matrix calculation of the mirror coatings for the 10 pair planar, 10 pair featured and 20 pair featured mirrors. Shown on a log-intensity scale for clarity.

$$\frac{1-R_p}{1-R_fR_p} \approx \frac{T_p}{T_f+T_p} \tag{4.9}$$

Where $R_{f,p}$ are the reflectivities of the featured and planar substrates respectively with $T_{f,p}$, the transmission. Figure 4.17b, shows the relative reflectance of a 10-pair planar mirror (low index termination), with two alternative featured substrates. The fraction of light coupled through the planar mirror is displayed in figure 4.17, over the stop-band range. By forming a cavity with the 20-pair featured substrate, the out coupling from the cavity mode, along the optical axis, will be almost unity. This cavity is implemented in the main LT results of section 7.2, whilst the 10 pair-10 pair cavity is implemented in the RT measurements of chapter 5 and the preliminary LT measurements in section 7.1.

4.9 Theoretical Methods

4.9.1 Finite Difference Time Domain simulations

Finite Difference Time Domain (FDTD) simulations [Software: Lumerical Solutions] are able to simulate the electromagnetic environment of the emitter. The basic principle of FDTD is that it can serve as a computational test bench to analyse of propagation of electromagnetic waves within photonic structures. The structural parameters, such as L, β and the mirror thicknesses can be defined along with the refractive indices of each element, thus defining the electromagnetic environment. The source of electromagnetic radiation is also specified, in this case a dipole emitter at a given orientation. On the initialisation of source emission, the software calculates the propagation of emitted light through the structure in the time domain. To achieve this, the whole simulation region is partitioned into an array of three dimensional 'Yee' cells, of a defined refractive index. The propagation across each cell is calculated by solving Maxwell's equations across the interface. The cell size must be much less than the operating wavelength, and must be able to resolve the intricacy of any structural interfaces. Across a basic structure such as the planar DBR the mesh size limit is relaxed. Around the nanodiamond and the concave mirrors however, a fine mesh is required in order to simulate the spherical surfaces accurately. A 2D schematic of the simulation is defined region is show in figure 4.18. The mesh size around the 100nm nanodiamond of n=2.4, is set to be 5nm. The field must be allowed to fully decay, in this case 10ps, in 5fs time increments, before the simulation is ended.

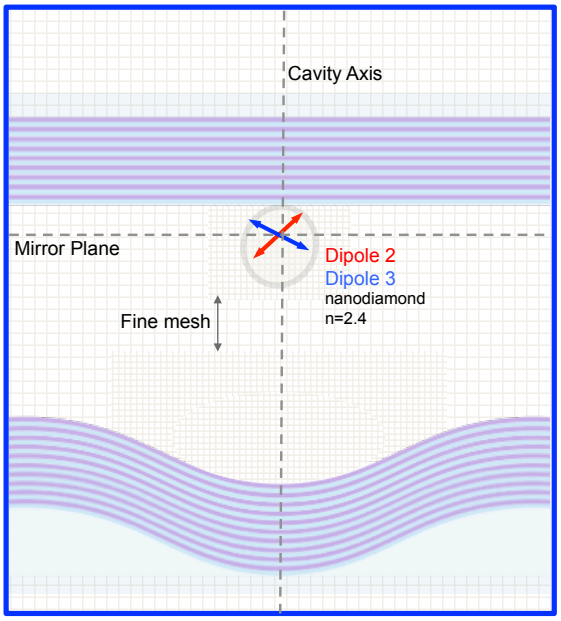

FIGURE 4.18: The FDTD Method. Schematic of the in-cavity simulations. Calculations are performed for dipoles inside a 100nm sphere of n=2.4, on the cavity axis. The simulation mesh is represented by the grid and is set to be 5nm around the ND and the concave mirror. To simulate the half-cavity case, the concave mirror is simply removed from the simulation.

4.10 Conclusion

The experimental and theoretical methods involved in this work have been presented. The materials characterisation methods were essential in establishing good quality nanodiamond samples, where single NV centres could be reliably identified. The cavity-coupling experimental methods have also been fully described starting from the fabrication of the cavity features by FIB, through to the finer details of emitter identification at LT. This chapter gives an appreciation of the meticulous preparation that is involved to ensure the success of these experiments, especially at LT. Aside from the cavity fabrication process, the success of the low temperature emitter-cavity coupling has heavily relied on four key experimental procedures and developments, which can be summarised as:

1. Fabrication of registration features onto the planar mirror
2. Manual iterative alignment the cavity mirrors using interference fringes
3. Custom built lens-holder to maintain relative plinth and objective alignment at LT
4. Being able to identify single emitters through the mirror substrate

The fabrication of registration features is essential and would remain a component in any future experiments. For the remaining points there is certainly a capacity for improvement. The additional degrees of freedom, such as tip-tilt piezos and additional lateral stepper motors would relax the requirements for point 2, 3. The final point requires appropriate spectral filtering and long image integration, which of course would benefit from improved count rates and a better SNR. This is unlikely to come from the objective lens, since already incorporates a high NA into a specialised LT design. Improvements may have to come through wavefront aberation correction, implemented using a deformable mirror. This may allow the emitters to be more readily identified.

Chapter 5

Room Temperature Cavity Coupling

5.1 NV Ensemble-Cavity Coupling

This section describes investigations into room temperature NV-cavity coupling, which was conducted with nanodiamond samples containing ensembles of NV centres [Columbus Nanoworks, FND, 200nm, 1mg/ml]. These fNDs were initially chosen as it would readily allow and exploration of the cavity coupling process. The samples are prepared and mounted as in section 4.3. The experiment proceeds in the stages outlined in figure 5.1. The orientation of the mirrors is chosen such that the cavity emission can be directly compared with the emission free space (emitters only on the planar mirror), in one experiment. This enables the enhancement of the light-matter interaction to be quantified. Here the fNDs are initially imaged on the planar mirror, shown in figure 5.1(a), with 7mW of CW excitation. A low NA objective lens is chosen (0.4NA x20), to allow sufficient working distance through the featured substrate as shown. The samples display an inhomogeneity in the NV concentration per crystal, with intensities varying over an order of magnitude from 2×10^5 to 2×10^6 counts/s. A well isolated bright nanodiamond (2×10^6 counts/s) is chosen for cavity coupling.

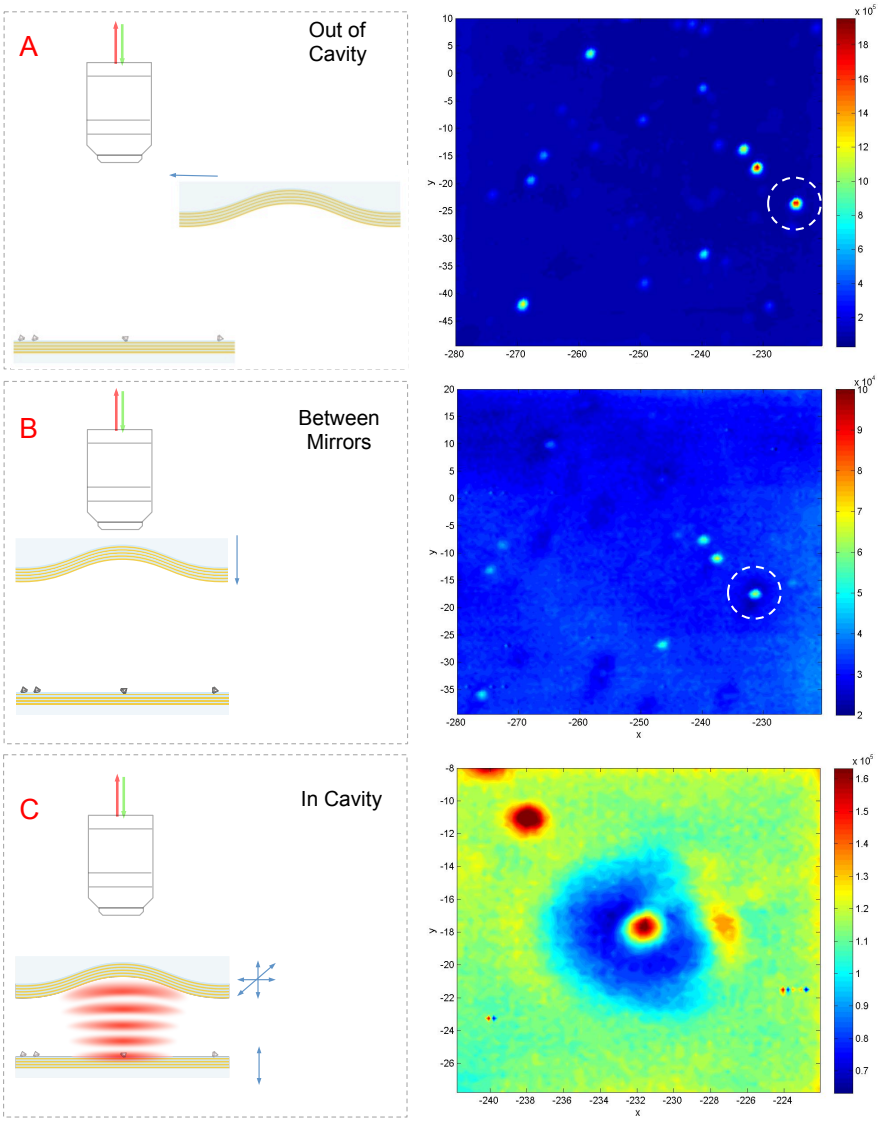

FIGURE 5.1: Schematic diagrams of the room temperature cavity coupling experiments with corresponding PL images - Lengths are in μm, whist the colour scale indicates counts/s on the SPAD. A 0.4NA x20 objective lens is used. A: Out of cavity imaging of the fNDs on the planar substrate. B. The featured substrate is moved across and the fNDs are imaged through the featured mirror. The fND under investigation is shown in the white circle. C: The substrate separation is reduced and the cavity is formed over this feature.

Figure 5.1(b), shows the PL imaging through the featured mirror of the same substrate area. This step is required prior the cavity coupling, as the inevitable angle of the featured substrate causes refraction of the image, as seen by the differing co-ordinates of the feature highlighted. Thus the location of the free-space feature needs to be confirmed between the mirrors before moving a cavity into position. Imaging the emitters prior to cavity coupling presents a technical challenge as the stop-band of the mirror is designed to mostly reflect the emission spectrum of the NV centre. This was discussed in section 4.8.

Imaging through the featured mirror substrate not only alters the collection of fluorescence, but alters the excitation conditions. Firstly the mirror coatings have a residual reflectivity at the excitation wavelength, transmitting only 57% of incident 532nm excitation (calculated for normal incidence). Figure 4.6c, showed the thickness of the featured substrate to be 1mm. This is likely to cause spherical aberrations of the excitation spot, reducing the excitation power density of the focal spot. This is difficult to quantify as the profile of the point-spread function will be mostly extended in the z-direction [119]. The best way to experimentally verify this is to take a power saturation measurement. With a low NA objective it is difficult to saturate the emission of the NV ensemble with CW excitation. Pulsed excitation is instead used [repetition rate 20KHz, pulse width 0.75ns, energy/pulse 2.5μJ]. The power saturation measurement both in free space and between the mirrors can be seen in figure 5.2

This saturation power shows the altered excitation conditions and the parameters obtained from the fits are listed in table 5.1

TABLE 5.1: Fit Parameters

	Between Mirrors	Free Space
P_{sat} (μW)	31.8±3	13.1±1.8
I_{sat} (counts/sec)	445±18	7304±13

The saturation power has increased by a factor of 2.43 in-between the mirrors, through a combination of reflection at the mirror and aberrations of the focal spot. This value is used to set the relative excitation power in and out of the cavity, in order to get a

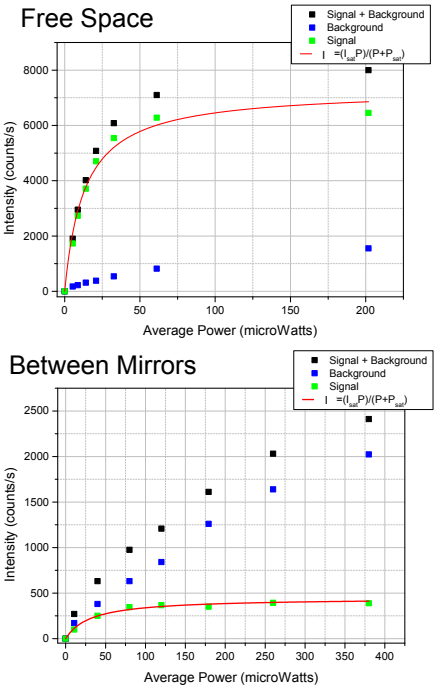

FIGURE 5.2: Pulsed power saturation measurements of same fND in free space (above) and between the mirrors (below). The red line indicates a fit to the function $I = (I_{\text{sat}}P)/(P + P_{\text{sat}})$ to the fluorescence signal after background substation (green)

quantitative comparison of the relative emission intensities. In practice the in-cavity excitation power is set to be high ($\approx$ 7mW), and the free space excitation is lowered accordingly. A cavity of nominal $\beta = 10\mu$m is chosen for these measurements.

A comparison of the free space and cavity emission properties for the same fND can be seen in 5.3. The spectra are taken with an identical integration time and the same relative excitation conditions. On coupling to the cavity it can be seen that the collected emission spectrum is now dictated by the emission into the longitudinal TEM_{00} cavity modes, with some minimal coupling into higher-order transverse modes observed. This indicated that the emitter is well aligned within the cavity mode. Consequently for the shortest cavity lengths it can be seen that the peak intensity of the TEM_{00} mode at 690nm is over a factor of 5 greater than that of the NV PSB peak. The sequence of spectra highlight the tunability of the system as the cavity length is modified through piezo actuation of the featured mirror. As the cavity length is increased from 3.15μm to 10.8μm, a greater number of resonant frequencies are permitted between the mirrors signified by a increased number of longitudinal modes coupling to the PSB emission.

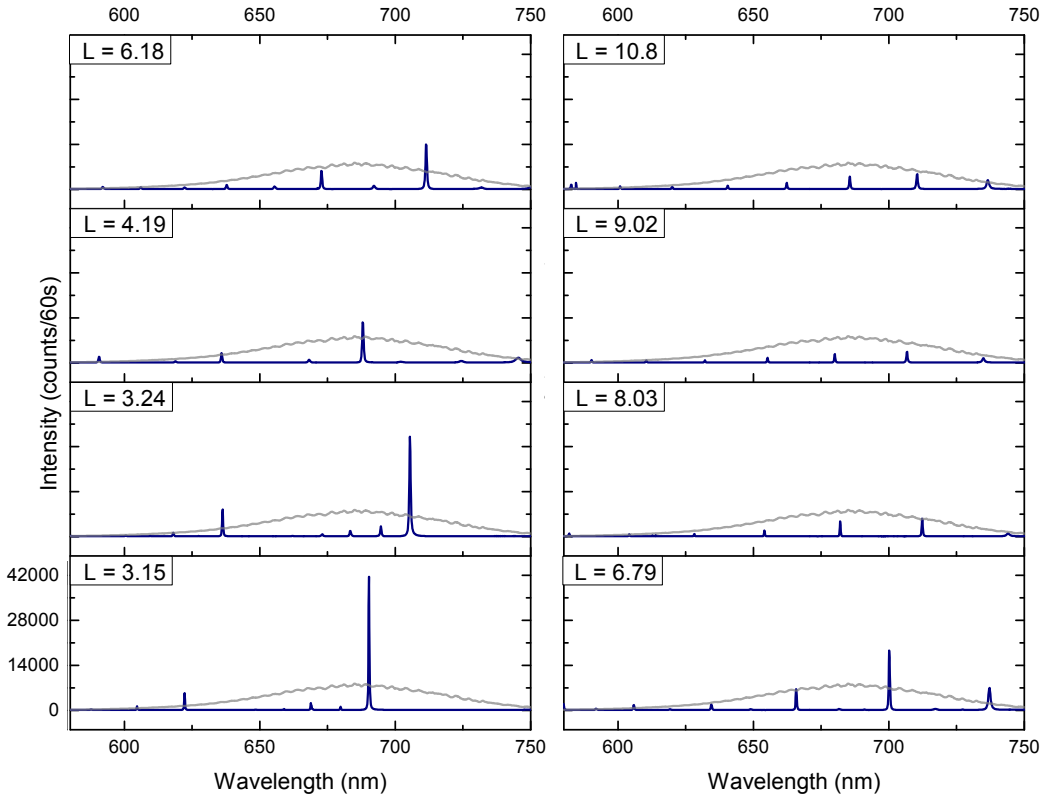

FIGURE 5.3: Comparison of in/out of cavity emission for the same fluorescent ND. Sequence of cavity coupled spectra (blue) are shown, the optical cavity length, L is indicted in microns. The free space spectrum for the same excitation conditions (grey) is shown on each axis for comparison. All spectra have the same relative intensity scale.

The peak intensities are drastically reduced as the cavity length is increased. From the position of the adjacent longitudinal modes and the corresponding transverse mode spacing, all the relevant parameters of the cavity can be extracted according to the analytic expressions defined in section 3.1.2. The cavity parameters for the shortest cavity in figure 5.3 are summarised in table 5.2:

TABLE 5.2: Cavity Parameters for $L = 3.15\mu$m

L_{opt}	β	$\omega_0(\mu\text{m})$	V(μm^3)	V (λ^3)	$\mathcal{F}$	Q	$\Delta\lambda$(nm)
3.15	10.6	1.0	2.47	8.4	202	2000	68

For the cavity length $L_{\text{opt}} = 3.15\mu$m, the mode at 690nm corresponds to longitudinal mode index $q = 7$. Accounting for the penetration of the field into the mirrors yields a geometrical length, $L_{\text{geo}} = 2.6\mu$m corresponding to the minimum physical mirror separation achieved in this experimental run.

Whilst there is theoretically scope for shorter cavity lengths, they are in practice limited by relative angle of the mirror substrates and the dimensions of the featured plinth. Efforts are always made to couple cavities that are at the thin end of the wedge between the substrates, however it is inevitable that an edge will come into contact before the cavity is able to be fully closed. Extrusions on the edge of the plinth after the substrate cutting process may serve separate the mirrors further.

One way to quantify the effects of the cavity is to look at the spectral density of the photon emission. This can be observed from the spectra in figure 5.3, as the number of photons emitted into the spectral bandwidth. A comparison between the $L_{\text{opt}} = 3.15\mu$m cavity and the free space spectral density is shown in table 5.3.

TABLE 5.3: Spectral Density - Cavity and Free Space emission

	L = 3.15μm, q=7	Free Space
Spectral Bandwidth	212GHz	48.7THz
Photons/s in Band	2600	83,000
Raw Spectral Density (Photons/s.GHz)	12.1	1.75
Corrected Spectral Density (Photons/s.GHz)	105	21

The raw data values for each of the strongest fundamental resonances in figure 5.3 are now plotted in figure 5.4, with respect to the free space value. To prove that the observed spectral densities are beyond that expected from filtering effects, the collection efficiencies in each case must be taken into account (these are detailed in section 5.2). The collection efficiency for the mode at 690nm, in the $L_{\text{opt}} = 3.15\mu$m cavity, stands at 11.5%, whilst in free space this is 8.3%. The corrected spectral densities for both cases are listed in table 5.3, showing a factor of 5 increase when cavity coupled.

5.2 The Effective Purcell Factor

The Purcell factor compares the emission into the cavity with the emission into free-space, and with the data presented, a comparison between these scenarios can be made. At room temperature the cavity coupling proceeds well within the bad emitter regime of cavity QED and only a fraction of the NV emission will be coupled to the cavity mode,

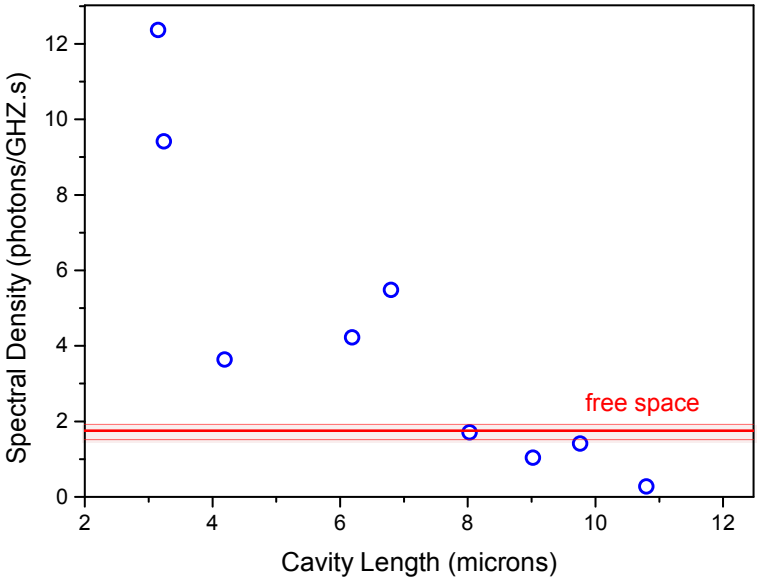

FIGURE 5.4: Scaling of the spectral density with cavity length. Each data point represents emission into the strongest fundamental mode for each cavity spectrum in 5.3. The free space value represented by the red line, whilst the shaded region indicates the experimental uncertainty in this value.

reducing the Ideal Purcell factor to an effective one. The anticipated Purcell factors will be marginal such that PL lifetime changes would be challenging to observe. This is particularly true for longer cavity lengths. Instead, a relative comparison between the total emission, in and out of the cavity, is made. Experimentally, this manifests itself as the ratio of integrated intensity in the cavity mode $P_c(\lambda_0)$, to the total integrated intensity in free space P_{fs}. This comparison is displayed graphically in figure 5.5, where the shaded regions indicate the integration region. The cavity mode is integrated in a narrow region across the resonance, whilst the the free space emission is integrated across the entirety of the spectrum from 600-780nm, encompassing the full ZPL + PSB emission. The treatment of the experimental data builds on from the work by Kaupp et al [79] (discussed in chapter 2).

Once such a comparison has been made, the experimental collection efficiency in each case must be carefully considered, as these vary between the free space and the cavity emission. The collection efficiency in the cavity also has a dependence on the cavity length as diffraction losses start to to occur. The final expression for the experimental effective Purcell factor is shown in equation 5.1.

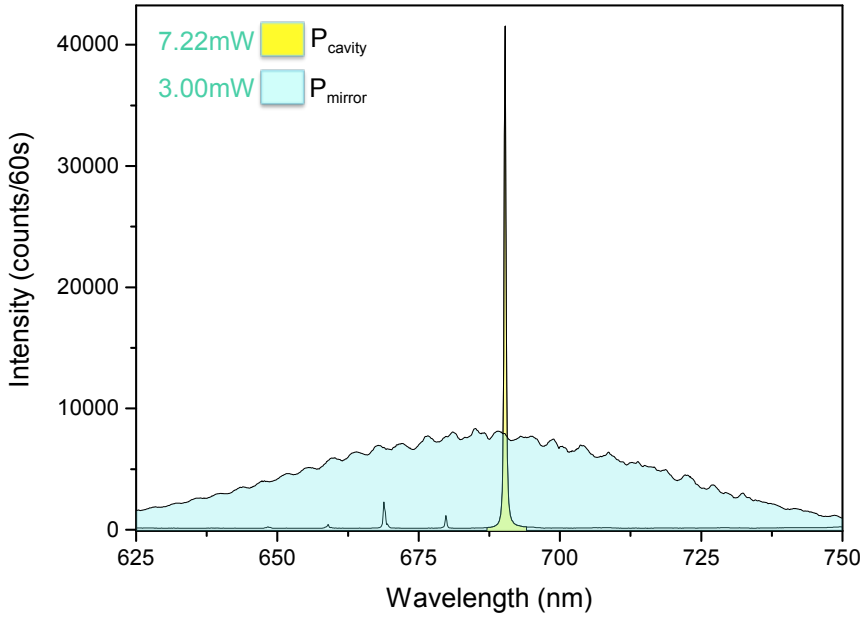

FIGURE 5.5: Comparing the integrated intensity in the cavity mode, P_c = 23 000 (yellow) to that of the free space emission P_{fs} = 606 000 (blue). The relative CW excitation conditions are shown

$$F(\lambda_0) = \frac{P_c(\lambda_0)}{P_{fs}} \frac{C_{fs}}{C_{cav}} \tag{5.1}$$

5.2.0.1 Collection Efficiency from the Cavity

The collection efficiency in the cavity depends strongly on the following factors:

- Transmission of the planar and featured mirrors
- Intracavity losses - absorption, scattering & diffraction

With the experimental set-up in question, it is assumed that the cavity mode is well coupled to the external optics. With a beam waist of ω_0 =1μm at a TEM_{00} = 690nm, equation 3.18 can be used and the numerical aperture of the mode is calculated to be NA = 0.21. This should couple well to the external optics with NA = 0.4.

The planar and featured substrates are both coated with 10 $\frac{\lambda}{4n}$ pairs of n=1.4/2.1. However as discussed in section 4.8, the planar mirror is terminated with an additional

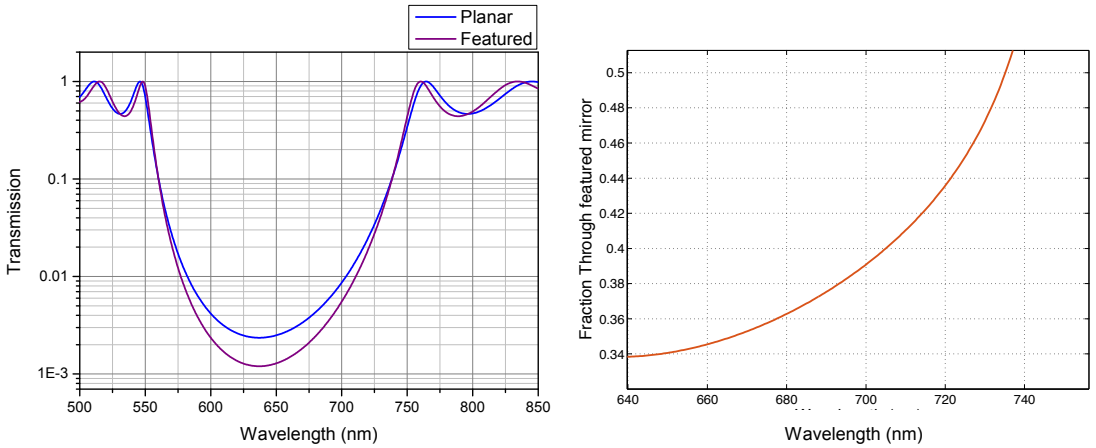

FIGURE 5.6: Left: Transfer Matrix simulations of the planar (blue) and featured (purple) mirrors, plotted on a log scale for clarity. Right: equation 5.5 evaluated across the spectral region shown. The majority of the light is directed through the planar mirror

low index layer. This serves to alter the relative reflectivities of the substrates, leading to the featured mirror being more reflective than the planar substrate. In the current configuration, it means a greater proportion of light leaking from the cavity will be emitted through the planar mirror, away from the collection objective.

The difference in the transmissions of the planar and featured mirrors are plotted in figure 5.6. It is clear that the planar mirror is more transmissive than the featured mirror for wavelengths within the region of the stop band. equation 5.5 is evaluated in the region from 640-750nm on the right of figure 5.6. It is shown that a greater proportion of the light is directed through the planar mirror from 640-735nm, varying between 34-50%.

The transmissions of the mirror coatings are not the only loss mechanism within the cavity. The losses in the system will be related to the observed finesse. Taking the TEM_{00} = 690nm mode from figure 5.5, the finesse is expected to be:

$$\mathcal{F} = \frac{\pi(R_f R_p)^{\frac{1}{4}}}{1 - \sqrt{R_f R_p}} = 654 \tag{5.2}$$

This is over a factor of 3 greater than the measured value of $\mathcal{F} = \frac{\delta\lambda}{\mathrm{FSR}}$=202. Indicating an additional intra-cavity loss mechanisms. It was seen in section 3.1 that the Finesse

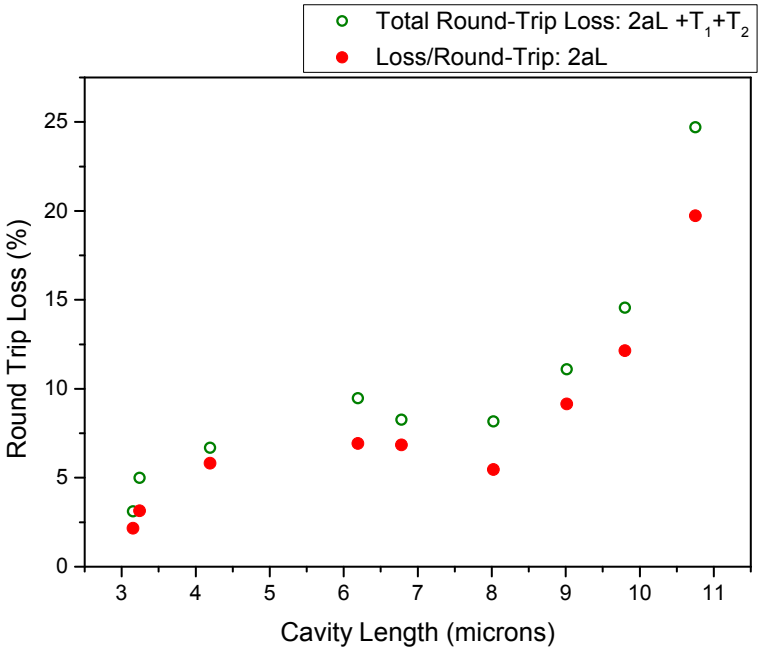

FIGURE 5.7: Left: Evolution of the round trip loss with cavity length for each fundamental mode contributing to the effective Purcell factor calculation. The total round trip losses $\mathcal{L}$ are represented by the green points. The intrinsic losses, $2\alpha L$, are shown in red

is related to the total round-trip loss factor $\mathcal{L}$ by:

$$\mathcal{F} = \frac{2\pi}{\mathcal{L}} \tag{5.3}$$

$$\mathcal{L} = 2\alpha L + T_{\mathrm{p}} + T_{\mathrm{f}} \tag{5.4}$$

$\mathcal{L}$ is the sum of the intrinsic $2\alpha L$ losses (scattering, absorption, diffraction) and the transmission losses $T_{\mathrm{p}} + T_{\mathrm{f}}$. Equation 5.4 is evaluated for each fundamental mode contributing to the effective Purcell factor calculation and the evolution of this parameter is plotted in figure 5.7.

It is clear that the intrinsic losses are the dominant loss mechanism in the cavity system. The size of the fNDs used were 200nm, this will be a factor causing significant scattering losses per round-trip. As $\mathcal{L}$ increases with greater cavity length, this strongly indicates that the system experiences diffraction losses, as the mode waist on the featured mirror becomes large enough to start clipping the edges of the concave feature.

Now the intra-cavity losses have been determined, the collection efficiency in the cavity is adjusted accordingly as:

$$C_{\text{cav}} = \frac{T_{\text{f}}}{2\alpha L + T_{\text{f}} + T_{\text{p}}} = \frac{T_{\text{f}}}{\mathcal{L}} \tag{5.5}$$

5.2.0.2 Collection Efficiency in Free Space

The collection efficiency of the lens is determined by the solid angle Ω subtended by its numerical aperture over the full 4π steradians of free space, so that:

$$C_{\text{fs}} = \frac{1}{2}(1 - \cos(\arcsin(\text{NA})) \tag{5.6}$$

For the NA=0.4 lens used in these measurements, the free space collection efficiency would be C_{fs}=4.17%, in the limit of isotropic emission. With the emitters situated on the planar mirror, the emission will not be isotropic as the mirror coatings are designed to reflect almost the entire emission spectrum. As a crude approximation, one may expect the mirror substrate to double the collection efficiency such that C_{fs}=8.34%. This approximation would be appropriate for dipoles well aligned to the mirror plane. A more refined approach would need to account for the distribution of randomly oriented dipoles that are present in these nanodiamonds.

5.2.0.3 Determining The Effective Purcell Factor

The final correction to make is due to the detuning of the contributing modes from the maximum of the PSB emission (λ_0 =685nm). Detuning from this maximum reduces the coupling, which varies according to the profile of the PSB emission. This is calculated for each data point and represented by the factor η_λ in equation 5.7 [79].

$$F_{\text{P}}(\lambda_0) = \frac{P_{\text{c}}(\lambda_0)}{P_{\text{fs}}} \frac{C_{\text{fs}}}{C_{\text{cav}}\eta_\lambda} \tag{5.7}$$

With the collection efficiencies known in each case, the Purcell factor is obtained. The theoretical function is shown in equation 5.8, using the Q-factor of the emitter in free space to be Q_{em}= 9.7, evaluated at λ_0=685nm with a linewidth of 71nm obtained from a fit to the PSB. Here ξ is the dipole orientation factor which equates to unity when the NV dipole is perfectly aligned to the cavity field.

$$F_{\text{P}} = \xi^2 \frac{3\lambda^3}{4\pi^2} \frac{Q_{\text{em}}}{V} \tag{5.8}$$

The scaling of the effective Purcell factor is shown in 5.8. A maximum effective Purcell factor of 3% is achieved. Whilst this enhancement is fractional, it still represents a fair achievement considering the extent to which the coupling proceeds within the bad emitter regime. Two theoretical predictions have been shown on the figure for comparison with the experimental data. It is seen that the maximum expected Purcell factor for a perfectly aligned emitter and cavity electric dipole vector consistently over estimates the experimental data points. In reality there is a large ensemble of NV centres with random dipole orientations within the same nanodiamond. Averaging over all possible dipole orientations with respect to the electric field, leads to $\xi^2 = 1/3$ in equation 5.8 [90], which is seen to represent the observed behaviour well. For the final data points in the sequence a significant deviation from the predicted behaviour is observed as the resonator geometry nears the stability criterion.

The error bars indicate the uncertainty in the measurement. The major source of this arises from the estimation of the in-cavity excitation conditions, which follow from the comparison of the saturation power, in and out of the cavity. With the associated error from the power dependence fit parameters are shown in table 5.1, leading to a scaling factor of 2.4±0.4. The excitation conditions out of the cavity were varied to account for this in order to get an estimation of the error in the free-space integrated intensity. Further error in the determination of the in-cavity excitation conditions, which has *not* been quantified, will be due to the planar modes between the substrate at the excitation wavelength, leading to the standing waves seen in figure 4.8. This produces a larger

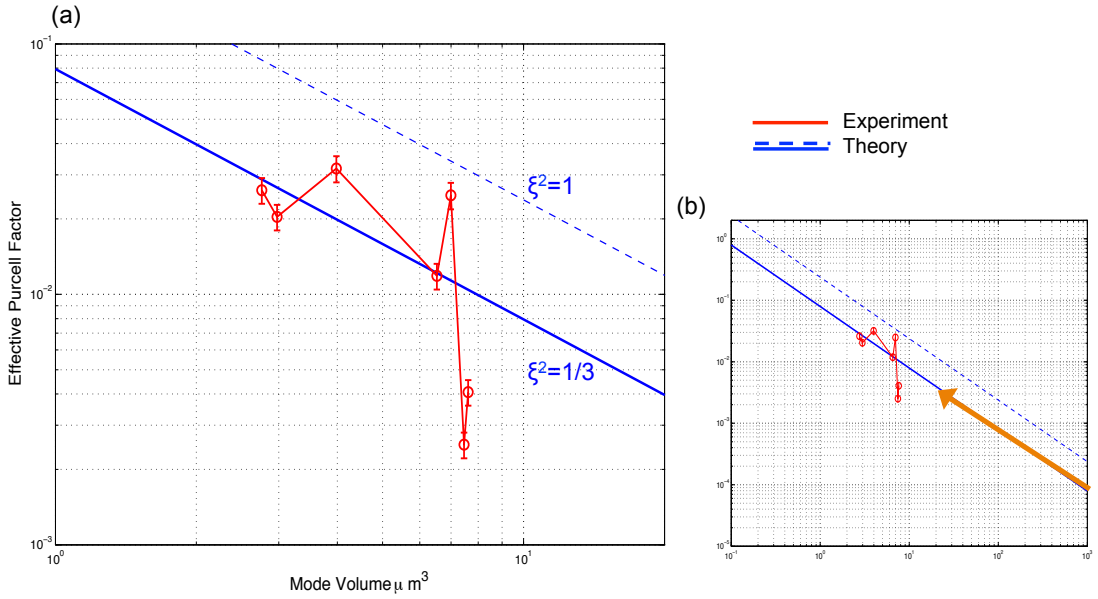

FIGURE 5.8: (a) Dependence of the effective Purcell factor on the mode volume of the cavity. The data points (red) connected by a line to indicate the spectral sequence from which the value were obtained. The blue dashed line represents the theoretical prediction for perfect dipole orientation $\xi^2 = 1$, whilst the solid line is the theoretical prediction obtained by averaging over random distribution of dipole vectors such that $\xi^2 = 1/3$. (b) Presenting results in the context of the literature - Larger scale version of plot (a), with the orange arrow indicating the work of Kaupp et al [79]

uncertainty in the P_{fs}. This periodically modulates the in-cavity saturation power, according to the cavity length, and is likely to account for the oscillatory nature of the data points, indicated by the red line in figure 5.8. A more complete characterisation of the in-cavity saturation power as a function of cavity length will be needed to complete this picture.

5.3 Cavity Mode Mapping

One of the merits of the open cavity system is the direct access of the emitter to the electric field maximum in the cavity mode. By laterally positioning the emitter within the cavity, or vice versa, this coupling can be completely optimised. This is demonstrated in the following section, along with an investigation of the coupling to the high-order transverse modes. The Hermite-Gauss mode structure is experimentally mapped out

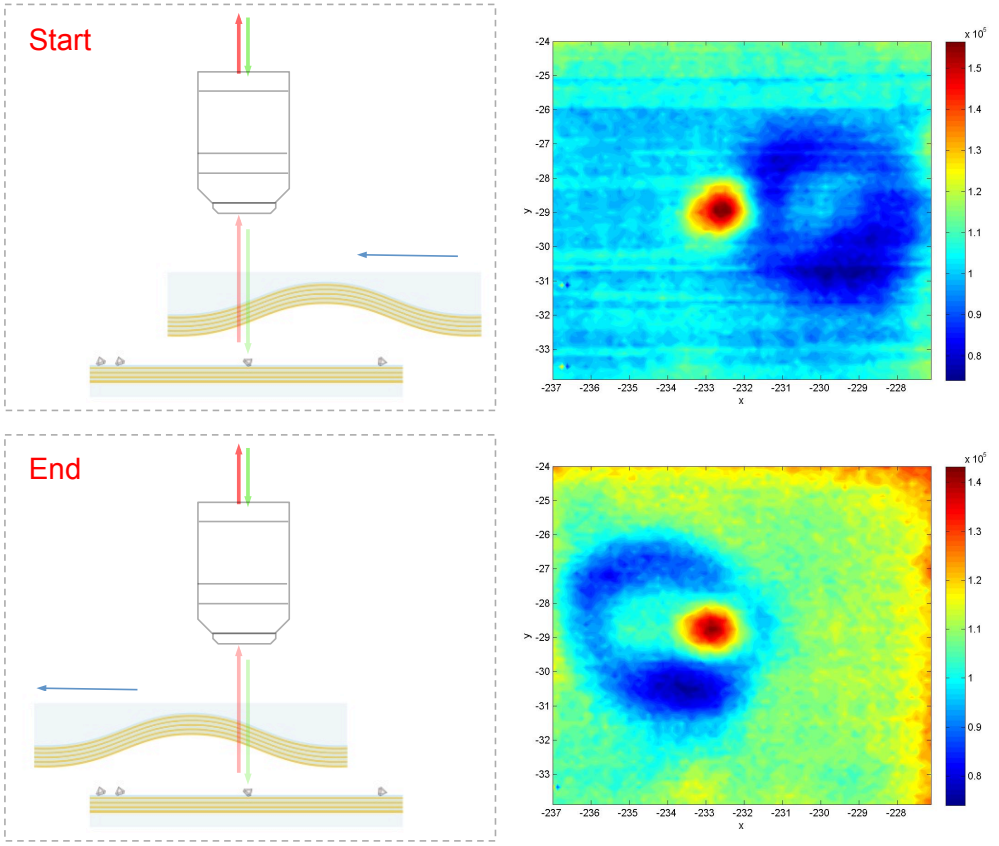

FIGURE 5.9: Steps in the mapping of the mode structure. The cavity is moved laterally whilst the position of the NV excitation and collection are fixed. Accompanying PL images show this process, allowing the step-size to be calibrated. Lengths are in μm.

with the fluorescence of the NV emission, and a comparison to the theoretical intensity distributions are made.

With the same experimental configuration as in the previous section, the fNDs are coupled the same $\beta = 10\mu$m cavity. As the featured mirror has all the translational degrees of freedom, stepwise lateral scanning of the cavity can be performed and the coupling to the longitudinal and transverse modes can be identified. The pizeo actuators are stepped by 160nm increments in one dimension. A spectrum is taken at each step of the cavity. This process is shown schematically in figure 5.9.

Figure 5.10 shows the mode mapping of the fND as the cavity is stepped across the emitter. A family of modes corresponding to $q = 8$ are shown, with the longitudinal and first three transverse excited modes visible. The coupling into the $\text{TEM}_{m+n=0}$ mode is the most clearly evident, as it couples well to the external optics. The higher order

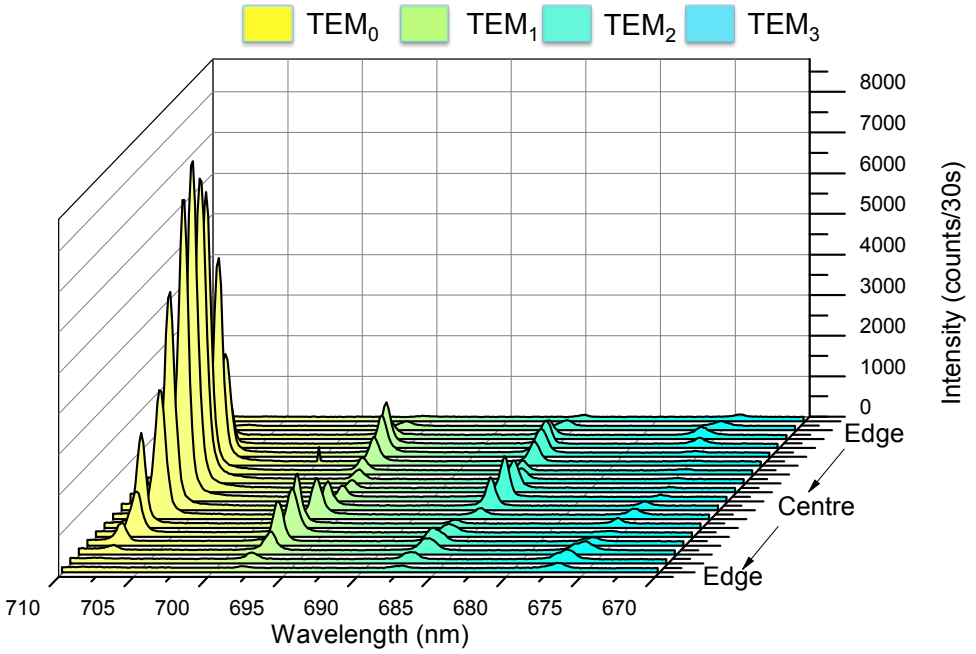

FIGURE 5.10: Waterfall plot of the emission of the into the cavity modes as a function of the lateral step number of the cavity substrate. A family of modes from $\mathrm{TEM}_{m+n=0,1,2,3}$ are shown corresponding to a longitudinal mode number $q = 10$ is shown. The wavelength scale has been reversed for clarity

$\mathrm{TEM}_{m+n=1,2,3}$ are less evident, as coupling to external optics is reduced with the increased NA of each mode. Each higher order transverse peaks comprises of spatially distinct but energetically degenerate modes. Breakdown the symmetry of the cavity leads to a lifting of this degeneracy. This is not observed in the higher order peaks suggesting the degeneracy is maintained within the resolution of the spectrometer. Each peak will thus be the sum of the individual transverse modes satisfying the $n + m$ criterion. For example, the $\mathrm{TEM}_{m+n=3}$ peak will be the sum of the individual $\mathrm{TEM}_{30,21,12,30}$ modes. The intensity distributions and individual contributions to each of the $\mathrm{TEM}_{m+n=0,1,2,3}$ modes are summarised in figure 5.11

The intensity distributions of the individual Hermite-Gauss modes have a cartesian symmetry. The summed $\mathrm{TEM}_{m+n=1,2,3}$ modes however, have a circular symmetry. Monitoring the emission into these modes as a function of lateral cavity position amounts to taking an arbitrary line cut across the the intensity distribution of these modes. This is illustrated in figure 5.12

The peak intensities are normalised to the maximum of the mode intensity, such that

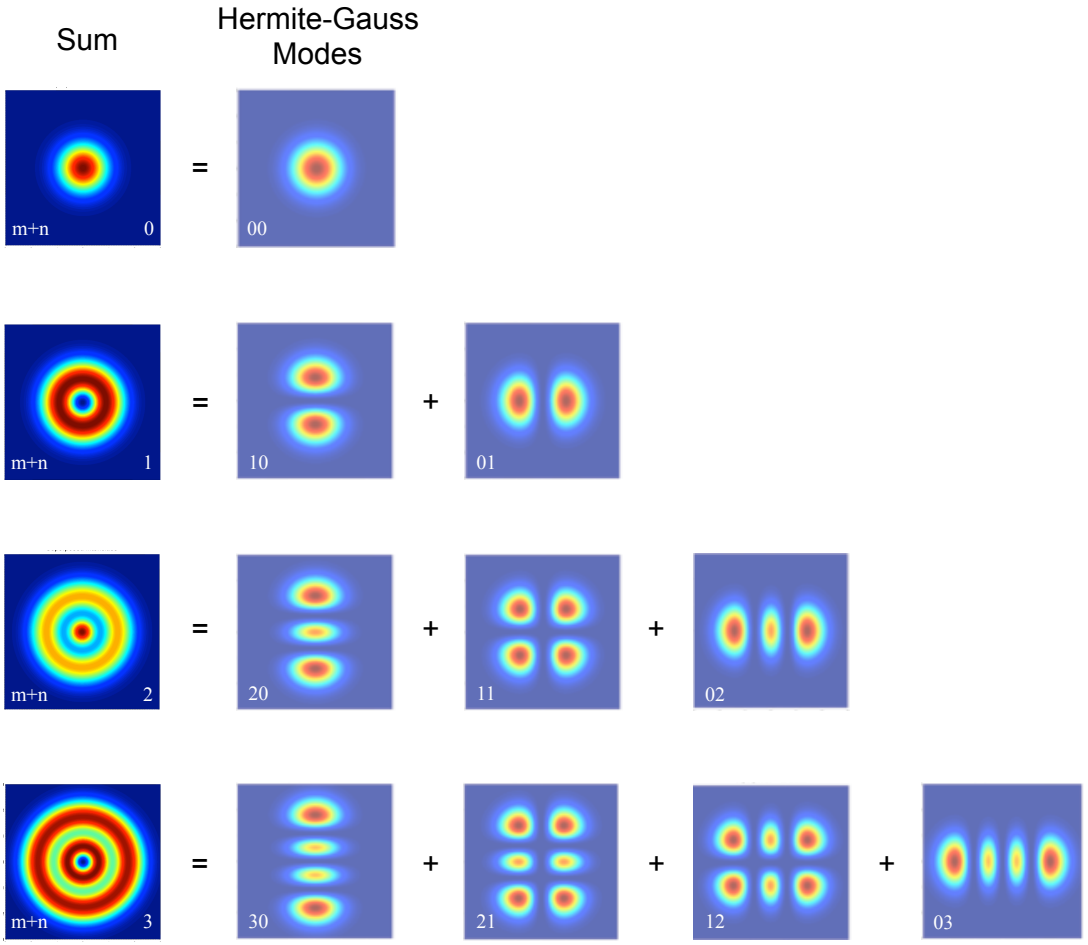

FIGURE 5.11: Theoretical intensity distributions of the Hermite-Gauss modes of the cavity geometry $L = 3.6\mu$m, $\beta = 10\mu$m. The plot dimensions are 6x6μm. The individual Hermite-Gauss modes are represented by the semi-transparent plots, and their summed distributions are shown on the left hand side. The mode indices, m,n are indicated in the inset of each plot

a comparison to the mode profiles can be made. A match of the data to the profiles of the $\text{TEM}_{m+n=0,1,2,3}$ modes are clearly observed. The TEM_0 data points fit extremely well to the theoretical mode waist. The reduced coupling of the higher order modes to the objective results in lower signal levels, as in figure 5.10, which are more susceptible to noise. In turn, the peak intensities deviate from the theoretical values, despite the general profile remaining the same. What is clear however, is that the observed higher-order peaks are in fact the summation of the degenerate mode profiles, and a cut of the intensity profile along an experimentally arbitrary direction through the centre of the optical axis, matches the circular symmetry of the summed modes.

Mode mapping is demonstrated across for alternative cavity parameters for the same

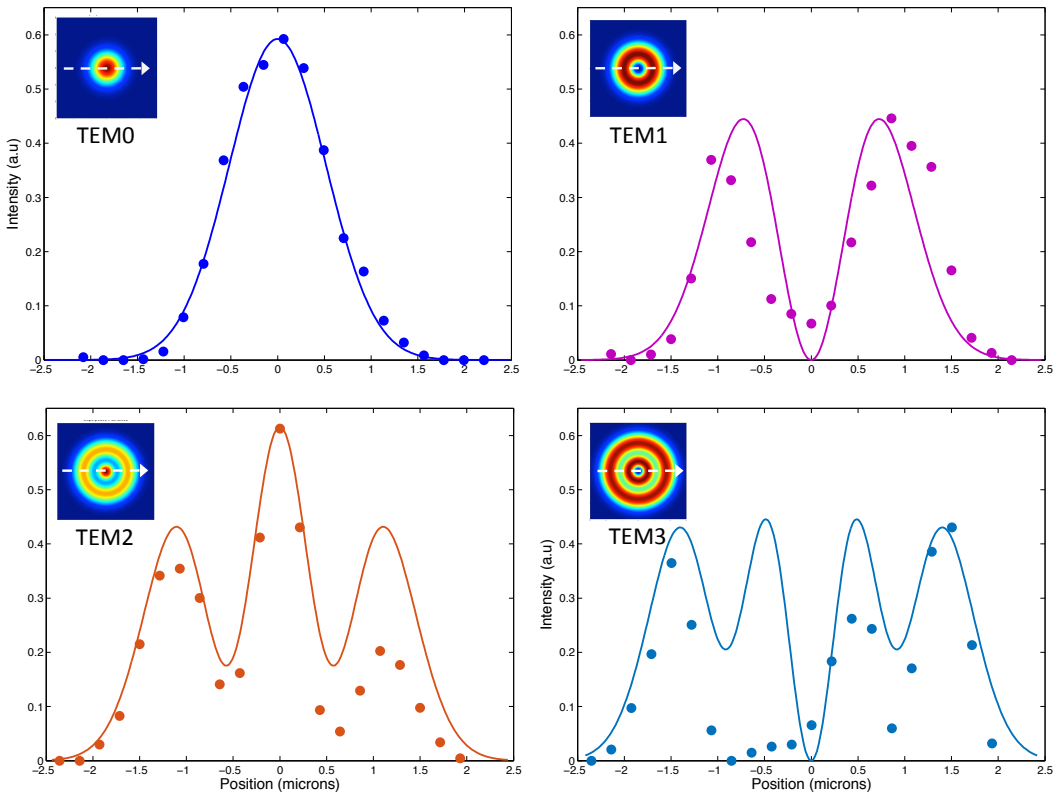

FIGURE 5.12: Cross sectional intensity-position plots for each of the TEM$_{m+n=0,1,2,3}$ modes. The cross section direction is indicated by the white arrow in the corresponding 2D plot of the mode. The theoretical values are represented by the solid lines, all on the same intensity axis. The peak intensity of each of the cavity modes in figure 5.10 as a function of lateral cavity displacement, are normalised to the theoretical values, represented by the dots

emitter. Figure 5.13a shows the same β=10μm cavity now at L=8.83μm. Coupling into transverse modes is not identified, even with as the acquisition time was increased by 50%. Coupling into 5 TEM$_0$ modes are seen across the emission of the NV centre as the cavity is scanned across the emitter. Using a β=16μm cavity a half-scan is presented going from the centre to the edge of the cavity in figure 5.13(b),(c). Only a set of modes of identical q, are shown. A greater number of transverse mode indices are observed here. Modes with odd-values of TEM$_{m+n}$ are shown to have no component of the electric field at the centre of the cavity, as expected from figure 5.11. The TEM$_{0,1,2}$ modes show the expected intensity profile as the cavity was scanned.

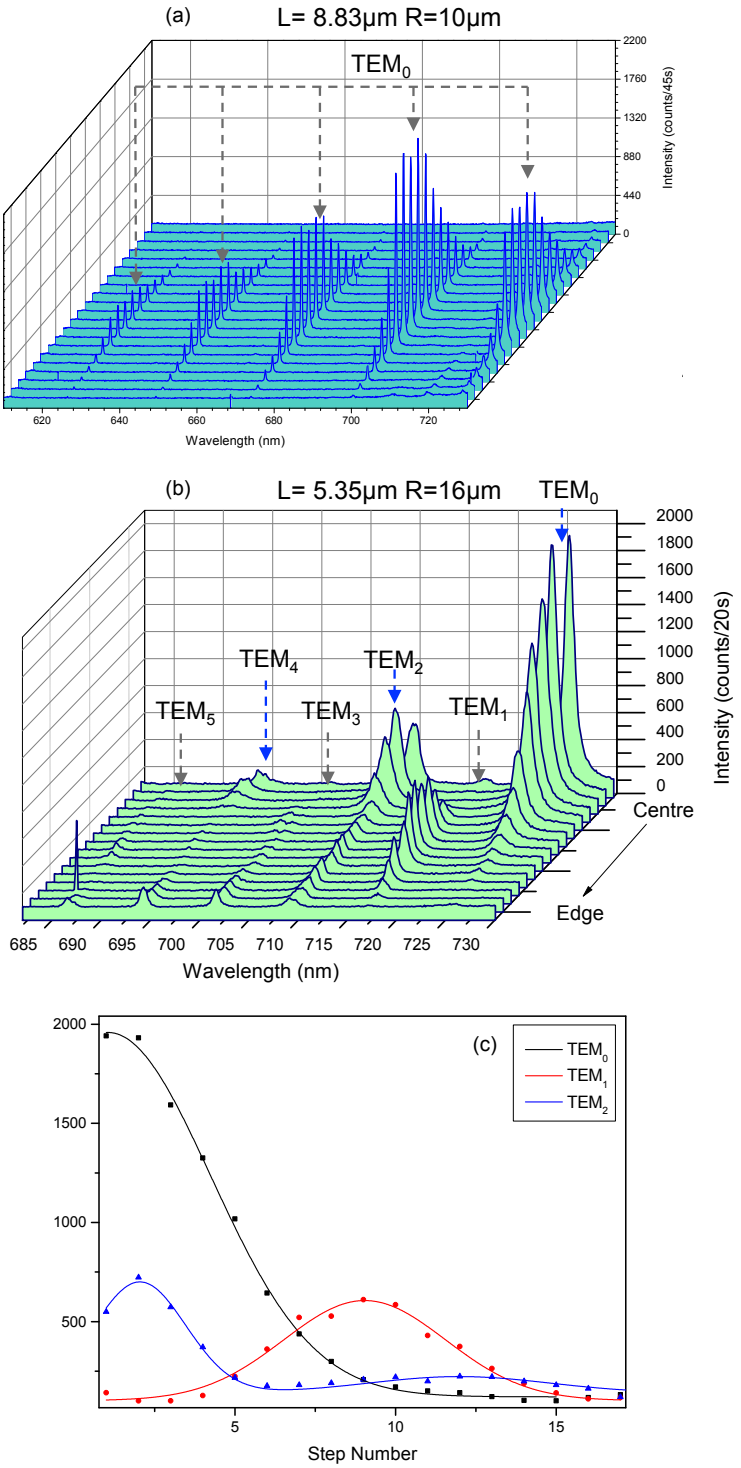

FIGURE 5.13: Mode Mapping for alternative cavity parameters. (a) Waterfall plot of the β=10μm cavity at L=8.83μm. Only coupling into the longitudinal mode is seen as the cavity is scanned across the emitter (b) Waterfall Plot of the β=16μm cavity at L=5.35μm. All modes have identical q. Only a half-cavity scan was conducted. (c) The Peak intensities of the $TEM_{0,1,2}$ plotted as a function of scan number. The Gaussian fits are a guide to the eye.

5.4 Conclusion

In summary, this chapter has described the ensemble NV-cavity coupling experiments. Clear modification of the spectral emission was observed as the NVs emitted strongly into the cavity modes, particularly for small mode volumes. The experimental method allowed a direct comparison for the in cavity and free space emission properties of the emitters - crucial for determining the enhancement of the light matter interaction. After a careful consideration of the subtleties in the differing collection efficiencies in each case, such as the differing reflectivities and the intra cavity losses, a determination of the effective Purcell factor in the bad emitter regime was made. The scaling with the mode volume was also observed, yielding a 3% increase in the emission rate for the smallest mode volume. With smaller mode volumes within reach, this starts to approach a regime, where small lifetime changes may be observable. This theoretical treatment, following on from the work for Kaupp et al [120], approximated the NV emission spectrum to be a single broadened transition centred at 690nm, with a low Q_{em}. This simple model was appropriate to describe the cavity coupling process of the NV ensembles. The more sophisticated cavity feeding model discussed in section 3.4.1 [78], was not chosen in this instance. This describes a coupling mechanism that is closer to the physics of the NV centre, whereby the highly broadened transitions from the individual vibronic sub-levels in the PSB, channel emission into the cavity mode. The implementation of this model requires the emission properties of a single NV centre to be accurately determined, such as the free space decay rate γ and therefore the coherent emitter-cavity coupling rate g. This would not have been easy in this case of the NV ensembles, with likely variation of these parameters between centres due to different locations within the nanodiamond. For example, the variation of γ would yield a multi-exponential lifetime decay curve, making the extraction of the individual time constants challenging.

Finally, the direct access of the emitter to the electric field maximum was demonstrated by tuning the emitter position within the cavity. NV emission into the Hermite-Gauss

modes of the half-symmetric resonator geometry, was also studied, with a good theoretical comparison made. This section highlights the strengths of the open-cavity system, in being able to deterministically couple to desired emitters and to have absolute and reversible control over the cavity coupling parameters in-situ.

Chapter 6

Characterisation of Single NV Centres in Nanodiamond

NV centres hosted in nanodiamond crystals are used exclusively throughout this thesis. Their size facilitates their inclusion in the open-cavity geometry, allowing the substrate separation to be minimised. This chapter presents sample preparation and the optical characterisation of single NV centres in nanodiamond in two parts. All experimental methods have been described in chapter 4.

NDs are commonly found to form large aggregates, as a consequence of their synthesis. In this situation it becomes experimentally demanding to isolate the single quantum systems desired for emitter-cavity coupling. It was necessary to subject the ND materials to surface treatments in order to obtain well isolated ND crystals. An investigation was conducted into adequate sample preparation through oxygen-annealing. This involved the materials characterisation techniques of TGA, Raman spectroscopy and DLS.

Optical spectroscopy of the treated ND sample will then be presented. It will be shown that single NV centres are now readily identified across the sample through HBT measurements. A full characterisation of their spectral properties will take place, including determination of the ZPL widths that are so crucial for cavity coupling. The out of cavity emission rates are also established. Particular prominence is given to 'NV2', the

results of which are presented separately for clarity. It was for this emitter that the main, low temperature cavity coupling results were obtained in section 7.2.

6.1 Nanodiamond Purification Investigation

This section outlines an investigation into the material properties of nanodiamond with a view to establishing an appropriate sample preparation protocol for single NV identification. Preliminary investigations into the optical properties of NV centres in NDs were carried out [Samples synthesised via HPHT, provided by Prof Steven Prawer, University of Melbourne], however single centres in unagglomerated NDs, were not readily identifiable. Dilution techniques were not successful in rectifying this as can be seen through typical confocal PL scans in figure 6.1. Applying a high-power ultrasonication [750W, Sonics Vibra-Cell VCX-750] to the solutions aided the dispersions, however large aggregates still persisted. It was therefore necessary to carry out surface treatments. With limited NV-rich nanodiamond powder available, it was decided that the parameter space for the purification process must be carefully understood. The Oxygen annealing process was chosen to be the most appropriate strategy for purification. Largely because it is a straightforward process allowing for an efficient investigation of the experimental parameters. The procedure is also safe in comparison with the alternative of tri-acid reflux techniques. This investigation is based on that of Osswald et al at who demonstrated the selective oxidation of NDs in air [52].

Two further ND powders were obtained from a collaborator [Dr Oliver Williams, Cardiff University, UK] as shown in 6.2. Both highly graphitic (sample A) and purified (sample B) powders were provided. Sample A, allowed sufficient source material with which to conduct an investigation, whilst sample B represented a benchmark for purification. These powders had not been subject to NV creation and did not display reliable native NV emission. On first inspection of figure 6.2 one can see the dark coloration of sample A as might be expected from sp^2 form carbon. On the other hand the purified powder looks to be a light grey. The difference between the samples are confirmed by the representative

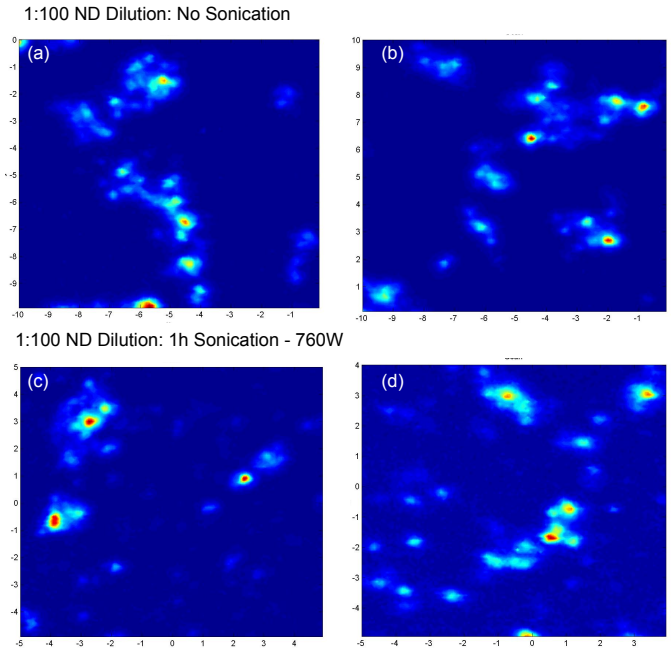

FIGURE 6.1: Typical confocal PL images of the NDs dispersed on fused-silica substrates, prior to surface treatment. (a)(b) ND dilutions, with no ultrasonication. Large aggregates can be seen. (c)(d) ND dilutions, that have been treated to ultrasonication for 1h at 750W [Sonics Vibra-Cell VCX-750]. There is some progress in breaking the crystals but larger aggregates remain. Taken with a x100 1.25NA Oil-immersion lens. The length scale is in μm

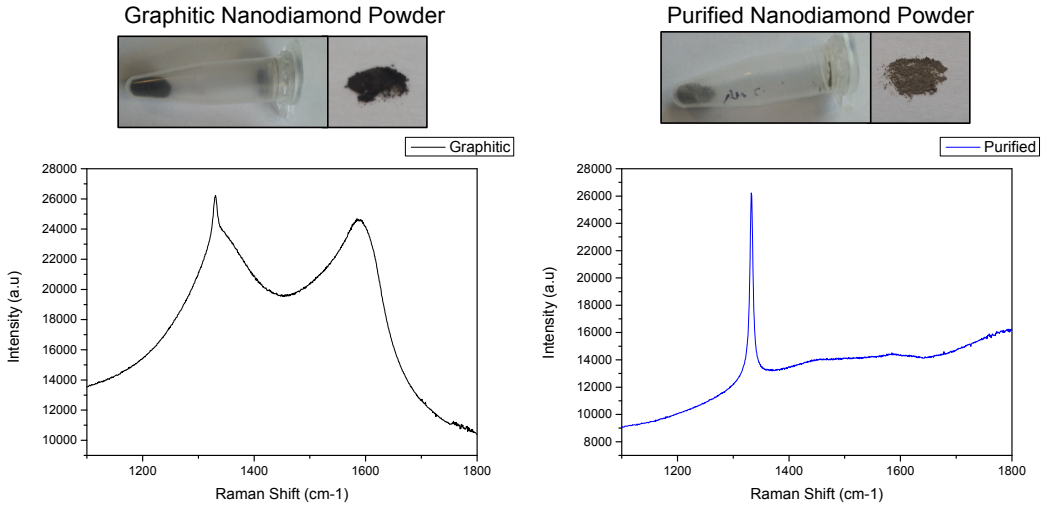

FIGURE 6.2: Above: photographs of the graphitic and purified nanodiamond powder. Below: representative raman spectra for each sample

raman spectra below in 6.2. The nanodiamond powders were firstly analysed using TGA to determine the correct conditions for the annealing stage.

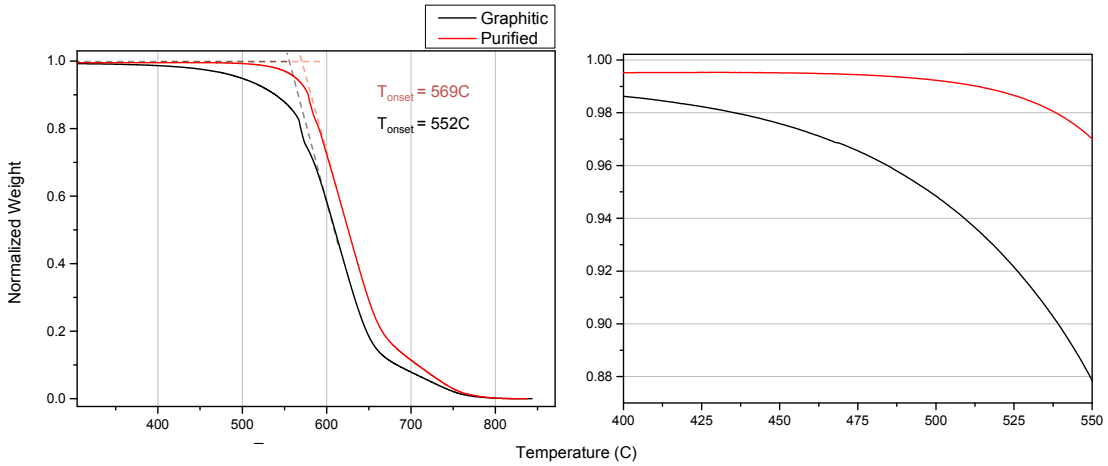

FIGURE 6.3: Thermogravimetric curves of the graphitic and purified nanodiamond powders in the 300-850°C range (left). The onset temperatures for each curve are indicated by the dashed lines. The profile of the 400-550°C range for the same curve is shown (right) to illuminate the difference in weight loss between the samples. The weights have been normalised

6.1.1 Thermogravimetric Analysis

The thermogravimetric curves for the pure and graphitic samples are shown in figure 6.3. Separate measurement runs were conducted for the respective samples, with 6mg of the powder placed in the ceramic crucible. A constant ramp rate of 10°C/min was chosen in this experiment. The ramp rate is important when trying to identify phase transitions in the material, a slower rate will achieve a better resolution, however for nanodiamond samples this rate has been shown to be sufficient [52]. The accuracy of the balance is quoted to be 0.5μg. A clear difference between the samples is demonstrated in the figure 6.3, with the graphitic sample starting to deviate from the pure sample at 400°C, indicating the onset of sp^2 oxidation. Only after 500°C does the significant mass loss for the pure sample start to occur: the onset of sp^3 diamond oxidation. The right hand side of figure 6.3 demonstrates this difference clearly. A quantitative estimate of the onset of oxidation is usually defined by the point at which the starting mass line meets the gradient of the main slope. This shown to be 552°C and 569°C for the graphitic and pure samples respectively. Due to the mixed composition of the graphitic nanodiamond, it is difficult to precisely separate the onset of the sp^2 and sp^3 oxidation. However the overall onset is lower as the graphitic materials start to oxidise first. The maximal oxidation

rates occur at 612°C and 617°C respectively, which will be predominately dictated by the oxidation of diamond.

By employing the isothermal capabilities of the TGA, more information on the relative material properties can be extracted. A separate experimental run is conducted on both materials with the same starting conditions. The thermal gradient is initially set at 10°C/min as usual, however this time it is held isothermally at specified temperatures for 5 minutes before the ramp recommences. A comparison of the two materials at different isothermal conditions can be shown in figure 6.4. At 450°C, the dM/dt traces are linear for both samples. This strongly indicates that only the sp^2 phase is being oxidised whilst the diamond remains in tact. The already pure sample loses only 0.5μg/min over the duration, which is on the margins of what the instrumental accuracy. The graphitic sample etch proceeds a faster by a factor of ≈40. When held at 600°C, the rate loss is non-linear for both samples. This is an indication that both phases are now being oxidised but with different individual rates contributing to this decay. There may be an additional contribution surface to volume ratio increases through the etching process. Because of these effects it is non-trivial to extract the individual contributions for the constituent phases. The left of figure 6.4 compares the relative rate losses for each sample individually.

Thermogravimetric analysis has proven to be a valuable tool in analysing the thermal properties of these nanodiamond powders. Strong evidence for the selective etching process has been demonstrated through the sample comparison, particularly at isothermal conditions. To complete this picture, Raman spectroscopy is used to distinguish between the relative carbon phases.

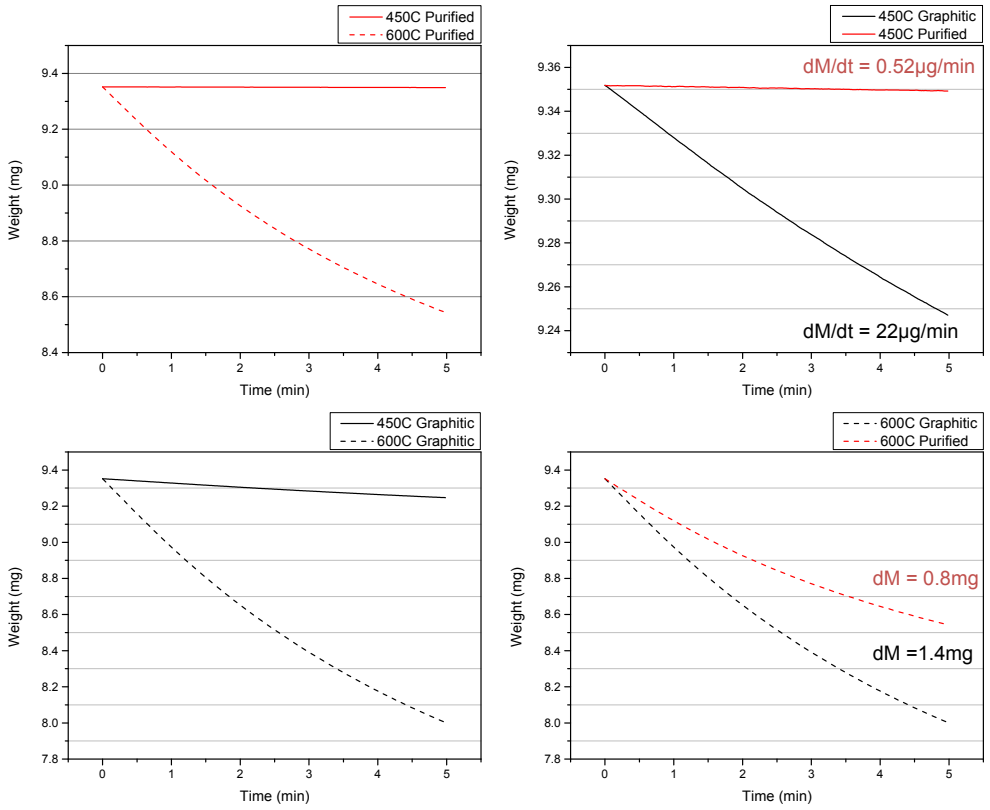

FIGURE 6.4: Isothermal curves for the graphitic and pure samples at 450 and 600°C. Direct comparisons are shown in each panel of the figure.

6.1.2 Raman Spectroscopy

To complement the TGA investigation in 6.1.1, an investigation into the corresponding Raman spectra was conducted to get an indication of the relative sp^2/sp^3 ratio in the samples. Starting with 5mg of the graphitic powder, four separate thermal oxidation experiments were carried out at 450, 500, 550 and 600°C for a duration of 3h. The samples were loaded into a ceramic boat (80x13x9mm) and placed into a box furnace [Carbolite RWF1200]. Care was taken to spread the powder across the surface to try and maximise the material exposed to the air atmosphere. A relatively fast temperature ramp (20°C/min) was chosen to bring the sample to the target temperature before the start of the 3h. After the anneal the remaining material was dispersed in de-ionised water with a 1mg/ml dilution. The sample vials were placed in a sonicating bath before being spin coated onto Silicon wafers for Raman analysis. 532nm excitation was used in this study and representative raman spectra subsequent to the annealing stages are shown in figures 6.5 and 6.6.

The starting point for this investigation is represented in 6.2, showing a typical spectrum for the graphitic nanodiamond sample. These samples displayed evidence of the diamond peak at 1332cm^{-1}, however this peak is mostly dominated by a broad profile in the 1300-1400cm^{-1} range. It is likely that this originates from the D band for corresponding to breathing modes of aromatic sp^2 rings. The D-peak is a dispersive Raman feature, which means it has dependence on the excitation wavelength. Pocsick et al determined that it disperses between 1300-1420cm^{-1} as excitation is varied from Infra-red to the UV range however for 532nm excitation it was observed to appear at 1350cm^{-1} in microcrystalline graphite [121]. This is accompanied by a broad prominent G band corresponding to bond stretching of sp^2 pairs. The peak intensity of this band appears equal in amplitude to that of the combined diamond-D peak. The dominance of the G and D peaks confirm the presence of a significant amount of sp^2 material, which was indicated by the visual appearance of the starting material. The sp^2 phase is highly disordered indicated by the existence of aromatic rings and therefore lacks crystallinity.

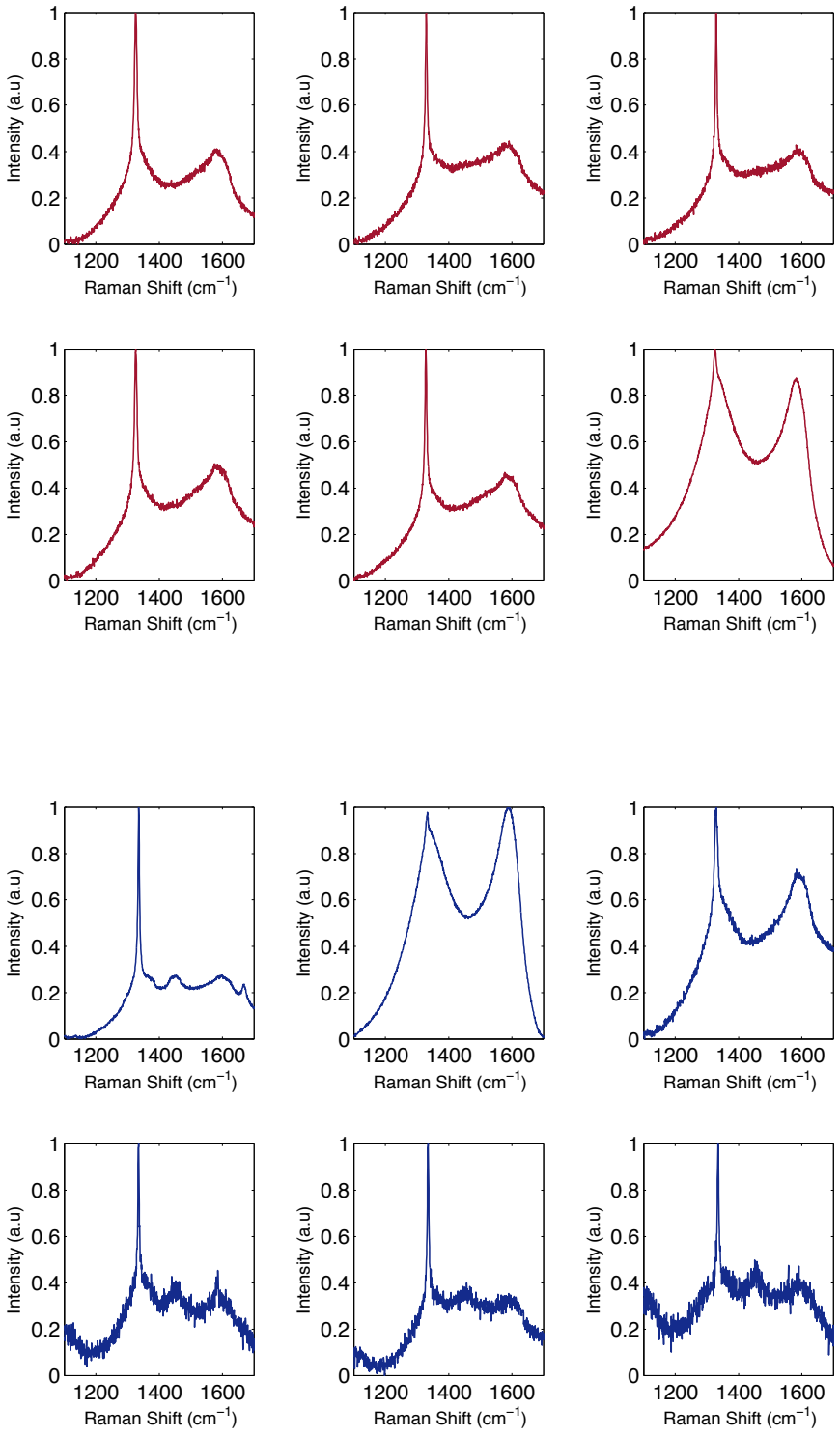

FIGURE 6.5: Representative Raman spectra at 532nm excitation of the graphitic nanodiamond sample after annealing for 3h at 450°C (brown) and 500°C (blue)

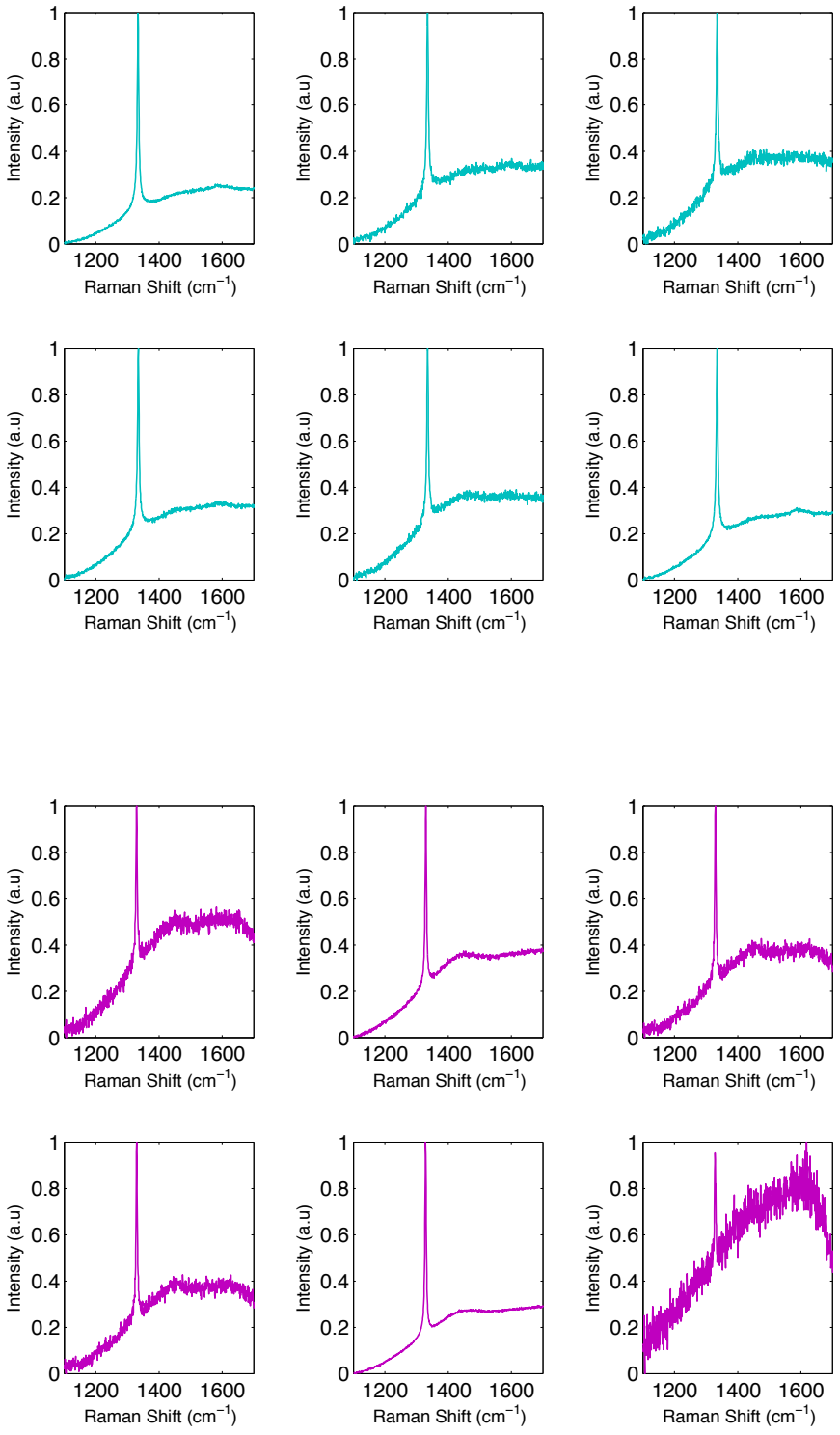

FIGURE 6.6: Representative Raman spectra at 532nm excitation of the graphitic nanodiamond sample after annealing for 3h at 550°C (turquoise) and 600°C (purple)

This situation is dramatically changed after a 450°C anneal. The narrow diamond peaks are already mostly clear to see, and now come to dominate over the D-band scattering. Correspondingly the G-peak amplitude is vastly reduced by a factor of ≈ 2.5 relative to the diamond. There has clearly already been a significant improvement in the sp^2/sp^3 ratio. It must be noted that there are still examples of material with the original profile. This can be attributed to buried parts of the powder that may have been less exposed to the air within the furnace.

Annealing at 500°C yields a similar results, with an indication that the G and D peaks are reduced still further with respect to the diamond. However there still exist some crystals that are of a graphitic nature. In the well-oxidised spectra, there is a regular appearance of a new Raman feature at 1450cm^{-1}. This has been attributed previously to polyacetylene (a long chain polymer $(C_2H_2)_n$), appearing at grain boundaries in CVD nanocrystalline diamond films [113, 122]. It can be speculated that as the etching of the outer layers of sp^2 take place, the nanodiamond facets and boundaries at which these materials might exist, become exposed and thus appear in the Raman spectra. However, this will not be pursued further in this investigation.

At 550°C, there is very little evidence of any sp^2 related features remaining. With only a narrow diamond peak appearing to be prominent. It is now evident that there is a rising background profile in many of these raman spectra. With 532nm excitation, it is likely that excitation of NV^- and/or NV^0 colour centres may be the cause of this. Full spectra would be needed to confirm this.

Finally at 600°C. There is some evidence that the height of the diamond peak has been reduced relative to the side intensity-band at 1400-1600cm^{-1}. This is unsurprising as 600°C is well into the oxidation phase of the sp^3 material, as is clearly apparent in the TGA data. There also is some appearance of the 1450cm^{-1} peak.

It has been demonstrated that the relative sp^2/ sp^3 are controlled by selective oxidation, with improvements in the diamond peak starting at a 450°C anneal, with a corresponding reduction in the D and G peaks. From 500°C onwards the spectral features of the treated

sample appear identical with those of the as-purified sample in 6.2 The analysis of the Raman spectra has been qualitative in this discussion. A quantitative analysis is beyond this scope of this thesis. To quantify the ratios of the Diamond to sp^2 peaks, spectra need to be taken over a longer range to be able to determine the baseline, which can be challenging due to the potential for background PL from colour centres. In addition there is going to be some selection bias in the measurement. The optical microscope on the Raman spectrometer as in figure 6.2, the features were pre-selected to undergo Raman spectroscopy. Efforts were made to select the smallest crystals visible, and to conduct a survey of many features across the sample. However this is always going to be limited by the resolving power of the microscope. The larger the crystals, the more likely they are to be bound into larger matrices. The trends established in this section are sufficient for the purposes of this investigation.

6.1.3 Dynamic Light Scattering

The DLS was employed in this investigation in order to determine the size distributions after the annealing process. Centrifugation is typically used to separate out heavier particles suspended in solution as they experience a greater relative centrifugal force. The effectiveness of this method was also investigated. After annealing at 450-600°C, 1ml of each solution was placed into a micro centrifuge at 10000RPM for 10mins [Sanyo Micro-centaur]. The solutions were contained in micro-centrifuge tubes [Eppendorf CF]. After centrifugation a sediment had crashed out of the solution. The light coloured supernatant was extracted for DLS analysis. The Zetasizer requires that the samples be dilute to avoid multiple photon scattering processes, whilst at the same time, having enough material to produce a scattering signal. The guidelines are state that "whenever possible, the sample concentration should be selected such that the sample develops a slightly milky appearance - or in more technical terms, gets slightly turbid" [117]. The supernatant met this criterion, however the control solution had to be diluted to 0.1mg/ml to achieve a similar appearance. DLS measurements before and after centrifugation are shown in 6.7. The results are expressed as intensity-size distributions,

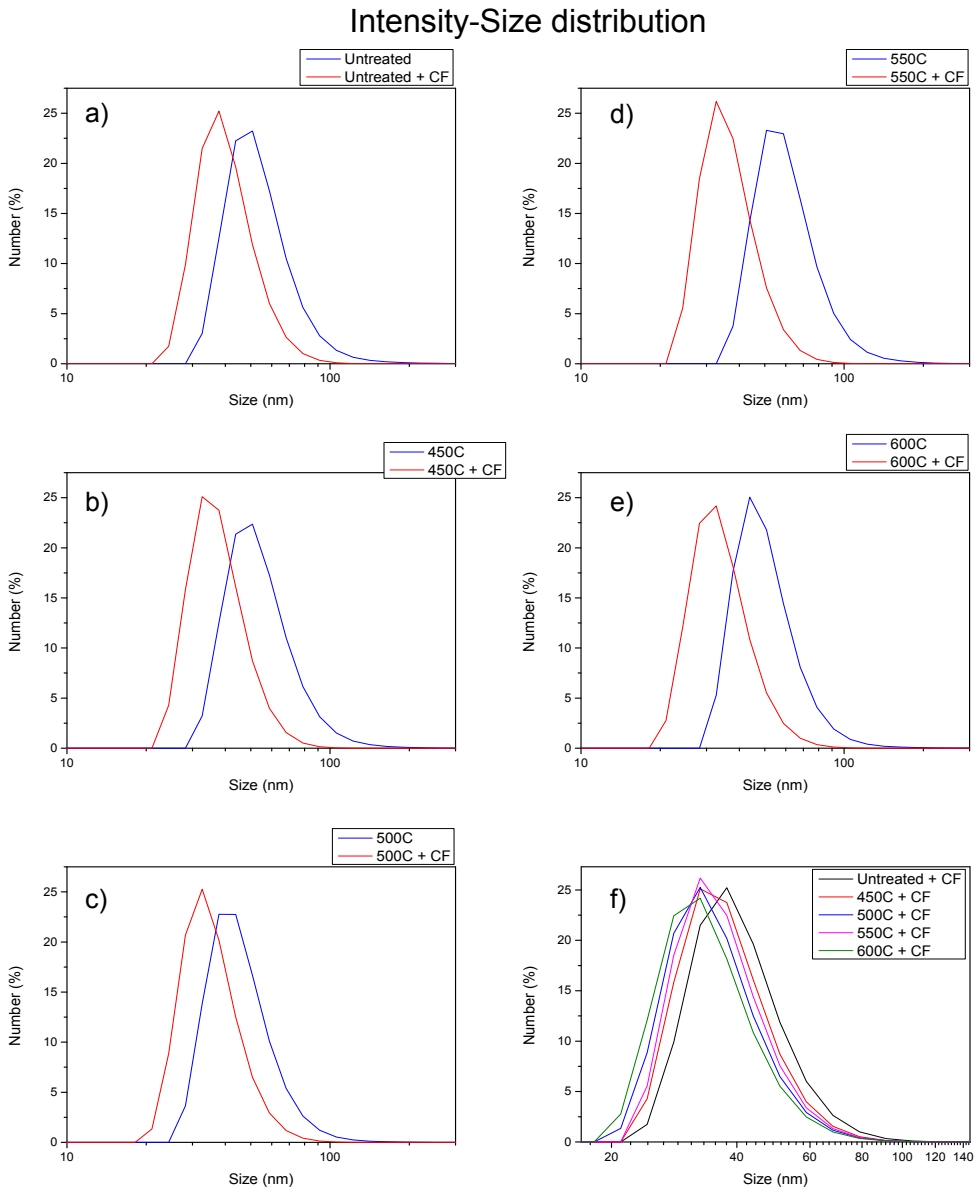

FIGURE 6.7: Intensity-size distributions for the untreated control sample a) and air annealed samples b) - e), before (blue) and after centrifugation (red). f) intensity-size distributions as a function of annealing temperature (centrifuged samples only)

with logarithmic size-scale. The distributions are broadly peaked with a skew to larger particle sizes indicating some poly-dispersity. The centrifugation process is shown to be effective in reducing the peak size by 12-15nm in all cases, however a skewed distribution still persists. The reduction in particle size with annealing temperature was also studied, with the results comparing the centrifuged samples shown in 6.7f. There is a general shift to smaller sizes with increased annealing temperature, however the 550°C sample appears to buck this trend slightly.

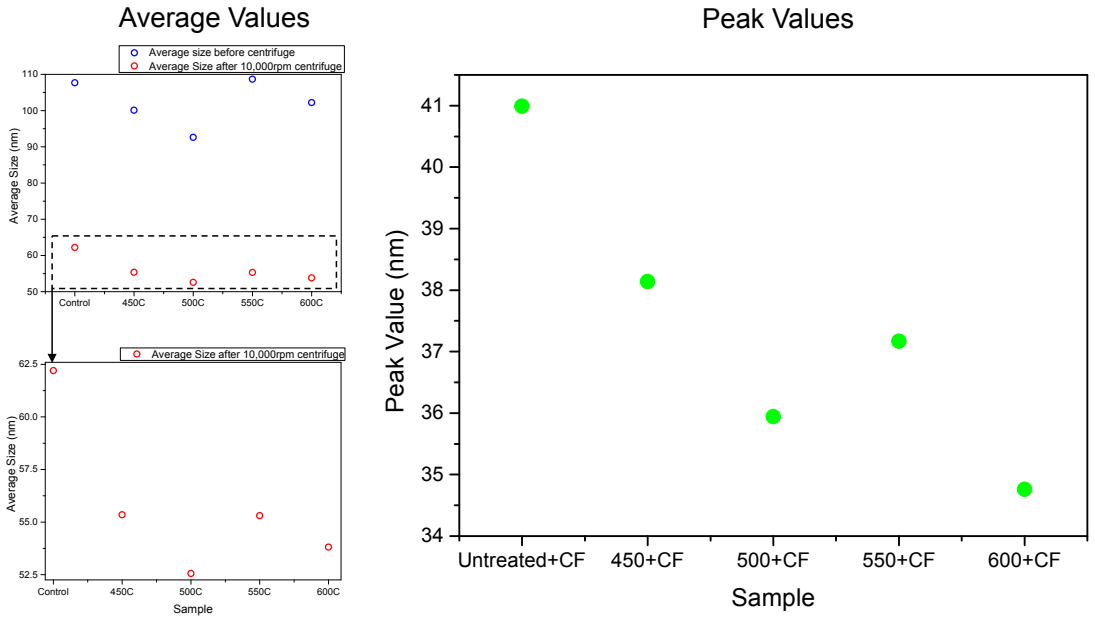

FIGURE 6.8: Left: Average particle sizes as a function of annealing temperature before and after centrifugation. Right: Distribution peak values as a function of annealing temperature. Centrifuged samples only

The size-distribution peak shifts after centrifugation are summarised in figure 6.8b. A shift of 6nm is observed with respect to the un-treated control sample. Improvements can potentially be made by ultracentrifugation [123], which exert a greater centrifugal forces than the one used in this study. With these, the NDs may be able to reach the 5nm core particulate regime. The system also outputs an average particle size as in figure 6.8, which in this case appears to be greater the peak value of the distribution. To obtain this quantity, the instrument fits a polynomial the the log of the correlation function - $\log(g^{(2)}) = a + bt + ct^2$. Then b is converted to a size using the dispersant velocity and some instrumental constants [117]. It is likely the discrepancy lies with the skew of the distribution to larger particle sizes. Using the average size, the centrifugation effect is more apparent, reducing the particle size by ≈45nm.

In summary the DLS measurements confirm the reduction in size of average particulate, with the annealing process. However size reduction with increased temperature was only slight. Centrifugation is shown to be an important part of the sample preparation process with smaller size distributions obtained as the larger agglomerates crash out. Improved methods for dispersion and ultracentrifugation would be suggested to yield

the smallest core particle sizes.

6.1.4 Summary

Through the Raman spectroscopy and TGA, the onset of the sp^2 etching was observed. The investigation is summarised in figure 6.9. at 450°C, there was a selected etching of the sp^2 phase, whilst the diamond phase stayed relatively in-tact. This was really highlighted by the isothermal TGA measurements in figure 6.4, comparing the graphitic and purified nanodiamond powders. In the graphitic sample the dM/dt rate was a factor of 40 greater than the purified source material. Beyond 450°C there is an apparent improvement in the sp^2/sp^3 relative content. The onset temperature of oxidation for the purified sample was seen to be 569°C. It is no surprise then that there is a there significant dM/dt rate for this sample at 600°C isothermal conditions.

The DLS measurements presented some evidence towards the reduction in average particle size and size distribution with increasing annealing temperature. This picture is not complete in this investigation, with the 550°C annealed ND powder bucking the trend. What is explicitly clear is the benefits on the centrifugation in the sample preparation process.

With a thorough investigation on the obtained ND material, attention was focused on the original NV-rich ND powder which was the motivation for this investigation. With only 2.7mg of material available, a 450°C anneal was chosen at 3h to oxidise the sp^2 content. Following from the isothermal TGA trace, $\approx 90\mu$g of material was expected to be lost through this process, whilst the annealing temperature is well below the sp^3 oxidation onset. The resultant materials were then re-dispersed in de-ionised water using a sonicating bath for 1h. The solution was centrifuged for 10mins at 10,000rpm, after which the supernatant was extracted. The sample performance was much improved and a characterisation of the single NV centres identified will be presented in the following section.

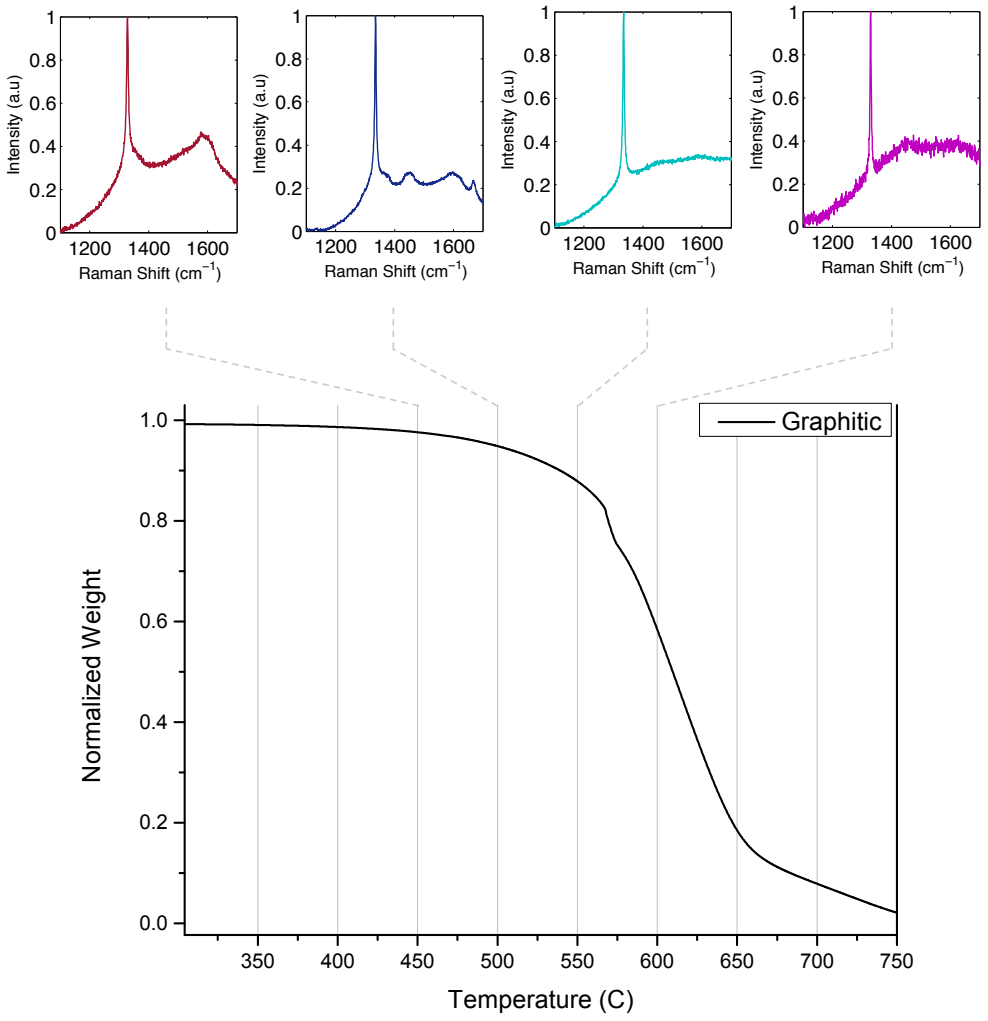

FIGURE 6.9: Summary of the TGA measurements with representative Raman shown at each temperature. The TGA trace shown corresponds to the graphitic sample. It is seen that the 600°C anneal is well into the main oxidation stage of the nanodiamond material, whilst the 550°C anneal is just at onset of diamond oxidation.

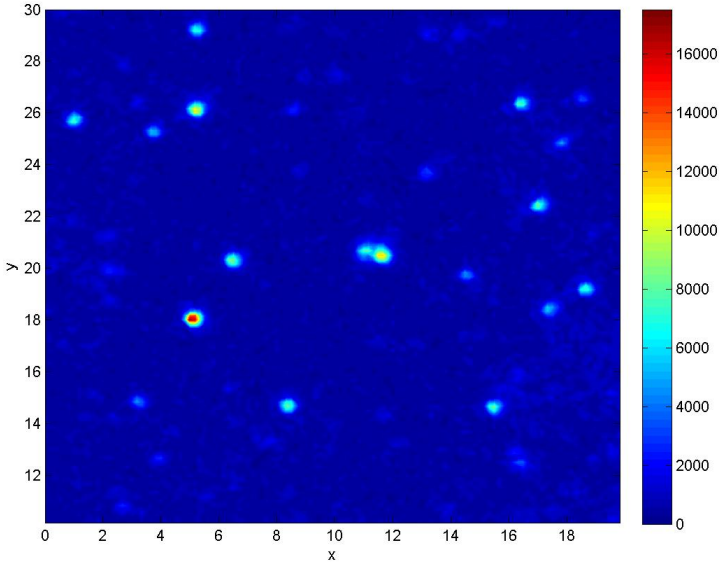

FIGURE 6.10: Typical PL image of the ND dispersed on a cover glass. Taken with x100 1.25NA Oil-immersion objective. The nanodiamonds are well dispersed and singe NVs are readily observed

6.2 Single NV Characterisation

The newly obtained nanodiamonds are spin-coated onto the substrate, as outlined in section 4.3, and a typical dispersion is shown in figure 6.10. Single NV centres in nanodiamonds are now readily observed.

6.2.1 Single NV Survey

This section will present a full optical characterisation of single NV centres in nanodiamond both at room temperature and 77K to identify the ZPL linewidths. HBT measurements will verify single photon emission and PL lifetime measurements will serve as a benchmark for any enhanced cavity emission rate. To illustrate the reliability of single NV identification, a short HBT survey, of NDs found within one $50\times50\mu$m registration square, is presented in figure 6.11. Single NV4 is highlighted in blue as this is used for the preliminary NV-cavity coupling experiments at low temperature, 7.1.

For the case of NV4, the measurement SNR of 2.33 leads to an expected $g^{(2)}(0) = 0.51$, which matches the observed value, verifying that NV4 is a single emitter. These expected

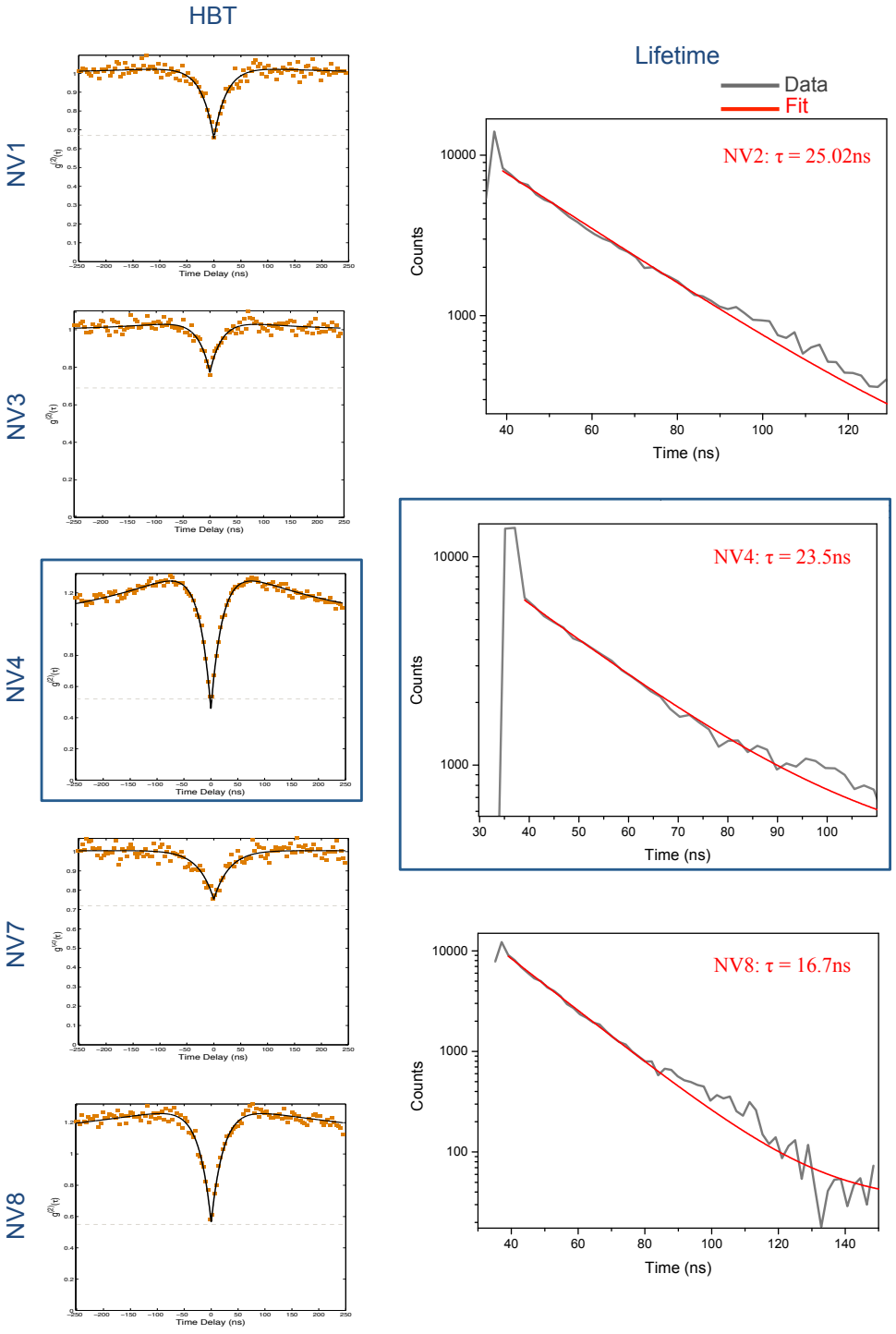

FIGURE 6.11: HBT/Lifetime survey of NV centres in nanodiamond in a 50×50μm registration square on a planar DBR mirror. Left: HBT measurements. The black line is a fit to the correlation function. The grey dashed line represents the baseline for $g^{(2)}(0)$ expected from the background contribution to the measurement. Right: PL lifetime data for NV1, 4, 8. The decay constant for the single exponential fit (red) to the data (grey) is shown inset.

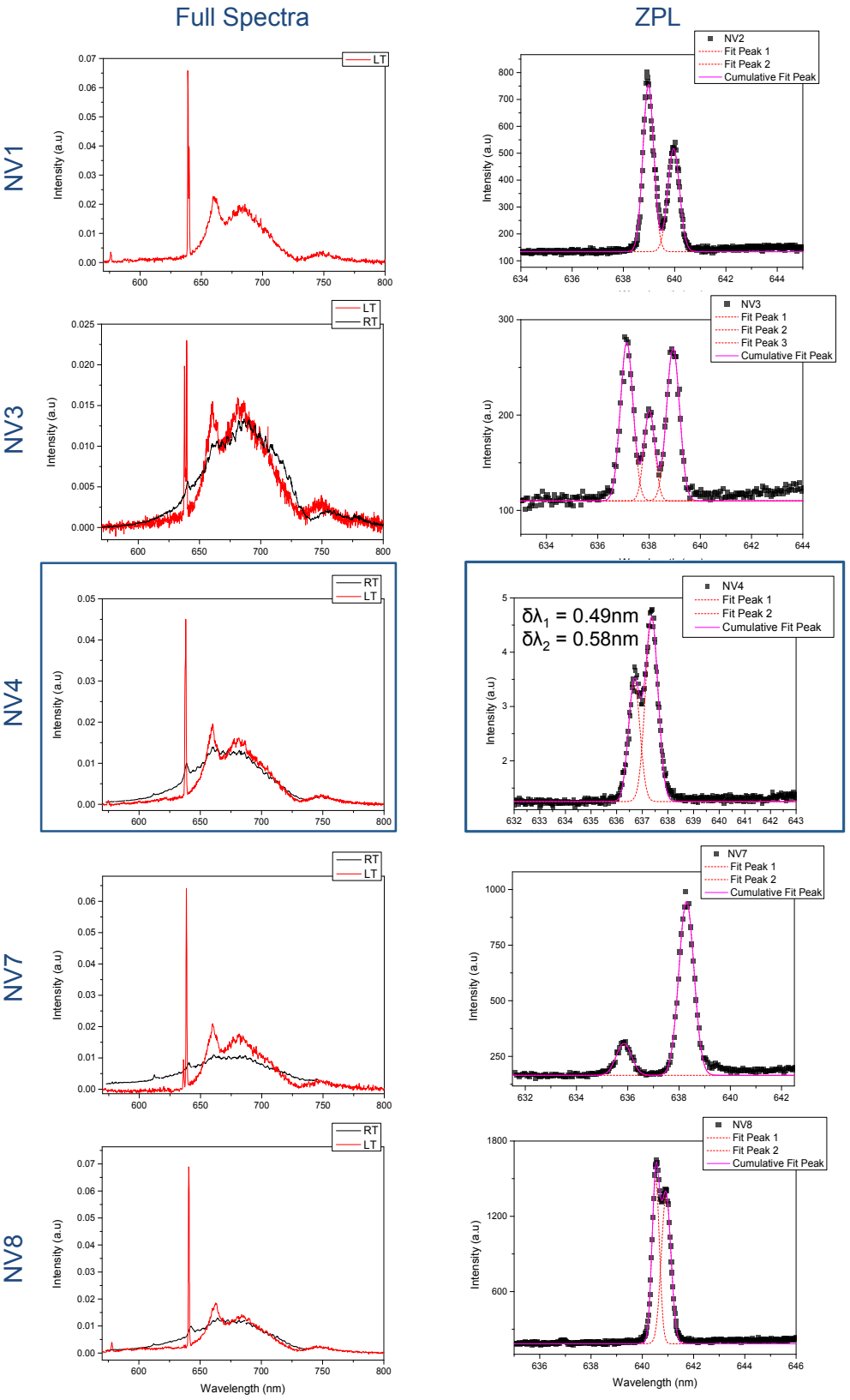

FIGURE 6.12: Spectral survey of NV centres in nanodiamond on a DBR mirror. Left: RT spectra (black) and LT spectra (red) in the 570-800nm range. Data has been normalised for comparison. Right: Spectra taken with 0.03nm resolution on the ZPL. A 2-5minute integration time is typically used. Individual peaks are fit with gaussians (red dashed line), with the cumulative fit shown (magenta). NV4 is highlighted in blue, with FWHM shown inset

values for single photon emission are calculated using equation 4.4, represented by the grey dashed lines. The NVs presented mostly show good agreement, with NV3/7 showing slight deviations. This imperfect anti-correlation, and is a common scenario encountered in the characterisation of this sample. Despite this deviation, it still strongly indicates one single emitter provides the dominant contribution to the PL.

Figure 6.11 also presents the PL lifetime of NV1, 4, 8, that were unambiguously identified as single NV centres. The observed lifetimes contain a fast decay component in the first 3ns. This is attributed to the residual background fluorescence of the mirror coatings. A single-exponential decay curve is thus fit from the second or third time-bin after the start of the decay, with the single NV lifetimes found to be in the range 16-25ns. The NV centre in the bulk has a corresponding lifetime of 12ns [124]. NV hosted in nanodiamond consistently show slower decay times and the lifetimes measured here are typical of those observed in the literature [105]. This is often attributed to the reduction in the optical density of states as the size of the host crystal is reduced, consequently inhibiting the spontaneous emission rate. [106].

Low temperature spectra are shown in figure 6.12 with a comparison to room temperature made where possible. The spectra have been normalised for comparison. Something that is consistently observed with NV centres on the DBR mirror ($[SiO_2/TiO_2/]^{10}/SiO_2$), is a slight modification of the PSB emission at $\approx$ 730nm. This may well be an effect of the DBR substrate.

The narrowing of the ZPL is observed at low temperature, through a reduction in the pure-dephasing rate $\gamma*$, leading to a dramatic increase in the peak intensity with respect to the RT spectrum. This is also reflected in the PSB emission, particularly at the 660nm peak of the PSB emission. The reduction of $\gamma*$ affects all transitions from the excited state. However the non-radiative transitions rates $\gamma_{i,i-1}$, through the vibrational sub-levels of the ground state, are still the dominant broadening mechanism of the PSB. Corresponding high-resolution spectra (0.03nm) of the ZPL are shown for each case, to illuminate the structure of the excited state. For the confirmed single centres of NV1, 4, 8 there is a large strain splitting in all cases, lifting the degeneracy of the $E_{x,y}$ orbital

doublets. For NV4, the ZPL doublet is split by 470GHz. whilst this approaches 1THz for NV7. The absence of any additional ZPL for NV7 suggests that it is indeed a single centre as indicated by the HBT measurement. For NV3 on the other hand, the presence of three lines is shown, which could suggest one strain split ZPL, with another degenerate ZPL. However there is not enough information contained in the spectrum alone to draw meaningful conclusions. The large strain splittings in these spectra are typical of many of the single NVs investigated through the course of this project. This behaviour is not unexpected, as HPHT nanodiamonds often have large strain fields within them, and proximity for a surface is likely to enhance this. Similarly large strain splittings have also been observed in CVD grown bulk diamond [97].

A crucial parameter to define is the ZPL linewidth. It is exclusively observed that all spectral lineshapes are well fitted with a Gaussian function, indicating an inhomogeneous broadening of the transition. The extracted FWHMs (full-width at half-maximum) for NV4 of $\delta\lambda_{\mathrm{ZPL}} = 0.49\pm0.58$nm ($\approx$ 350GHz), are over 5 times greater than the linewidth expected from pure dephasing alone, for NV centres in bulk diamond [101]. Again this is a result of the spectral diffusion from ionised impurities in the host. This will be detrimental to cavity coupling, particularly if it occurs over a range greater than the cavity linewidth. A survey of the ZPLs interrogated through the duration of this project is displayed in figure 6.13. These include strain split NVs and nanodiamonds hosting multiple NVs. 43 ZPLs are studied with an average FWHM of $\delta\lambda_{\mathrm{ZPL}} = 0.49$nm and a standard deviation of 0.13nm.

6.2.1.1 HBT Power Dependence

Figure 6.14(a) shows the power dependence of the correlation functions for NV4. A clear bunching effect at intermediate time-delays is observed due to pumping into the metastable state, and the bunching is shown to be more pronounced with excitation power. The power dependent parameters of the fits are also summarised in figure 6.14(c). The τ_2 decay is tends to the spontaneous emission lifetime of 23.5$\pm$1.3ns within the fitting error. It must be noted that the errors from the least squares fit are larger at

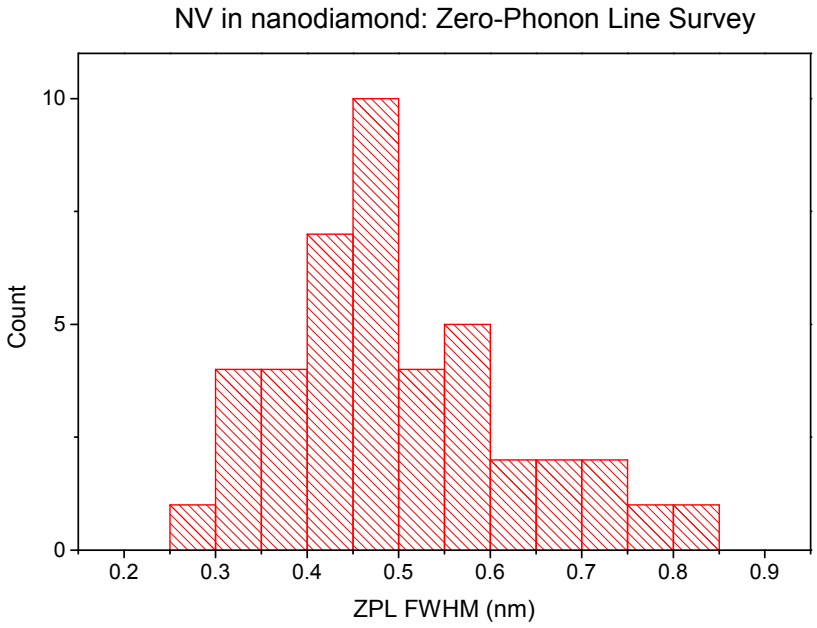

FIGURE 6.13: Survey of the FWHM for 43 ZPL hosted in nanodiamond at 77K. NVs with strain splitting and nanodiamonds containing multiple NVs are included in the survey

the lower pumping powers, as a consequence of the shot noise associated with the low emission rates. NV4 was observed to have a saturation intensity $I_{\text{sat}} = 98{,}000\text{c/s}$, which is amongst the highest observed in this project.

6.2.2 Properties of NV2

Here the properties of NV2 are presented. This is the emitter with which the main LT cavity coupling results in section 7.2. For clarity, they are presented separately to the previous NV survey, as it will require a more in-depth analysis.

The HBT measurement in 6.15(c), shows clear single-photon emission. However from the SNR, the expected $g^{(2)}(0) = 0.309$. So it is clear that, as with NV3, whilst most of the light comprises of single photon emission, there is another less intense emitter, preventing the correlation function from reaching the level expected by the background. It is no surprise that there are multiple lines appearing in the the ZPL spectrum taken in figure 6.15(a). Care was taken to attain the same excitation conditions for the spectrum

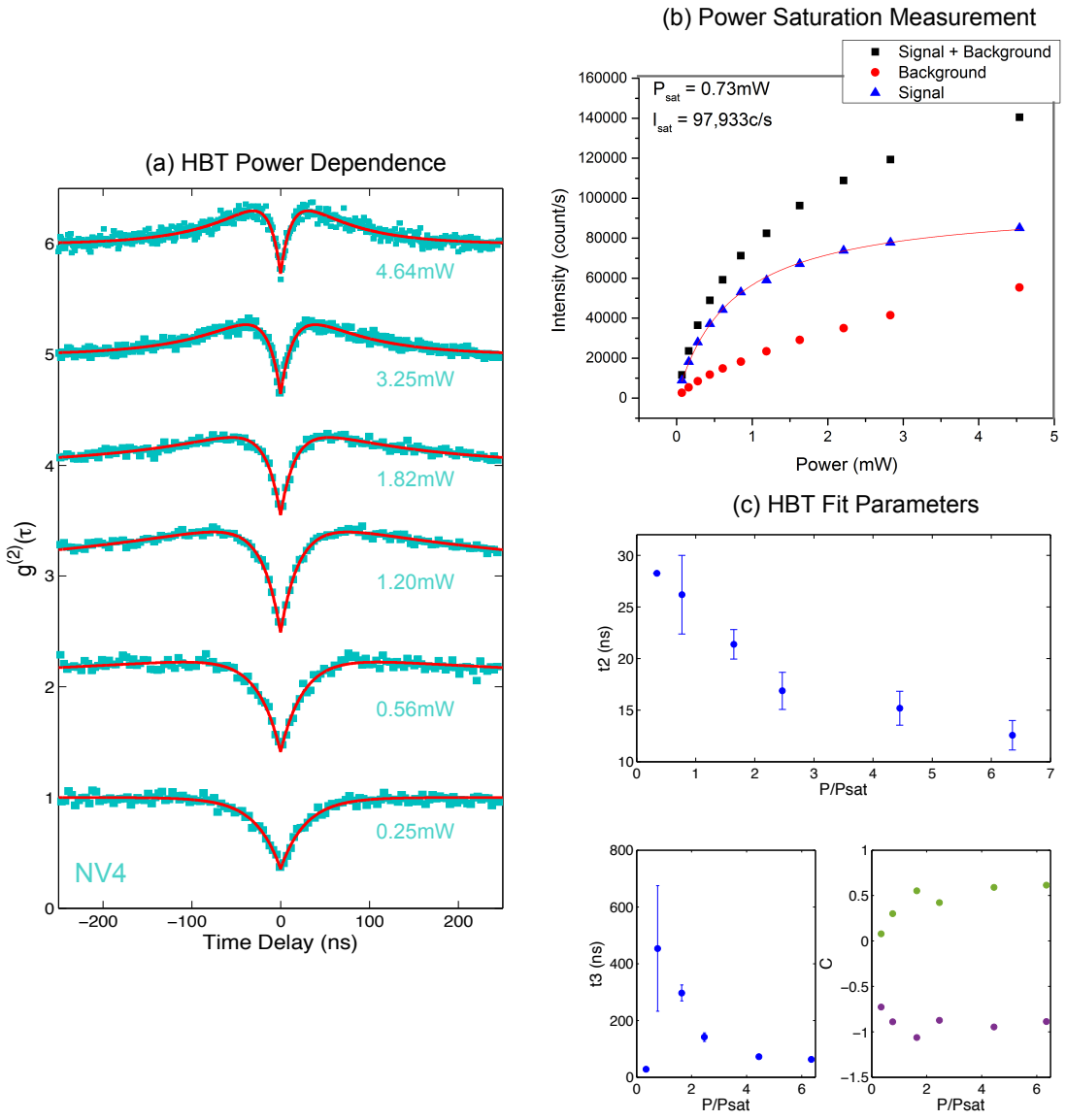

FIGURE 6.14: (a) Power dependent HBT measurements of NV4 (Objective 0.82NA). The data points are all fit to the equation 3.53. (b) Power saturation measurement in the 670-810nm spectral window with parameters shown inset. (c) Evolution of the fit parameters of equation 3.53 as a function of P_{sat}. Errors bars represent 95% confidence intervals from the function fitting. The first error bar for t_2 is not shown as the fitting error was large

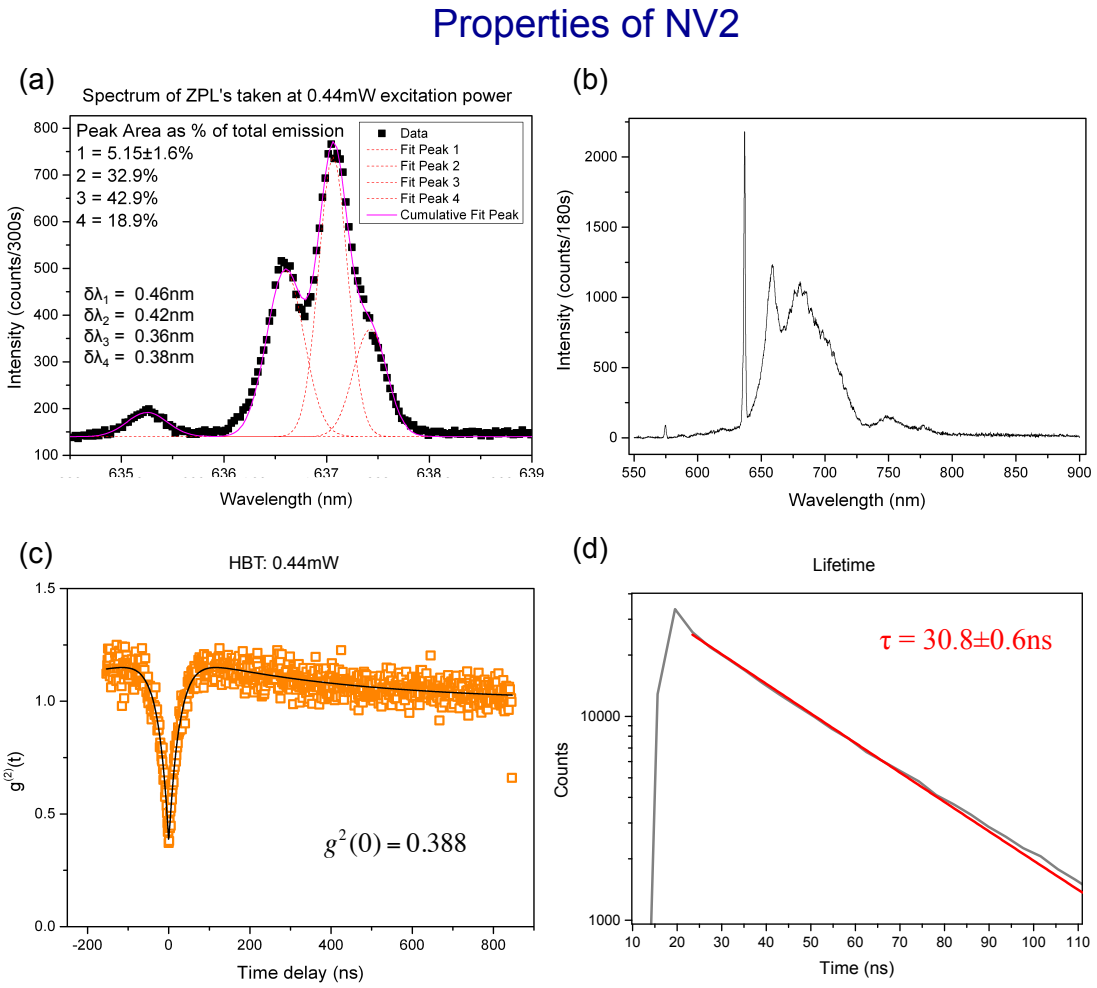

FIGURE 6.15: The Properties of NV2. (a) ZPL spectrum at 77K, 0.03nm resolution. The FWHM and relative integrated intensities are shown inset. (b) Full Spectrum of NV2. (c) HBT at RT. 670-810nm spectral window. (d) PL lifetime measurement at 77K. 670-810nm spectral window. The data (grey) is shown with a single exponential fit (red). The decay constant is shown inset.

and the HBT, with 0.44mW CW power. From the correlation function and measurement SNR, the relative contribution of the second emitter can be quantified with equation:

$$g^{(2)}(0) = 1 - P_{\text{signal}}^2(1 - 2\alpha + 2\alpha^2) \tag{6.1}$$

From the SNR, $P_{\text{signal}} = 0.830$ whilst $g^{(2)}(0) = 0.388$. The contribution to the total signal can then be quantified as:

$$P_{\mathrm{A}} = (1-\alpha)P_{\mathrm{sig}} = 0.9407P_{\mathrm{sig}}$$

$$P_{\mathrm{B}} = \alpha P_{\mathrm{sig}} = 0.0593P_{\mathrm{sig}}$$

Where $\mathrm{P_{A,B}}$ is the probability of receiving a photon from $\mathrm{NV_{A,B}}$. Consequently 94% of the signal is from a single emitter, whilst the other centre is only fractionally as bright. Figure 6.15(a) shows the relative integrated intensities inset. Peak 1 constitutes 5.16% of the signal, and this well supported by the value of α within the fitting error. This allows for peak 1 to be assigned as the second emitter.

Peaks 2 & 3 dominate the emission are assigned to be the strain split orbital doublet of a single NV centre, with strain splitting of 347GHz. The polarisation measurements on the orbital doublets are shown in section 6.2.2.1. There is a shoulder on peak 3 that can be fit as a separate ZPL with a splitting of 270GHz from peak 3. The HBT rules out the possibilities that it is associated with peak 1, or that it arises from a third emitter in the crystal. It is possible that the complex electronic environment of the host crystal may be the cause, with the presence of ionised impurities and charge traps leading to spectral diffusion and jumps due to the Stark effect. A single electron within 10nm of the defect centre is enough to induce a Stark shift on the 100GHz energy scale [104]. Spectral jumps of similar magnitude have been observed in near infra-red single colour centres in nanodiamond at low temperature [125].

Finally the lifetime is measured to be $\tau = 30.8\pm0.6$ns, which is amongst the longest measured in the duration of this project. This will serve as the out-of cavity decay rate when quantifying the Purcell enhancements.

6.2.2.1 Polarization Measurements

To quantify the NV-dipole orientation factor ξ, it is necessary to take polarisation measurements. Figure 6.16(a), shows a schematic of the measurement with the NV crystal

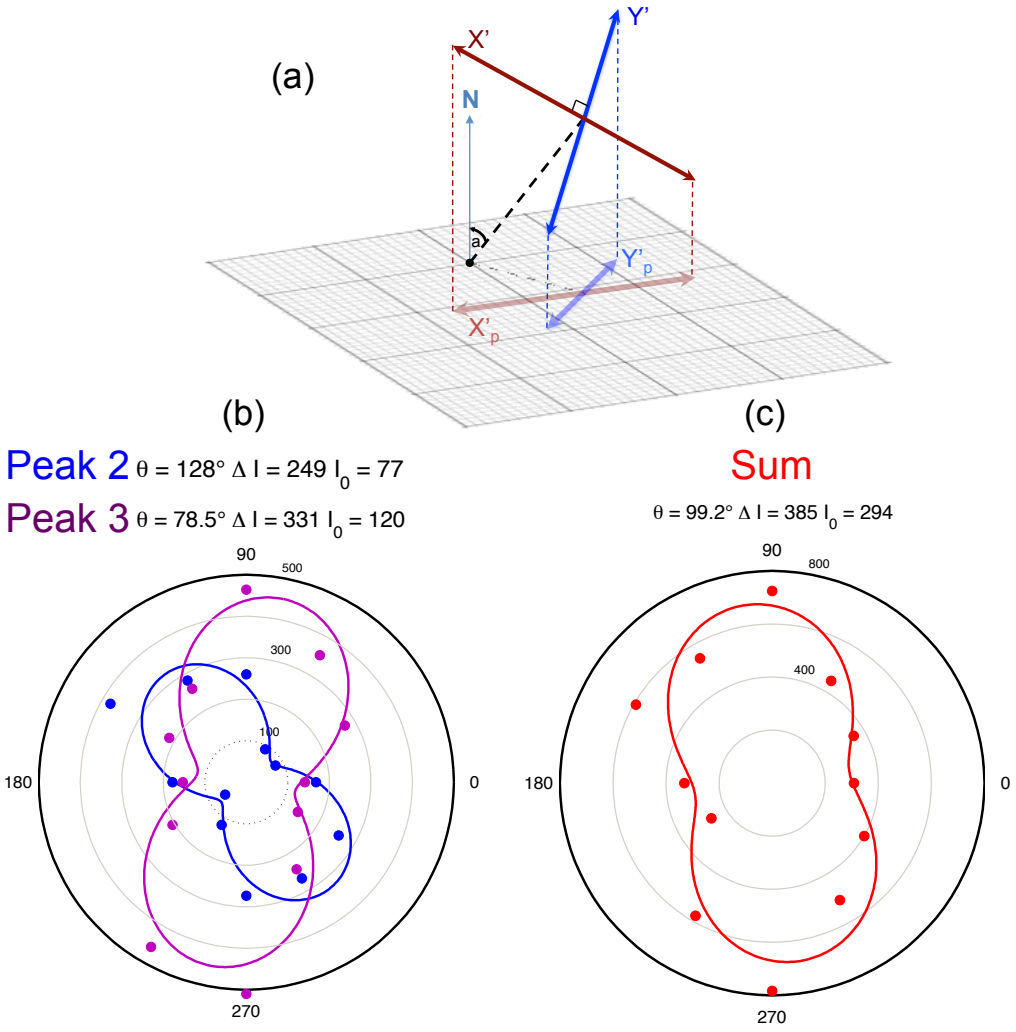

FIGURE 6.16: Polarisation measurements of NV4 & NV2. The solid lines are a fit to the equation 6.2. Peaks 2 & 3 of NV2 are taken to be the strain split orbital doublet of a single NV centre. Each data point represents the fitted area of the individual peak, as a function of linear polariser angle

axis at an arbitrary polar angle (a) to the mirror plane. The measurement is sensitive to the projections of these dipoles on the mirror plane.

The polarisation measurement comprising the integrated intensity of peaks 2, 3 as a function of the linear polariser angle is shown in 6.16(b) in 30° intervals. A clear dipole behaviour is shown. Each of the peaks is shown to have an independent polarisation and the data is fit to Malus' Law, to obtain the intensity as function of polariser angle $I(\phi_p)$.

$$I(\phi_p) = I_0 + \Delta I \cos^2(\phi_p + \theta) \tag{6.2}$$

Where I_0 is the intensity minima and ΔI is the amplitude of the $\cos^2$ function. To determine the angle between the dipoles and the plane of the mirror the strain splitting is utilised.

The model assumes that each dipole is of equal magnitude. The angle of the defect to the optical axis, a, is directly related to the sum of each dipole polar intensity distribution in figure 6.16(c) as:

$$I_{min} = I_0 \cos^2(a) \tag{6.3}$$

The rotation of the defect about the NV axis (angle b) is then related to the ratio between the peak intensities.

$$R_{2/3} = \frac{\sin^2(a)\sin^2(b) - \sin^2(a) + 1}{1 - \sin^2(a)\sin^2(b)} \tag{6.4}$$

This allows for a full description of the NV orientation. Finally the angle between the dipole and the plane of the mirror is found by taking the dot product of the original dipole vector with the planar projection. The full derivation of this can be found in the appendix A.

Before the model is applied, the thermalisation at 77K between orbital doublet $E_{X,Y}$ must be considered. The average populations will be described by a boltzmann distribution [101]. The ratio between the population depends on the energy splitting between the sub levels and this must be accounted for in order to scale the higher-energy dipole (peak 2) to be of equal magnitude. It is found that the population ratio between peak2:peak3 is 0.8:1. The measured intensities of peak 2 in figure 6.16(a) have been scaled by 1.25 to account for this. The angle a is found to be 49°, whilst the angle to the plane of peaks 2 & 3 are found to be 39° and 24° respectively.

6.3 Conclusion

This chapter has presented a detailed investigation into the sample preparation and optical properties of single NV centres in nanodiamond. A nanodiamond sample suffering from consistent aggregation was shown to be much improved after the application of an Oxygen anneal at 450°C for 3h. This was enabled by a detailed study into the thermal etching process supported by TGA analysis and Raman spectroscopy to qualitatively determine the relative sp^2/sp^3 phases of carbon at each temperature interval. DLS measurements indicated some reduction in crystal size, but mainly emphasised the importance of the centrifugation process in the sample preparation. The result of this study was to develop a robust protocol for nanodiamond preparation.

The quality of the sample was demonstrated through a survey of the optical properties of single NV centres, which were shown to be regularly identified. NV4 and NV2 were highlighted as the emitters with which the majority of LT coupling experiments were conducted. Strain split ZPLs were regularly observed with FWHMs averaging 0.45±0.13nm at 77K. These are over a factor of 5 greater than the observed literature values of the ZPL in bulk diamond. The lineshapes were exclusively shown to undergo inhomgeneous broadening, which is one of the limiting factors for the cavity coupling of NV centres in nanodiamond. This would be especially detrimental if occuring over an energy scale greater than the cavity linewidth.

For the cases of NV4/NV2 there is significant overlap of the individual strain split ZPL transitions. The cavity resonance would not resolve the individual peaks, and the modified emission rate will encompass a contribution from both ZPLs.

A novel method to determine the NV2 defect orientation was presented utilising the strain splitting of the ZPL. This was use to calculate the angle of the excited state dipoles to the plane of the mirror, and thus the orientation electric field within the cavity. All of this will be informative in the analysis of the low-temperature coupling results.

Both emitters showed strong photon anti-bunching in HBT measurements, after accounting for background emission. NV4 was shown to be a perfect single. NV2 was determined to have a second, fractionally bright, emitter contributing to the correlation function. This is not a concern for the cavity coupling experiments as 94% of the PL is from a single photon emitter. The out of cavity lifetime of the NV centres on the mirror substrate have been shown to be over twice that of the typical bulk value, which is usually assigned to be due to the change in the local optical density of states in nanodiamond. This provides a benchmark for quantifying any Purcell effect observed in the cavity. This chapter forms the experimental foundation for the coupling of single NV centres to the open-cavity at low temperature.

Chapter 7

Low Temperature Cavity Coupling

The following chapter describes the low temperature cavity coupling of single NV centres in nanodiamond. To date, this is one of the first times, that a colour centre in diamond has been coupled to the open-cavity system at cryogenic temperatures, bringing with it all the advantages of the open-cavity as described throughout this thesis.

The low temperature results will be shown in two stages corresponding to separate experimental runs. The first stage represents some of the preliminary results coupling to single NV4 (see section 6.2 for a the full out of cavity properties). Tuning of the cavity resonance through the ZPL will be firstly be demonstrated, along with a tuning through the PSB, exhibiting low bandwidth single photon emission across the spectral range of the NV [126]. Successive longitudinal modes are coupled to the ZPL from q=6-27, demonstrating the open-cavity system as a platform to sample a large subsection of the CQED parameter space.

The significant experimental developments made on the system between low temperature experimental runs, justify the separation of these results into two sections. Herein lie the key cavity coupling experiments that really illustrate the capabilities of the open cavity system. Results are achieved with the coupling of NV2 (see section 6.2.2). Single

photon emission of the cavity coupled ZPL is verified at low temperature. A more precise tuning through the ZPL is now demonstrated, whilst the saturation counts into the ZPL are measured to be 15,100c/s. The enhancement of the light-matter interaction is definitively confirmed through lifetime measurements on the cavity coupled ZPL, with an explicit dependence on the mode volume also established. These results form the highlight of this thesis and have positive implications for applications in solid-state quantum computing architectures.

The discussion will analyse the primary cavity-coupling results in detail, within the framework of the generalised Purcell factor. The discussion is split into an analytical treatment of the cavity coupled ZPL, with separate FDTD simulations to account for the full optical density of states and the off-resonant suppression of the PSB. It will be seen by incorporating the inhomogeneous broadening of the cavity mode, the theoretical analysis begins to approach the enhanced decay rates observed. Improvements in the theoretical treatment are also discussed.

7.1 Preliminary Low Temperature Cavity-Coupling

Conducting the low temperature experiments initially presented a significant technical challenge, which were described in chapter 4. This section presents the first successful cavity coupling experiments that were achieved with NV4. A cavity with a nominal $\beta = 12\mu$m is chosen for these coupling experiments. Here the mirror pair configuration is planar[10]:concave[10] with an expected $\mathcal{F} = 1754$ calculated from a coating simulation. The mirror orientation is now such that the emitters are imaged through the planar mirror, which has all the lateral degrees of freedom (rather than through the featured substrate as in chapter 5). The cavities have only axial tuning in this case. Figure 7.1 displays a longitudinal mode index of $q = 6$ coupled to the ZPL of NV4 at low temperature. The free spectral range of 91nm is such that the $q = 5$ set of modes can be seen at the edge of the stop-band. Once at 77K there is no scope for adjusting the relative alignment of the mirrors.

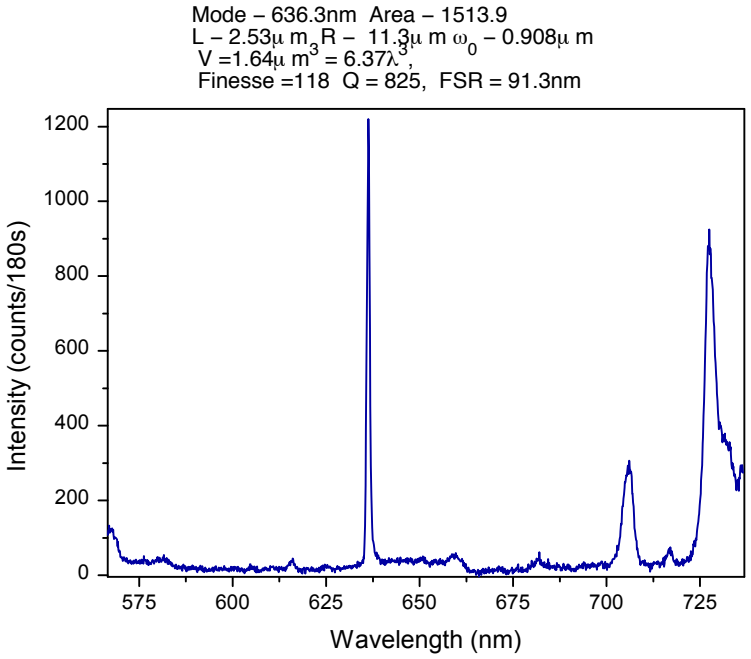

FIGURE 7.1: The cavity coupled ZPL of NV4 corresponding to $q = 6$. The Spectrum is taken with 0.13nm resolution. The cavity parameters are calculated through the free spectral range and transverse mode spacing

7.1.1 Zero-Phonon Line Tuning

Tunable coupling of the $q = 6$ mode to the ZPL is demonstrated in figure 7.2. Selected tuning spectra are displayed both with a fixed relative intensity axis and a magnified axis to clarify the line shapes. All resonances appear to be well fit with a Lorentzian line shape indicating a good mechanical stability of the cavity mirrors in this experimental run. Off-resonance, the cavity linewidth is 1.42nm, with $Q_{\text{cav}} = 400$. As the cavity mode is red-tuned through the ZPL, the observed spectral profiles are governed by the product of the individual line shapes. The peak intensity increases by a factor of 7.5 when on resonance. The low cavity Q and low resolution grating on the spectrometer mean that the coupling to the individual strain split ZPLs is not resolved.

All tuning spectra are presented in a sequential 2D plot in figure 7.3. With stepper actuation, the precise control over the tuning process is limited. The piezos are operated at the lowest limit of their threshold voltage to achieve minimum step size. If the stepper motion was not initiated, the voltage was increased in the next spectrum. This explains the behaviour seen in steps 6-14 where full motion was not initiated with the cavity

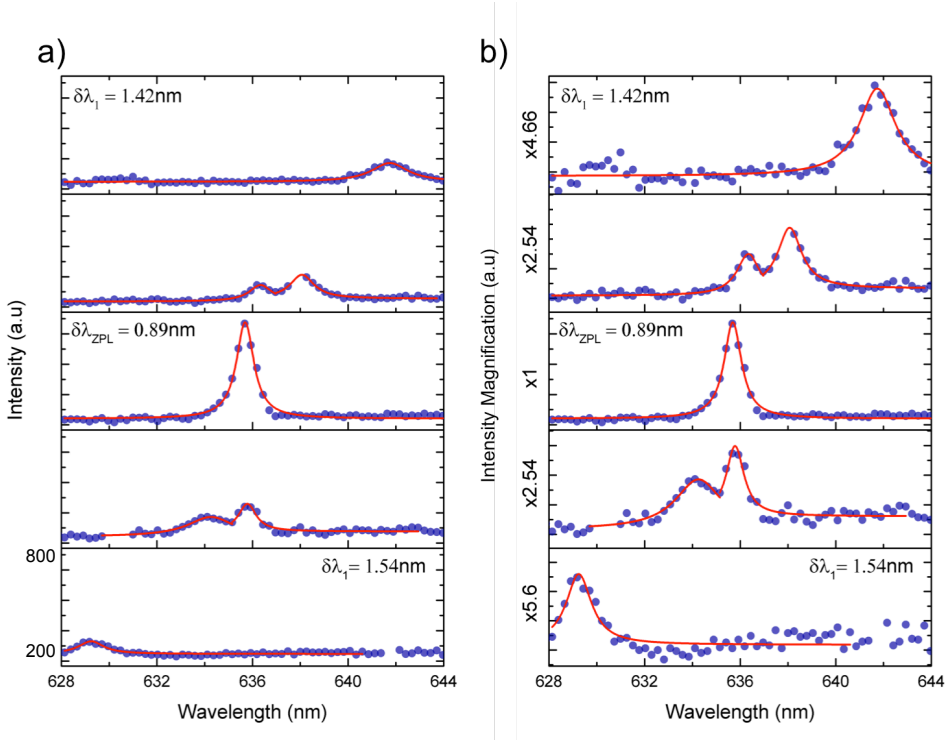

FIGURE 7.2: Selected tuning spectra for the $q = 6$ longitudinal mode index coupling to the ZPL of NV2. The spectral resolution here is 0.13nm. Left: Data points are shown on same intensity axis. Right: a magnification is applied to the individual intensity axes to illuminate the line profile. Lorentzian fits are shown in red. Cavity coupled and off-resonant line widths are indicated inset.

mode coupled to the ZPL. The voltage is subsequently increased and the mode jumps off resonance in spectrum 15.

7.1.2 Phonon Side-Band Tuning

With the broadband emission of the NV centre, single photon emission occurs over a large spectral range. It was seen in section 6.2.1 that the PSB emission remains largely unchanged at low temperature. The pure dephasing of the excited state $\gamma*$ is reduced, however the dominant contribution to the broadening, due to the non-radiative vibrational sub-level transitions $\gamma_{i,i-1}$ remain. Figure 7.4, shows the systematic tuning of the q=6 longitudinal mode across the PSB of the single NV centre, thereby channeling this broadband emission into a narrowband resonance. This was first demonstrated in an open-cavity by Albrecht et al [78], realising an inherently tunable single photon source, well suited for photonic integration. As the cavity resonance is tuned towards

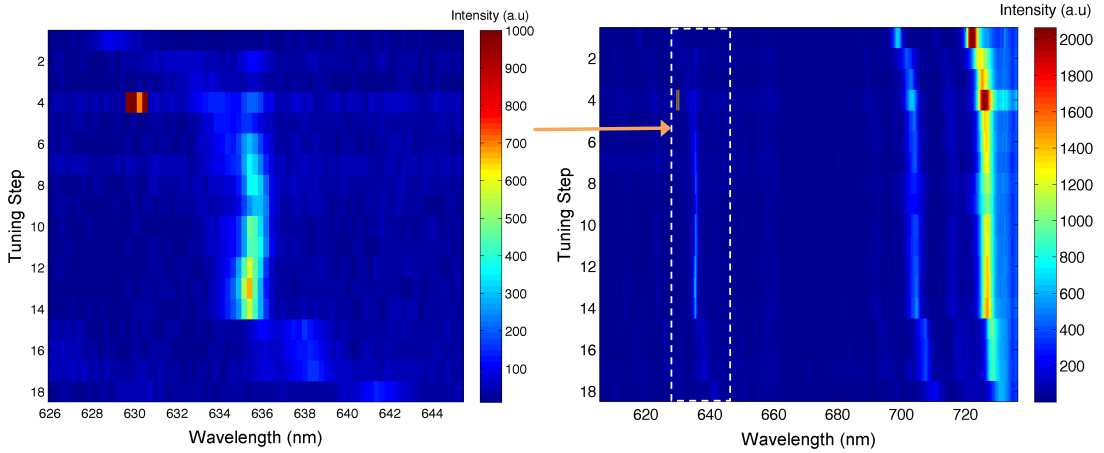

FIGURE 7.3: 2D plot of all cavity tuning spectra in sequence. Right: Whole stop band of the cavity. Left: ZPL region only. Each spectrum indicated the actuation of the stepper motor at the threshold voltage. On becoming clear that the stepper motion had not been initiated, the voltage was increased, leading to the cavity jumping off the resonance in step 15.

740nm, the finesse of the cavity drops through the increased transmission of the mirror coatings. This is demonstrated by the increase in linewidth by over a factor of 2 as the mode is tuned away from the centre of the stop band. The system again demonstrates its versatility through being able to sample a range of cavity Q factors in-situ. The increasing linewidth allows more of the broadband NV emission to be channelled into the cavity mode, seen through an increase in the integrated intensity towards 710nm, which subsequently reduces in line with the profile of the PSB.

7.1.3 Mode Index Tuning

The open cavity system allows an exploration of the cavity-coupling parameter space. This section demonstrates the coupling of successive longitudinal modes to the ZPL of NV4 in the range of q=6-27, spanning cavity lengths of 2.54-8.77μm for the $\beta = 12\mu$m cavity. Figure 7.5 shows a small selection of these spectra, including a profile of the ZPL coupled mode and the corresponding mode structure in the stop-band. The Q-factor scales with the mode index and therefore with length, as the photon time within the cavity increases. The linewidth for the corresponding mode is reduced for each longitudinal mode index, as can be observed in the figure. As with 7.2, the Lorenztian lineshapes are maintained. With the very shortest cavity lengths, some mechanical

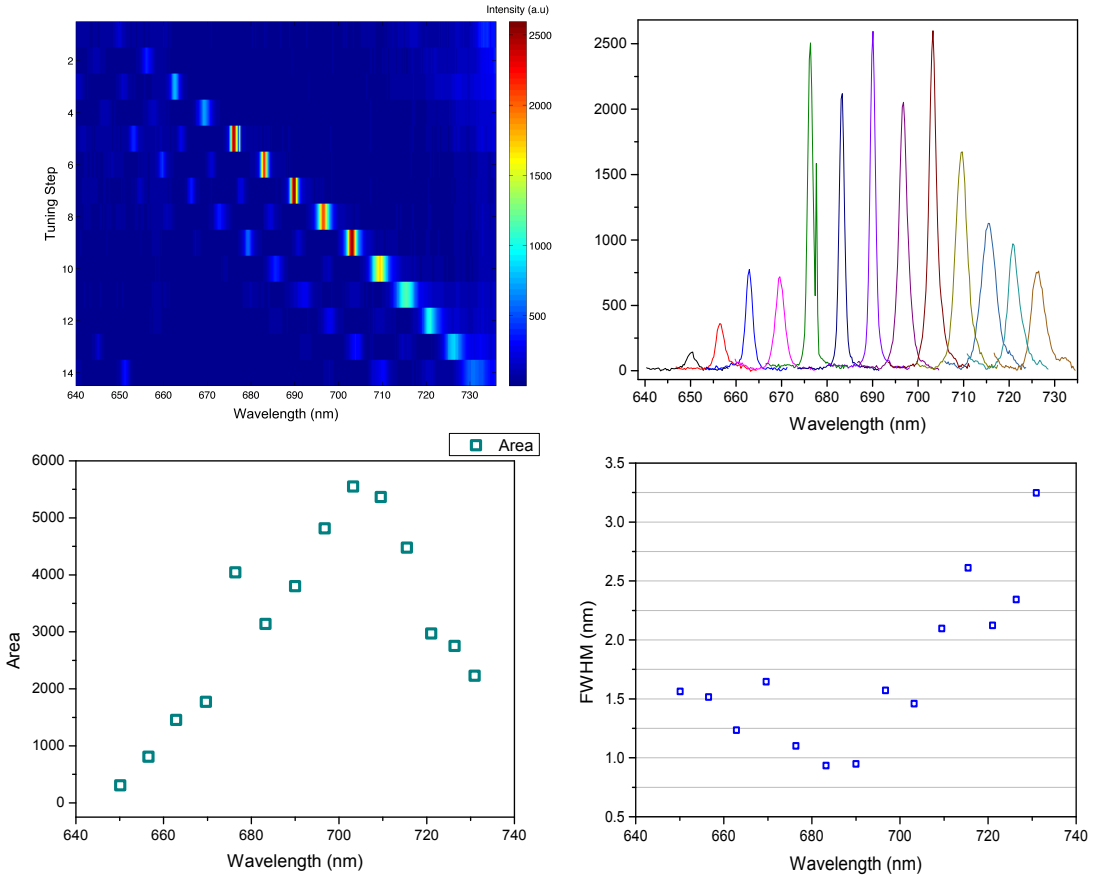

FIGURE 7.4: Top left: 2D plot of a TEM_{00} $q = 6$ mode, tuning through the PSB of NV4. Top right: TEM_{00} mode as a function of spectral position. Only a 6nm region around the resonance has been plotted for clarity. Bottom Left: Integrated intensity into the cavity mode as a function of spectral position. Bottom right: Evolution of the linewidth as a function of spectral position.

stability can be achieved as the substrates come into contact. This is not the case for the mode numbers shown in figure 7.5, which illustrates that cavity sample stage and mounting was, for the most part, stable in this experimental run. The linewidth of the ZPL coupled mode decreases from $\delta\lambda = 0.75$-0.39nm, approaching the 0.13nm resolution of the spectra. With a ZPL linewidth of $\delta\lambda = 0.45$nm, this system is demonstrates itself as a platform for which the transition between the good & bad emitter regime of CQED can be interrogated, giving the open cavity system a unique perspective within CQED.

Figure 7.6 shows a 2D plot of all spectra in sequence. Starting from q=6 where, the next mode can be seen with $\Delta\lambda = 91.5$nm, up to q=27, where $\Delta\lambda = 23.8$nm and four longitudinal mode indices are seen within the stop-band, coupling to the PSB. The figures allows the relative intensities of all peaks to be observed. The TEM_{00} modes are

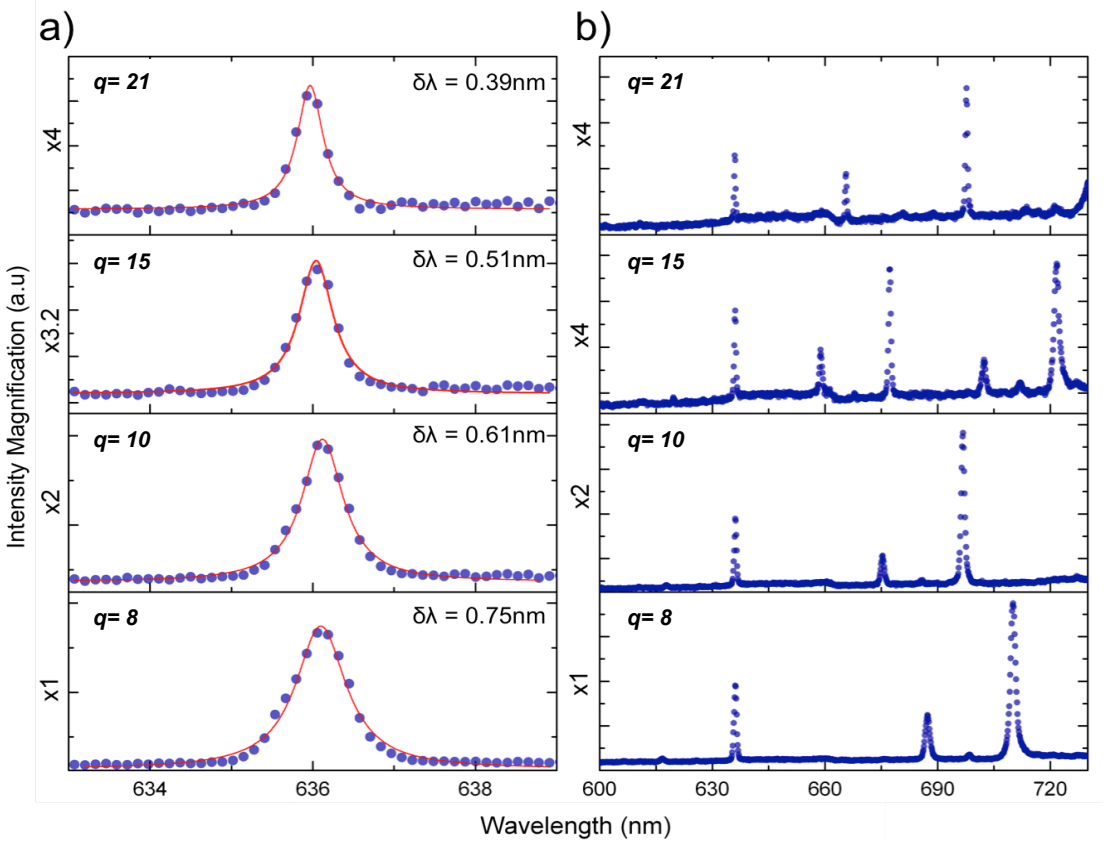

FIGURE 7.5: Left. Selection of mode indices coupled to the ZPL of NV4. A magnification is applied to the individual intensity axes to illuminate the decreasing cavity linewidth. The data points (blue) are fit with a Lorentzian function (red), with the linewidths indicated inset. Right: Corresponding spectra of the whole stop-band. More and more fundamental resonances are permitted within the stop-band as the cavity length is increased

indicated on the figure. Beyond $q = 21$, corresponding to tuning step 15, the transverse mode indices were no longer observed within the integration time of the measurement. The adjacent figure highlights the ZPL-coupled modes only. The limitation of the cavity positioning within this experimental run can be seen as the precision and reproducibility of the mode position is sub-optimal, indicating that a development needed to be made.

By positioning the successive cavity modes at the same wavelength, the evolution of the cavity parameters can be investigated to a good approximation. The integrated intensity into the mode, the Q-factor, Finesse and the Q/V ratio are all shown as a function of cavity length in 7.7. Since the Purcell factor has an explicit dependence on the cavity-Q/V (in the good emitter regime) the evolution of this ratio is highlighted. The observed finesse is significantly down from the expected value from the mirror

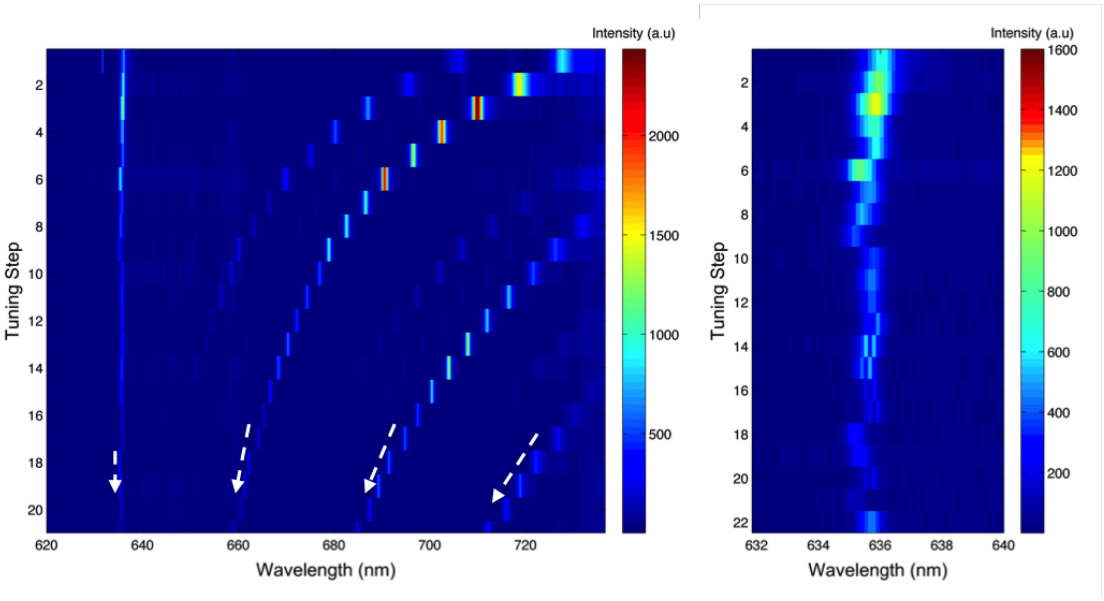

FIGURE 7.6: 2D plot of successive mode indices coupled to the ZPL. Left: The stop-band. Fundamental resonances are indicated by the white arrows. Right: Profile of the cavity coupled ZPL. The precision of the mode positioning is limited by the stepper actuation

coating simulations, which is expected to be $\mathcal{F} = 1765$ at 637nm. This likely due to scattering from the ND crystal. The finesse shows a modest decrease with cavity length until the onset of diffraction losses after which the finesse crashes. This effect is also reflected in the Q-factor. Finally the enhancement of the integrated intensity into the ZPL-coupled cavity mode can be seen, however any analysis of this is limited by the deficiencies in the mode positioning.

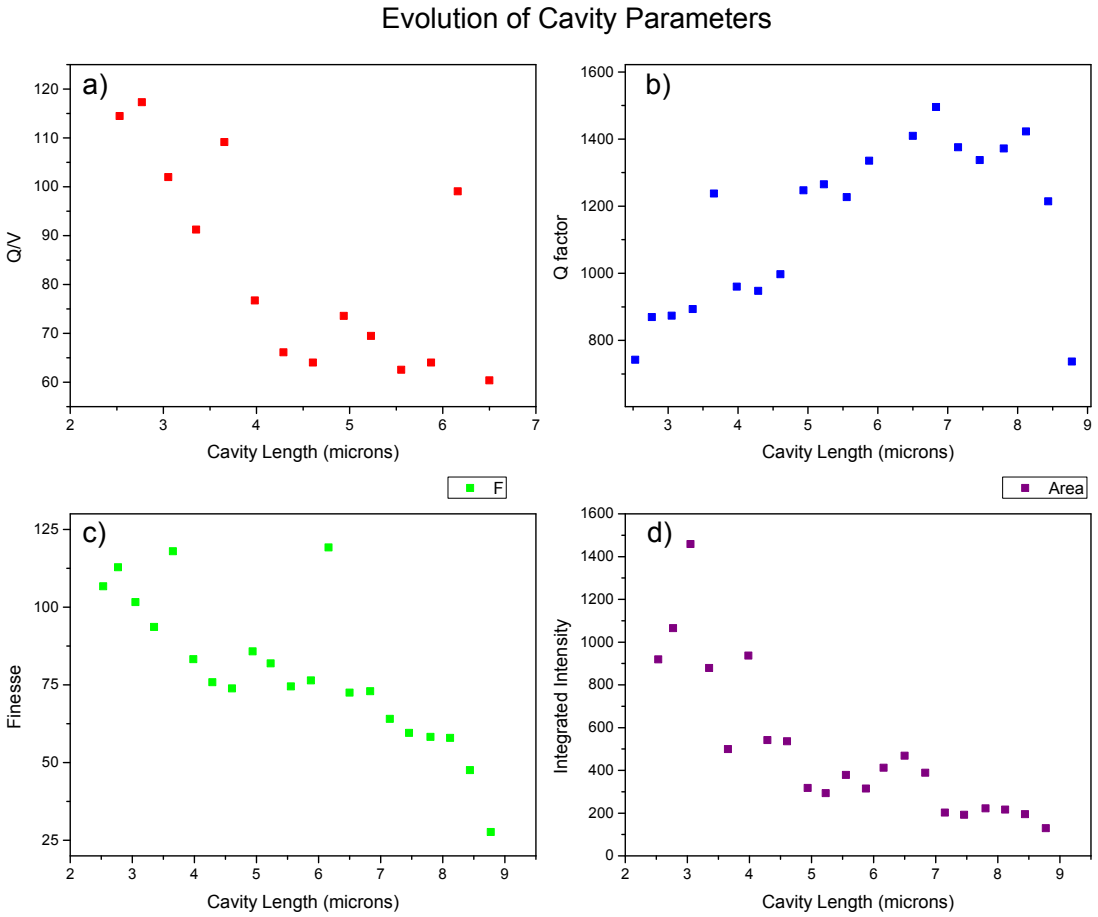

FIGURE 7.7: Evolution of the key cavity parameters, with cavity length, extracted from figure 7.6. a) Q/V ratio b) Q-factor c) Finesse d) Integrated intensity into the fundamental mode

7.1.4 Summary

In summary, the first results of the low-temperature cavity coupling to the ZPL of a single NV centre have been discussed. These results have been presented together as they were obtained from the same experimental run, and clearly show the capabilities of this system in the low temperature and narrow emitter environment. The on-resonant coupling of the ZPL with a mode number q=6 has been demonstrated, along with a implementation of the tuning across ZPL. This alone is significant for cavity QED as it represents the first time these low temperature coupling experiments have been achieved on single colour centres, without the requirement for technically demanding tuning processes. At the same time it has been demonstrated that large subset of the cavity parameter space can be explored through altering the mirror separation and coupling to the ZPL over 21 longitudinal mode indices was observed. The change in cavity linewidth over this range highlights the possibility that the open-cavity system can be a platform for investigating the good-bad emitter regime transition. All resonances in these experiments were shown to be of Lorentzian lineshape, indicating a good stability to a first approximation. The intra-cavity stability is an important criterion that must be demonstrated and is an area in which the monolithic resonator structures have a natural advantage.

Subsequent to these preliminary results, several developments were made to the experimental method, before the next low temperature experiments. These are summarised as:

- Acquisition of a 633-647nm band-pass filter: Lifetime and HBT measurements
- Implementation of piezo scanning: Optimal ZPL coupling
- Featured Mirror with 20-pair DBR coating [Laseroptik]: Improved Photon Collection

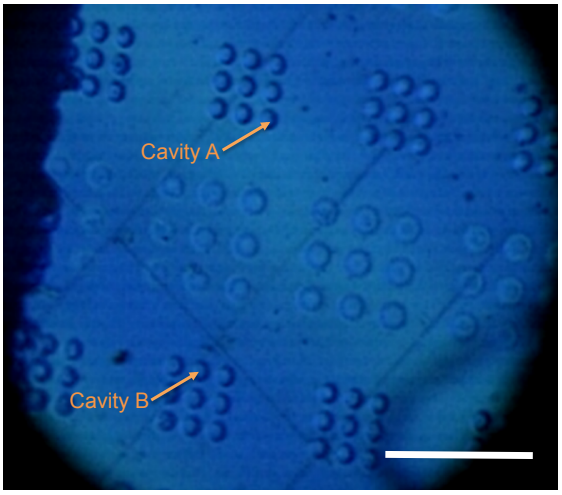

FIGURE 7.8: White light transmission image of the featured substrate with 20 pair DBR [Laseroptik], seen through the planar substrate during the low temperature cavity experiment. The substrates are almost in contact. The plinth contains 3x3 clusters of $\beta = 25\mu$m, & 7μm. The registration grid of the planar substrate can also be seen. The cavities A, B used in each stage of this investigation are indicated. The scale bar denotes 50μm. The arrows indicated the direction of the fringes as the cavity is closed

7.2 Main Cavity ZPL Coupling Results

The following results presented were aided by the developments made to the experimental set-up as outlined above. Here the mirror pair configuration is planar[10]:concave[20] with a calculated $\mathcal{F} = 2664$, a factor of 1.5 greater than the configuration in the previous section. This substrate has cavities with $\beta = 25\mu$m, & 7μm only. Hence, only the β=7μm cavities are used in the following investigation to achieve the smallest mode volumes possible. All the subsequent data is obtained with NV2. A further distinction is made between between two stages of the experiment. Figure 7.8 outlines cavity A used at the first stage, which was initially chosen as having the best compromise between being central in the field of view and close to the edge of the plinth. In the final stage, NV2 was taken to cavity B, this time away from the central region, which could achieve shorter cavity lengths.

7.2.1 7μm cavity A

A longitudinal mode of $q = 5$ is shown coupled to the ZPL of NV2 in figure 7.9. The spectra are taken at 0.13nm resolution with a 120s integration time and a laser power

of 1.25mW. These spectra are far superior to that in figure 7.1, especially since a lower excitation power and integration time are currently used. The peak intensity here is greater by a factor of nearly 7. Clearly the benefits of a highly reflective featured mirror and the improved tuning precision are of benefit. An out of cavity spectrum is also shown in figure 7.9a for comparison. In both cases the excitation power is chosen to be at $P_{opt} = P_{sat}$, such that the excitation conditions are identical in and out of the cavity. A direct comparison can thus be made. The cavity coupled peak intensity is greater by a factor of 5.5. Neither spectrum has been background corrected. Figure 7.9b, displays the same spectrum over a larger range to 850nm. The mirror background fluorescence outside of the stop band can be seen here, emphasising the dominance of the cavity coupled peak.

Putting a 640±7nm bandpass filter, isolates the cavity coupled ZPL, allowing for saturation measurements into the ZPL, along with an HBT. This is compared to the out of cavity HBT in 7.10. For the cavity coupled measurement the mode is coupled optimally to peak 3 in the ZPL helping to isolate the contribution of the second emitter at peak 1. Single photon emission into the cavity mode is verified with $g^{(2)}(0) = 0.28$ in the measurement. This is a key result and is the first time the single photon emission into an open-cavity coupled ZPL has been demonstrated at low temperature. This can serve as a foundation for entanglement protocols, amongst other solid state photonic quantum technologies. As usual, neither spectrum has been corrected for the contribution of the mirror background fluorescence.

Table 7.1 summarises the experimental conditions in the HBT measurements. The in-cavity HBT was driven at the saturation power P_{sat}. This was to be able to obtain a reasonable total count rate of 4600c/s, whilst minimising the metastable shelving rate to ensure a good resolution of the anti-correlation dip. With such a low count rate an acquisition time of 2 hours was found to be necessary accumulate sufficient co-incidence counts. The out of cavity HBT was taken at $0.5P_{sat}$, as the total count rates were 32,500c/s due to the large collection bandwidth. A long, 44 minute, acquisition time was used to curtail measurement noise. It is clear that there is a pronounced bunching effect

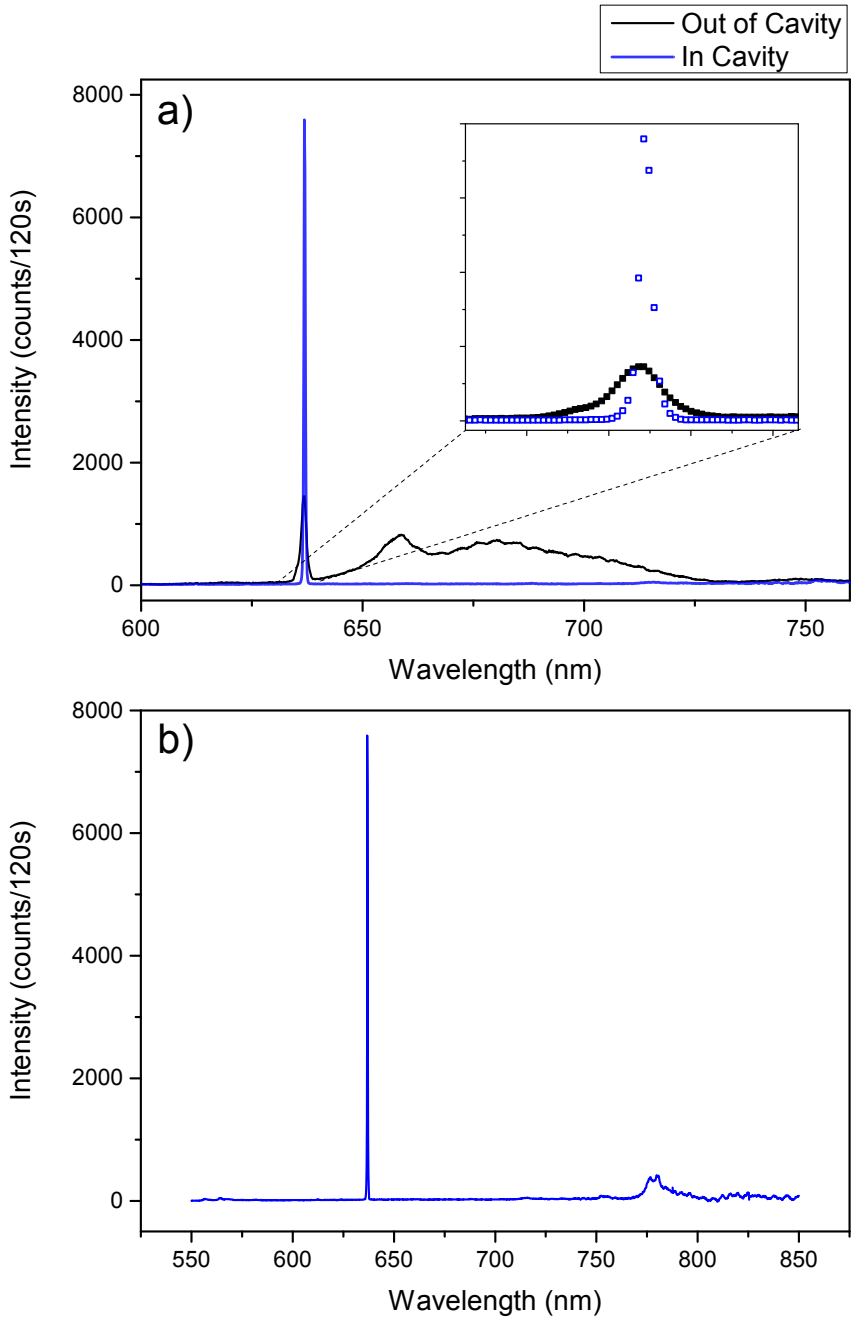

FIGURE 7.9: Cavity coupled spectra. No background correction has been applied. a) PL spectrum of cavity mode q=5 coupled to the ZPL of NV2 (blue). Spectra are taken at 0.2nm resolution with 120s integration under P_{opt}=P_{sat}=1.25mW excitation conditions. An out of cavity spectrum of NV2 is shown for comparison. Here P_{opt}=P_{sat}=1.05mW, for the same integration time. The ZPL region in detailed inset. b) Identical in-cavity PL spectrum. The spectral window here has been extended to 850nm to incorporate the mirror background fluorescence, emphasising the dominance of the cavity coupled peak.

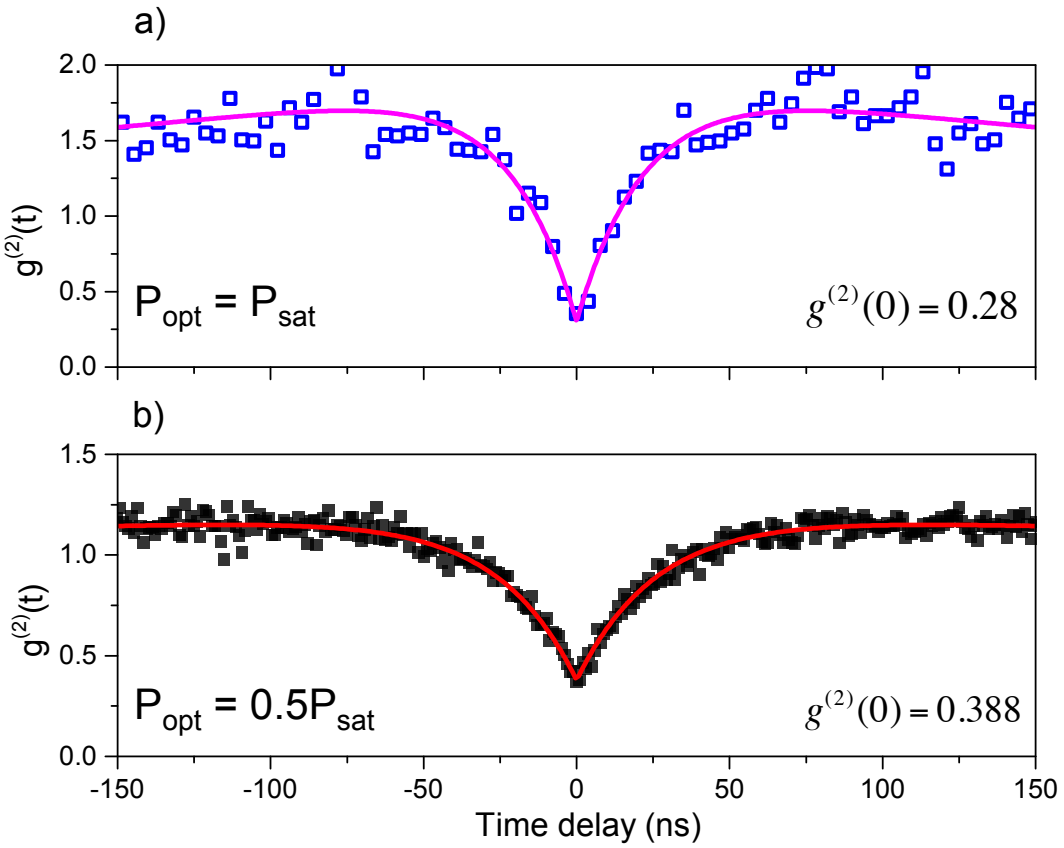

FIGURE 7.10: HBT measurements of NV2 in and out of the cavity at low temperature. a) HBT on the cavity coupled ZPL, taken in the spectral window 633-647nm. b) The out of cavity HBT taken in the spectral window 650-810nm. The solid lines indicate a fit of the data points to the equation 3.53. The value of $g^{(2)}(0)$ from the fit is shown inset. The excitation conditions for each measurement are indicated in the figure

in the cavity relative to the free space measurement, as expected from the higher driving power. Comparatively similar signal to noise ratios are obtained in each measurement. Due to the lower count rate, the estimated errors on the SNR measurement are larger in the cavity. The error propagates to the expected value of $g^{(2)}(0) = 0.32\pm0.06$ for a single emitter, calculated from equation 4.4. The measured value of $g^{(2)}(0) = 0.28$ matches the single emitter limit within error. By selectively coupling to peak 3, the cavity mode is sufficiently detuned from peak 1 to reject the emission from this second emitter, leading to a reduced $g^{(2)}(0)$ value for the cavity coupled ZPL.

TABLE 7.1: HBT parameters

	Laser Power (P_{sat})	SNR	Expected $g^{(2)}(0)$	Measured $g^{(2)}(0)$
Out of Cavity	$0.5P_{sat}$	4.9±0.02	0.31±0.004	0.388
In Cavity	P_{sat}	4.65±0.31	0.32±0.06	0.28

TABLE 7.2: HBT fit parameters

	τ_2(ns)	τ_3(ns)	c_1	c_2
Out of Cavity	26.1±0.7	412±17	-0.8	0.2
In Cavity	21.8±2.8	284±51	-1.5	0.8

Table 7.2 displays the fit parameters from the HBT measurements in figure 7.10. The metastable shelving rate τ_3 is larger in cavity, as anticipated from the higher pumping rate. In the low power limit the $\tau_2 = \tau_{\text{rad}}$ and the Purcell factor could possibly be derived from a power dependent HBT analysis. However the fitting error on the in cavity parameters are relatively large due to measurement noise, thus a decision was made against such an investigation and PL lifetime measurements are anticipated to provide a more robust measurement of τ_{rad}

7.2.2 7μm cavity B

To attain a shorter cavity length, NV2 was positioned at cavity B as in figure 7.8. The spectrum is shown in figure 7.11, with $q = 4$ coupling to the ZPL. The FSR is large enough such that it cannot accurately be determined from the observed spectrum. The cavity was closed further as seen in the black spectrum such that both longitudinal modes can be seen. The cavity length L=2.49μm represents the shortest optical cavity length attained in this experimental run, corresponding to a FSR of 89nm and a smallest mode volume of $V = 5\lambda^3$, an improvement on cavity A.

With the longitudinal mode in the vicinity of the ZPL, the cavity is blue-tuned across the resonance as shown in figure 7.12. Here the piezo scanning is implemented, and the precision with which the cavity mode can be manipulated supersedes those which have been shown previously. The piezo is extended using increments of 0.03V applied by the external voltage source. This actuates the cavity position by an average of 0.132nm, as determined from fitting the first 6 spectra of the sequence, with the cavity mode initially coupled to the PSB. The tuning spectra have been compressed in figure 7.12a, with the colour scale manipulated such that the transverse mode structure can be seen tuning in line with the longitudinal mode. Higher order modes can be seen at 680nm & 695nm,

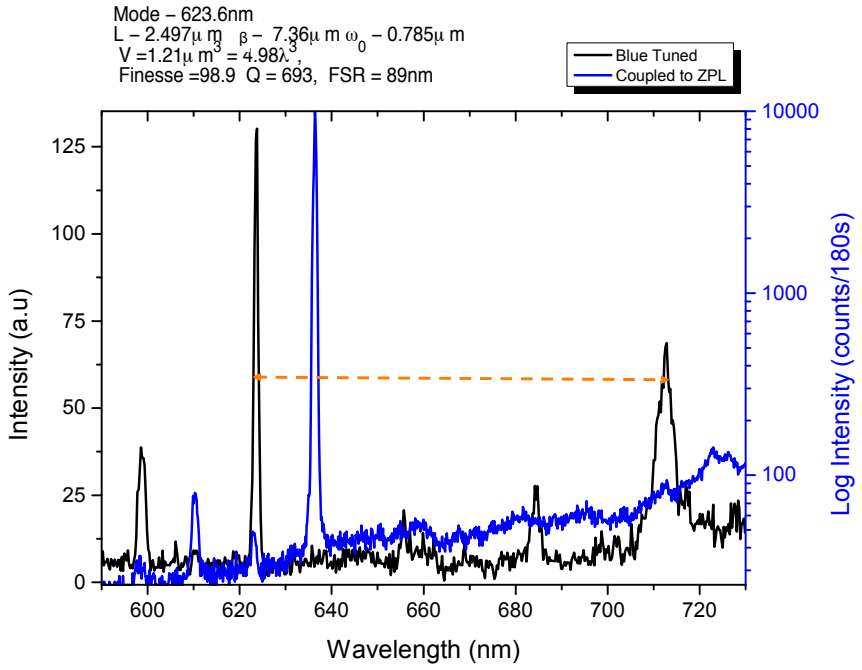

FIGURE 7.11: Cavity coupled spectra of q=4 coupled to the ZPL (blue), which is shown on a log-intensity scale. The cavity was closed further to observe the next longitudinal mode (black). The FSR is denoted by the orange arrow

corresponding to the next longitudinal mode index. On normalising the colour scale in figure 7.12b, It can be seen how the cavity coupled ZPL dominates the emission into the stop-band of the mirrors. There is no significant emission from the PSB. With the cavity mode initially off resonant at 638.4nm, the peak intensity is seen to be 330counts. This increases by a factor of 29 when optimally coupled to peak 3 at 636.4nm. This is better illustrated in the surface plot of the same tuning spectra in 7.12c.

To better resolve the coupling to the individual ZPL peaks the high resolution (0.03nm) grating is used. The initial cavity mode detuned from the PSB max is shown below in figure 7.13. It is clear from the fit that it is well reproduced by a Gaussian line shape. This is in contrast to the first low temperature experimental data discussed in section 7.1, where cavity modes with Lorenztian lineshapes were readily observed. This is a clear indication that there is a degree of structural instability in this experimental run leading to a broadening of the resonance. This has significant implications for the theoretical analysis of these results as disused in section 7.3.3. The FWHM of the peak is 0.92nm. This fitted peak is plotted in relation to the individual fitted Gaussian peaks

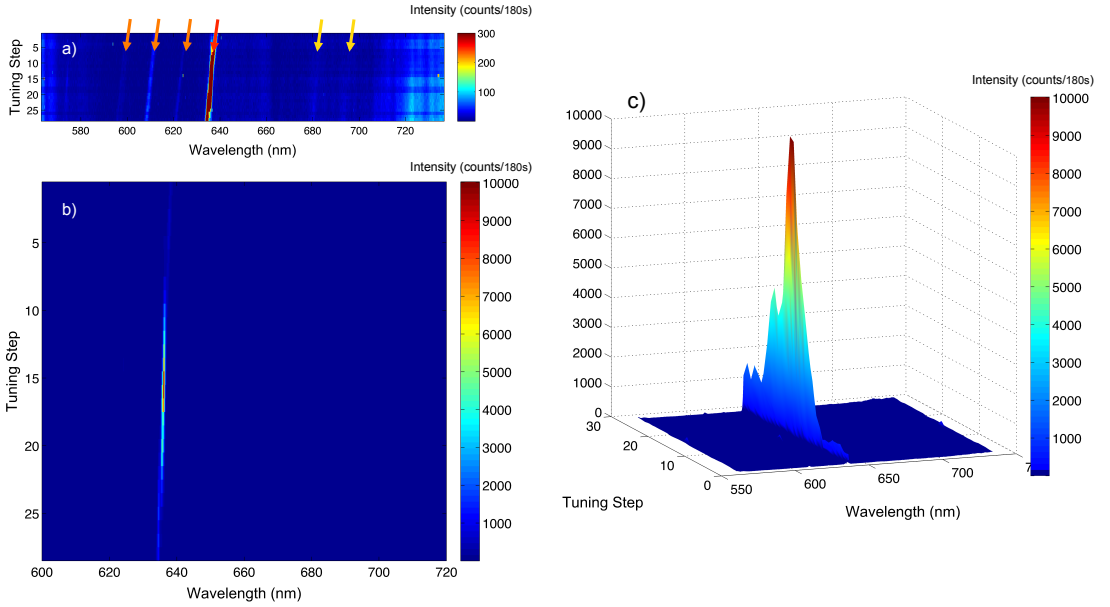

FIGURE 7.12: Tuning of the cavity mode across the ZPL of NV2, taken with the low resolution grating of the spectrometer. The laser power used in this data set is 2.3mW. a) Compressed plot of tuning data with adjusted colour scale to highlight the mode structure within the stop-band. The longitudinal mode coupling to the ZPL is indicated by the red arrow, with the higher-order mode shown in orange. Transverse modes from the next longitudinal mode index are shown in yellow. b) Normal colour scale - highlighting the dominant emission of the cavity coupled ZPL mode in the stop band. c) 3D surface plot, illustrating the peak intensity when coupled to the ZPL.

of the NV2 ZPL. The cavity mode is almost twice that of the ZPL resonances.

Figure 7.14 shows the tuning of the same cavity mode across the ZPL of NV2 taken with the high resolution grating. The coupling to each of the individual peaks 2 & 3 can now be resolved. The coupling to peak 4 is not clear due to its proximity to peaks 3 along with the broad cavity linewidth.

The tuning spectra here demonstrate one of the compelling advantages of the open cavity system. Both blue and red wavelength tuning can be reversibly achieved in a relatively simple manner by adjusting the substrate separation in-stiu. Of course such a capability currently requires a macroscopic apparatus around the cavities such as the 3-axis piezo stack. However despite the elegance of this process, it is still necessary to demonstrate the enhancement of the light-matter interaction, to prove that this system is competitive with others in the field.

The saturation counts on the cavity coupled ZPL are presented in figure 7.15a,b as

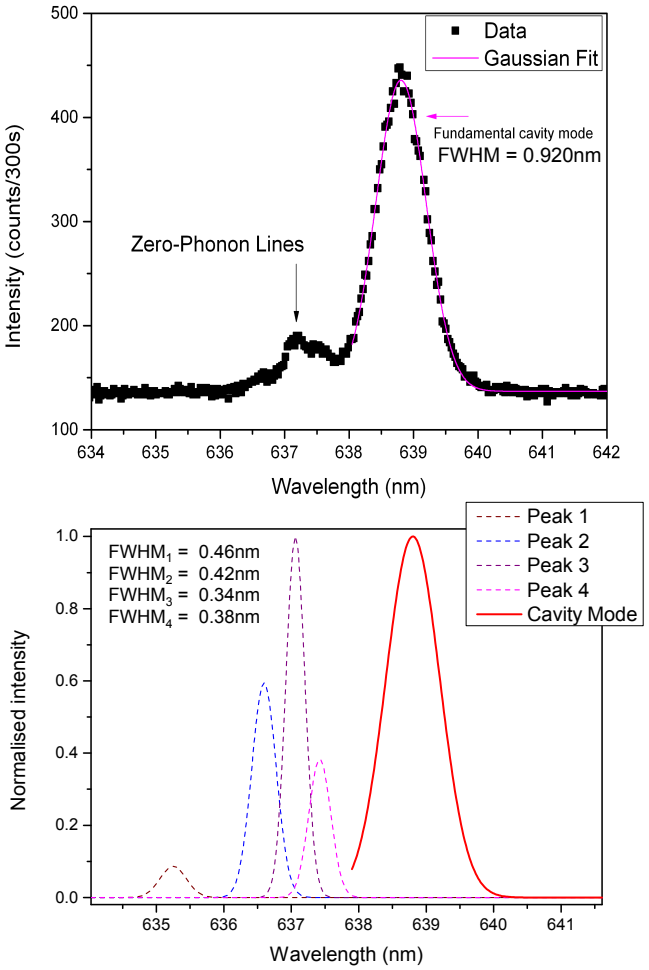

FIGURE 7.13: Detuned cavity mode prior to ZPL coupling. Above: The data points of the cavity mode are fit with a Gaussian function with a 0.92nm FWHM. The vicinity of the ZPL of NV2 are indicated. Below: Fitted Gaussian of the detuned cavity mode (solid line), plotted in comparison with the individual peak fits for the ZPL of NV2 (dashed line). The peak height has been normalised for comparison. The relative peak heights of the individual ZPL peaks have been maintained.

a function of increasing longitudinal mode index. A clear scaling is seen with mode number. The maximum saturation counts into the ZPL is shown to be 15,100c/s. The decreasing linewidth of the cavity mode is also demonstrated in figure 7.15c,d as the Q-factor of the open-cavity increases. Both the q=4 and q=7 modes are fit by a Gaussian lineshape.

Finally, the enhancement of the light matter interaction is demonstrated in figure 7.16. This represents the key experimental result of this thesis. PL lifetimes as shown for the out-of-cavity emission and the $q = 4$ coupled ZPL at 77K. The lifetime changes from

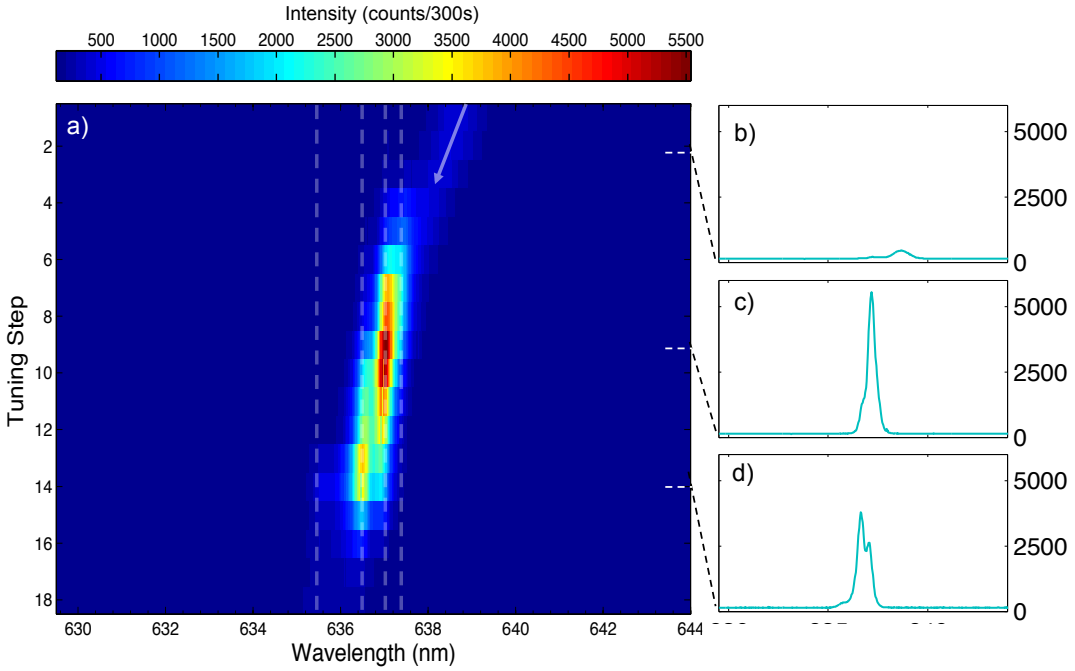

FIGURE 7.14: a) 2D plot of the high resolution tuning spectra taken with a 0.03nm spectral resolution. A 5 minute integration time was used for each of the 18 spectra taken. A piezo step size of 0.03V was again used here. The dashed lines indicate the location of peaks 1-4. The arrow represents the position of the cavity mode as it is blue tuned across the ZPL. Individual spectra are shown on the right for the case of b) detuned c) peak 3 resonant d) peak 2 resonant

30.8±0.6ns to 22.1±0.4ns showing a clear enhancement of the PL decay rate corresponding to an increase of 39.5±0.7% due to the Purcell effect. As further robust evidence of the Purcell effect, the PL lifetime is shown to have an explicit dependence on the cavity mode volume in figure 7.17, with cavity modes q = 4-7 tuned to the ZPL in succession. The discussion of these results will take place in the following section.

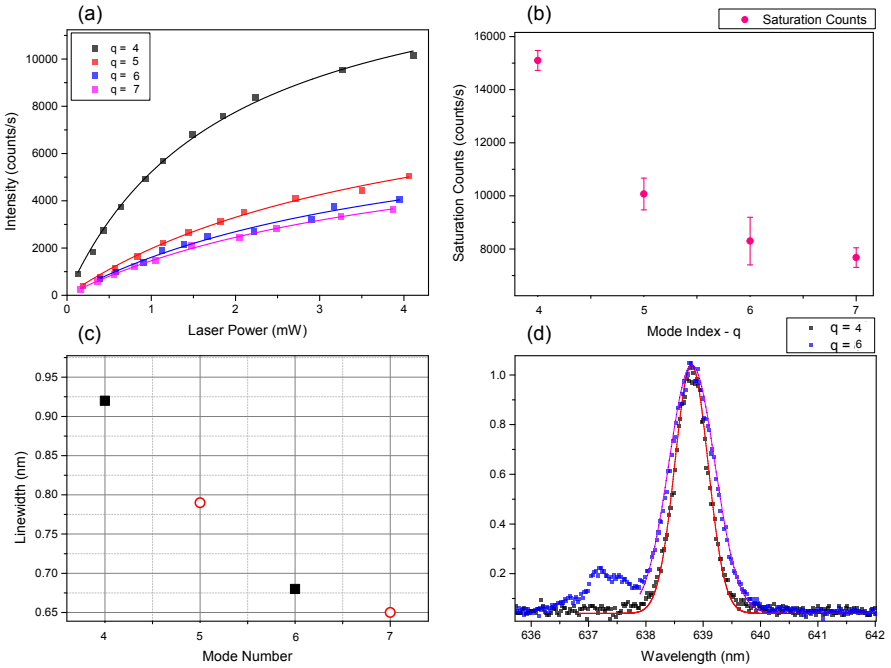

FIGURE 7.15: (a) The power saturation curves for the ZPL emitting in the cavity mode as a function of longitudinal mode index. The saturation values are shown in (b), with the errors arising from the standard error of the fit. (c) The cavity mode FWHM as measured by detuning the resonance towards the PSB at 639nm as shown in (d). The black squares correspond to the experimental data for q=4,6. No comparable data sets were available for q=5,7 and these were calculated from the $\mathcal{F}$=89 shown in figure 7.11.

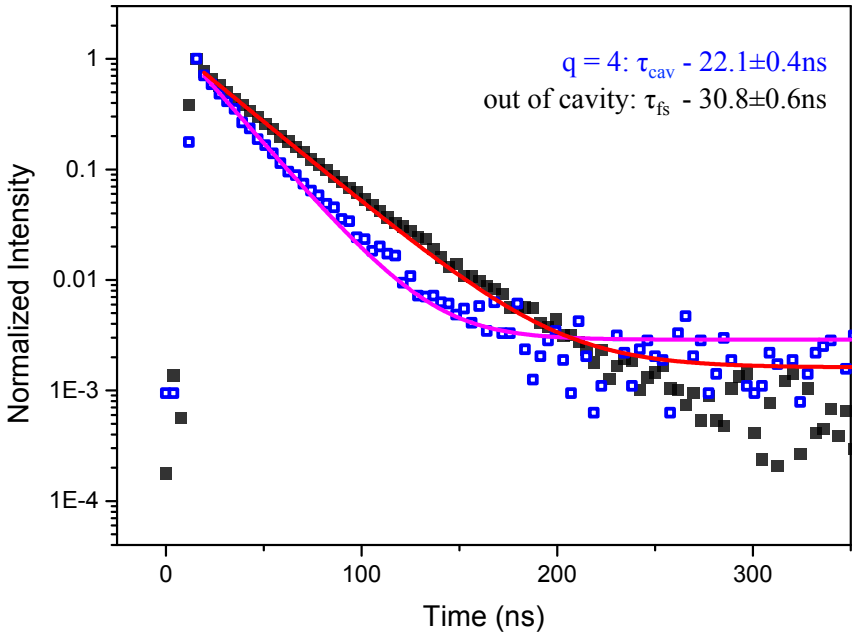

FIGURE 7.16: A comparison between the in and out of cavity PL decay curve. The in-cavity measurement corresponds to the q=4 mode coupled to the ZPL of NV2 taken in the spectral window between 633-647nm. The out of cavity decay was taken with NV2 on the planar mirror in the 670-810nm spectral window. The clearly demonstrates the Purcell enhancement of the NV centre

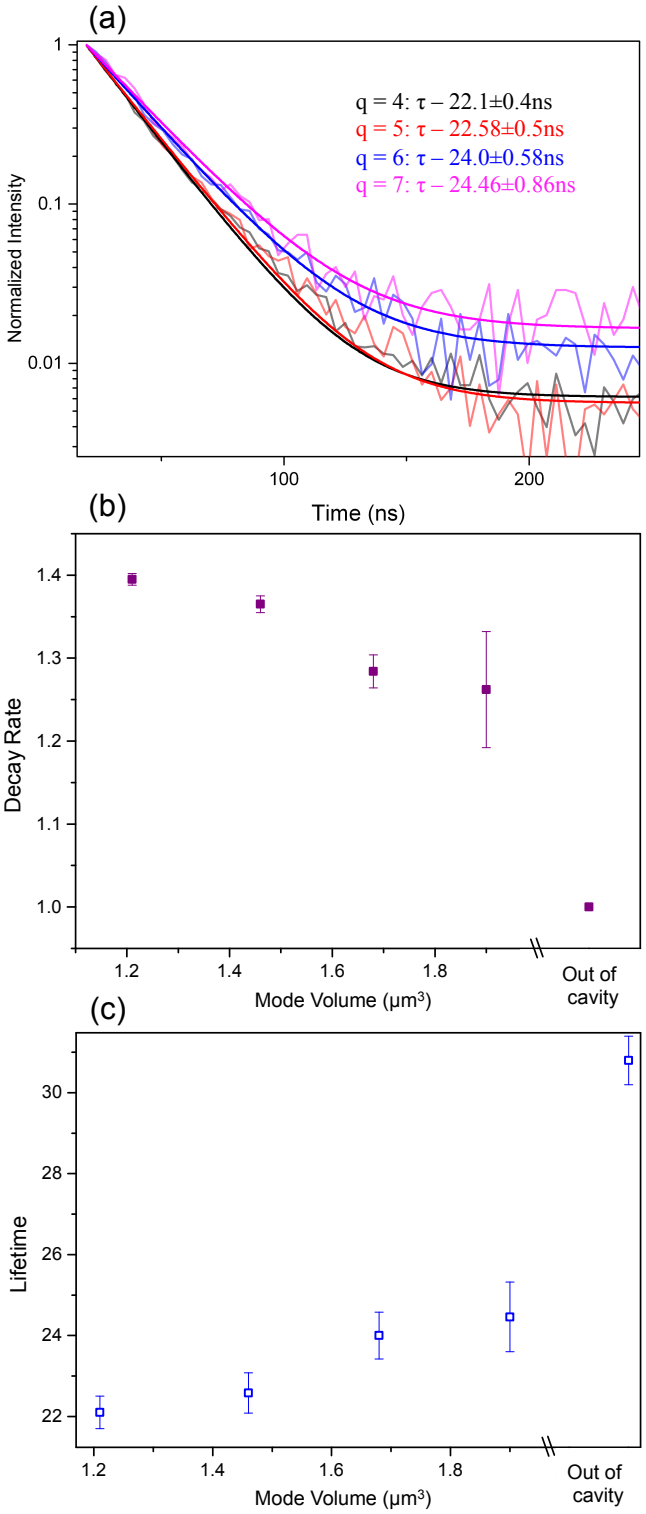

FIGURE 7.17: (a) PL decay curves of the cavity mode coupled to the ZPL for q=4-7. (b) The enhanced spontaneous emission rate into the cavity mode as a function of mode volume. (c) The values of the decay constant τ_{cav}. The out of cavity lifetime is shown for comparison

7.2.3 Summary

The data presented in this section form the central results of this thesis. A comprehensive range of cavity coupling experiments have been demonstrated culminating in the observation of the enhanced decay rate when coupled to the ZPL, with the mode volume dependence additionally shown. This is an unambiguous effect of the enhanced light-matter interaction. Along with the controlled tuning of the cavity resonance through the ZPL, this data merits a more in-depth discussion where comparisons to theory are made.

7.3 Discussion

Two approaches are necessary in this discussion, which focuses entirely on the observed decay rate enhancements when coupling to the ZPL. Firstly there will be a determination of the Purcell factor on the ZPL by analytic means, related to the generalised Purcell factor outlined in section 3.2. The second approach is to use FDTD to simulate the the emission into the cavity. This allows for the full optical density of states surrounding the emitter and any off-resonant suppression to be quantified, as well as a more accurate determination of the geometrical parameters of the cavity. The analytic treatment was developed in collaboration with theoreticians from Institut NEEL, Grenoble, namely Thomas Grange, Gaston Hornecker and Alexia Auffeves. The FDTD Simulations were conducted by Jason Smith and Philip Dolan.

7.3.1 Analytic Treatment

The initial treatment makes an assumption that the emitter and cavity linewidths are *homogeneously* broadened. It will then be seen that the effect of the inhomogeneously broadened cavity mode (see figure 7.15), will need to be introduced as a development of this simple model. First seen in equation 3.44, the Purcell factor as a function of detuning can be expressed in terms of λ as:

$$F_{\mu}(\lambda) = \xi_{\mu} F^{\max} \frac{1}{1 + 4Q_{\text{cav}}^2 \left(\lambda/\lambda_{\text{cav}} - 1\right)^2} \tag{7.1}$$

Here the label μ will refer to the particular ZPL peak in figure 7.18. $F^{\max}$ is the Purcell factor at perfect resonance and optimal spatial alignment as in equation 3.46. The spatial orientation factor is $\xi_{\mu} = \left(\frac{|\mu.\mathcal{E}|}{|\mu||\mathcal{E}_{\max}|}\right)^2$, includes both the relative angle, θ between the electric dipole to the cavity field, and the spatial position relative to the electric field maximum. It has been shown in section 5.3, that the emitter can be optimally placed within the maximum of the electric field in the cavity by changing the relative lateral alignment of the mirror substrates. The same alignment process is applied to the single

emitters in these measurements. Therefore the assumption is made that $\mathcal{E} = \mathcal{E}_{\max}$ and $\xi_\mu = \cos^2(\theta)$ in this analysis. The angle of the dipoles to the plane of the mirror were calculated by polarisation measurements of NV2 in section 6.2.2.1, and determined to be 39° and 24°, for peaks 2 & 3 respectively. The final term denotes the deviation from $F^{\max}$ away from λ_{cav}.

The modified emission rate of the ZPL, F_{ZPL}, will be given by a convolution of the normalised emitter spectrum $S_\mu(\lambda)$ and Purcell factor across the cavity resonance, $F_\mu(\lambda)$ as:

$$F_{\text{ZPL}} = \sum_\mu n_\mu \int d\lambda S_\mu(\lambda) F_\mu(\lambda) \tag{7.2}$$

The terms $S_\mu(\lambda)$ incorporate the Debye-Waller factor, determined from the out-of cavity emission spectrum to be $\zeta = 0.044$.

With rapid thermalisation between the orbital doublets of the ZPL, the time averaged population ratio between peaks 2 and 3 is 0.8:1 due to the 347GHz energy splitting. The relative populations are therefore given by, the factors $n_2 = 0.44$ and $n_3 = 0.56$. As the cavity is resonantly coupled to peak 3, it is necessary to include the contribution from peak 2, due to its proximity and the large cavity linewidth, $\delta\lambda_{\text{cav}}$, shown schematically in figure 7.18.

It must be noted here that $S_\mu(\lambda)$ is the emission spectrum of each peak over all directions, which is required by definition. The spectrum emitted along the cavity axis is defined as:

$$S_{\text{axial}}(\lambda) = \frac{\sum_\mu n_\mu \xi_\mu S_\mu(\lambda)}{\sum_\mu n_\mu \xi_\mu} \tag{7.3}$$

The modified emission rate into the cavity is finally:

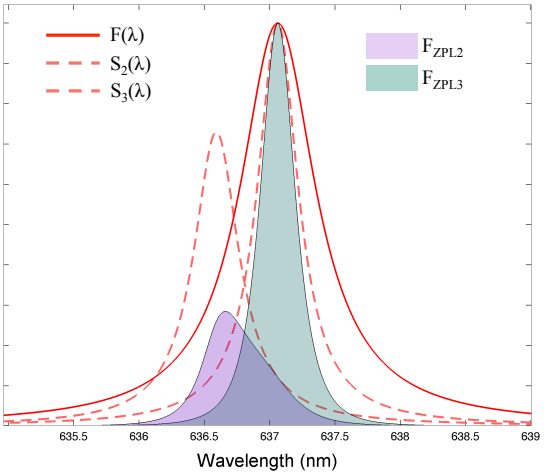

FIGURE 7.18: A schematic of the analytic calculation in equation 7.2. The homogeneously broadened cavity mode $\delta\lambda_{\text{cav}} = 0.7\text{nm}$ (red line) is optically coupled peak 3, $S_3(\lambda)$. There will be some coupling to peak 2 and the individual convolutions between the cavity and the emitter peaks are shown by the shaded areas $F_{\text{ZPL1,2}}$

$$F_{\text{ZPL}} = F^{\max}\left[\sum_{\mu} n_\mu \xi_\mu\right] \int d\lambda \frac{1}{1 + 4Q_{\text{cav}}^2 \left(\lambda/\lambda_{\text{cav}} - 1\right)^2} S_{\text{axial}}(\lambda) \tag{7.4}$$

The high-resolution tuning simulation data in figure 7.14 are best fit with a Lorentzian cavity linewidth of 0.7nm according to.

$$S_{\text{cav}}(\lambda) \propto \frac{S_{\text{axial}}(\lambda)}{1 + 4Q_{\text{cav}}^2 \left(\lambda/\lambda_{\text{cav}} - 1\right)^2} \tag{7.5}$$

A linear scaling factor is applied to the fitting function, $S_{\text{cav}}(\lambda)$, to match the experimental intensities. The fits to the data are observed in figure 7.19. With a cavity linewidth of 0.7nm, the emission rate into the cavity mode is found to be $F_{\text{ZPL}} = 0.25$. The total emission rate is then $F_{\text{tot}} = 1.21$. Accounting for $\zeta = 0.044$ and $n_3 = 0.56$, the Purcell factor acting on peak 3 alone is $\text{F}_{\text{P,3}} = 7.8$. However this picture is not complete and the effects of the off resonant PSB suppression still needs to be quantified.

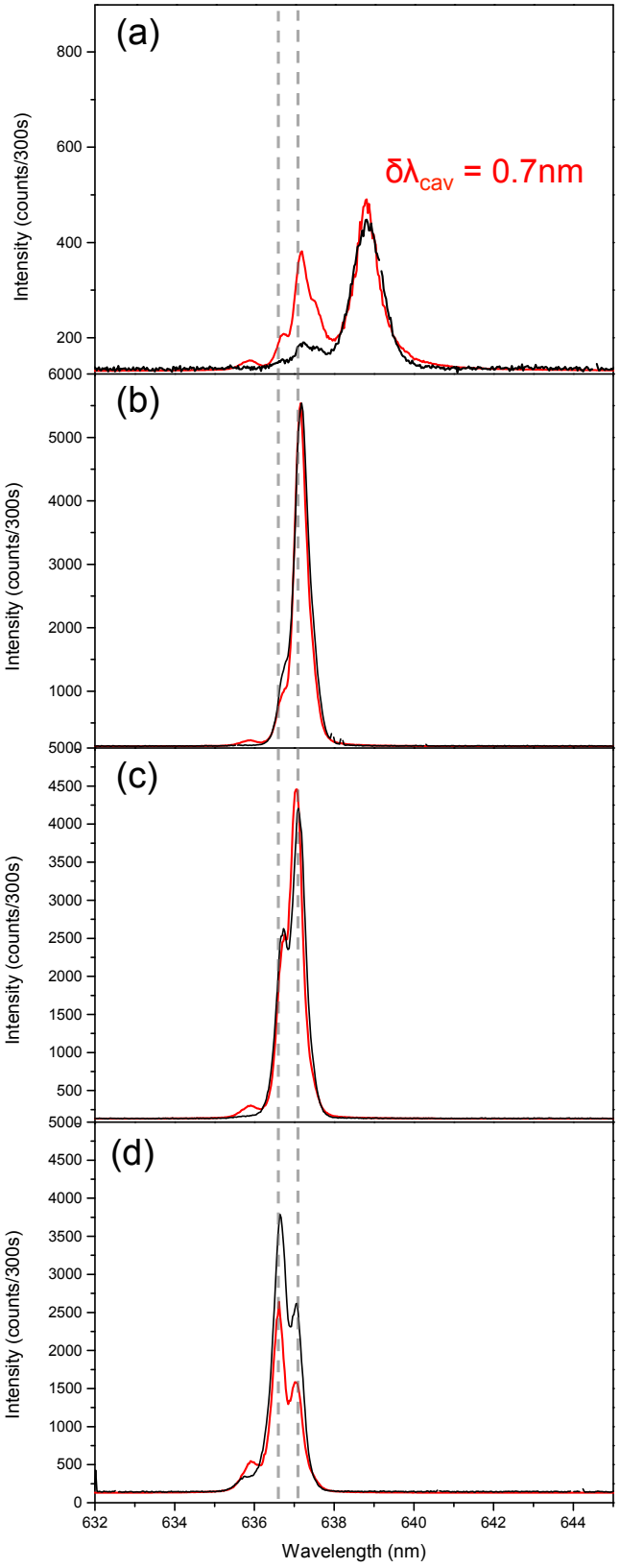

FIGURE 7.19: Simulations (red) of the tuning spectra (black) of the q=4 cavity mode across the ZPL of NV2 from figure 7.13 for selected scans 1 (a), 10(b), 12(c) and 14(d). The data points are best fitted using equation 7.5, with a cavity linewidth of $\delta\lambda_{\text{cav}}$=0.7, which justifies it's use in this analysis. The same scaling factor is applied to all simulated curves, in order to match the experimental intensities.

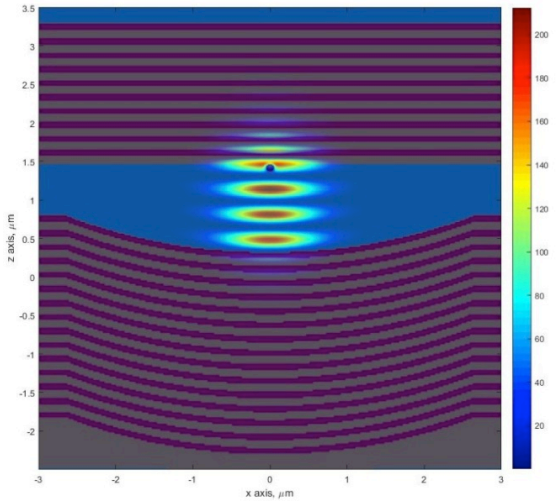

FIGURE 7.20: A 2D section of the electric field intensity along the cavity axis with q=4 between the substrates. The planar mirror has 10 DBR pairs (n=1.52(grey)/2.1(purple)) with an additional low index termination. The concave mirror is simulated to have 15 DBR pairs rather than the 20 pairs actually used. This decreased the calculation time without compromising the results.

7.3.2 Finite-Difference Time-Domain Simulations

The analytical expressions here are unable to quantify the modified emission rate into the PSB. The free spectral range is sufficiently large and the optical density of states will be much reduced at these frequencies, leading to some suppression of the PSB emission. For longer cavity lengths there will be PSB coupling into cavity modes as more resonances are permitted within the stop band. The FDTD method (described in section 4.9.1) will be able to fully account for this.

Two separate simulations were run for the NV dipoles at 24° and 39° to the mirror plane respectively. The dipole sources were placed 20nm from the planar mirror surface within the 100nm ND. The dipoles are given a broad spectral profile to span the whole mirror stop-band. The simulations were run for both the case of the half-cavity (emitter on the planar mirror) and the cavity coupled case. The software is able to monitor the total power emitted by the dipole as a function of wavelength. The Purcell factor is then simply the ratio of the optical power emitted in each case. Figure 7.21a shows the experimental spectrum for q=5 coupled to the ZPL. The FDTD simulation of the Purcell factor experienced by the dipole is shown in figure 7.21b. The experimental spectrum

is well reproduced with a cavity $\beta = 7.6\mu$m, which is within 4% of the $\beta = 7.9\mu$m value calculated from the analytic expression in figure 7.11. Coupling into additional longitudinal and transverse modes is also observed. Since the simulated dipole is placed on the cavity axis, there is no coupling into transverse modes of odd-indices as there is no component of the electric field on axis. The absence of such modes from the experimental spectrum suggests that the dipole is indeed well placed on the cavity axis and thus the assumption that $\mathcal{E} = \mathcal{E}_{\text{max}}$ is justified.

To obtain the total in-cavity emitted power density, in spectrum 7.21c, the Purcell factor is multiplied by the full normalised, half-cavity, emission spectrum of NV2. Finally to quantify enhancement or suppression of the PSB, spectrum 7.21c is integrated between 640-740nm.

For the smallest cavity length with $q = 4$, the suppression of the PSB emission is calculated to be 6%, as $F^{\text{P}}_{\text{PSB}} = 0.93$. The values for $F^{\text{P}}_{\text{PSB}}$ and $F^{\text{P}}_{\text{ZPL}}$ are summarised in figure 7.22. The total emission rate into the cavity, including both the ZPL rate and the suppression of the PSB is $F_{\text{tot}} = F_{\text{ZPL}} + F_{\text{PSB}} = 1.14$. which gives a more complete picture and shows that the current analysis underestimates the observed cavity rate of 1.39 (shown previously in figure 7.17b) .

7.3.3 Inhomogeneous Broadening

Clearly a development on the theoretical picture is required. With the mode coupled to the ZPL, the intensity in the cavity after a single emission event will have the usual exponentially decaying dependence on time as:

$$I(t) = Ae^{-\gamma_{\text{cav}}t} \tag{7.6}$$

Where γ_{cav} is the decay rate into the cavity mode, with A being the amplitude of the decay function. The fraction of light emitted into the cavity mode, defined as the $\mathcal{B}$

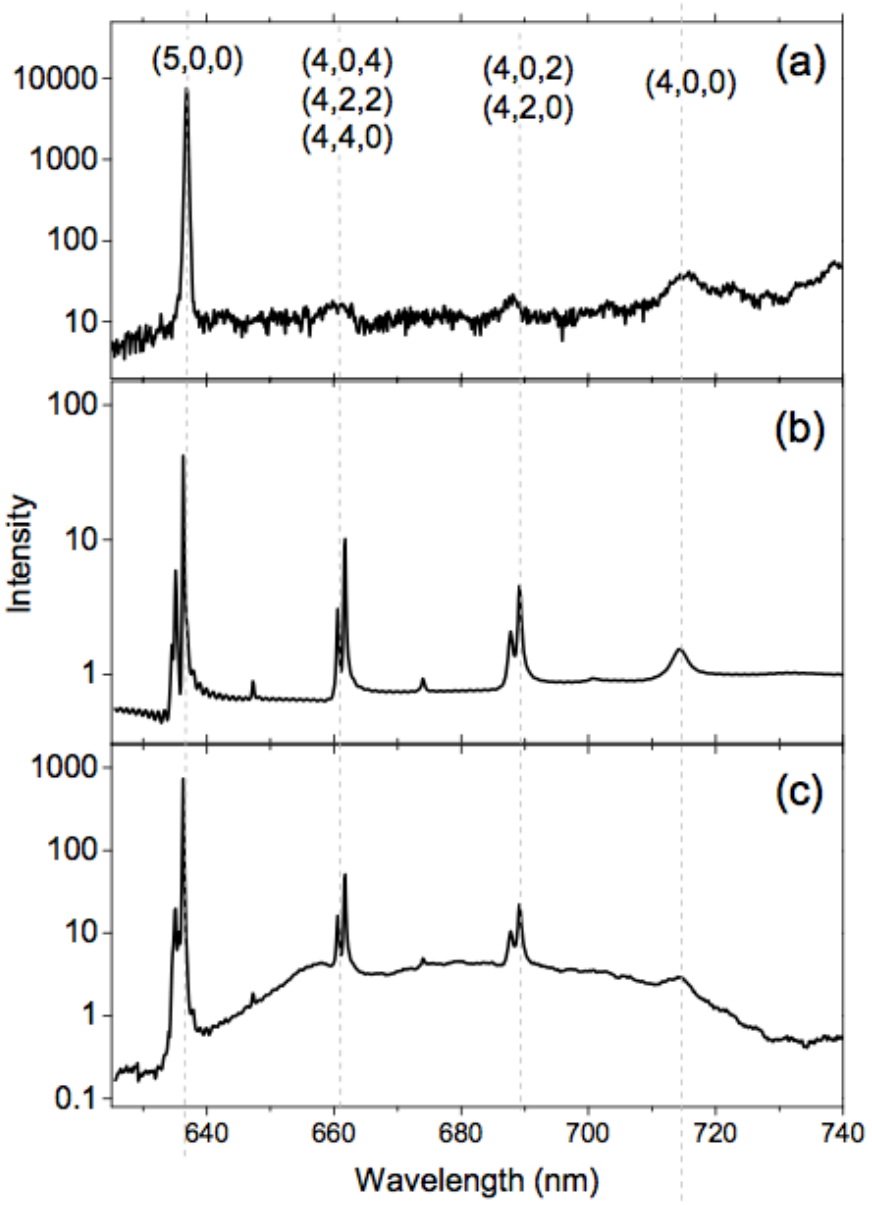

FIGURE 7.21: Experimental spectra and FDTD simulations of the Purcell factor and emitted power density, plotted on a log-linear axis. (a) The experimental spectrum for mode index q=5 coupled to the ZPL (peak 3) of the NV centre at 77K (b) FDTD output of the Purcell factor as a function of wavelength for a broadband dipole (described in text). The mode structure qualitatively reproduces the experimental spectrum, with a cavity $\beta = 7.6\mu$m. (c) The semi-empirical emitted power density spectrum. The vertical lines are a guide to the eye, representing the mode indices (q, m, n) shown

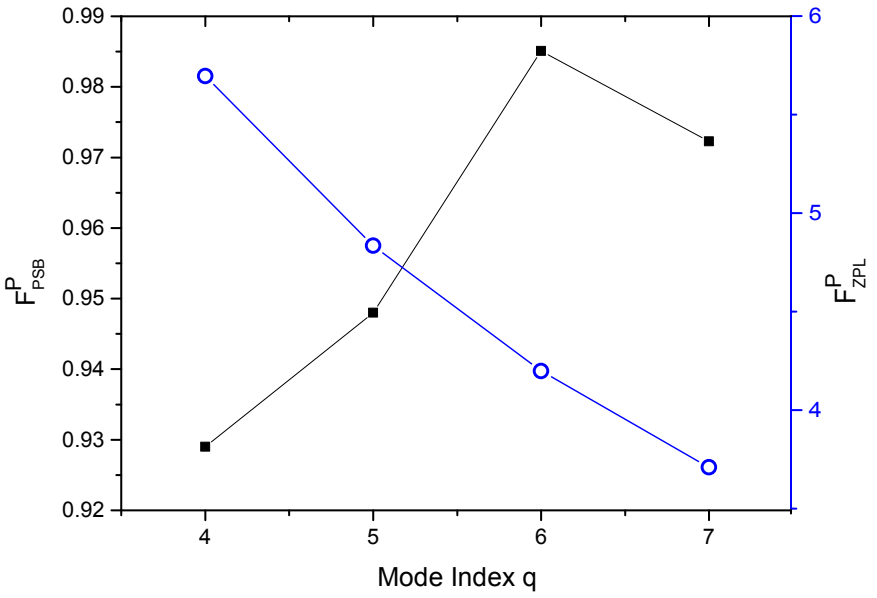

FIGURE 7.22: Summary of $F^{\mathrm{P}}_{\mathrm{PSB}}$ (black squares) as a function of mode index calculated from the FDTD simulations. The analytic calculations from equation 7.4 for the Purcell factor on the on the ZPL emission $F^{\mathrm{P}}_{\mathrm{ZPL}}$ (after accounting for $\zeta = 0.044$) are also summarised (blue circles).

factor, will be proportional to the integral of this intensity over the full emission decay as:

$$\mathcal{B} = \frac{F_{\mathrm{ZPL}}}{1 + F_{\mathrm{ZPL}}} \propto \frac{A}{\gamma_{\mathrm{cav}}} \tag{7.7}$$

Where F_{ZPL} was defined in equation 7.4 to incorporate the Debye-Waller factor of the ZPL. For a stationary cavity mode, the Purcell factor will of course remain constant. However it was seen in figure 7.15 that the cavity mode has undergone inhomogeneous broadening due to the mechanical instability of the cavity apparatus in this experimental run. This will clearly affect the dynamics of the emission rate into the cavity, as the cavity mode rapidly detunes from the ZPL over the course of a lifetime measurement.

This picture assumes that the detuning of the cavity mode occurs on timescales less than the spontaneous emission rate ($\approx 10^7$Hz). With mechanical instability likely caused by acoustic vibrations ($<\approx 10^4$Hz), this is a reasonable assumption [91]. The detuning only occurs within the envelope of the Gaussian profile, which defines the probability distribution of the cavity position. The homogeneously broadened cavity mode is therefore

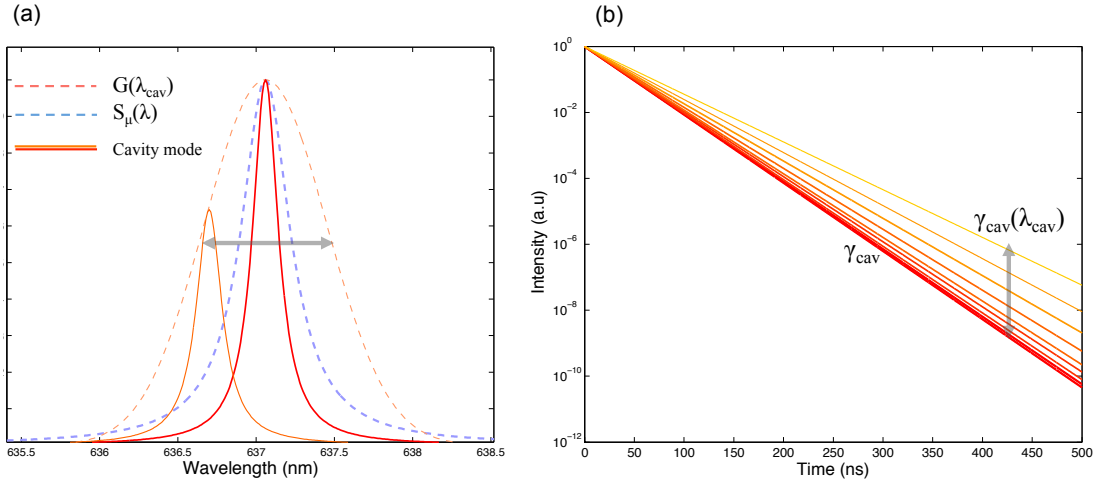

FIGURE 7.23: (a) Schematic of the inhomogenously broadened cavity mode detuning across the emitter linewidth $S_\mu(\lambda)$. The homogenous cavity mode (red - optimally coupled, orange - detuned) with $\delta\lambda_{\text{cav}} = 0.2$nm, sweeps out a Gaussian profile with $G(\lambda_{\text{cav}})$ of 0.5nm FWHM. (b) The decay rate into the cavity mode. When optimally coupled the fast decay rate is γ_{cav} (red line). Detuning introduces a spectral dependence to the decay rate $\gamma_{\text{cav}}(\lambda_{\text{cav}})$, however the greatest contributions will be from near resonant alignment.

likely to have a linewidth less than the previously defined $\delta\lambda_{\text{cav}} < 0.7nm$, which in turn would lead to an increase in Q_{eff}, dominated by near resonant cavity detuning.

This introduces as spectral dependence on the emission rate into the cavity. The total intensity is then given by the average over these positions:

$$I(t) = \int G(\lambda_{\text{cav}}) A(\lambda_{\text{cav}}) e^{-\gamma_{\text{cav}}(\lambda_{\text{cav}})t} d\lambda_{\text{cav}} \tag{7.8}$$

Where the cavity mode has been has been convolved with the Gaussian lineshape, $G(\lambda_{\text{cav}})$ and integrated over the spectral range λ_{cav}. The decay rate of the intensity due to inhomogeneous broadening of the cavity mode, γ_{inhom}, is now given as:

$$\gamma_{\text{inhom}} = -\frac{dI}{Idt}\bigg|_{t=0} = \frac{\int d\lambda_{\text{cav}}\ G(\lambda_{\text{cav}})\gamma^2_{\text{cav}}(\lambda_{\text{cav}})\mathcal{B}(\lambda_{\text{cav}})}{\int d\lambda_{\text{cav}}\ G(\lambda_{\text{cav}})\gamma_{\text{cav}}(\lambda_{\text{cav}})\mathcal{B}(\lambda_{\text{cav}})} \tag{7.9}$$

Since $A(\lambda_{\text{cav}}) \propto \mathcal{B}(\lambda_{\text{cav}})\gamma_{\text{cav}}(\lambda_{\text{cav}})$. Remembering that the decay rate into the cavity is related to the Purcell factor acting only on the ZPL by $\gamma_{\text{cav}} = 1 + F_{\text{ZPL}}(\lambda_{\text{cav}})$, The emission rate into the inhomogenously broadened cavity mode can now be defined:

$$F_{\mathrm{ZPL,inhom}} = \frac{\int d\lambda_{\mathrm{cav}}\ G(\lambda_{\mathrm{cav}})(1 + F_{\mathrm{ZPL}}(\lambda_{\mathrm{cav}}))F_{\mathrm{ZPL}}(\lambda_{\mathrm{cav}})}{\int d\lambda_{\mathrm{cav}}\ G(\lambda_{\mathrm{cav}})F_{\mathrm{ZPL}}(\lambda_{\mathrm{cav}})} \tag{7.10}$$

Where a substitution for $\mathcal{B}(\lambda_{\mathrm{cav}}) = F_{\mathrm{ZPL}}(\lambda_{\mathrm{cav}})/(1 + F_{\mathrm{ZPL}}(\lambda_{\mathrm{cav}}))$ has been made. The cavity linewidth is set to $\delta\lambda_{\mathrm{cav}} = 0.2$ nm, which is observed in stable transmission measurements on similar cavities. With an additional inhomogeneous broadening of 0.5 nm, this yields $F_{\mathrm{ZPL,inhom}} = 0.364$. With the inclusion of the PSB suppression, $F_{\mathrm{tot}} = 1.25$. This is a better match to the observed value of $F_{\mathrm{tot}} = 1.39$, however it is still apparent that further developments will be required in the analysis.

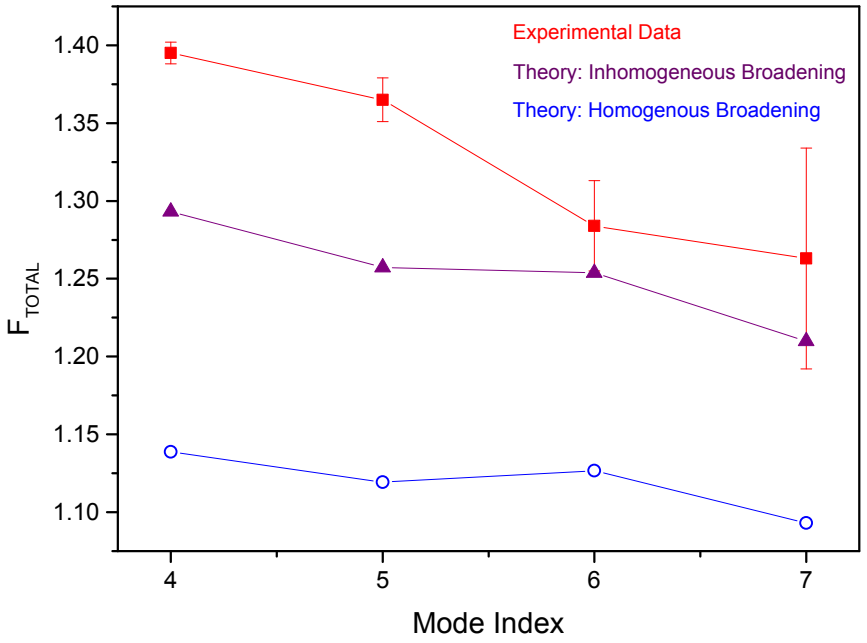

FIGURE 7.24: Theoretical prediction of the total increase in emission rate in the context of the experimental data set (red). The errors on the measured decay rate arise the lifetime fitting procedure. The theoretical predictions assuming a homogeneously broadened cavity mode (blue) are found to underestimate the total enhancement. On the incorporation of the inhomogeneous broadening of the cavity mode into the mode (purple), an improvement is made on this picture.

7.3.4 Summary

The results of the two analyses can be seen with a comparison to the experimental data in figure 7.24. There is a better overall match to the experimental data on the incorporation of the inhomogeneous broadening of the cavity mode into the theoretical model, indicating that the analysis is heading in the right direction however there is still an consistent underestimation of the observed decay rate. The picture may be completed by including the effects of the inhomogeneously broadened ZPL. It was seen from the out of cavity spectra that the measured ZPLs took a Gaussian profile, where the FWHMs were over a factor of 5 greater than the value expected at 77K for NV centres in bulk diamond. Inputting $\delta\lambda_{\mathrm{cav}} = 0.2$ and an emitter line of $\delta\lambda_{\mathrm{em}} = 0.07$nm (77K) in equation 7.1, yields $F_{\mathrm{P},3} = 33.6$ for peak 3 and the total emission rate increase as $F_{\mathrm{tot}} = 1.71$. This gives an indication of the potential improvements in the theoretical model. The Purcell factors (corresponding to $F_{\mathrm{P},3}$) for a dipole oriented at $\theta = 24^{\circ}$ to the plane are summarised in figure 7.25 as a function of emitter and cavity linewidth.

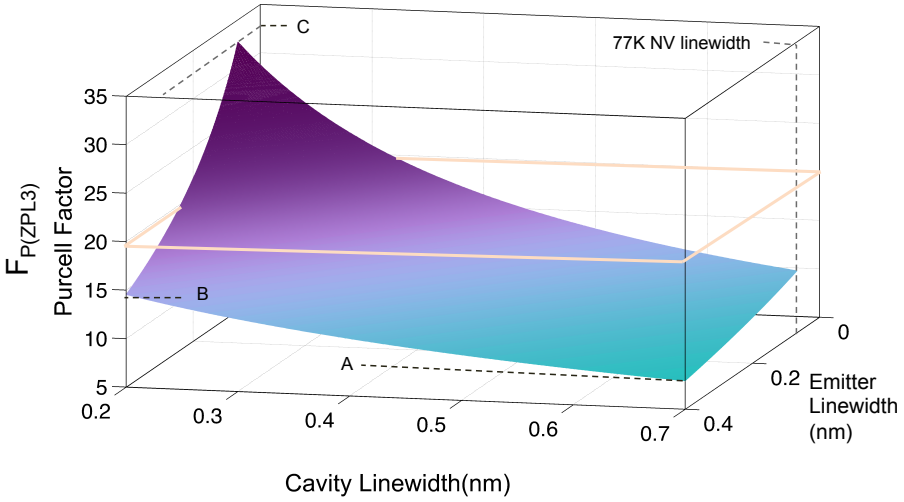

FIGURE 7.25: Summary of cavity-coupling parameter space for an emitter at θ=24° to the electric field, coupling to V=1.24μm^3. The Purcell factor as a function of cavity and emitter in width is represented by the surface plot. A: $\delta\lambda_{\text{cav}} = 0.7$nm, $\delta\lambda_{\text{em}} = 0.4$nm. B: $\delta\lambda_{\text{cav}} = 0.2$nm, $\delta\lambda_{\text{em}} = 0.4$nm. C: $\delta\lambda_{\text{cav}} = 0.2$nm, $\delta\lambda_{\text{em}} = 0.07$nm. The plane bounded by the orange line represents the measurement.

The regimes for all the analyses in this discussion can be seen in the figure. The orange plane represents $F_{\text{P,3}} = 20.1$, estimated from the measured value F_{tot} 1.39 and accounting for ζ= 0.044 and $n_3 = 0.56$. Point A corresponds to $F_{\text{P,3}} = 7.8$, which was first calculated for both emitter and cavity homogeneous broadening in section 7.3.1. B indicates the resonant alignment of $\delta\lambda_{\text{cav}} = 0.2$nm, with $\delta\lambda_{\text{em}} = 0.4$nm. This highlights maximum enhancement that could be achieved in the discussion of section 7.3.3. The overall emission rate into the cavity will be reduced from this maximum as the mode detunes from the emitter, however the near-resonant alignment should dominate. Finally point C shows the theoretical maximum in this discussion, on the incorporation of $\delta\lambda_{\text{em}} = 0.07$nm for the ZPL at 77K. As previously stated, this figure is designed to visualise the parameter space in which the system may be operating. It demonstrates that there is potential for a more complete description if the natural linewidth of the emitter is included. The caveat to this statement is that there is an open question as to whether the NV centres hosted in nanodiamond are subject to a greater degree pure dephasing (γ^*) through electron-phonon scattering, as the size and quality of the crystal is reduced. This would lead to greater line widths than in the bulk crystal.

Chapter 8

Conclusions & Outlook

This section will firstly summarise the key experimental results, before considering the future prospects for this work. The coupling of NV centres to an open-cavity system has been demonstrated. The experimental configuration of the cavity mirrors was shown, mounted on a piezo apparatus specifically designed for low temperature operation. The initial experiments were conducted at room temperature, coupling bright fluorescent nanodiamonds with ensembles of NV centres. A determination of the coupling procedure was enabled by these emitters, facilitating the imaging and relocation of the NVs prior to cavity coupling. The NVs showed strong emission into the cavity modes with the mirror radius $\beta = 10\mu$m. The configuration allowed for a direct comparison of the in-cavity and free space emission. After a consideration of the collection efficiencies in both cases, the small mode volumes allowed a Purcell factor of 3% to be determined when coupling to the PSB emission in the bad emitter regime of CQED. A scaling with mode volume was also shown with a reasonable fit to the data. One of the key aspects of the open-cavity is the direct access of the emitter to the electric field maximum on the planar mirror. To illustrate this point, the $\beta = 10\mu$m cavity mirror was laterally tuned across the emitter. The NV fluorescence was seen emitting into the fundamental TEM_{00} and higher order $\mathrm{TEM}_{m+n>1}$ Hermite-Gauss modes which were mapped out as a function of position. The intensity distributions were well matched to theory.

The central aim of this project was the coupling of single NV centres to the open-cavity at low temperature. A protocol for the sample preparation and isolation of single NV centres in nanodiamond was established. A selective thermal etching process was employed, based on the work of Osswald et al [52]. A materials investigation into this process was conducted using thermogravimetric analysis, Raman spectroscopy and dynamic light scattering. Once the optimal procedure was determined, there was a much improved sample performance. Optical spectroscopy of nandiamond highlighted the regular identification of single centres, showing good single photon emission. The low temperature ZPLs all showed inhomogeneous broadening at 77K, with an average FWHM of 0.49nm, 5 times greater than the literature values for NV in bulk diamond. There was great variety in ZPL spectral locations, with strain splitting of the excited state doublet also common. The out of cavity lifetimes were also determined. Particular prominence was given to NV4 & NV2, for which the low temperature cavity results were achieved. A novel method for the determination of the NV defect orientation was presented, utilising the strain split ZPL doublet, which is of consequence to the Purcell factor.

Finally, the low temperature cavity coupling of single NV centres was achieved. The preliminary results with NV4 showed tuning of the cavity through the narrowed ZPL, as well as the coupling of consecutive mode indices by opening the cavity. Developments in the experimental procedure allowed a more comprehensive range of experiments to be conducted. Single photon emission from the cavity coupled ZPL was then verified by an HBT measurement. Implementation of an external voltage source for the piezos allowed a precise positioning of the cavity mode, and a controlled tuning across the ZPL. The saturation counts into the cavity mode were measured to be 15,100c/s. Lifetime measurements showed a 39% enhancement into the cavity coupled ZPL, with an explicit mode volume dependence also demonstrated. This result forms the highlight of this thesis.

A comparison to theory was made, using a combination of the analytic expressions for the generalised Purcell factor on the ZPL and FDTD simulations to quantify the Purcell

suppression of the PSB. It was shown that simply using the measured linewidths of the emitter and cavity were not sufficient to replicate the observed enhancements. From the experimental data it was clear that the cavity mode was inhomogeneously broadened, through mechanical instability of the system. On accounting for this, there was an improvement in the model. The inhomogeneous broadening of the emitter is thought to account for the remaining discrepancy.

It is clear that the spectral drift in of NV in nanodiamond, combined with the mechanical instability of the low temperature cavity set-up is a major limiting factor in the analysis of these results. This reduces the potential for sophisticated theoretical treatments of the emitter-cavity coupling process. The first step will be to achieve stable cavity modes at low temperature. A passive stabilisation is possible through better shielding of the dewar from the environment and a more robust mounting of the top mirror substrate. In the limit of high-finesse it will become necessary to provide an active cavity locking process whereby a reference cavity mode is monitored in conjunction with a piezo-feedback mechanism.

Nanodiamonds fabricated by HPHT methods have been used exclusively, as these are easily incorporated within the open-cavity geometry. Their observed spectral properties are clearly undesirable. The coupling of NVs in bulk would require the preparation of diamond membranes. Certainly a top-down fabrication may be possible, as demonstrated by work on PCC cavities, which have been successful in thinning 5μm films down to 200nm membranes prior to PCC fabrication [58]. Additionally, this allows a greater control over the starting material. Using low nitrogen content, type IIa, films has been shown to reduce observed spectral drift [28]. It has been seen throughout the course of these experiments, the finesse observed has been much lower than the theoretical value, most likely due to scattering from the nanodiamond crystal. Diamond membranes will offer a better optical surface quality [57].

The smallest mode volume achieved here was $V = 1.24\mu\text{m}^3 \approx 5(\frac{\lambda}{\text{n}})^3$, with $q = 4$ antinodes between the mirror. There is scope for a reduction in cavity length, currently limited by the alignment of the mirror substrates at low temperature. The incorporation of piezos

with angular degrees of freedom would allow for the optimisation of the cavity alignment in-situ.

In the context of remote entanglement protocols, (outlined in chapter 1), the optical microcavity will be of enormous benefit in the generation of indistinguishable photons. Firstly through enhanced photon collection. Secondly through enhancement of the fraction of light emanating from the ZPL ($\mathcal{B}$). With the same enhancement applied on 2 remote NV centres, the entanglement generation rate increases by $(\mathcal{B}/\zeta)^2$ [59]. Finally a Purcell enhanced transition line will undergo lifetime broadening, serving to mask the effects of spectral drift and increasing efficiency still further. It is expected that with the developments outlined, the NV open-cavity system may soon demonstrate enhancements that are competitive with some best systems outlined in chapter 1, making them strong candidates for the spin-photon interfaces required in distributed QIP.

The potential of the NV open-cavity system has been shown here for the first time at low temperature. The deterministic placement of the emitter within the cavity mode and in-situ optimisation of the cavity detuning from the ZPL are potentially of great benefit in the scalability of future quantum photonic technologies.

Appendix A

Determining NV Centre Orientation

The NV has an arbitrary rotation as shown in figure A.1. Peaks 2 and 3 in figure A.2 will be treated as coming from the strain split Ex and Ey dipoles of the same NV centre, which dominate the emission. The polarisation plots for peaks 2 and 3 are shown in figure A.3, corresponding to the projections of these dipoles onto the plane of the mirror.

What is known from the sum of the polarisation plots of peaks 2 and 3, is the polar angle of rotation a as in the equation below.

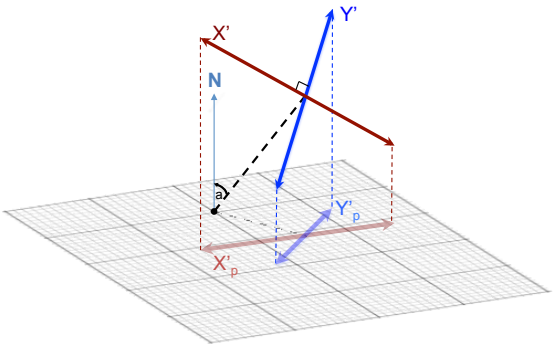

FIGURE A.1: NV centre, with an arbitrary orientation. The NV defect axis is represented by the black dashed line, with two orthogonal electric dipoles X' and Y'. The polarisation measurement is sensitive to the projections of these dipoles onto the plane of the mirror, X'_p and Y'_p

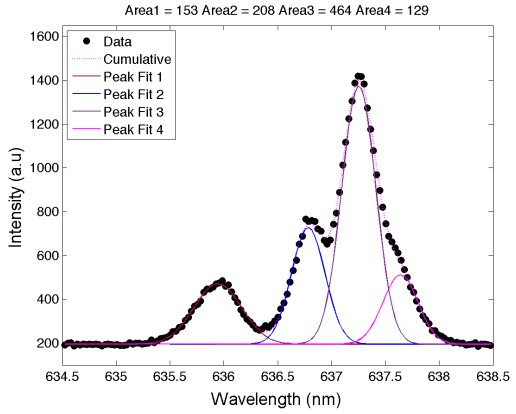

FIGURE A.2: Spectrum of the ZPL's of NV2 with the polarisation analyser rotated to 90°, with Gaussian fits to the individual lines shown. Areas of each individual peak are indicated above the figure

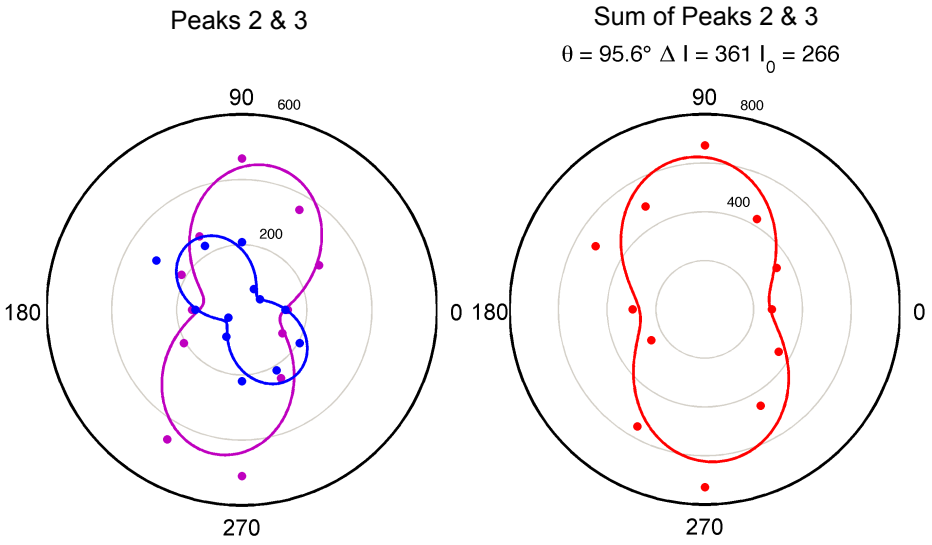

FIGURE A.3: Left: Polar plots of peaks 2 & 3. Right: Polar plot of the sum of peaks 2 & 3. The solid lines are fits to the function $I = I_0 + \Delta I \cos^2(\phi_p + \theta)$

$$I_{\min} = I_0 \cos^2(a) \tag{A.1}$$

$$a = \cos^{-1} \sqrt{\frac{I_{\min}}{I_0}} \tag{A.2}$$

From the measurement the ratio R of the intensities of the X'_p and Y'_p projected dipoles is known. Remembering that $I \propto E^2$:

$$R = \frac{Y_p'^2}{X_p'^2} \tag{A.3}$$

What *is not* known is the rotation of the NV about it's defect axis b. The strategy is to find the relationship between these angles and the projection of the dipoles onto the plane. Knowing a and the ratio R between the dipoles allows b to be found.

A.1 Generating Rotation

To generate any arbitrary rotation, the staring vectors X, Y & Z correspond to the E_x, E_y & the NV axis respectively as in figure A.1.

$$X = \begin{pmatrix} 1 \\ 0 \\ 0 \end{pmatrix}, Y = \begin{pmatrix} 0 \\ 1 \\ 0 \end{pmatrix}, Z = \begin{pmatrix} 0 \\ 0 \\ 1 \end{pmatrix}$$

Using the rotation matrix R_z the NV defect is rotated through angle b, about the z axis. The rotation matrix R_x then 'tips' the defect through polar angle, a, about about the x axis.

$$R_x(a) = \begin{pmatrix} 1 & 0 & 0 \\ 0 & \cos(a) & -\sin(a) \\ 0 & \sin(a) & \cos(a) \end{pmatrix}, \tag{A.4}$$

$$R_z(b) = \begin{pmatrix} \cos(b) & -\sin(b) & 0 \\ \sin(b) & \cos(b) & 0 \\ 0 & 0 & 1 \end{pmatrix} \tag{A.5}$$

Combining these matrices gives the total rotation $R_{tot}(a, b)$ that will act on these vectors:

$$R_{tot}(a,b) = R_x(a)R_z(b) = \begin{pmatrix} \cos(b) & -\sin(b) & 0 \\ \cos(a)\sin(b) & \cos(a)\cos(b) & -\sin(a) \\ \sin(a)\sin(b) & \sin(a)\cos(b) & \cos(a) \end{pmatrix} \tag{A.6}$$

This is now applied to X

$$R_{tot}(a,b)X = X' \tag{A.7}$$

$$\begin{pmatrix} \cos(b) & -\sin(b) & 0 \\ \cos(a)\sin(b) & \cos(a)\cos(b) & -\sin(a) \\ \sin(a)\sin(b) & \sin(a)\cos(b) & \cos(a) \end{pmatrix} \begin{pmatrix} 1 \\ 0 \\ 0 \end{pmatrix} = \begin{pmatrix} \cos(b) \\ \cos(a)\sin(b) \\ \sin(a)\sin(b) \end{pmatrix} \tag{A.8}$$

To find the projection onto the xy plane, the third element in the vector is set to 0

$$X'_p = \begin{pmatrix} \cos(b) \\ \cos(a)\sin(b) \\ 0 \end{pmatrix} \tag{A.9}$$

Now the magnitude of the projected dipole vector is squared, since $I \propto E^2$.

$$X'^2_p = \begin{pmatrix} \cos(b) & \cos(a)\sin(b) & 0 \end{pmatrix} \begin{pmatrix} \cos(b) \\ \cos(a)\sin(b) \\ 0 \end{pmatrix} = \cos^2(b) + \cos^2(a)\sin^2(b) \tag{A.10}$$

Which simplifies to

$$X'^2_p = 1 - \sin^2(a)\sin^2(b) \tag{A.11}$$

Similarly for the Y'_p dipole

$$Y'^2_p = \sin^2(a)\sin^2(b) - \sin^2(a) + 1 \tag{A.12}$$

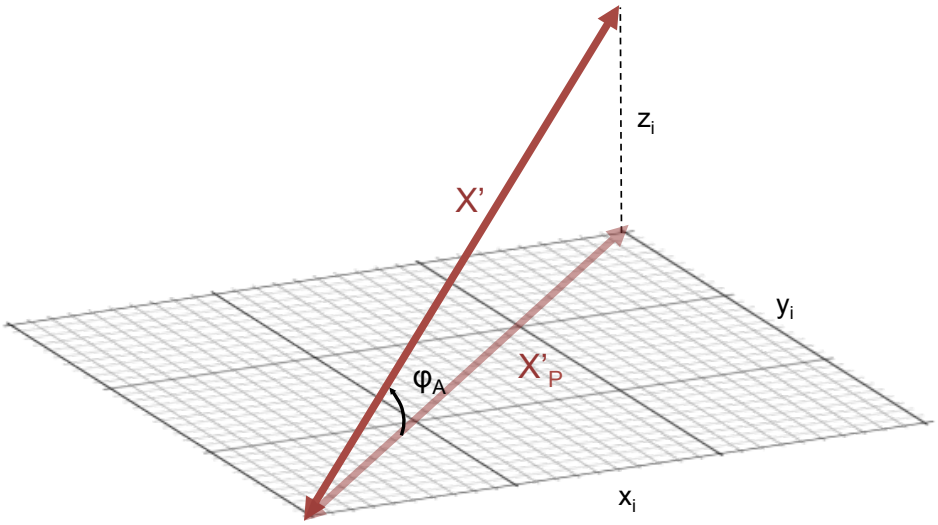

FIGURE A.4: Schematic of the original dipole X' and it's projection onto the plane X'_P. The angle between these is the angle we need to find out

The relationship between a and b and the projections of the resulting dipoles, along with the ratio of the intensities in the measurement, are now established.

$$R = \frac{Y_p'^2}{X_p'^2} = \frac{\sin^2(a)\sin^2(b) - \sin^2(a) + 1}{1 - \sin^2(a)\sin^2(b)} \tag{A.13}$$

Checking if this is sensible: in the special case that $a = 90°$ the NV axis will be parallel to the mirror plane. with $b = 45°$, it is expected that the ratio of the projections of the dipole should be equal as in fig 5. Substituting these into the above equation yields $R = 1$ as expected.

Re-arranging to find the rotation angle b, in terms of R and a that are known from the measurement:

$$\sin^2(b) = \frac{R + \sin^2(a) - 1}{\sin^2(a)(R+1)} \tag{A.14}$$

Now a, b and R, are known. It is still necessary to find the angle between the original dipole and the projected dipole in order to get the angle between the original dipole and the electric field in the plane of the cavity as in figure A.4

The vector dot product is used:

$$\vec{X'} \cdot \vec{X'_P} = |X'||X'_P| \cos\phi_A$$
$$\frac{x_1^2 + y_1^2}{\sqrt{x_1^2 + y_1^2}\sqrt{x_1^2 + y_1^2 + z_1^2}} = \cos\phi_A$$
$$\sqrt{x_1^2 + y_1^2 + z_1^2} = 1$$
$$\sqrt{x_1^2 + y_1^2} = X'_P$$
$$\phi_A = \cos^{-1}\sqrt{1 - \sin^2(a)\sin^2(b)}$$

Similarly for Y

$$\vec{Y'} \cdot \vec{Y'_P} = |Y'||Y'_P| \cos\phi_A$$
$$\phi_B = \cos^{-1}\sqrt{\sin^2(a)\sin^2(b) - \sin^2(a) + 1}$$

Bibliography

[1] T. D. Ladd, F. Jelezko, R. Laflamme, Y. Nakamura, C. Monroe, and J. L. O'Brien, "Quantum computers.," *Nature*, vol. 464, pp. 45–53, Mar. 2010.

[2] R. P. Feynman, "Simulating physics with computers," *International Journal of Theoretical Physics*, vol. 21, pp. 467–488, 1982.

[3] P. W. Shor, "Polynomial-Time Algorithms for Prime Factorization and Discrete Logarithms on a Quantum Computer," p. 28, 1995.

[4] B. P. Lanyon, J. D. Whitfield, G. G. Gillett, M. E. Goggin, M. P. Almeida, I. Kassal, J. D. Biamonte, M. Mohseni, B. J. Powell, M. Barbieri, a. Aspuru-Guzik, and a. G. White, "Towards quantum chemistry on a quantum computer.," *Nature chemistry*, vol. 2, no. February, pp. 106–111, 2010.

[5] C. Bennett and D. P. DiVincenzo, "Quantum Information and Computation," *Nature*, vol. 404, 2000.

[6] B. E. Kane, "A silicon-based nuclear spin quantum computer," *Nature*, vol. 393, pp. 133–137, 1998.

[7] L. M. Duan, M. D. Lukin, J. I. Cirac, and P. Zoller, "Long-distance quantum communication with atomic ensembles and linear optics.," *Nature*, vol. 414, no. 6862, pp. 413–418, 2001.

[8] C. Cabrillo, J. I. Cirac, P. Garcia-Fernandez, and P. Zoller, "Creation of entangled states of distant atoms by interference," *Physical Review A*, vol. 59, no. 2, p. 10, 1998.

[9] S. C. Benjamin, B. W. Lovett, and J. M. Smith, "Prospects for measurement-based quantum computing with solid state spins," *Laser & Photonics Reviews*, vol. 3, pp. 556–574, 2009.

[10] T. Harty, D. Allcock, C. Ballance, L. Guidoni, H. Janacek, N. Linke, D. Stacey, and D. Lucas, "High-Fidelity Preparation, Gates, Memory, and Readout of a Trapped-Ion Quantum Bit," *Physical Review Letters*, vol. 113, no. 22, pp. 2–6, 2014.

[11] P. E. Barclay, "Principles of QIP using diamond," in *Quantum Information Processing with Diamond* (I. Aharonovich and S. Prawer, eds.), ch. 1, p. 329, 2014.

[12] A. Zaitsev, *Optical Properties of Diamond: A Data Handbook*. Springer, 1st ed., 2001.

[13] N. Bar-Gill, L. Pham, C. Belthangady, D. Le Sage, P. Cappellaro, J. Maze, M. Lukin, a. Yacoby, and R. Walsworth, "Suppression of spin-bath dynamics for improved coherence of multi-spin-qubit systems," *Nature Communications*, vol. 3, no. May, p. 858, 2012.

[14] H. Bernien, B. Hensen, W. Pfaff, G. Koolstra, M. S. Blok, L. Robledo, T. H. Taminiau, M. Markham, D. J. Twitchen, L. Childress, and R. Hanson, "Heralded entanglement between solid-state qubits separated by three metres," *Nature*, vol. 497, no. 7447, pp. 86–90, 2013.

[15] S. D. Barrett and P. Kok, "Efficient high-fidelity quantum computation using matter qubits and linear optics," p. 5, 2004.

[16] K. J. Vahala, "Optical Microcavities," vol. 424, no. August, pp. 839–846, 2003.

[17] I. Aharonovich, A. D. Greentree, and S. Prawer, "Diamond photonics," *Nature Photonics*, vol. 5, pp. 397–405, June 2011.

[18] I. Aharonovich and E. Neu, "Diamond Nanophotonics," *Advanced Optical Materials*, vol. 2, pp. 911–928, July 2014.

[19] C. Hepp, T. Müller, V. Waselowski, J. N. Becker, B. Pingault, H. Sternschulte, D. Steinmüller-Nethl, A. Gali, J. R. Maze, M. Atatüre, and C. Becher, "Electronic structure of the silicon vacancy color center in diamond," *Physical Review Letters*, vol. 112, no. 3, pp. 1–5, 2014.

[20] L. Rogers, K. Jahnke, and M. Doherty, "Electronic structure of the negatively-charged silicon-vacancy center in diamond," *arXiv preprint arXiv: ...*, p. 8, 2013.

[21] T. Müller, C. Hepp, B. Pingault, E. Neu, S. Gsell, M. Schreck, H. Sternschulte, D. Steinmüller-Nethl, C. Becher, and M. Atatüre, "Optical signatures of silicon-vacancy spins in diamond.," *Nature communications*, vol. 5, p. 3328, 2014.

[22] L. Du Preez, *No Title*. PhD thesis, University of Witwatersrand, 1965.

[23] J. Loubser and J. van Wyk, "Electron spin resonance in the study of diamond," *Rep. Prog. Phys.*, vol. 41, p. 1201, 1978.

[24] M. Glasbeek and E. V. Oort, "Optically detected spin coherence of the diamond N-V centre in its triplet ground state," *Journal of Physics C: Solid State Physics*, p. 4835, 1988.

[25] a. Gruber, "Scanning Confocal Optical Microscopy and Magnetic Resonance on Single Defect Centers," *Science*, vol. 276, pp. 2012–2014, June 1997.

[26] C. Kurtsiefer, S. Mayer, P. Zarda, and H. Weinfurter, "Stable Solid-State Source of Single Photons," *Physical Review Letters*, vol. 85, pp. 290–293, July 2000.

[27] F. Jelezko, T. Gaebel, I. Popa, a. Gruber, and J. Wrachtrup, "Observation of Coherent Oscillations in a Single Electron Spin," *Physical Review Letters*, vol. 92, pp. 1–4, Feb. 2004.

[28] P. Tamarat, T. Gaebel, J. R. Rabeau, M. Khan, a. D. Greentree, H. Wilson, L. C. L. Hollenberg, S. Prawer, P. Hemmer, F. Jelezko, and J. Wrachtrup, "Stark shift control of single optical centers in diamond," *Physical Review Letters*, vol. 97, no. August, pp. 1–4, 2006.

[29] a. Batalov, V. Jacques, F. Kaiser, P. Siyushev, P. Neumann, L. J. Rogers, R. L. McMurtrie, N. B. Manson, F. Jelezko, and J. Wrachtrup, "Low Temperature Studies of the Excited-State Structure of Negatively Charged Nitrogen-Vacancy Color Centers in Diamond," *Physical Review Letters*, vol. 102, no. May, pp. 1–4, 2009.

[30] E. Togan, Y. Chu, a. S. Trifonov, L. Jiang, J. Maze, L. Childress, M. V. G. Dutt, a. S. Sø rensen, P. R. Hemmer, a. S. Zibrov, and M. D. Lukin, "Quantum entanglement between an optical photon and a solid-state spin qubit.," *Nature*, vol. 466, no. 7307, pp. 730–734, 2010.

[31] J. P. Hadden, J. P. Harrison, a. C. Stanley-Clarke, L. Marseglia, Y.-L. D. Ho, B. R. Patton, J. L. OBrien, and J. G. Rarity, "Strongly enhanced photon collection from diamond defect centers under microfabricated integrated solid immersion lenses," *Applied Physics Letters*, vol. 97, no. 24, p. 241901, 2010.

[32] H. Bernien, L. Childress, L. Robledo, M. Markham, D. Twitchen, and R. Hanson, "Two-photon quantum interference from separate nitrogen vacancy centers in diamond," *Physical Review Letters*, vol. 108, no. January, pp. 1–5, 2012.

[33] a. Sipahigil, M. L. Goldman, E. Togan, Y. Chu, M. Markham, D. J. Twitchen, a. S. Zibrov, a. Kubanek, and M. D. Lukin, "Quantum interference of single photons from remote nitrogen-vacancy centers in diamond," *Physical Review Letters*, vol. 108, no. April, pp. 1–5, 2012.

[34] M. V. G. Dutt, L. Childress, L. Jiang, E. Togan, J. Maze, F. Jelezko, a. S. Zibrov, P. R. Hemmer, and M. D. Lukin, "Quantum register based on individual electronic and nuclear spin qubits in diamond.," *Science (New York, N.Y.)*, vol. 316, pp. 1312–6, June 2007.

[35] P. Neumann, N. Mizuochi, F. Rempp, P. Hemmer, H. Watanabe, S. Yamasaki, V. Jacques, T. Gaebel, F. Jelezko, and J. Wrachtrup, "Multipartite entanglement among single spins in diamond.," *Science (New York, N.Y.)*, vol. 320, pp. 1326–9, June 2008.

[36] G. Balasubramanian, I. Y. Chan, R. Kolesov, M. Al-Hmoud, J. Tisler, C. Shin, C. Kim, A. Wojcik, P. R. Hemmer, A. Krueger, T. Hanke, A. Leitenstorfer, R. Bratschitsch, F. Jelezko, and J. Wrachtrup, "Nanoscale imaging magnetometry with diamond spins under ambient conditions.," *Nature*, vol. 455, pp. 648–51, Oct. 2008.

[37] J. M. Taylor, P. Cappellaro, L. Childress, L. Jiang, D. Budker, P. R. Hemmer, a. Yacoby, R. Walsworth, and M. D. Lukin, "High-sensitivity diamond magnetometer with nanoscale resolution," *Nature Physics*, vol. 4, pp. 810–816, Sept. 2008.

[38] M. S. Grinolds, S. Hong, P. Maletinsky, L. Luan, M. D. Lukin, R. L. Walsworth, and a. Yacoby, "Nanoscale magnetic imaging of a single electron spin under ambient conditions," *Nature Physics*, vol. 9, pp. 215–219, Feb. 2013.

[39] H. J. Mamin, M. Kim, M. H. Sherwood, C. T. Rettner, K. Ohno, D. D. Awschalom, and D. Rugar, "Nanoscale nuclear magnetic resonance with a nitrogen-vacancy spin sensor.," *Science (New York, N.Y.)*, vol. 339, pp. 557–60, Feb. 2013.

[40] T. Staudacher, F. Shi, S. Pezzagna, J. Meijer, J. Du, C. a. Meriles, F. Reinhard, and J. Wrachtrup, "Nuclear magnetic resonance spectroscopy on a (5-nanometer)3 sample volume.," *Science (New York, N.Y.)*, vol. 339, pp. 561–3, Feb. 2013.

[41] L. Rondin, T. Hingant, P. Maletinsky, and V. Jacques, "Magnetometry with nitrogen-vacancy defects in diamond," 2013.

[42] F. Dolde, H. Fedder, M. W. Doherty, T. Nöbauer, F. Rempp, G. Balasubramanian, T. Wolf, F. Reinhard, L. C. L. Hollenberg, F. Jelezko, and J. Wrachtrup, "Electric-field sensing using single diamond spins," *Nature Physics*, vol. 7, pp. 459–463, Apr. 2011.

[43] D. M. Toyli, C. F. de las Casas, D. J. Christle, V. V. Dobrovitski, and D. D. Awschalom, "Fluorescence thermometry enhanced by the quantum coherence of single spins in diamond.," *Proceedings of the National Academy of Sciences of the United States of America*, vol. 110, pp. 8417–21, May 2013.

[44] L. Hall, D. Simpson, and L. Hollenberg, "Nanoscale sensing and imaging in biology using the nitrogen-vacancy center in diamond," *MRS Bulletin*, vol. 38, pp. 162–167, Feb. 2013.

[45] D. Le Sage, K. Arai, D. R. Glenn, S. J. DeVience, L. M. Pham, L. Rahn-Lee, M. D. Lukin, a. Yacoby, a. Komeili, and R. L. Walsworth, "Optical magnetic imaging of living cells.," *Nature*, vol. 496, pp. 486–9, Apr. 2013.

[46] S. Pezzagna, D. Rogalla, D. Wildanger, J. Meijer, and A. Zaitsev, "Creation and nature of optical centres in diamond for single-photon emissionoverview and critical remarks," *New Journal of Physics*, vol. 13, p. 035024, Mar. 2011.

[47] Y. Chu, N. D. Leon, B. Shields, B. J. M. Hausmann, R. Evans, M. J. Burek, M. Markham, A. Stacey, A. Zibrov, D. Twitchen, M. Loncar, H. Park, P. Maletinsky, and M. D. Lukin, "Coherent optical transitions in implanted nitrogen vacancy centers Coherent optical transitions in implanted nitrogen vacancy centers," 2014.

[48] A. Krueger, "Diamond Nanoparticles: Jewels for Chemistry and Physics," *Advanced Materials*, vol. 20, pp. 2445–2449, June 2008.

[49] E. sawa, "Monodisperse single nanodiamond particulates," *Pure and Applied Chemistry*, vol. 80, no. 7, pp. 1365–1379, 2008.

[50] J. E. Butler and A. V. Sumant, "The CVD of nanodiamond materials," *Chemical Vapor Deposition*, vol. 14, pp. 145–160, 2008.

[51] a. Krüger, F. Kataoka, M. Ozawa, T. Fujino, Y. Suzuki, a.E. Aleksenskii, a. Y. Vul, and E. sawa, "Unusually tight aggregation in detonation nanodiamond: Identification and disintegration," *Carbon*, vol. 43, pp. 1722–1730, July 2005.

[52] S. Osswald, G. Yushin, V. Mochalin, S. O. Kucheyev, and Y. Gogotsi, "Control of sp2/sp3 carbon ratio and surface chemistry of nanodiamond powders by selective oxidation in air.," *Journal of the American Chemical Society*, vol. 128, pp. 11635–42, Sept. 2006.

[53] J. Tisler, G. Balasubramanian, B. Naydenov, R. Kolesov, B. Grotz, R. Reuter, J.-P. Boudou, P. a. Curmi, M. Sennour, A. Thorel, M. Borsch, K. Aulenbacher, R. Erdmann, P. R. Hemmer, F. Jelezko, and J. Wrachtrup, "Fluorescence and Spin Properties of Defects in Single Digit Nanodiamonds.," *ACS nano*, vol. 3, pp. 1959–1965, July 2009.

[54] C. Bradac, T. Gaebel, N. Naidoo, M. J. Sellars, J. Twamley, L. J. Brown, a. S. Barnard, T. Plakhotnik, a. V. Zvyagin, and J. R. Rabeau, "Observation and control of blinking nitrogen-vacancy centres in discrete nanodiamonds.," *Nature nanotechnology*, vol. 5, pp. 345–9, May 2010.

[55] T. Gaebel, C. Bradac, J. Chen, J. Say, L. Brown, P. Hemmer, and J. Rabeau, "Size-reduction of nanodiamonds via air oxidation," *Diamond and Related Materials*, vol. 21, pp. 28–32, Jan. 2012.

[56] J. Hees, A. Kriele, and O. a. Williams, "Electrostatic self-assembly of diamond nanoparticles," *Chemical Physics Letters*, vol. 509, pp. 12–15, June 2011.

[57] J. Riedrich-Möller, L. Kipfstuhl, C. Hepp, E. Neu, C. Pauly, F. Mücklich, A. Baur, M. Wandt, S. Wolff, M. Fischer, S. Gsell, M. Schreck, and C. Becher, "One- and two-dimensional photonic crystal microcavities in single crystal diamond.," *Nature nanotechnology*, vol. 7, pp. 69–74, Jan. 2012.

[58] A. Faraon, C. Santori, Z. Huang, V. M. Acosta, and R. G. Beausoleil, "Coupling of Nitrogen-Vacancy Centers to Photonic Crystal Cavities in Monocrystalline Diamond," pp. 2–6, Feb. 2012.

[59] L. Li, T. Schröder, E. H. Chen, M. Walsh, I. Bayn, J. Goldstein, O. Gaathon, M. E. Trusheim, M. Lu, J. Mower, M. Cotlet, M. L. Markham, D. J. Twitchen, and D. Englund, "Coherent spin control of a nanocavity-enhanced qubit in diamond," *Nature Communications*, vol. 6, p. 6173, 2015.

[60] B. J. M. Hausmann, B. J. Shields, Q. Quan, Y. Chu, N. P. De Leon, R. Evans, M. J. Burek, a. S. Zibrov, M. Markham, D. J. Twitchen, H. Park, M. D. Lukin, and M. Loncr, "Coupling of NV centers to photonic crystal nanobeams in diamond," *Nano Letters*, vol. 13, pp. 5791–5796, 2013.

[61] A. Faraon, P. E. Barclay, C. Santori, K.-M. C. Fu, and R. G. Beausoleil, "Resonant enhancement of the zero-phonon emission from a colour centre in a diamond cavity," *Nature Photonics*, vol. 5, pp. 301–305, Apr. 2011.

[62] J. Wolters, A. W. Schell, G. Kewes, N. Nusse, M. Schoengen, H. Doscher, T. Hannappel, B. Lochel, M. Barth, and O. Benson, "Enhancement of the zero phonon line emission from a single nitrogen vacancy center in a nanodiamond via coupling to a photonic crystal cavity," *Applied Physics Letters*, vol. 97, no. 14, p. 141108, 2010.

[63] D. Englund, B. Shields, K. Rivoire, F. Hatami, J. Vučković, H. Park, and M. D. Lukin, "Deterministic coupling of a single nitrogen vacancy center to a photonic crystal cavity.," *Nano letters*, vol. 10, pp. 3922–6, Oct. 2010.

[64] A. E. Siegman, *Lasers*. University Science Books, first ed., 1990.

[65] M. Trupke, E. a. Hinds, S. Eriksson, Z. Moktadir, E. Kukharenka, and M. Kraft, "Microfabricated high-finesse optical cavity with open access and small volume, Applied Physics Letters 87, pp. 211106," vol. M, pp. 4–6, 2005.

[66] T. Steinmetz, Y. Colombe, D. Hunger, T. W. Hänsch, a. Balocchi, R. J. Warburton, and J. Reichel, "Stable fiber-based Fabry-Pérot cavity," *Applied Physics Letters*, vol. 89, no. 2006, pp. 1–4, 2006.

[67] A. Muller, E. B. Flagg, M. Metcalfe, J. Lawall, and G. S. Solomon, "Coupling an epitaxial quantum dot to a fiber-based external-mirror microcavity," *Applied Physics Letters*, vol. 95, no. 2009, pp. 22–25, 2009.

[68] G. Cui, J. M. Hannigan, R. Loeckenhoff, F. M. Matinaga, M. G. Raymer, S. Bhongale, M. Holland, S. Mosor, S. Chatterjee, H. M. Gibbs, and G. Khitrova, "A hemispherical, high-solid-angle optical micro-cavity for cavity-QED studies.," *Optics express*, vol. 14, no. 6, pp. 2289–2299, 2006.

[69] A. Muller, E. B. Flagg, J. R. Lawall, and G. S. Solomon, "Ultrahigh-finesse, low-mode-volume Fabry-Perot microcavity.," *Optics letters*, vol. 35, no. 13, pp. 2293–2295, 2010.

[70] R. J. Barbour, P. a. Dalgarno, A. Curran, K. M. Nowak, H. J. Baker, D. R. Hall, N. G. Stoltz, P. M. Petroff, and R. J. Warburton, "A tunable microcavity," *Journal of Applied Physics*, vol. 110, no. 2011, 2011.

[71] D. Hunger, C. Deutsch, R. J. Barbour, R. J. Warburton, and J. Reichel, "Laser micro-fabrication of concave, low-roughness features in silica," *AIP Advances*, vol. 2, no. 2012, pp. 0–6, 2012.

[72] D. Hunger, T. Steinmetz, Y. Colombe, C. Deutsch, T. W. Hänsch, and J. Reichel, "A fiber FabryPerot cavity with high finesse," *New Journal of Physics*, vol. 12, p. 065038, June 2010.

[73] L. Greuter, S. Starosielec, D. Najer, A. Ludwig, L. Duempelmann, D. Rohner, and R. J. Warburton, "A small mode volume tunable microcavity: development and characterization," vol. 121105, pp. 1–5, 2014.

[74] P. R. Dolan, G. M. Hughes, F. Grazioso, B. R. Patton, and J. M. Smith, "Femtoliter tunable optical cavity arrays.," *Optics letters*, vol. 35, pp. 3556–8, Nov. 2010.

[75] Z. Di, H. V. Jones, P. R. Dolan, S. M. Fairclough, M. B. Wincott, J. Fill, G. M. Hughes, and J. M. Smith, "Controlling the emission from semiconductor quantum dots using ultra-small tunable optical microcavities," *New Journal of Physics*, vol. 14, 2012.

[76] R. Albrecht, A. Bommer, C. Pauly, F. Mücklich, A. W. Schell, P. Engel, T. Schröder, O. Benson, J. Reichel, and C. Becher, "Narrow-band single photon emission at room temperature based on a single Nitrogen-vacancy center coupled to an all-fiber-cavity," vol. 073113, 2014.

[77] F. Ding, T. Stöferle, L. Mai, A. Knoll, and R. F. Mahrt, "Vertical microcavities with high Q and strong lateral mode confinement," *Physical Review B - Condensed Matter and Materials Physics*, vol. 87, pp. 1–5, 2013.

[78] R. Albrecht, A. Bommer, C. Deutsch, J. Reichel, and C. Becher, "Coupling of a Single Nitrogen-Vacancy Center in Diamond to a Fiber-Based Microcavity," *Physical Review Letters*, vol. 110, p. 243602, June 2013.

[79] H. Kaupp, C. Deutsch, H. C. Chang, J. Reichel, T. W. Hänsch, and D. Hunger, "Scaling laws of the cavity enhancement for nitrogen-vacancy centers in diamond," *Physical Review A - Atomic, Molecular, and Optical Physics*, vol. 88, pp. 1–8, 2013.

[80] J. Riedrich-Moller, C. Arend, C. Pauly, F. Mucklich, M. Fischer, S. Gsell, M. Schreck, and C. Becher, "Deterministic coupling of a single silicon-vacancy color center to a photonic crystal cavity in diamond," *Nano . . .*, vol. 14, pp. 5281–5287, 2014.

[81] S. Schwarz, S. Dufferwiel, P. M. Walker, F. Withers, a. a. P. Trichet, M. Sich, F. Li, E. a. Chekhovich, D. N. Borisenko, N. N. Kolesnikov, K. S. Novoselov, M. S. Skolnick, J. M. Smith, D. N. Krizhanovskii, and a. I. Tartakovskii, "Two-dimensional metal-chalcogenide films in tunable optical microcavities," 2014.

[82] B. E. A. Saleh, M. C. Teich, S. Editor, and J. W. Goodman, *Fundamentals of Photonics (Wiley Series in Pure and Applied Optics)*. 1991.

[83] G. Brooker, *Modern Classical Optics*. Oxford University Press, first ed., 2002.

[84] A. A. P. Trichet, J. Foster, N. E. Omori, D. James, P. R. Dolan, G. M. Hughes, C. Vallance, and J. M. Smith, "Open-access optical microcavities for lab-on-a-chip refractive index sensing," *Lab Chip*, vol. 14, no. 21, pp. 4244–4249, 2014.

[85] E. Hecht, *Optics 4th edition*. Addison Wesley, 4th ed., 2001.

[86] H. Mabuchi and a. C. Doherty, "Cavity quantum electrodynamics: coherence in context.," *Science (New York, N.Y.)*, vol. 298, no. 5597, pp. 1372–1377, 2002.

[87] J.-M. Gerard, "Solid State Cavity-Quantum Electrodynamics with Self-Assembled Quantum Dots," in *Single Quantum Dots: Fundamentals, Applications and New Concepts* (P. Michler, ed.), p. 352, Springer, 2003.

[88] H. J. Kimble, "Strong Interactions of Single Atoms and Photons in Cavity QED ," *Physica Scripta*, vol. T76, no. 1, p. 127, 1998.

[89] E. M. Purcell, "Proceedings of the American Physical Society," *Physical Review*, vol. 69, no. 11, 1946.

[90] M. Fox, *Quantum Optics: An Introduction*, vol. 67. Oxford University Press, 2006.

[91] a. Auffèves, D. Gerace, J. M. Gérard, M. F. Santos, L. C. Andreani, and J. P. Poizat, "Controlling the dynamics of a coupled atom-cavity system by pure dephasing," *Physical Review B - Condensed Matter and Materials Physics*, vol. 81, pp. 1–10, 2010.

[92] A. Auffèves, J. M. Gérard, and J. P. Poizat, "Pure emitter dephasing: A resource for advanced solid-state single-photon sources," *Physical Review A - Atomic, Molecular, and Optical Physics*, vol. 79, pp. 1–5, 2009.

[93] M. W. Doherty, N. B. Manson, P. Delaney, F. Jelezko, and L. C. L. Hollenberg, "The nitrogen-vacancy colour centre in diamond," pp. 1–101.

[94] I. Aharonovich, S. Castelletto, D. a. Simpson, C.-H. Su, a. D. Greentree, and S. Prawer, "Diamond-based single-photon emitters," *Reports on Progress in Physics*, vol. 74, p. 076501, July 2011.

[95] M. W. Doherty, N. B. Manson, P. Delaney, and L. C. L. Hollenberg, "The negatively charged nitrogen-vacancy centre in diamond: the electronic solution," *New Journal of Physics*, vol. 13, p. 025019, Feb. 2011.

[96] J. R. Maze, a. Gali, E. Togan, Y. Chu, a. Trifonov, E. Kaxiras, and M. D. Lukin, "Properties of nitrogen-vacancy centers in diamond: the group theoretic approach," *New Journal of Physics*, vol. 13, p. 025025, Feb. 2011.

[97] F. Grazioso, B. R. Patton, P. Delaney, M. L. Markham, D. J. Twitchen, and J. M. Smith, "Measurement of the full stress tensor in a crystal using photoluminescence from point defects: The example of nitrogen vacancy centers in diamond," *Applied Physics Letters*, vol. 103, no. 2013, pp. 9–13, 2013.

[98] W. Pfaff, *Quantum Measurement and Entanglement of Spin Quantum Bits in Diamond*. PhD thesis, Delft University of Technology, 2013.

[99] R. Albrecht, *Coupling of a Single Nitrogen-Vacancy Center in Diamond to a Fiber-Based Microcavitiy*. PhD thesis, Universitat des Saarlandes, 2014.

[100] M. Fox, *Optical Properties of Solids*. Oxford University Press, 2001.

[101] K.-M. C. Fu, C. Santori, P. E. Barclay, L. J. Rogers, N. B. Manson, and R. G. Beausoleil, "Observation of the Dynamic Jahn-Teller Effect in the Excited States of Nitrogen-Vacancy Centers in Diamond," *Physical Review Letters*, vol. 103, p. 256404, Dec. 2009.

[102] Y. Shen, T. Sweeney, and H. Wang, "Zero-phonon linewidth of single nitrogen vacancy centers in diamond nanocrystals," *Physical Review B*, vol. 77, p. 033201, Jan. 2008.

[103] T. Plakhotnik, M. W. Doherty, and N. B. Manson, "The electron-phonon processes of the nitrogen-vacancy center in diamond," *arXiv*, vol. 081203, no. 1, pp. 1–6, 2015.

[104] J. Wolters, N. Sadzak, A. W. Schell, T. Schröder, and O. Benson, "Measurement of the ultrafast spectral diffusion of the optical transition of nitrogen vacancy centers in nano-size diamond using correlation interferometry," *Physical Review Letters*, vol. 110, no. January, pp. 1–5, 2013.

[105] F. Inam, M. Steel, and S. Castelletto, "Effects of the hosting nano-environment modifications on NV centres fluorescence emission," *Diamond and Related Materials*, vol. 45, pp. 64–69, May 2014.

[106] A. Beveratos, R. Brouri, T. Gacoin, J.-p. Poizat, and P. Grangier, "Nonclassical radiation from diamond nanocrystals," *Physical Review A*, vol. 64, pp. 2–5, 2001.

[107] H.-Q. Zhao, M. Fujiwara, M. Okano, and S. Takeuchi, "Observation of 1.2-GHz linewidth of zero-phonon-line in photoluminescence spectra of nitrogen vacancy centers in nanodiamonds using a Fabry-Perot interferometer.," *Optics express*, vol. 21, pp. 29679–86, Dec. 2013.

[108] C.-H. Su, A. D. Greentree, and L. C. L. Hollenberg, "Towards a picosecond transform-limited nitrogen-vacancy based single photon source," *Optics Express*, vol. 16, p. 6240, Apr. 2008.

[109] R. Albrecht, A. Bommer, C. Deutsch, J. Reichel, and C. Becher, "Supplemental Material : Coupling of a single NV center in diamond to a fiber-based microcavity," *Physical Review Letters*, vol. 83, no. 425, pp. 1–12, 2013.

[110] M. S. Kaurav, *Engineering Chemistry with Laboratory Experiments*. PHI Learning, 2011.

[111] T. Dieing, O. Hollricher, and J. Toporski, *Confocal Raman Microscopy*. Springer, 2010.

[112] J. Hodkiewicz and T. F. Scientific, "Characterizing Carbon Materials with Raman Spectroscopy," tech. rep.

[113] S. Prawer and R. J. Nemanich, "Raman spectroscopy of diamond and doped diamond.," *Philosophical transactions. Series A, Mathematical, physical, and engineering sciences*, vol. 362, pp. 2537–65, Nov. 2004.

[114] A. C. Ferrari, "Raman spectroscopy of graphene and graphite: Disorder, electron-phonon coupling, doping and nonadiabatic effects," *Solid State Communications*, vol. 143, pp. 47–57, July 2007.

[115] J. Filik, "Raman spectroscopy : a the lightest touch," vol. 17, no. 5, 2005.

[116] A. C. Ferrari and J. Robertson, "Raman spectroscopy of amorphous, nanostructured, diamond-like carbon, and nanodiamond.," *Philosophical transactions. Series A, Mathematical, physical, and engineering sciences*, vol. 362, pp. 2477–512, Nov. 2004.

[117] Malvern, *Zetasizer Nano User Manual*. mano317 ed., 2007.

[118] P. R. Dolan, *Ultra-Small Open Access Microcavities for Enhancement of the Light-Matter Interaction*. PhD thesis, University of Oxford, 2012.

[119] B. Sun, P. S. Salter, and M. J. Booth, "High conductivity micro-wires in diamond following arbitrary paths," *Applied Physics Letters*, vol. 105, no. 23, p. 231105, 2014.

[120] H. Kaupp, C. Deutsch, H.-c. Chang, J. Reichel, and W. H. Theodor, "Scaling laws of the cavity enhancement for NV centers in diamond," pp. 1–8, 2013.

[121] I. Pocsik, M. Hundhausen, M. Koos, and L. Ley, "Origin of the D peak in the Raman spectrum of microcrystalline graphite," pp. 1083–1086, 1998.

[122] a. Ferrari and J. Robertson, "Origin of the 1150-cm-1 Raman mode in nanocrystalline diamond," *Physical Review B*, vol. 63, no. 12, pp. 2–5, 2001.

[123] O. A. Williams, J. Hees, C. Dieker, W. Ja, L. Kirste, and C. E. Nebel, "Size-Dependent Reactivity of Diamond," *ACS nano*, vol. 4, no. 8, 2010.

[124] A. Faraon, C. Santori, Z. Huang, V. M. Acosta, and R. G. Beausoleil, "Coupling of Nitrogen-Vacancy Centers to Photonic Crystal Cavities in Monocrystalline Diamond," *Physical Review Letters*, vol. 109, p. 033604, July 2012.

[125] P. Siyushev, V. Jacques, I. Aharonovich, F. Kaiser, T. Müller, L. Lombez, M. Atatüre, S. Castelletto, S. Prawer, F. Jelezko, and J. Wrachtrup, "Low-temperature optical characterization of a near-infrared single-photon emitter in nanodiamonds," *New Journal of Physics*, vol. 11, 2009.

[126] R. Albrecht, A. Bommer, C. Deutsch, J. Reichel, and C. Becher, "Coupling of a Single Nitrogen-Vacancy Center in Diamond to a Fiber-Based Microcavity," *Physical Review Letters*, vol. 110, p. 243602, June 2013.